2018

Investigation of Iron Selenide Superconducting Thin Films Fabricated by Pulsed Laser Deposition

Wenbin Qiu
University of Wollongong

UNIVERSITY
OF WOLLONGONG
AUSTRALIA

Investigation of Iron Selenide Superconducting Thin Films Fabricated by Pulsed Laser Deposition

A thesis submitted for fulfilment of the requirements for the award of the academic degree

DOCTOR of PHILOSOPHY

From the

UNIVERSITY OF WOLLONGONG

By

QIU Wenbin

B. Eng., M. Sc.

Institute for Superconducting and Electronic Materials

Faculty of Engineering and Information Sciences

University of Wollongong, NSW Australia

6th September 2018

Certification of Originality

I, Wenbin Qiu, declare that the work presented in this thesis was totally carried out by myself in the Institute for Superconducting and Electronic Materials (ISEM), at the University of Wollongong, NSW, Australia unless otherwise referenced or acknowledged. This document has not been submitted to any other academic institution for a qualification.

Wenbin Qiu

6th September 2018

Dedication

To my beloved family

Acknowledgements

First of all, I would like to express my highest appreciation to my principal supervisor, Dr. Zongqing MA. With the support of his Discovery Early Career Researcher Award (DECRA) project, I experienced a start to my Ph.D. career by receiving comprehensive support from not only my academic supervision, but also my strong financial funding. Dr. MA's active guidance and encouragement in my work and life are of great significance to me. I really cherish the time that we worked together and made achievements, one after another!

I am so pleased to show my gratitude to one of my co-supervisors, Prof. Shi Xue DOU, who is also acting as the director of the Institute for Superconducting and Electronic Materials (ISEM), University of Wollongong (UOW). Prof. DOU is a legend to me as he established the ISEM in 1994 based on his world-leading research power and managed the institute to develop as the state-of-the-art research organization that it is nowadays. Thanks to the world-class scientific platform provided by ISEM, I was able to start my research from a higher level and pursue more meaningful results. In addition, I would like to thank Prof. Dou for accepting my Ph.D. application and recommending me to Dr. Zongqing MA in 2014. His kind support and advice helped me greatly during my Ph. D. study.

My sincere thanks to Dr. Md Shahriar Al Hossain, another co-supervisor of mine. Dr. Hossain was always ready to give me valuable help from various aspects, including experimental issues, article suggestions, tips on living, financial support, etc. I really admire his tremendous network management skills, which have promoted the well-developed cooperation between our group and numerous collaborators.

I would like to acknowledge Dr. Gilberto Casillas Garcia, Dr. David Mitchell, Mr. Tony Romeo, and Dr. Mitchell Nancarrow for their kind help with technical support with respect to the electron microscopes in the Electron Microscopy Center (EMC), UOW. Their great expertise significantly improved the quality of our works.

My cordial gratitude to A/Prof. Germanas Peleckis for offering instrument-related advice, arranging administrative issues, and providing the training on the PPMS and XRD. I sincerely acknowledge Dr. Xun XU and Dr. Dongqi SHI for their technical support in regard to various instruments, Prof. Xiaolin WANG, A/Prof. Zhengxiang CHENG, Dr. Zhi LI, and Dr. Wenping SUN for fruitful discussions and critical

comments on my works, Mr. Robert Morgan, Mr. Paul Hammersley, Mr. John Wilton, and Mr. Mathew Davies for the workshop support, Mrs. Crystal Mahfouz, Mrs. Narelle Badger, Mrs. Naomi Davies, and Mr. Paul Scully for the daily administration and procurement, Mrs. Joanne George and Dr. Candace Gabelish for their responsible management of laboratory safety, and Dr. Konstantin Konstantinov, the Head of Postgraduate Studies (HPS), for providing kind support in regard to higher-degree research. I am grateful to Dr. Tania Silver for the critical reading of my manuscripts and thesis.

I would like to thank my friends and colleagues Dr. Dipak Patel, Dr. Jonathan Knott, Dr. Jincheng ZHUANG, Mr. Haifeng FENG, Dr. Özlem Çi çek, Dr. Lina SANG, Mr. Hyunseock Jie, Dr. Chandrasekar Subramaniyam, Dr. Sudipta Pramanik, Mr. Guoqiang ZHAO, Dr. David Cortie, Dr. Feixiang XIANG, Dr. Hong GAO, Dr. Dan ZHANG, Mr. Weiyao ZHAO, Ms. Lei CHEN, Mr. Long REN, Mr. Zhixin TAI, Ms. Yajie LIU, Mrs. Yanhua SUN, Mr. Alaa HAMED, and Mr. Yao LU for their kind support and discussions. My Ph.D. studies would have been far less delightful without you.

I owe great thanks to Prof. Chuanbing CAI at Shanghai University for his supervision during my master's degree and for providing me with the opportunity to study for a Ph.D. in ISEM. I also want to thank my collaborators from Tianjin University, Prof. Yongchang LIU, Ms. Qingshuang MA, Ms. Fang CHENG, Ms. Xin WEN, Ms. Xinhua LI, Ms. Huanhuan ZHAO, Mr. Zhi DONG, and Mr. Nan LIU for their helpful discussions and collaborations.

This thesis work has been conducted under the Australian Research Council (ARC) DECRA project (No. DE140101333) of Dr. Zongqing Ma. The tuition and stipend were supported by the University Postgraduate Award (UPA) and the International Postgraduate Tuition Award (IPTA), which were kindly offered by the University of Wollongong.

My utmost appreciation to my parents, Mr. Jianliang QIU and Mrs. Panqiu TAO, for bringing me into this world. Very special thanks to my beloved wife, Mrs. Wangweilai XIANG for unconditionally supporting me since the first day we met. What you have sacrificed and compromised over these years deserves my highest compliment!

In the end, I would like to express my sincere gratitude to all the people who have supported me so far. Without your selfless endeavors, I would definitely not have been able to complete this thesis. Thank you again for helping me to come through all

the problems that I have encountered. Live long and prosper!

Abstract

Superconductivity is one of the most attractive research projects in condensed matter physics. Among various types of different superconductors, the family of iron-based superconductors has always been a lively topic since the discovery of the superconductivity in $LaFeAsO_{1-x}F_x$ in 2008. The conflict between the necessity of Fe element in this type of superconductor and the superficial thinking on the detrimental effect of ferromagnetism on superconductivity makes iron-based superconductivity both intriguing and unconventionally elusive. In material science, iron selenide (FeSe) is a very promising candidate for exploring the mechanism of iron-based superconductivity due to its having the simplest binary composition and much less toxicity than iron-based superconductors containing As. Since the sign of a dramatically high superconducting transition temperature (T_c) over 77 K in a 1 unit-cell FeSe layer grown on $SrTiO_3$ (STO) substrate was reported in 2012 by a group from China, a flourishing upsurge of FeSe thin films was triggered, and the popularity of superconducting research was rejuvenated. The veil between the scientists and the mystery of iron-based superconductivity has never been so thin. However, plenty of issues still remained to be solved, such as why the same thin film material, FeSe, shows totally different superconducting behaviors in the monolayer and the film with typical thicknesses. In this thesis work, the research subject is FeSe superconducting thin film fabricated by the pulsed laser deposition (PLD) method. The emphasis is on the interface effect and the influence of the external coating process on the superconductivity of FeSe thin films. Enhanced superconducting performance was obtained, and the corresponding mechanism was clarified, based on various characterization methods such as physical property measurements and high-resolution electron microscopy.

The investigations into the interfaces of FeSe thin films on various substrates have manifested the great potential for high-temperature-superconductivity in this unique system. Single-crystal calcium fluoride (CaF_2) (100) substrate was chosen as the growth substrate for the FeSe thin films in this work. The first part of this work is related to the interlayer between FeSe and CaF_2 substrate. FeSe thin films with a series of thicknesses were grown on CaF_2 substrates by the PLD technique, and detailed information was gleaned from the FeSe/CaF_2 interface by using scanning transmission electron microscopy (STEM). Intriguingly, the universal presence of a calcium selenide

(CaSe) interlayer was discovered, with a thickness of approximately 3 nm between FeSe and CaF_2 in all the samples, regardless of the thickness of the FeSe layers. A slight Se-deficiency occurs in the FeSe layer due to the formation of the CaSe interlayer. This Se-deficiency is generally negligible except for the case of an ultra-thin FeSe film (8 nm in thickness), in which the stoichiometric deviation from FeSe is big enough to suppress the superconductivity. Meanwhile, in the overly thick FeSe layer (160 nm in thickness), vast precipitates were found and characterized as Fe-rich phases, which bring about degradation in superconductivity. Consequently, the thickness dependent critical temperature (T_c) of the FeSe thin films was investigated, and one of our atmosphere-stable FeSe thin films (127 nm) possesses the T_c^{onset} / T_c^{zero} ratio of 15.1 K / 13.4 K, currently the highest on record in the class of FeSe thin films with practical thickness. Our results provide a new perspective for exploring the mechanism of superconductivity in FeSe thin film via high-resolution STEM. Moreover, approaches that might improve the quality of FeSe/CaF_2 interfaces are also proposed for further enhancing the superconducting performance in this system.

The stability of the as-grown FeSe thin film at atmosphere is of great importance for the potential application. FeTe has been widely used as a protecting layer for monolayer and multilayer FeSe thin films fabricated by molecular beam epitaxy (MBE), and a FeTe layer with about 10 unit cells is capable of making the underlying FeSe layer robust enough for a variety of characterizations. However, very few works were focusing on interfacial effect between FeTe and FeSe layers prepared by PLD method. The second part of this research work was focused on bilayer PLD-FeTe/FeSe heterostructures and the subtle variation of the Fe 3d orbital was revealed by electron energy loss spectroscopy (EELS). Unlike monolayer Fe-chalcogenide (Fe-*Ch*)/ STO, which possesses the potential for high-temperature superconductivity (HTS), regular Fe-*Ch* thin film that is grown on a non-STO substrate by the PLD method shows totally different superconducting behaviour and a different mechanism. Although regular Fe-*Ch* thick films grown on CaF_2 generally show the highest T_c compared with those grown on any other substrates, considerable suppression of T_c always occurs when the Fe-*Ch* layer is reduced to only a few atomic-layers (~ 10 nm), with the reason still under debate. Here, an enhanced $T_c \approx 17.6$ K in a iron telluride (FeTe)/FeSe bilayer heterostructure grown on CaF_2 substrate was reported. Generally, the Fe-*Ch* film on CaF_2 is expected to be one order of magnitude greater in thickness to achieve similar performance. Hall effect measurements revealed the dominant hole-type carriers in the

films in this work, which is similar to the case of pressurized bulk FeSe single crystal and other PLD-grown multilayer FeSe films, while in sharp contrast to heavily electron-doped HTS systems. According to EELS results, direct evidence of the nanoscale phase separation with a form of a fluctuation of Fe-L_3/L_2 ratio near FeTe/FeSe interface was observed. In detail, a several-unit-cell-thick Fe(Se,Te) diffusion layer showed a higher Fe-L_3/L_2 ratio than either FeTe or FeSe layers, which reflects the low Fe *3d* electron occupancy and its possible relationship with enhanced T_c in this work. Our work clarifies the importance of the FeTe/FeSe interface in reviving the superconductivity in ultrathin Fe-*Ch* grown on CaF_2 substrate, contributing to a more unified understanding of the unconventional Fe-*Ch* superconductivity.

A post-deposition of K element onto non-superconducting multilayer FeSe thin film has been well developed in reviving the HTS which is generally absent once the FeSe layer is more than one unit-cell. Inspired by the heavy electron-doping introduced by alkali metal, K, the exploration of the Mg-coating process onto the FeSe thin films grown by PLD method is presented in the third part. In contrast to its bulk crystal, FeSe in thin film form exhibits better superconductivity performance, which recently has attracted much interest around the world towards its fundamental research as well as its potential applications. In this work, tuning the superconductivity in FeSe thin films was achieved by a simple Mg coating technique. T_c was enhanced from 10.7 K in the pristine FeSe films with a thickness of 60 nm to 13.4 K with an optimal amount of Mg-coating process, which is approximately 1.5 times higher than that of bulk crystals. This is the first time that the enhancement of T_c has been achieved in regularly-prepared FeSe thin films via an external coating process with the element Mg. Moreover, these Mg-coated FeSe films are quite stable in atmosphere with an upper critical field (H_{c2}) as high as 32.7 T and T_c^{zero} as high as 12 K, implying their outstanding potential for high-field applications. It was found that the Mg-coating process does introduce some electron-doping and results in a distinct increase in superconducting performance, but the electron-type carriers were not strong enough to overturn the hole-dominant condition in all the samples regardless of the deposition time of the Mg-coating process. This is probably because Mg only diffused onto the top few layers of FeSe thin films, which was confirmed by cross-sectional EELS results. In addition, Mg-coating was able to induce the superconducting transition in ultrathin-FeSe thin films as well. This was attributed to the effect of external electron-doping, similar to other alkaline-element doping scenarios. These results provide a new strategy to improve the superconductivity

of 11 type Fe-based superconductors and will help us to understand the intrinsic mechanism of this unconventional superconducting system.

Table of Contents

List of Figures

List of Tables

Nomenclature

Abbreviations

ISEM	Institute for Superconducting and Electronic Materials
AIIM	Australian Institute for Innovative Materials
UOW	University of Wollongong
HDR	Higher Degree Research
FeSe	Iron selenide
UC	Unit-cell
STO	$SrTiO_3$
PLD	Pulsed laser deposition
CaF_2	Calcium fluoride
STEM	Scanning transmission electron microscope
CaSe	Calcium selenide
EELS	Electron energy loss spectroscopy
Fe-*Ch*	Fe-Chalcogenide
FeTe	Iron telluride
HTS	High-temperature superconductivity
LN_2	Liquid nitrogen
3D, 2D	Three-dimensional, two-dimensional
BCS	Bardeen, Cooper, and Schriefer
LHe	Liquid helium
GPa	Gigapascal
YBCO	Yttrium barium copper oxide
MgB_2	Mg diboride
AFM	Antiferromagnetism
Nb_3Sn	Niobium tin
NbTi	Niobium titanium
MRI	Magnetic resonance imaging
SQUID	Superconducting quantum interference device
MBE	Molecular beam epitaxy
DFT	Density functional theory
DOS	Density of states
Nd:YAG	Neodymium-doped yttrium aluminium garnet (Nd: $Y_3Al_5O_{12}$)
MgO	Mg oxide
LSAT	$(La, Sr)(Al, Ta)O_3$
LAO	$LaAlO_3$
PVD	Physical vapour deposition
UHV	Ultra-high vacuum
IBAD	Ion beam assisted deposition
KrF, ArF	Krypton fluoride, Argon fluoride
bcc	Body-centred cubic
SDW	Spin-density-wave
ARPES	Angle-resolved photoemission spectroscopy
NMR	Nuclear magnetic resonance
SIT	Superconducting-insulating transition
EDLT	Electric double-layer transistor
YSZ	Yttrium-stabilized zirconia
LSAO	$LaSrAlO_4$
TEM	Transmission electron microscope
EDS	Energy dispersive X-ray spectroscopy

RABiTS	Rolling assisted Bi-axially Textured Substrate
FST	$FeSe_{1-x}Te_x$
HRTEM	High-resolution transmission electron microscopy
eV	Electron volt
FeS	Iron sulfide
DC	Direct current
AC	Alternating current
STM	Scanning tunneling microscope
EDC	Energy distribution curve
STS	Scanning tunneling spectroscope
RHEED	Reflection high-energy electron diffraction
CAS	Chinese Academy of Sciences
PID	Proportional-integral-derivative
XRD	X-ray diffraction
FIB	Focused ion beam
PPMS	Physical Property Measurement System
SEM	Scanning electron microscope
SE	Secondary electron
BSE	Backscattered electron
MFP	Mean free path
SAED	Selected-area electron diffraction
HAADF	High-angle annular dark-field
CCD	Charge-coupled device
VSM	Vibrating sample magnetometer
ZFC	Zero-field cooling
FC	Field cooling
MR	Magnetoresistance
PCA	Principal component analysis
FESEM	Field-emission scanning electron microscope
FFT	Fast Fourier transform
XPS	X-ray photoelectron spectroscopy
r.t.	Room temperature
PIT	Powder-in-tube
ITER	International Thermonuclear Experimental Reactor
TF	Toroidal field
PF	Poloidal field
CS	Central solenoid
CC	Correction coil
NIFS	National Institute for Fusion Science

Symbols

λ_L	London Penetration Depth
μ_0	Magnetic permeability of free space
ζ	Coherence length
κ	Ginzburg-Landau Parameter
γ	Anisotropy factor
θ^{GB}	Grain-boundary angle, misorientation angle
λ	Wavelength
ρ	Electrical resistivity
χ	Magnetic susceptibility
$\lambda(\omega)$	Electron-phonon coupling strength
T_c, T_c^{onset}, T_c^{zero}	Superconducting transition temperatures

K	Kelvin
$\boldsymbol{J_c}$	Critical current density
$\boldsymbol{H_c}$	Critical magnetic field
$\boldsymbol{T}$	Temperature
$\boldsymbol{B}$	Magnetic induction
$\boldsymbol{H}$	Magnetic field intensity
$\boldsymbol{M}$	Intensity of magnetization
$\boldsymbol{j_s}$	Superconducting current density
$\boldsymbol{n}$, $\boldsymbol{n_s}$	Density of superconducting electrons
T	Tesla (a unit of magnetic flux density)
$\boldsymbol{H_{c1}}$/$\boldsymbol{H_{c2}}$	Lower/higher critical field
$\boldsymbol{\Delta^{SC}}$	Superconducting energy gap
$\mathbf{N(E_F)}$	Energy density at the Fermi energy
$\boldsymbol{H_{irr}}$	Irreversibility field
$\boldsymbol{\Delta T_c}$	Width of superconducting transition
$\boldsymbol{T_s}$	Structural transition temperature
$\boldsymbol{T_N}$	Néel temperature
$\boldsymbol{R_H}$	Hall coefficient
$\boldsymbol{F_P}$	Pinning force
$\boldsymbol{k_B}$	Boltzmann constant
$\mathbf{V_G}$	Bias voltage
$\boldsymbol{e}$	Electron
$\boldsymbol{R_{xy}}$	Hall resistance
$\boldsymbol{n}$	Charge carrier concentration
at. %	Atomic percentage
wt. %	Weight percentage
$\boldsymbol{I_c}$	Transport critical current

Chapter 1

1 Introduction

1.1 Background of the Thesis Research Project

To cope with the worldwide energy crisis, the issue of "how to make use of energy in an efficient way" has been raised for decades. Because they feature zero-loss in transporting current, the applications of superconductors will no doubt save considerable energy from power source that would have been wasted by using conventional conductors. Furthermore, the scientific management of energy is expected to be improved due to the much larger capacity of superconductors for carrying engineering current than conventional ones. In most cases, however, very low ambient temperature (generally lower than the boiling point of liquid nitrogen (LN_2)) is a prerequisite for enabling superconductors. Hence, efforts need to be made to either increase the superconducting critical transition temperature (T_c) of current superconductors or discover new kinds of superconductor with higher T_c and other superconducting performance.

Fe element used to be considered incompatible with superconductivity because the locally polarized spin will prevent any Cooper pairs from bonding together[1]. After the discovery of superconductivity in layered $La[O_{1-x}F_x]FeAs$[2], however, an upsurge of iron-based superconductors was triggered, and the topic has been hot for almost a decade. In the iron-based superconducting family, iron selenide (FeSe)[3] has the simplest structure with a binary chemical composition, which renders it an appropriate candidate for exploring the intrinsic mechanism of iron-based superconductors. FeSe in the thin film form is of great interest for fundamental research due to the unique properties that are only found in thin films and the abundant potential for improvement in its superconducting performance compared with bulk samples.

This thesis presents original research work done on FeSe thin films fabricated by the pulsed laser deposition (PLD) technique. Investigations have proceeded to clarify the intrinsic mechanism of as well as the various effects (e.g. interface, doping) on the superconductivity of FeSe thin films. Some of the results provide new avenues to

pursue higher superconductivity and simultaneously help to fill up the gaps in comprehensively interpreting the mechanism of this type of unconventional superconductor.

1.2 A Brief Introduction to Superconductivity

1.2.1 Discovery of Superconductivity

In some materials, the electrical resistivity suddenly vanishes to absolute zero when the ambient temperature is below a certain temperature. This phenomenon was discovered by Dutch physicist H. Kammerlingh Onnes in 1911 when he was trying to cool down mercury (Hg) to 4.2 K[4] (see Fig. 1-1). Then the discoverer named the phenomenon as "superconductivity"[5] to emphasize the significance. The astonishing discovery was followed by the reports of similar resistivity-vanishing phenomena in plenty of other metals under certain temperatures, such as Lead (7.2 K), Tin (3.7 K), Niobium (9.3 K), etc. The temperature at which the resistivity vanishes is called the *critical transition temperature* (T_c).

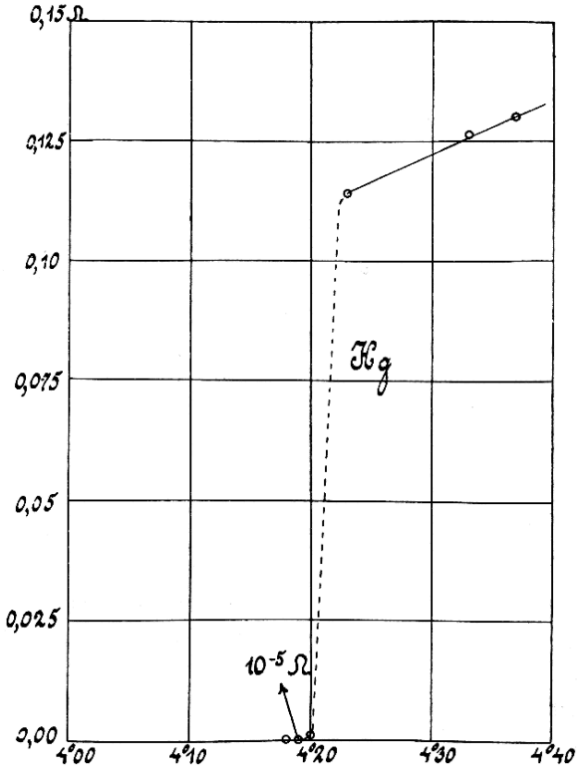

Figure 1-1. The original plot of the superconducting transition in mercury at 4.2 K[4].

Generally, superconductivity only survives at an ambient temperature below the T_c of the material. Apart from the temperature factor, superconductivity is also

restrained by the density of the current passing through the body and the surrounding magnetic field. That is to say, the *critical current density* (J_c) and the *critical magnetic field* (H_c) are another two crucial factors for evaluating the performance of a superconductor. In a particular material, there is a three-dimensional (3D) dome-shaped surface, which is called as the "critical surface" and can be illustrated based on the three factors (*T*, *H*, and *J*) serving as three axes. As can be concluded from Fig. 1-2, the material will always remain in a superconducting state as long as the state indicated by the three factors dwells within the 3D volume. Otherwise, passing above the critical surface in any direction will lead to the collapse of superconductivity, regardless of the other parameters. Furthermore, a parabolic law can be utilized to approximate $H_c(T)$ as per[6]:

$$H_c(T) \approx H_c(0)[1 - t^2]$$

where t equals to T/T_c.

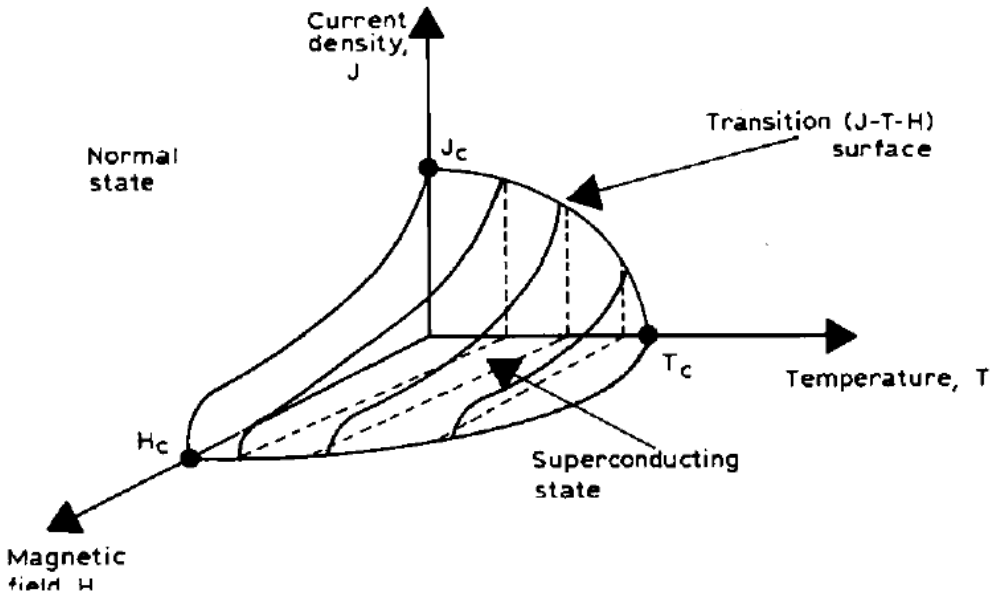

Figure 1-2. The ideal critical surface of a superconductor.[7]

1.2.2 Meissner Effect

In addition to the zero resistivity property, another unique characteristic exhibits in a superconducting material below T_c. It is called complete diamagnetism, or the well-known "Meissner Effect". In 1933, W. Meissner and R. Ochsenfeld found the magnetic field was completely expelled from the interior body of superconducting tin and lead bulks[8], irrespective of how the magnetic field was applied upon the samples. Fig. 1-3 simply shows how the external magnetic flux lines are expulsed from a material in

Meissner State. A spontaneous field is generated with opposite direction and exactly identical scale as the external field so that the net magnetic induction inside a superconductor is zero ($\boldsymbol{B} = 0$). In fact, Meissner Effect is more fundamental than the zero electrical resistivity in describing superconductivity because a perfect electrical conductor is a prerequisite for a material to become complete diamagnetic. Nowadays, Meissner Effect has been widely utilized in the application of superconductors, especially the notion of ultrahigh field superconducting magnets[9].

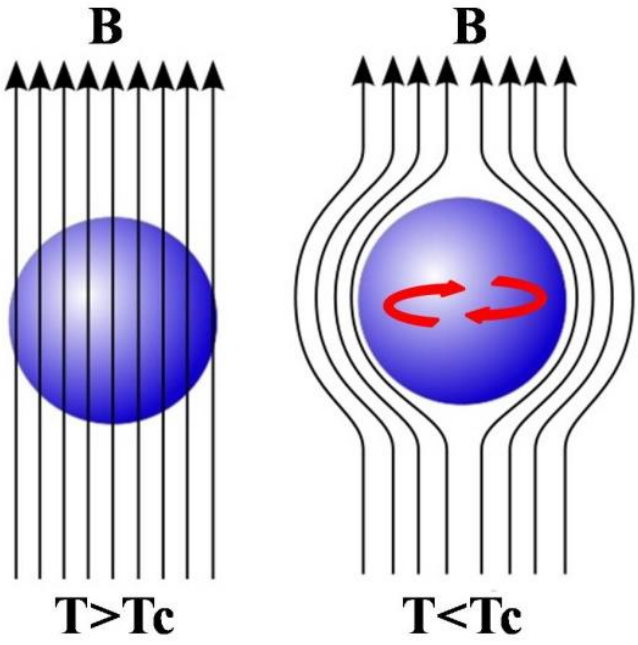

Figure 1-3. Diagram of the Meissner Effect. The black arrows indicate flux lines of the external magnetic field, while the red arrows show the surface supercurrent generated in the superconducting material.

1.2.3 Important Theoretical Works on Superconductivity

It is arbitrary to design, carry out, interpret or extend experimental work properly without the guide of solid theoretical studies, especially in the case of superconductivity in the early stage. Any systematic theory that can somehow reveal part of the mysteries in elusive superconductivity is considered as an astonishing breakthrough. For instance, three out of five Nobel Laureates in the field of superconductivity were mainly focused on theoretical demonstrations ("BCS Theory" in 1972, "Josephson Effects" in 1973, and "Superfluids & Superconductors" in 2003). There is no doubt that these precious contributions boosted the construction and cognitive level of our understanding of the concept of superconductivity.

1.2.3.1 London Penetration Depth (λ_L)

Magnetization basically consists of microcurrent. Hence, the Meissner Effect is

attributed to the permanent distribution of supercurrent on the surface of a superconductor, so that the internal part exhibits the state

$$\boldsymbol{B} = \boldsymbol{H} = \boldsymbol{M} = 0.$$

That is to say, there is an interior relationship between zero resistivity and the Meissner Effect, although they show a distinct difference in appearance. In 1935, a phenomenological theory[10] was proposed by F. London and H. London, which was expressed as

$$\nabla \times (\Lambda \boldsymbol{j}_s) = -\boldsymbol{B} \qquad (\Lambda = m/(n_s q^2))$$

to explain the diamagnetism effect in a superconductor, where n_s is the number of electrons without resistance and $\boldsymbol{j}_s$ is the superconducting current density. The Londons' further investigation showed that a superconductor cannot expel all the magnetic flux lines out of its interior. They put forward their observation on supercurrent flow within a penetration depth (λ_L) at the surface of a superconductor symbolized as

$$\lambda_L = \sqrt{\frac{m}{\mu_0 n q^2}}$$

where m and q stand for the mass and charge of an electron, respectively, and n is the density of the superconducting electrons. By using the London Equation, one can easily deduce that the magnetic field within λ_L exponentially decreases with increasing the distance from the edge of the specimen. In addition, λ_L is also found to diminish with falling temperature, which can be approximated by the following equation

$$\lambda(\mathrm{T}) \approx \lambda(0)\,[1 - t^4]^{-0.5}$$

where t equals to T/T_c. Actually, the behaviour of λ_L indicates the variation of the quantity of superconducting electrons n_s, which increases from zero beyond T_c to a maximum value at 0 K.

1.2.3.2 Coherence Length (ζ) and Type I and Type II Superconductors

It was found that the penetration depth $\lambda^{exp.}$ obtained from experiments was larger than λ_L in many cases. This discrepancy was solved by A. B. Pippard[11] in 1955 by introducing a parameter called the coherence length (ξ) for the non-local generalization of the London Theory. ξ is constant in value in the core part of a superconducting region. It gradually decreases upon approaching the normal region, and it eventually becomes zero. Fig. 1-4 shows how penetration depth λ and the coherence length ξ behave at a normal-superconducting interface. Usually, ξ is about 10^{-4} cm, much larger than λ_L, which is normally 10^{-6} cm.

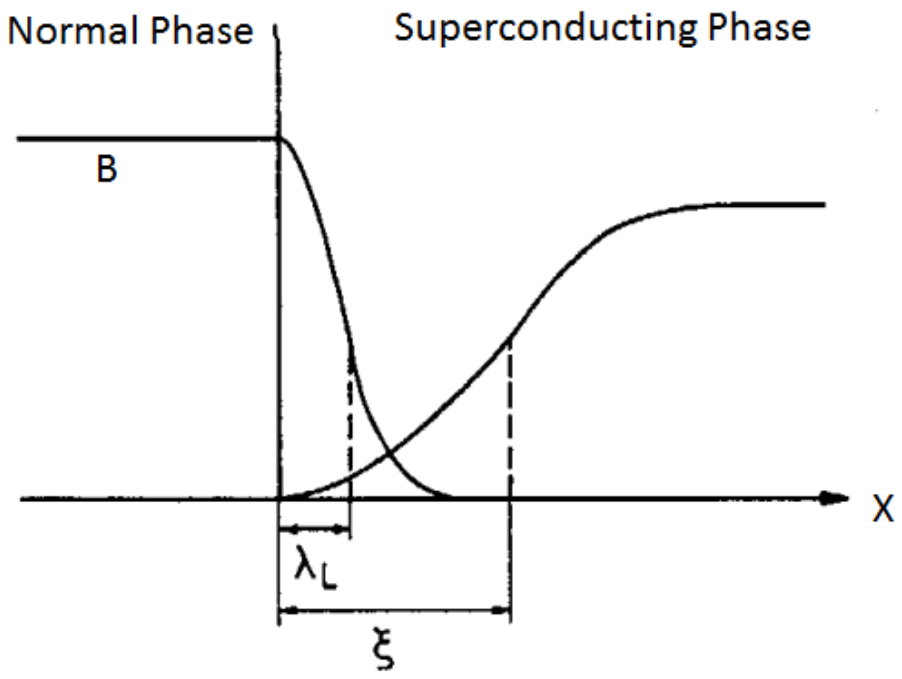

Figure 1-4. The typical distribution of Penetration Depth (λ) and Coherence Length (ζ) inside a superconductor at a normal-superconducting interface.

Many pure metals show zero resistance along with Meissner Effect at relatively low temperatures. They are classified as Type I superconductors, known as "soft superconductors". This type of superconductor strictly fulfils the diamagnetism property by leaving no interior magnetic field inside when they are in the superconducting state. Very small external magnetic field strength (typically less than 0.1 T), however, can lead to an abrupt transition from superconducting to the normal state. Hence, Type I superconductors are not very suitable in practice for real applications.

On the contrary, the other candidates, the Type II superconductors (also known as the "hard superconductors") are dramatically different. In 1930, when the superconductivity in lead-bismuth alloys was found survive a field of nearly 20,000 Gauss by W. de Haas and J. Voogd, the history of this novel kind of superconductor with quite good field-endurance began. Unlike a Type I superconductor, which has only one low critical magnetic field (H_c), there are two critical magnetic fields in Type II superconductors, the lower critical field (H_{c1}) and the upper critical field (H_{c2}). Up to H_{c1}, both types of superconductors completely expel magnetic field from their interior ("Meissner Phase"). When the external field lies between H_{c1} and H_{c2}, however, a mixed state (also called the "vortex state") consisting of both normal and superconducting region occurs only in Type II superconductors (see Fig. 1-5). In this

peculiar state, the superconductor is partially penetrated by flux lines, which appear to be pinned inside the bulk. Thanks to those metastable flux lines, Type II superconductors are able to carry much higher J_c than Type I superconductors under high magnetic fields. Once the external magnetic field exceeds H_{c2}, Type II superconductors are completely penetrated by flux lines and superconductivity no longer exists. Therefore, the prospects of Type II superconductors for practical applications are broad and highly promising.

Empirically, the ratio $\kappa = \lambda/\xi$ (known as the Ginzburg-Landau Parameter) is used to classify superconductors into two types. Type I superconductors are those with $0 < \kappa < 2^{(-1/2)}$, and Type II superconductors are those with $\kappa > 2^{(-1/2)}$.

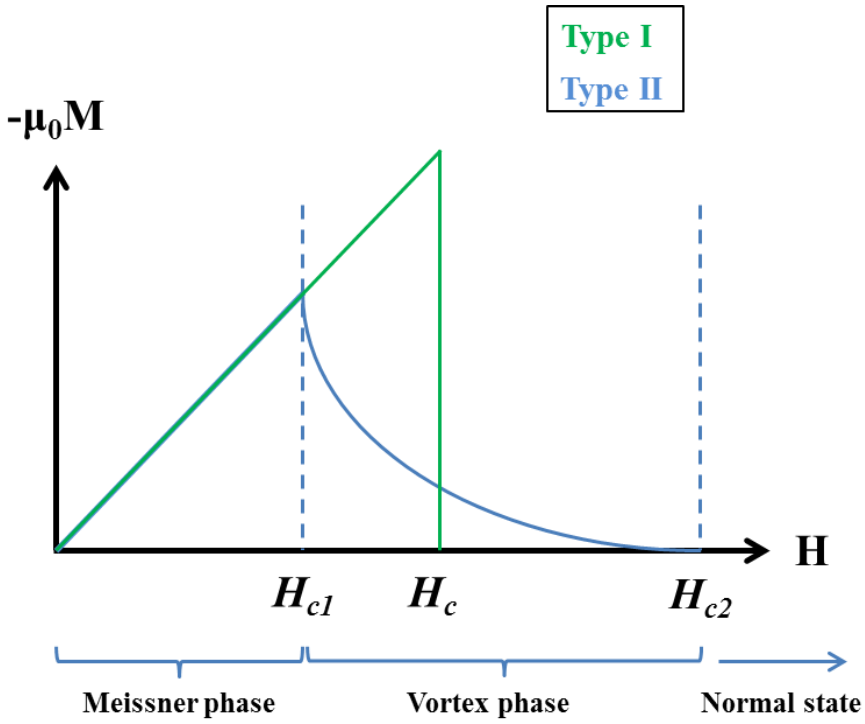

Figure 1-5. A schematic of Meissner Phase, vortex phase and normal state in Type I and II superconductors.

1.2.3.3 Isotope Effect and Bardeen-Cooper-Schrieffer (BCS) Theory

It was experimentally found in 1950 that an equation,

$$T_c M^{\alpha} = constant$$

, where M stands for the isotopic mass and α is an experimental constant (~ 1/2), always works for describing the relationship between the atomic mass and T_c superconducting elements with different isotopic masses. This means that T_c changes accordingly when different isotopes of the same element are mixed together. In mercury for example, T_c

varies from 4.185 to 4.416 K when its average atomic mass of 199.5 increases to 203.4 (atomic mass units). From then on, scientists realized that electron-lattice interaction might be at the root of superconductivity.

No one, even in the theory of London or Ginzburg-Landau, was able to clarify the microscopic origin of superconductivity until a splendid work was published by J. Bardeen, L. Cooper, and J. R. Schrieffer in 1957[12-13]. According to an impressive prediction in their theory, a special kind of bonded electrons ("Cooper Pairs") becomes condensed in the Meissner State in a superconductor. With the help of lattice phonons, each Cooper pair consists of two correlated electrons. Apparently, lower energy can be found in Cooper pairs only if the two electrons have opposite momentum and spin. Under this circumstance, Cooper pairs can freely travel through crystal lattices without producing any dissipation, which is considered the origin of resistance. Supported by BCS Theory, the properties of Type I superconductors can be modelled successfully.

Furthermore, the concept of the superconducting energy gap (Δ^{SC}) was also proposed. Based on BCS Theory, all the electrons near the Fermi level form Cooper pairs in the ground state (T = 0) of a system. In order to break the correlation, a minimum energy equal to $2\Delta^{SC}$ is required, and there is no way for electrons with energy between the ground state and $2\Delta^{SC}$ to exist. That is to say, an energy gap Δ^{SC} exists and can be symbolized as

$$\Delta^{SC} = 2\hbar\omega_L \exp\left[-1/N(E_F)G\right]$$

where $\hbar\omega_{\mathrm{L}}$ is the average phonon energy, $N(E_{\mathrm{F}})$ represents the energy density at the Fermi energy, and G refers to a coefficient describing the electron-phonon coupling strength. Apparently, superconductivity is more likely to emerge if $N(E_{\mathrm{F}})$ and G are relatively large. BCS Theory represents one of the most impactful works in the field of superconductivity. In recognition of their tremendous contributions to explaining the mechanism of conventional superconductivity, J. Bardeen, L. Cooper, and J. R. Schrieffer were awarded the Nobel Prize in Physics in 1972 (Fig. 1-6).

The Nobel Prize in Physics 1972

John Bardeen
Prize share: 1/3

Leon Neil Cooper
Prize share: 1/3

John Robert Schrieffer
Prize share: 1/3

The Nobel Prize in Physics 1972 was awarded jointly to John Bardeen, Leon Neil Cooper and John Robert Schrieffer *"for their jointly developed theory of superconductivity, usually called the BCS-theory"*.

Figure 1-6. BCS Theory - the Nobel Prize in Physics, 1972.[14]

1.3 References

(1) Day, C. Iron-based superconductors. *Phys. Today* **2009,** *62*, 36-40.
(2) Kamihara, Y.; Watanabe, T.; Hirano, M.; Hosono, H. Iron-based Layered Superconductor La[$O_{1-x}F_x$]FeAs (x = 0.05-0.12) with T_c = 26 K. *J. Am. Chem. Soc.* **2008,** *130*, 3296-3297.
(3) Hsu, F. C.; Luo, J. Y.; Yeh, K. W.; Chen, T. K.; Huang, T. W.; Wu, P. M.; Lee, Y. C.; Huang, Y. L.; Chu, Y. Y.; Yan, D. C.; Wu, M. K. Superconductivity in the PbO-type structure alpha-FeSe. *Proc. Natl. Acad. Sci. USA* **2008,** *105*, 14262-14264.
(4) Onnes, H. K. *Comm. Phys. Lab. Univ. Leiden. Suppl.* **1911,** *29*.
(5) Onnes, H. K. The resistance of pure mercury at helium temperatures. *Comm. Phys. Lab. Univ. Leiden* **1911,** *12*, 120.
(6) Onnes, H. K. Further experiments with liquid helium. . *Comm. Phys. Lab. Univ. Leiden* **1913,** *29*, 133b.
(7) Langhorn, J. B. Flux Pinning by Platinum and Rhodium in High Temperature Superconductors. *Platinum Met. Rev.* **1996,** *40*, 64-69.
(8) Meissner, W.; Ochsenfeld, R. Ein neuer Effekt bei Eintritt der Supraleitfähigkeit. *Naturwissenschaften* **1933,** *21*, 787-788.
(9) Brechna, H. *Superconducting magnet systems*, Springer: Berlin, Germany, 1973.
(10) London, F.; London, H. The Electromagnetic Equations of the Supraconductor. *Proc. R. Soc. London Ser. A* **1935,** *149*, 71-88.
(11) Pippard, A. B. An Experimental and Theoretical Study of the Relation between Magnetic Field and Current in a Superconductor. *Proc. R. Soc. London Ser. A* **1953,** *216*, 547-568.
(12) Bardeen, J.; Cooper, L. N.; Schrieffer, J. R. Microscopic theory of superconductivity. *Phys. Rev.* **1957,** *106*, 162-164.
(13) Bardeen, J.; Cooper, L. N.; Schrieffer, J. R. Theory of superconductivity. *Phys. Rev.* **1957,** *108*, 1175-1204.
(14) "The Nobel Prize in Physics 1972." *Nobelprize.org.* Nobel Media AB 2014. Web.: 2 May 2018. https://www.nobelprize.org/nobel_prizes/physics/laureates/1972/.

Chapter 2

2 Literature Review

This thesis work has been focused on the PLD-prepared FeSe and related superconducting thin films fabricated by PLD method. The ultimate prospect was to clarify the effect of various post-treatments to the superconductivity of the samples, such as interface effect and external coating process. Thus, this Literature Review is discussed mainly based on the context of the project.

At first, the concept of high-T_c superconductor (HTS), which is one of the most promising topics in condensed matter physics, will be briefly introduced. Then, the main section will discuss the development of iron-based superconducting thin films. In detail, the most studied three types on film fabrication will be reviewed in separate paragraphs as: 1111-type ($LaFeAsO_{1-x}F_x$), 122-type ($BaFe_2As_2$), and 11-type (FeSe). The section of the 11-type is further divided into two parts, conventional 11-type thin films and mono-/multi-layer 11-type thin films. Significant breakthroughs in the past decade are carefully reviewed together with the up-to-date achievements with respect to this unique system.

2.1 High-T_c Superconductors (HTS)

If one considers a material having superconductivity within the framework of BCS Theory, the theoretical limit for this material can be ascertained by tuning the parameters into a favourable state for achieving superconductivity, which means a high density of electron states at the Fermi level and strong electron-phonon coupling. Nevertheless, 30 K[1] is still an upper limit, above which, superconductivity was believed to be impossible to occur.

The cruel theoretical limitation on T_c to some extent reduced scientists' enthusiasm for exploring new type of superconductors at that time. This classic law was found to be no longer universal, however, after the discovery superconductivity in the Ba-La-Cu-O system in 1986 by G. Bednorz and K. Müller[2]. This kind of superconducting oxide exhibits much higher T_c than conventional superconductors and possesses unique properties that cannot be simply explained by BCS Theory. Since then, the freeway for exploring unusual HTS has been opened. After the discovery of

lanthanum-based cuprate perovskite material was awarded the Nobel Prize in Physics in 1987, the upper limit of T_c kept shooting up over the next 30 years. By replacing the lanthanum with yttrium, the T_c of $YBa_2Cu_3O_{7-\delta}$ (YBCO) could be raised to 92 K[3], which is even higher than the boiling point of liquid nitrogen (LN_2). Obviously, it is commercially important if T_c can be achieved by using LN_2, considering the much cheaper production cost of LN_2 compared with liquid helium (LHe) as the refrigerant. Furthermore, higher T_c also helps to relieve some existing difficulties in handling LHe, such as frozen air plugs and the potential hazard of its high expansion ratio (1: 696 for LH_2, 1: 757 for LHe). Up to now, the highest superconducting transition temperature at ambient pressure is found in the family of cuprate ceramics, $HgBa_2Ca_2Cu_3O_{8+\sigma}$, with T_c over 133 K[4] (160 K[5], under pressure). In the 21st century, new types of superconductors with unique properties were discovered in succession, including the family of iron-based superconductors[6-8] and hydrogen sulfide (H_2S, T_c ~ 203 K under extremely high pressure ~ 150 GPa)[9-10]. The former broke the widely accepted belief that ferromagnetic element Fe is antagonistic to superconductivity[11]. The latter possesses the top T_c value to date and has raised the prospect that even room-temperature superconductors could be discovered in other hydrogen-rich systems[10]. The development of superconductors since their discovery date is shown in Fig. 2-1.

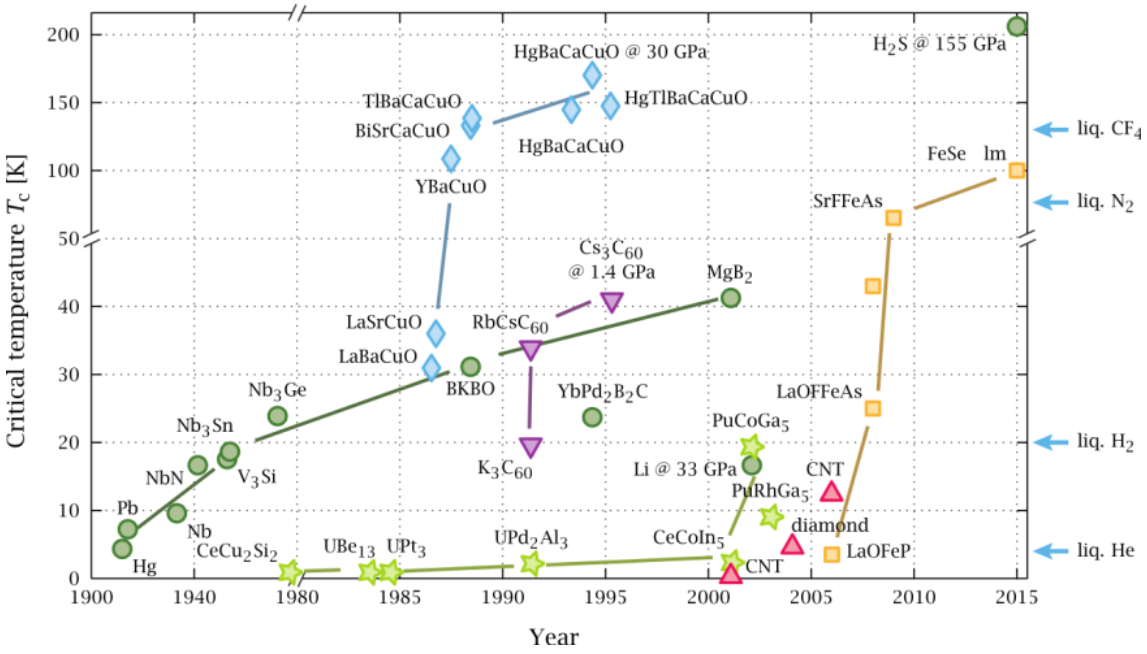

Figure 2-1. Timeline of discovering new superconductors from 1900 to 2015. Note the difference types of superconductors: BCS superconductors (green circles), cuprates (blue diamonds), iron-based superconductors (yellow squares) and other families.[12]

2.2 An overview of Iron-based Superconductors

15 years after the work on Ba-La-Cu-O, Mg diboride (MgB_2) was found to show superconductivity below 39 K which is one order of magnitude higher than common superconducting metals and alloy materials. Nevertheless, MgB_2 is classified as a conventional superconductor and well explained by BCS Theory. Before 2008, it seemed that high temperature superconductivity could only occur in copper oxide planes, although scientists have never given up finding new types of HTS by comparing differences and similarities in the possible HTS materials with the already known ones. Every time that there is a new discovery, we are getting closer to fully understand the mystery of superconductivity, and also to the ultimate achievement of room-temperature superconductivity. As a result, a completely new type of superconductor apart from cuprates was discovered by Y. Kamihara and his colleagues in 2006 for LaFePO[13], which is considered as the first iron-based superconductor historically, although the T_c was only 4 K. Two years later, the same group published the result of a striking superconducting transition at 26 K in the iron pnictide $LaFeAsO_{1-x}F_x$[8]. Soon after the discovery of superconducting LaFeAs(O,F), T_c was already doubled, up to 55 K in a $SmFeAs(O_{1-x}F_x)$[14] compound, obtained by substituting samarium on lanthanum sites. Since then, the frontier of superconductors has been widely broadened, and iron-based superconductors have now become one of the most exciting research subjects in the condensed matter physics field. Over 15k papers, both theoretical and experimental, have been published with respect to iron-based superconductors. The most discussed topic is no doubt the compatibility of superconductivity with the prominent magnetic moment from the Fe element. The ultimate answer must be revealing and will definitely lead to a fresh understanding of the origin of superconductivity.

According to early theoretical calculations on the band structure[15-19], iron-based superconductors have special electronic structures. The Fermi surface consists of several hole-pockets and electron-pockets around the Γ and M points (see Fig. 2-2 for an example), respectively, which reflects the multi-band feature of iron-based superconductors. Hence, the nesting of the hole- and electron-Fermi surfaces could result in fluctuations in orbitals/spin[18-22], which might give a hint to the pairing origin of the unconventional superconductivity.

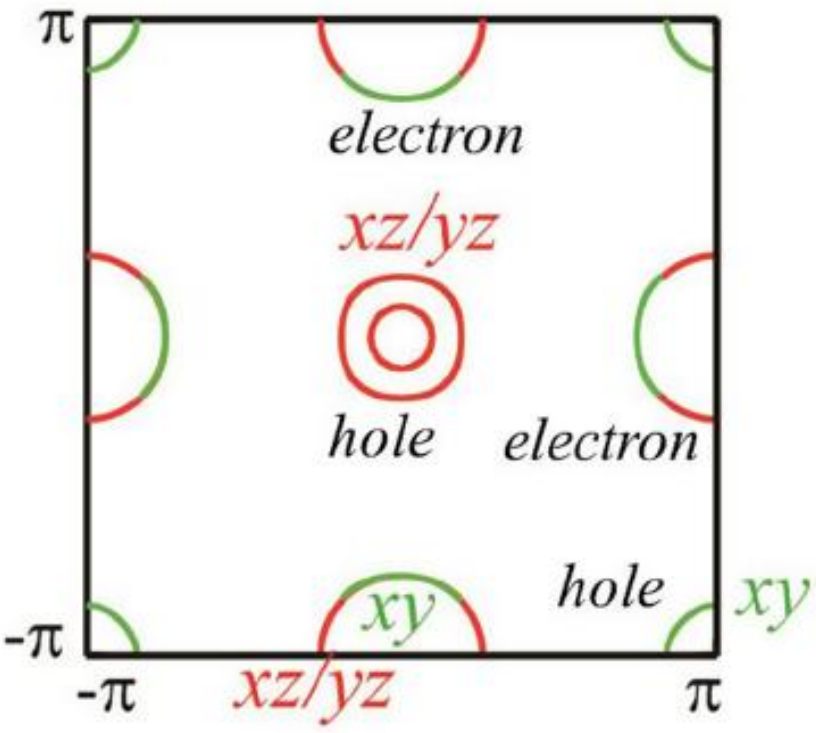

Figure 2-2. A typical five orbital Fermi surface of iron-based superconductor.[23]

What renders iron-based superconductors so popular? Apart from the unexpected co-existence of superconductivity and large magnetic spin moment, the application-meaningful features found in iron-based superconductivity are also worth investigating. For instance, the promisingly high T_c level above the LN_2 boiling point[24-25], low anisotropy[26-27], extremely large H_{c2}[28], etc. Table 2-1 which was mainly concluded by Hosono *et al.*[29] lists several properties that are critical for the application fields of three special HTS: iron-based superconductors, MgB_2, and cuprates (YBCO and BiSrCaCuO systems). These materials are compared in terms of their practical parameters (e.g., maximum T_c, H_{c2}, irreversibility field (H_{irr}), anisotropy factor (γ), and advantages/disadvantages for fabrication) and electronic/crystallographic features (e.g., their Fermi level, superconducting gap symmetry, crystallographic symmetry in the superconducting state, and critical grain-boundary angle (θ^{GB})). From the table, we can easily obtain information on some advantageous properties for the application of iron-based superconductors.

Table 2-1. Comparison of three HTS: iron-based superconductors, MgB_2, and cuprates. Mostly after Ref.[29].

	Iron-based Superconductors	**MgB_2**	**Cuprates**
Parent material	Antiferromagnetic (AFM) semimetal (T_N ~ 150 K	Pauli paramagnetic metal	AFM Mott insulator (T_N ~ 400 K)
Fermi level	Fe 3d 5-orbitals	B 2p 2-orbitals	Cu 3d single orbital
Maximum T_c (K)	55 (1111 type), 38 (122 type), over 100 (11 type monolayer)[25]	39	93 (YBCO), 133 (HgBaCaCuO under pressure), 110 (Bi2223)
Impurity	Robust	Sensitive	Sensitive
Superconducting gap symmetry	Extended *s*-wave	*s*-wave	*d*-wave
H_{c2} at 0 K (T)	100-200 (1111 type), 50-100 (122 type), ~50 (11 type)[25], 443 ((Li,Fe)OHFeSe)[28]	40	>100
H_{irr} (T)	>50 (4 K), >15 (20 K)	>25 (4 K), >10 (20 K)	>0 (77K, YBCO)
Anisotropy, γ	4-5 (1111 type), 1-2 (122 and 11 types)	2	5-7 (YBCO), 50-90 (Bi-system)
Crystallographic symmetry in SC state	Tetragonal	Hexagonal	Orthorhombic
Critical GB angle, θ_c (deg.)	8-9	No data	3-5 (YBCO)
Advantage	High H_{c2} (0), Easy fabrication	Easy fabrication	High T_c and H_{c2} (0)
Disadvantage	Toxicity	Low H_{c2} (0), Poor performance in fields	High cost due to the 3D alignment of crystallites

Cuprates no doubt possess the best potential in high-temperature (low refrigeration cost) applications due to their extremely high T_c level. So far, only "11 type" iron-based superconducting film with a special monolayer structure is able to show a superconducting transition at an ambient temperature over 100 K[24-25]. Nevertheless, this discovery is currently valued for fundamental investigation only, considering the difficulty in sample fabrication and the negligible critical current that

the single-layer structure can carry. It is thought that the strong electron correlation in the anti-ferromagnetic (AFM) Mott-insulating state (occurring at temperatures much higher than room-temperature) mainly contributes to the high T_c level in cuprates. In contrast, the parent material for iron-based superconductors is considered an AFM semimetal with a Néel temperature (T_N) around 150 K. Although the T_c range of this type of HTS barely exceeds 77 K, we can still anticipate excellent superconducting performances under high fields at temperatures accessible by refrigerators or liquefied hydrogen (20.3 K). In consideration of their higher H_{c2} and H_{irr} than MgB_2, cuprates, and conventional alloy superconductors (29 T for Nb_3Sn, 15 T for NbTi), a promising industrial application of iron-based superconductors in high-field magnets is strongly expected. On the contrary, MgB_2 superconductors with superconductivity that is hypersensitive to external fields are mostly utilized in the environments with relatively high temperature (15 - 20 K) and low magnetic fields (< 1.0 T), such as magnetic resonance imaging (MRI)[30-32]. Another obvious advantage of MgB_2 superconductors is their low fabrication cost, as the common elements boron and Mg are the only essential precursors, while rare-earth elements are required doe fabricating cuprates.

The anisotropy factor γ is determined by

$$\gamma = (\frac{m_c}{m_{ab}})^{1/2} = \frac{\xi_{ab}}{\xi_c} = H_{c2}^{//ab}/H_{c2}^{//c}$$

, where m, ξ, and H_{c2} are the effective mass, coherence length, and upper critical field, respectively. The subscripts represent the difference in properties along different chosen directions. The γ is found to be very small (lowest ~ 1-2) in iron-based superconductors compared with those of cuprates (even over 50 in Bi-system), and is comparable to that of MgB_2 (~ 2). That is to say, it is unnecessary to pay great attention to the performance degradation of iron-based superconductors when the external field direction varies, which is in sharp contrast with the case of YBCO coated conductors. Furthermore, high J_c tolerance to large grain boundary angles (θ^{GB}) is one of the most exciting features of iron-based superconductors that make them superior to cuprates. As shown in Fig. 2-3, the J_c degradation with increasing θ^{GB} is much slower[33] in iron-based superconductors ($BaFe_2As_2$:Co, θ_c = 8 - 9 °) than in cuprates (YBCO, θ_c^{YBCO} = 4 - 5 °). The abrupt degeneration of J_c in YBCO superconductors is generally attributed to the "weak-link" inter-grain effect, which exponentially reduces the current capability of superconductors such as YBCO once the θ^{GB} is somehow over 4 °.[34] That is the reason why achieving a highly oriented sample with biaxial texture is always discussed as the

top issue in the field of cuprate superconductors. In the case of iron-based superconductors, high J_c not only the can be sustained under θ^{GB} as high as 9 °, but also won't suddenly drop as a result of the metallic nature of the grain boundaries[23]. Overall, by integrally considering the potential due to their high T_c, phenomenal H_{c2}, small anisotropy γ, and high J_c tolerance to large θ^{GB}, iron-based superconductors are very appropriate candidates for applications in high-field environments where neither YBCO nor MgB_2 will show competitive performance. The average J_c level for Ba-122 superconducting thin films is around 10^6 - 10^7 A/cm^2.

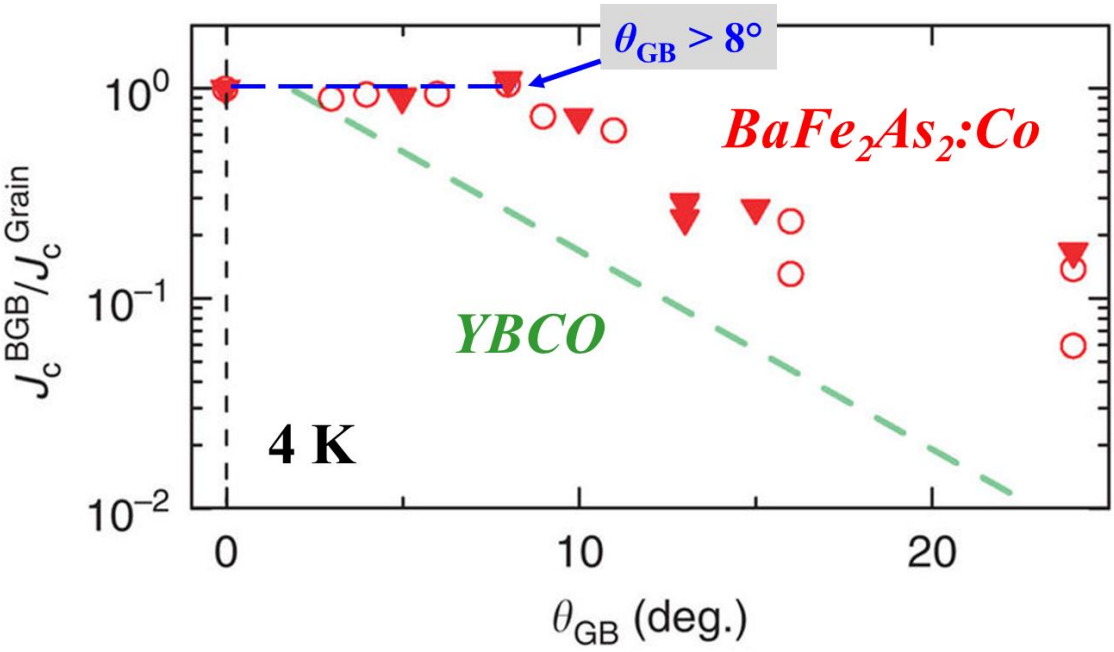

Figure 2-3. Grain-boundary angle θ^{GB} dependence of the critical current density ratio J_c^{BGB}/J_c^{Grain}. The data for iron-based superconductors, $BaFe_2As_2$:Co/MgO (open circles) and $BaFe_2As_2$:Co/lanthanum aluminum oxide-strontium aluminum tantalum oxide (LSAT) (closed triangles), and YBCO cuprate[35] (dashed line) are plotted together for comparison. After Ref. [33].

2.3 Iron-based Superconducting Thin Films

As mentioned above, iron-based superconductors feature several advantages, such as high T_c, high H_{c2}, low anisotropy, and high tolerance to large grain-boundary angles[33]. Such advantages make iron-based superconductors promising materials for ultrahigh-performance applications in the forms of thin film, wire, or tape. In condensed matter physics, thin film is always an important theme, as materials often exhibit novel properties if they are in a lower dimension form. Similarly, in the field of iron-based superconductors, research work focusing on iron-based superconducting thin films never fell behind. This is because thin film is not only essential for fabricating some

electronic devices[36] (such as superconducting quantum interference devices (SQUIDs) and Josephson devices), but also is an interesting subject with unique properties that might lead scientists to the truth of high T_c in iron-based superconductivity. Furthermore, films offer the possibility of investigating superconducting parameters such as the penetration depth (λ) and coherence length (ξ), and non-equilibrium processes. Various preparation methods can be used to fabricate high-quality iron-based superconducting thin films. For example, the fabrication of a FeSe (11 type) thin film has been successfully achieved by using PLD[37-40], molecular beam epitaxy (MBE)[41-43], metal-organic chemical vapour deposition[44], and chemical solution method[45] techniques. Among them, PLD and MBE are the two most preferred methods. In the following section, the research on iron-based superconducting thin films will be reviewed in detail.

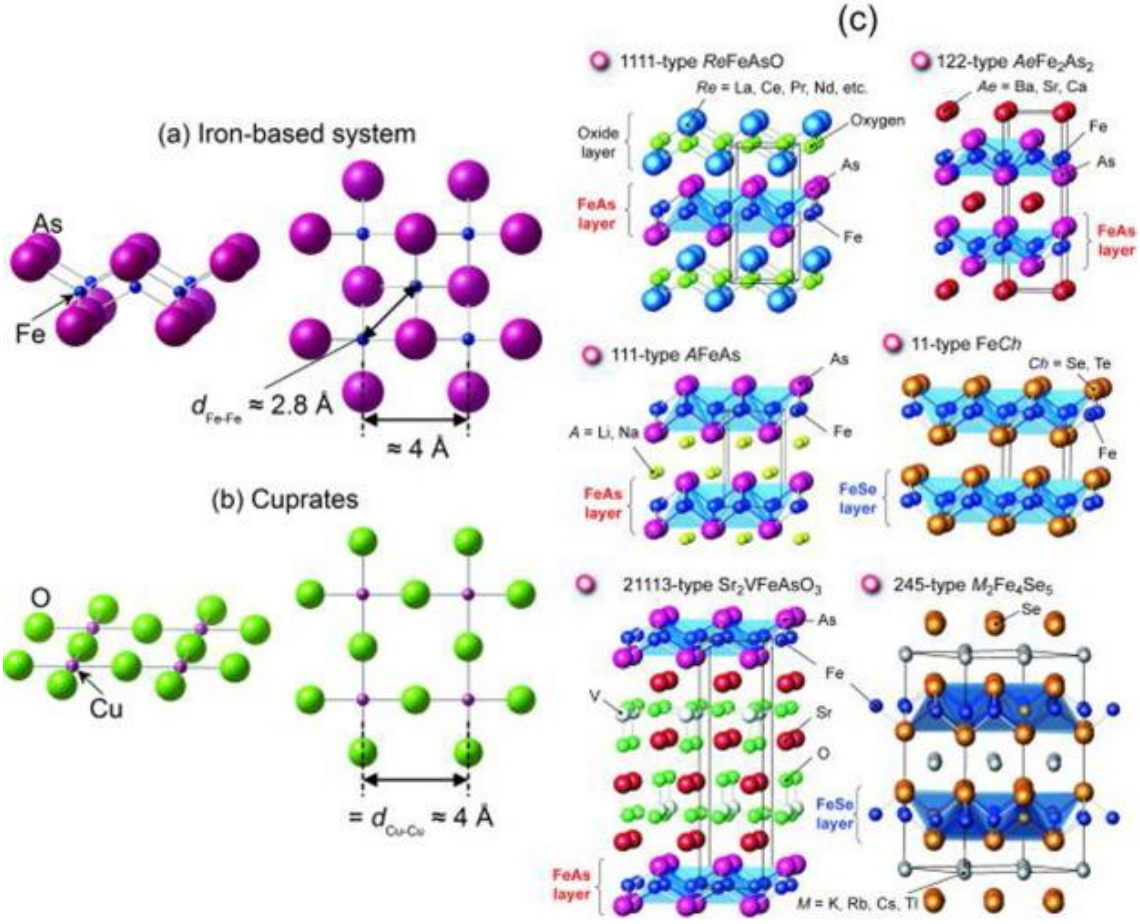

Figure 2-4. Crystal structures of various parent materials of iron-based superconductors and HTS cuprate superconductors. (a) Common structural unit of iron-based superconductors. A standard Fe-As layer is shown as an example. (b) Common structural unit of HTS cuprate superconductors. (c) Various parent compounds of iron-based superconductors. Abbreviations of the ratio of the constituent atoms are used to identify these parent compounds. After Ref.[29].

Fig. 2-4 shows the common structural units of various iron-based

superconductors[29]. In fact, the iron-based superconductors share a common layer-by-layer structure, which usually exhibits additional two-dimensional physical properties. The Fe-pnictogen or Fe-chalcogen plane usually serves as the major conduction layer with Fe^{2+} ions tetrahedrally coordinating with the pnictogen (P and/or As) or chalcogen (S, Se, and/or Te) ions. HTS cuprate superconductors contain Cu-O planes, as illustrated in Fig. 2-4 (b). An example of a standard Fe-As layer is shown in Fig. 2-4 (a) as an example. Several common characteristics have been found in different families of iron-based superconductors: (1) All lattices are tetragonal structures. (2) The layered structures are based on either Fe-pnictogen or Fe-chalcogen planes, which is reminiscent of the Cu-O planes in cuprate superconductors. (3) Carrier doping can be realized by element-intercalation between conduction layers to adjust performance. Furthermore, Density Functional Theory (DFT) calculations[16, 46] (examples shown in Fig. 2-5) have evidenced the common multi-band electronic structure, with the Fermi level predominantly occupied by Fe 3d orbitals, which play a critical role in iron-based superconductivity. In most cases, the unusual properties of iron-based superconductors result from the complex Fermiology with five Fe-related conduction bands. This is in distinct contrast to the situation in cuprate superconductors, in which the Fermi level is only associated with one 3d orbital (seen on the left of Fig. 2-4 (b)).

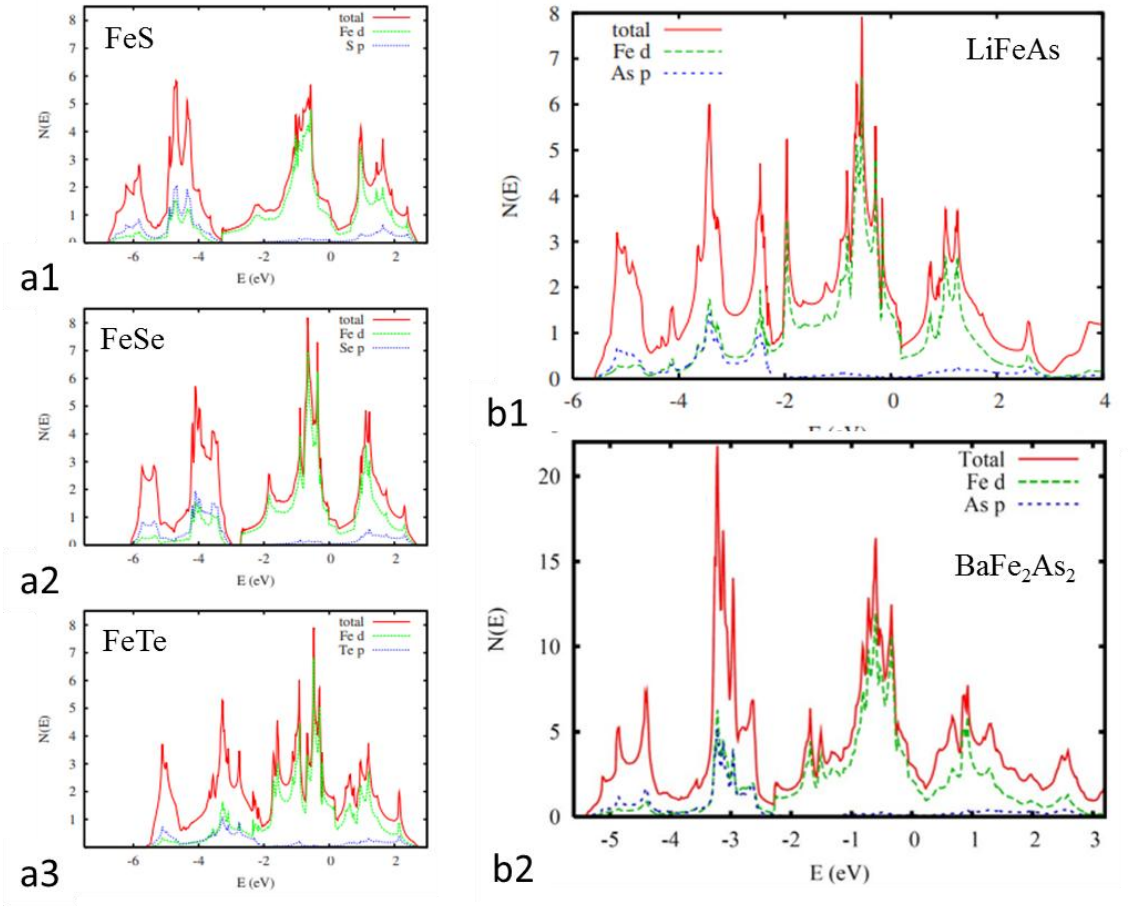

Figure 2-5. Examples of the calculated electron density of states (DOS) of some iron-based superconductors. (a1) - (a3) FS, FeSe, and FeTe[16]. (b1) & (b2) LiFeAs and $BaFe_2As_2$[46].

The most discussed types of iron-based superconductors for film fabrication are: 1111- (e.g. $LaFeAsO_{1-x}F_x$), 122- (e.g. $BaFe_2As_2$), 111- (e.g. LiFeAs), and 11- (e.g. FeSe) types (Fig. 1-10 (c)). As per these specific crystallographic structures, the next paragraphs will review each of them separately.

2.3.1 1111-type

The "1111-system" system contains the largest variety of elements among all the iron-based superconductors, with the type usually designated as LnFeAsO (Ln = La, Ce, Pr, Nd, Sm, etc). It has a ZrCuSiAs type structure, which belongs to the space group of tetragonal P4/*nmm*, as shown in Fig. 2-6 as an example[47]. Positively charged Ln-O layers (charge reservoir) and negatively charged Fe-As layers (superconductivity) are alternately stacked along the out-of-plane direction in this type of compound.

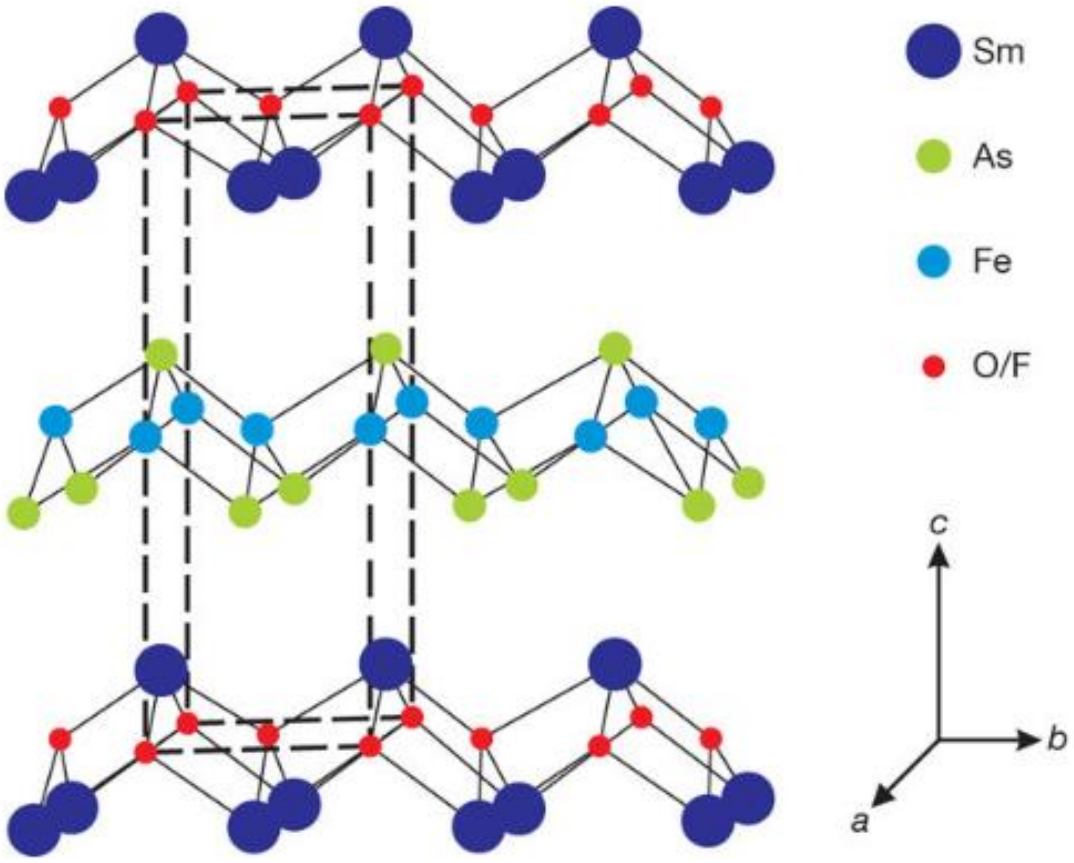

Figure 2-6. Model of $SmFeAsO_{1-x}F_x$ (1111-type) crystal with a tetragonal ZrCuSiAs-type structure[47].

2.3.1.1 PLD-1111

Considering that the first iron-based superconductor discovered was $LaFeAsO_{1-x}F_x$[8], it is not surprising that the first attempt[48] towards iron-based superconducting thin film growth was made on the same compound by the PLD technique (**neodymium**-doped yttrium aluminum garnet (Nd:YAG) laser, λ = 532 nm). In this work, $LaFeAsO_{1-x}F_x$ epitaxial thin films were successfully fabricated on MgO (001) and perovskite (La, Sr)(Al, Ta)O_3 (001) (LSAT) substrates, although none of these 1111-type films exhibited superconducting transitions. As is known from the case of LaFeAsO bulk samples, the pristine LaFeAsO is not superconducting due to a lack of F dopant, although T_c can be induced by partially replacing F anions on O sites[8], which introduces extra electron-type charge carriers. Unfortunately, it was found that the F ions from the F-doped $LaFeAsO_{0.9}F_{0.1}$ target could not be incorporated into the LaFeAsO system as effective donors. The unsolved problem was later attributed to the difficulty in controlling the stoichiometry of the thin film, which contains two different anions[49], and, of course, the highly volatile property of F and As materials. To avoid these issues in preparing superconducting La(O,F)FeAs thin films, researchers from IFW Dresden[50]

carried out a two-step *ex-situ* growth method consisting of room-temperature film deposition and post-annealing in an evacuated quartz tube. Finally, a superconducting T_c^{onset} at 11 K[50], as reflected by transport measurements, was obtained in a polycrystalline film deposited from a $LaFeAsO_{0.75}F_{0.25}$ target on $LaAlO_3$ (LAO) (001) substrate after two annealing steps. Then, the T_c of $LaFeAsO_{1-x}F_x$ thin film was much improved by the same group by optimizing the annealing conditions[51-52]. Reducing the oxygen partial pressure[53] during the post-annealing procedure was also effective for increasing T_c in the two-step *ex-situ* fabrication process. J_c of ~ 0.1 MA/cm^2 and the corresponding scaling anisotropy were also reported. The evolution of the superconductivity of the PLD-$LaFeAsO_{1-x}F_x$ thin film is summarized in Fig. 2-7. A comprehensive review with respect to the iron pnictide film synthesis was recently published by Haindl *et al.*[54].

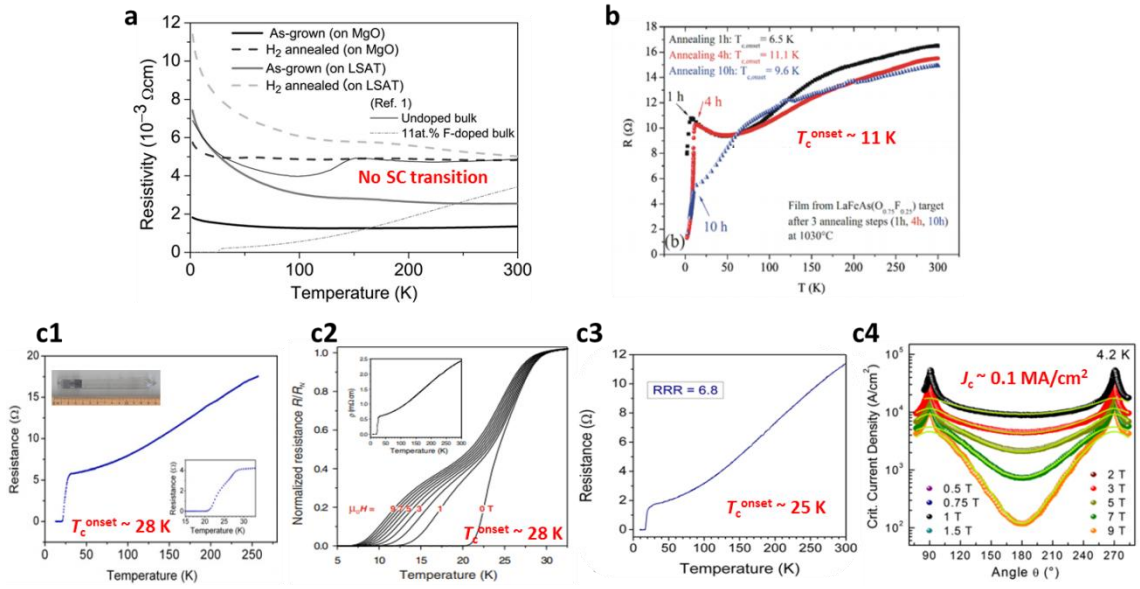

Figure 2-7. The evolution of the superconducting performance of PLD-$LaFeAsO_{1-x}F_x$ thin film. (a) The first attempt at a 1111-type iron-based superconductor[48]. No superconducting transition was observed due to the difficulty in F doping by the target. (b) The two-step *ex-situ* process invented by IFW Dresden realized a T_c^{onset} of ~ 11 K in a film deposited from a $LaFeAsO_{0.75}F_{0.25}$ target[50]. (c1) - (c4) Through optimization of the post-annealing process, the superconducting performances, including T_c and J_c, of La-1111 thin films were continuously improved[51-53, 55].

2.3.1.2 MBE-1111

Recently, Hosono's group[56] reported the realization of *in-situ* doping of F ions into 1111-type thin films by the PLD method. The best onset transition, as high as 40 K, was obtained in their $SmO_{1-x}F_xFeAs$ oxypnictide thin films grown on CaF_2 substrate, which acts as the F supplier during high-temperature growth. In fact, the thin film

growth of the materials in the 1111-system by regular physical vapor deposition (PVD) methods is extremely difficult because the relatively high deposition temperature can easily give rise to decomposition and/or preferential evaporation of F[23]. Hence, a more developed PVD method was in high demand to realize properly F-doped 1111-type iron-based superconducting thin films. MBE is one of the most widely used PVD methods for fabricating high-quality thin films. MBE is usually performed in an ultra-high vacuum (UHV) chamber so that the surface of the sample is always extremely flat. A typical schematic diagram of an MBE system is displayed in Fig. 2-8. The system contains the source oven (usually a Knudsen Diffusion Cell), shutters (controlling the growth time), a thermocouple (to detect the crucible temperature), a beam flux detector, and a cooling water circuit. LN_2 is introduced to improve the vacuum degree as well as minimizing negative effects from impurities. Inside the UHV chamber, material sources are heated up and deposited on the substrate through shutters. The beam flux is monitored by a real-time detector on the side. MBE possesses several advantages over other growth methods, such as accurate control of atomic layers, low substrate temperature, and nonequilibrium growth conditions, allowing the preparation of films that are hard to synthesize in the condition of thermal balance.

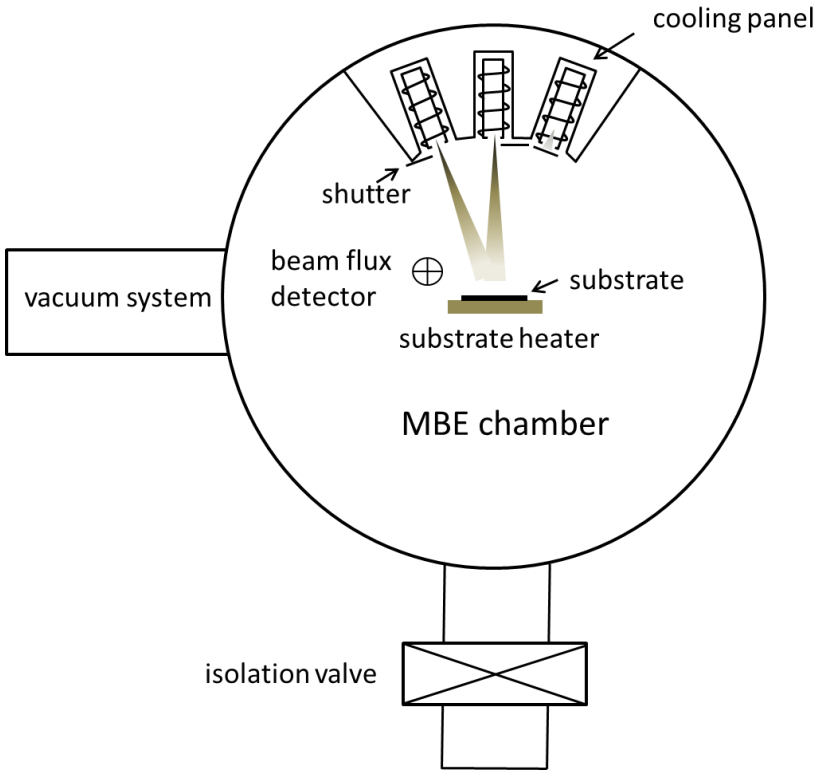

Figure 2-8. Schematic diagram of a typical MBE system.

As each element source can be controlled independently by varying the flux rate,

MBE is considered more suitable for fabricating 1111-type epitaxial thin films with T_c comparable to their bulk counterparts[57-58]. The successful fabrication of an MBE-NdFeAsO[59] (Nd-1111) epitaxial thin film was the first technical breakthrough for the application of MBE in 1111-type iron-based superconducting thin films. Although the superconducting transition was not initially observed, the reproducibility of single crystalline NdFeAsO film was achieved on GaAs substrate. Similar to the case of PLD, the problem of a lack of F incorporation is also a critical issue in 1111-type films fabricated by the MBE process[59]. Only one year later, the same group, Kawaguchi *et al.*[58], successfully realized a superconducting T_c in single crystalline F-doped Nd-1111 thin films grown by MBE. They found a strong dependence of the superconducting performance on the growth time of resultant Nd-1111 films. In detail, neither impurity phases nor superconductivity were observed inside the single crystalline films when the growth time was less than 3 hours. With a longer MBE growth time (more than 4 hours), some impurity phases (NdOF, FeAs, and Fe_2O_3) appeared together with the Nd-1111 as the major phase. For the films grown for 6 hours, an optimal superconducting $T_c^{onset}/T_c^{zero} \approx 48$ K/42 K was finally obtained. The realization of the superconducting transition was attributed to the formation of abundant NdOF impurity phase, which contains the crucial F dopant. This finding implies an effective way to introduce F dopant and obtain superconducting Nd-1111 films by employing a long MBE growth time. The only origin of the NdOF impurity is the NdF_3 raw material among all the Knudsen cells (apart from Fe, As, and Fe_2O_3), which results in difficulty in independently controlling the contents of Nd and F. This issue was overcome by a novel co-evaporation of gallium[60]. The Ga, which served as a getter, was very effective for removing the excess amount of F dopant and thus inducing a high superconducting T_c.

In addition to La-1111 and Nd-1111, new F-doping MBE techniques were also developed in Sm-1111 films. As reported by Ueda *et al.*[57], a F diffusion process was achieved by introducing a SmF_3 overlayer. In addition, the authors utilized fluoride substrates (CaF_2, BaF_2, and SrF_2) for depositing SmFeAsO epitaxial thin films. Combined with the upper SmF_3 overlayer and the fluoride substrate underneath, abundant F-doping was diffused into the Sm-1111 film and substituted on oxygen sites. Meanwhile, the resultant SmOF layer could act as an effective protective layer to prevent F from escaping. As a result, excellent superconducting performance, with a T_c^{onset} as high as 58 K and a J_c (5 K) as high as 2 MA/cm^2, was obtained in this work, as shown in Fig. 2-9. The high T_c was attributed to either tensile-strain from the substrate

or more F-doping. SmF_3 can also effectively realize F-doping into SmFeAs(O,F) in the form of a co-evaporation source[61]. Moreover, the selection of a CaF_2-buffered LAO substrate was found to be essential for obtaining a superconducting thin film. Then, continuous work was carried out by the same group, and more alternatives were found to be able to serve as effective F-doping sources by the co-deposition process, such as FeF_2[62] and FeF_3[63]. These F sources in the form of co-evaporation cells simplified the fabrication process into a one-step method by ruling out the necessity of an extra overlayer[57] (F-source), which is quite meaningful for applications in sandwich-type junctions[57-58]. Ueda *et al.*[61] summarized four types of external F sources that can be used in a UHV chamber to realize the one-step MBE-growth: (1) F-diffusion from fluoride substrates (CaF_2, BaF_2, SrF_2); (2) F from co-deposited LnF_3 (*Ln* = Sm, Nd); (3) atomic F as a result of the decomposition of FeF_3 or FeF_2; and (4) molecular F_2 gas (unrealistic due to extreme toxicity). Iida *et al.*[64] prepared highly textured MBE-NdFeAs(O,F) thin films on ion beam assisted deposition (IBAD)-MgO/Y_2O_3/Hastelloy substrates which are widely used in fabricating high J_c YBCO superconducting tapes with biaxial texture. A T_c of 43 K and a self-field J_c (5 K) of 70,000 A/cm^2 were obtained.

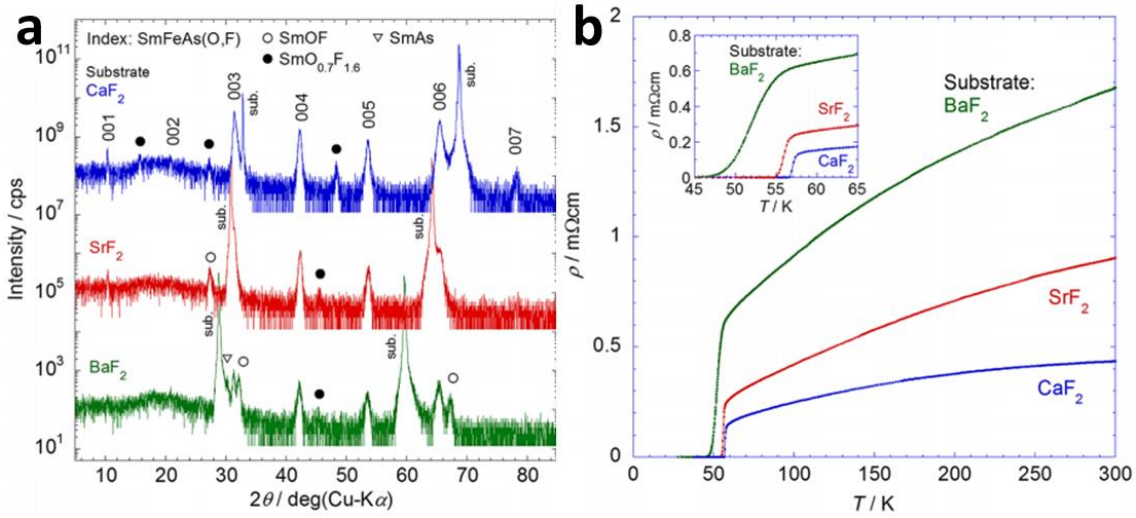

Figure 2-9. (a) XRD 2θ patterns and (b) ρ-T curves for SmFeAsO films grown on various fluoride substrates, CaF_2 (001), SrF_2 (001), and BaF_2 (001), with enlargement of indicated region shown in the inset. After Ref.[57].

2.3.1.3 Studies of J_c and H_{c2}

The upper limits of J_c and H_{c2} are the two most vital factors for the future application of superconductors. Unscattered supercurrent is sensitive to the surrounding

magnetic field. The superconducting state will be broken (returned to the normal state) once the current density (or magnetic field) reaches a critical value, which is called the J_c or H_{c2}. At the early stages, J_c was always below 10^3 A/cm^2 due to the poor quality of thin films. This phenomenon was thought to be caused by the inter-granular "weak-link effect"[51] at grain boundaries, which limits the transport current passing through grain boundaries. Moreover, the degradation of current density will be magnified with increasing inter-granular angle. The significant deterioration of J_c under a magnetic field is a typical consequence of the "weak-link effect". To overcome the negative effect, scientists are pursuing high-quality thin film samples with highly epitaxial texture, so that the inter-granular angle can be limited to a very low value (e.g. < 4 °). As a result, J_c performance was significantly enhanced after the improvement in thin film fabrication. For instance, an in-field J_c performance higher than 10^5 A/cm^2 at 4.2 K under ultrahigh fields over 20 T was achieved by Iida *et al.*[65] in MBE-grown Sm-1111 thin films on CaF_2 substrates, which indicates highly promising transport current in oxypnictide SmFeAs(O,F) superconducting thin films under high external fields. (Fig. 2-10).

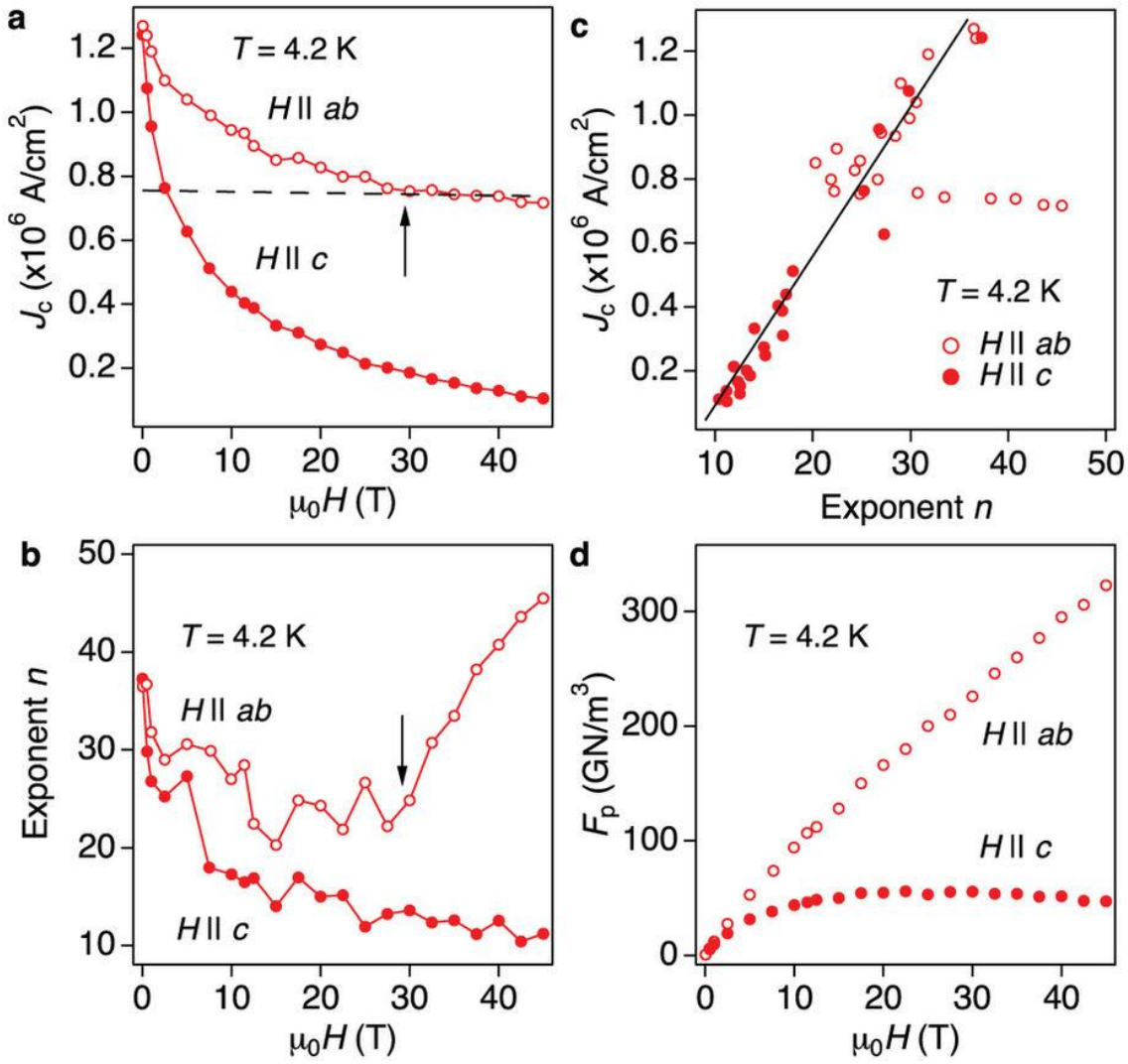

Figure 2-10. In-field J_c performance for Fe-doped Sm-1111 thin films grown by MBE. (a) J_c - H dependence measured at 4.2 K in fields up to 45 T. (b) J_c versus exponent n at 4.2 K. The arrow indicates the crossover from extrinsic to intrinsic pinning. (c) Scaling behaviour of the field-dependent J_c (exponent n vs. magnetic field) at 4.2 K. (d) Pinning force density F_P vs. magnetic field at 4.2 K. After Ref. [65].

In contrast to the transport J_c, H_{c2} shows much less correlation with "weak-link effect" and reflects more intrinsic properties of a superconductor instead. As seen from Fig. 2-11, a very high H_{c2} and a low anisotropy in magnetic field (~ 3)[52] are both obtained in this SmFeAs(O,F) system. According to the Werthamer-Helfand-Hohenberg (WHH) equation[66]:

$$H_c(0) = -0.69 \left(\frac{dHc}{dt}\right)_{t=1}$$

where $\left(\frac{dHc}{dt}\right)_{t=1}$ refers to the slope of the H_c when it is very close to T_c, the value of H_c at 0 K can be estimated by extrapolation. In consideration of the possible interference resulting from "Pauli paramagnetism", evaluation[67] of the BCS paramagnetism under

the condition of weak coupling is also required:

$$H_c(0) = 1.86\,T_c$$

Based on two models for calculation, the ultimate results of H_c are both over 100 T, demonstrating that this type of superconductor is expected to be a candidate for ultrahigh-field magnet applications.

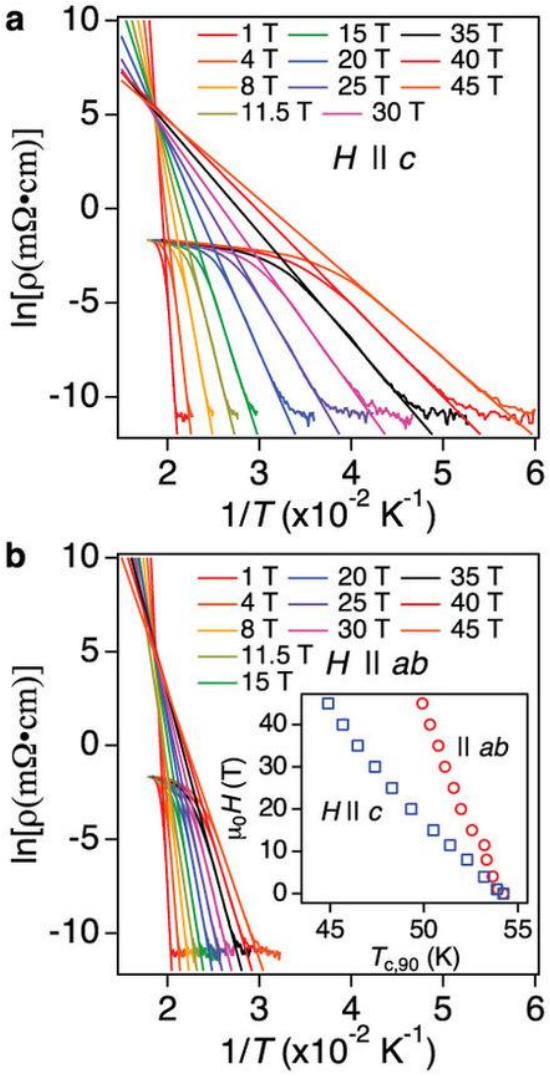

Figure 2-11. Arrhenius plots of ρ at various magnetic fields in the direction parallel to (a) *c*-axis and (b) the *ab*-plane. The inset in (b) shows the $\mu_0 H - T_c^{90\%}$ diagram of SmFeAs(O,F) film for *H*//*c* and *H*//*ab*. After Ref.[65].

To summarize, single-crystalline 1111-type iron-based superconducting thin films can be fabricated by PLD and MBE methods. Due to the critical influence of F-doping on the superconducting performance, finding a proper F source is a key issue in growing this kind of material. On the one hand, specific substrates containing F can provide F dopants through diffusion for both the PLD and the MBE methods. On the other hand, MBE makes it possible to realize effective F-doping from a precursor due to

the unique unbalanced-growth mechanism. Nevertheless, enhanced critical current performance and anisotropic properties for practical application are still highly anticipated by introducing effective vortex pinning centres into 1111-type films.

2.3.2 122-type

122-type iron-based superconductors have a "$ThCr_2Si_2$" crystal structure with the tetragonal space group *I4/mmm*[68]. This type of material is built up by the alternate stacking of alkaline-earth element layers (charge carrier layers) and a FeAs layers (superconducting layers), as shown in Fig. 2-12[69]. Among all the parent phases in iron-based superconductors, the 122-type contains the greatest number of compounds.

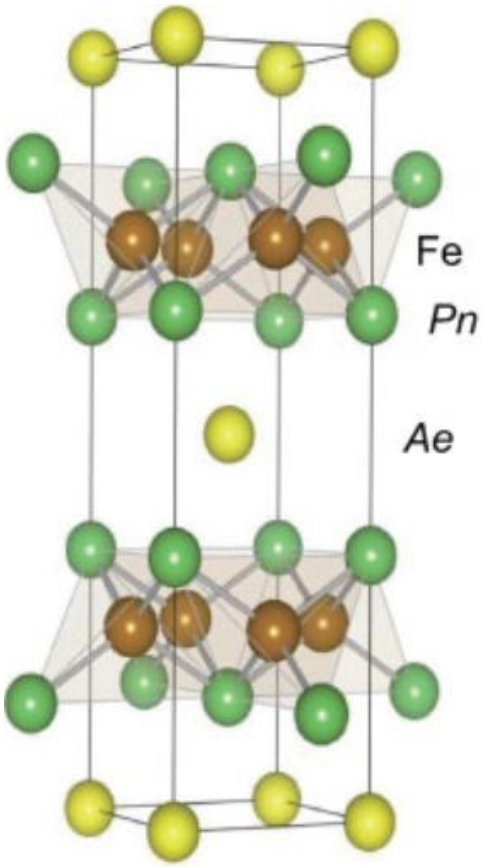

Figure 2-12. Crystal structure of 122-type iron-based superconductors ("$ThCr_2Si_2$ type", tetragonal I4/mmm space group). *Ae* stands for the elements Ca, Sr, Ba, K, Eu, etc., while *Pn* refers to P or As. After Ref.[69].

2.3.2.1 Sr-122

Hiramatsu *et al.*[49] published the discovery of superconductivity in $Sr(Fe,Co)_2As_2$ (Co-doped Sr-122) thin film grown on LSAT substrate by PLD (Nd:YAG) right after they reported the fabrication of La-1111 films[48]. Due to the much lower vapour pressure of cobalt than those of K or F, the cobalt doping into Fe sites was easier than K doping

into strontium sites in the case of 122-type compounds, or F doping into oxygen sites in the case of 1111-type compounds. Moreover, the film preparation process for a Co-doped Sr-122 compound which only contains one anion (As) is no doubt much simpler than for a mixed-anion 1111-type compound which contains two or three kinds of anions (As, O, and F). By using a KrF laser (248 nm) and a specially designed target that was 30 % As-enriched to compensate for the As-deficiency, Choi *et al.*[70] successfully fabricated high-quality *c*-axis oriented Co-doped Sr-122 thin films on LAO substrate. The highest T_c^{onset} of 20 K in this work was close to that of a polycrystalline bulk sample.

The parent phase of Sr-122 (pristine $SrFe_2As_2$) films is generally non-superconducting. Hiramatsu *et al.*[71] published work on the atmosphere-dependence of Sr-122 films grown on LSAT substrates by PLD method and pointed out that the parent Sr-122 system is very sensitive to air and moisture, and is unstable in the ambient atmosphere. By exposing the same batch of Sr-122 films to four different atmospheres (dry O_2 gas, dry N_2 gas, dry CO_2 gas, and H_2O vapor) at ambient pressure, it was found that a superconducting transition could be obtained only for the one that was exposed to the water vapor, which took place at ~ 25 K (higher than for Co-doped Sr-122 films). Fig. 2-13 illustrates the variation in the ρ-T curves of the four samples. This work clearly revealed water-induced superconductivity in the parent Sr-122 system, which was probably related to a reduction in the *c*-axis length. Nevertheless, the water-sensitivity property of the parent Sr-122 film rendered it unsuitable for applications.

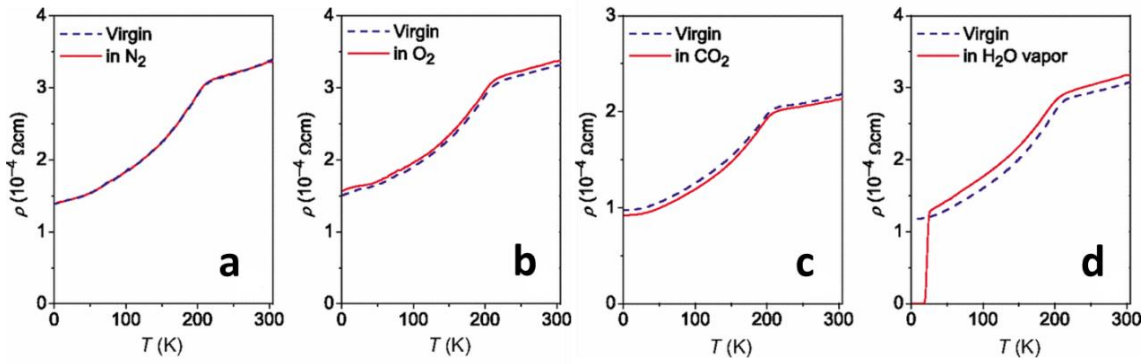

Figure 2-13. Variation in ρ-T curves of $SrFe_2As_2$ epitaxial films under exposure to four different atmospheres at ambient pressure: (a) dry N_2, (b) dry O_2, (c) dry CO_2, and (d) H_2O vapor. After Ref.[71].

2.3.2.2 Co-doped Ba-122

The first successful fabrication of superconducting Co-doped Ba-122 films was reported by Katase *et al.*[72] for their PLD-$Ba(Fe,Co)_2As_2$ epitaxial thin films. The Co-

doped Ba-122 films were found to be much more stable than Co-doped Sr-122[49, 70-71] films in an ambient atmosphere. Lee *et al.*[73] studied the weak-link behaviour of grain boundaries in Co-doped Ba-122 films by utilizing four kinds of $SrTiO_3$ (STO) bicrystal substrates with different misorientation angles (θ^{GB}). Their results showed that the current density J_c was significantly suppressed at θ^{GB} over 9 °, which is quite similar to the case of HTS cuprates (as eshown in Fig. 2-14).

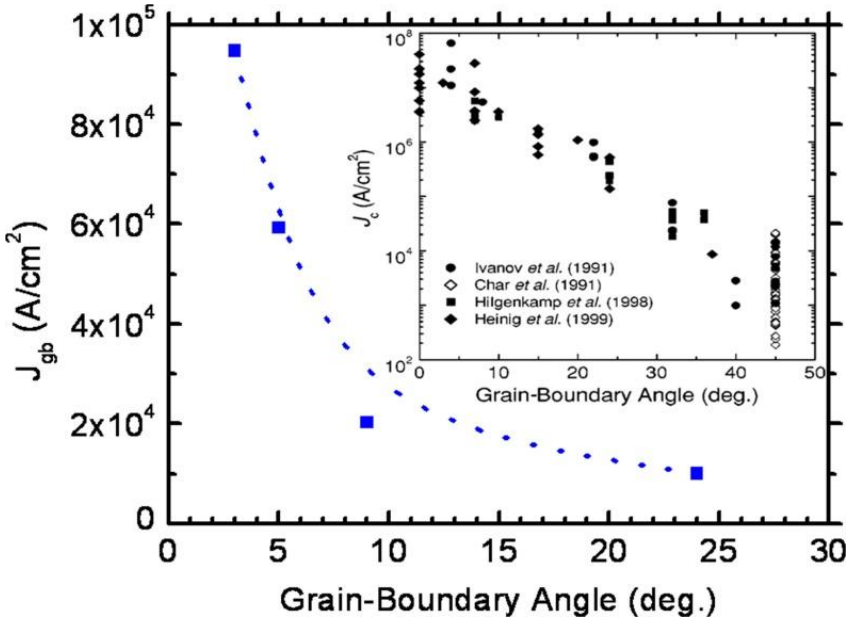

Figure 2-14. Dependence of the critical current density across grain boundaries J_{gb} (12 K, 0.5 T) as a function of the misorientation angle (θ^{GB}). Inset: the summary data for YBCO[35]. After Ref.[73].

Iida *et al.*[74] studied the strong T_c dependence of strained Co-doped Ba-122 thin films grown on different oxide substrates, including STO, LAO, LSAT, and $YAlO_3$. As shown in Fig. 2-15, different temperature dependence of resistivity is observed for the Co-doped Ba-122 films grown on the different substrates. A broad ΔT_c of over 3 K was detected for the films grown on $YAlO_3$, while the highest T_c^{onset} of 24.5 K with a sharp ΔT_c below 2 K was obtained in the film grown on STO. Moreover, the linear T_c dependence on the *c*/*a* ratio indicated the significant effect on superconductivity of lattice distortion.

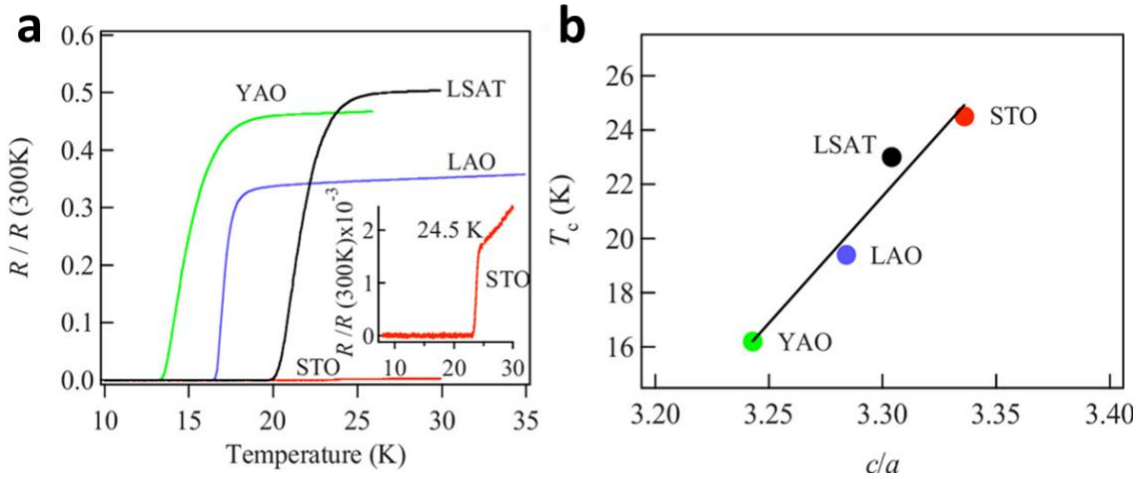

Figure 2-15. (a) ρ-T curves for the Co-doped Ba-122 thin films on various substrate materials. Inset: a T_c^{onset} of 24.5 K was obtained in the film grown on STO. (b) The linear relationship between T_c and the c/a ratio. After Ref.[74].

Buffer layers are widely used in the fabrication process for YBCO coated conductors. Lee *et al.*[75] proposed that the introduction of STO or $BaTiO_3$ buffer layers was quite effective for improving the quality of Co-doped Ba-122 single crystal thin films grown on LAO and LSAT substrates. Good superconducting performance was achieved: T_c^{onset}/T_c^{zero} of 22.8 K/21.5 K and J_c (self-field, 4.2 K) ~ 4.5 MA/cm^2. Iida's group carried out comprehensive investigations[76-78] on the positive effect of introducing a *bcc*-Fe buffer layer into Co-doped Ba-122 thin films. According to their results, the T_c values of films grown on Fe-buffered LSAT and MgO were increased by 2 - 4 K compared to those without the Fe buffer layer. The ultimate J_c (12 K) performance of the Fe-buffered Co-doped Ba-122 films reached 0.45 MA/cm^2, which is about 40 times higher than that of the one deposited directly on bare LSAT substrate[79]. The angular dependence of J_c for Co-doped Ba-122 thin film was also investigated. The mass anisotropy was found to increase with increasing temperature, indicating multiband superconductivity in this system[79]. Furthermore, via growing Co-doped Ba-122 films on fluoride AEF_2 (AE = Ba, Ca, Sr) substrates[80], the in-plane lattice parameter of Co-doped Ba-122 became smaller than that of the bulk sample, suggesting in-plane compressive strain inside the film. As seen in Fig. 2-16, the highest T_c^{90} was about 28 K, which was the first to be higher than those of bulk samples[81-82] in Co-doped Ba-122 compounds.

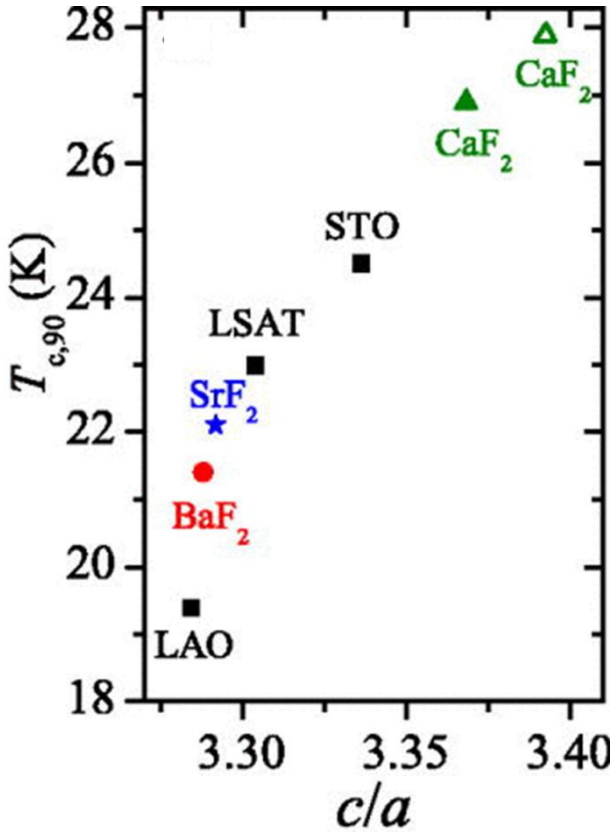

Figure 2-16. The *c*/*a* dependence of T_c^{90} appears nearly linear. The film with the highest *c*/*a* ratio shows the highest T_c^{90} of ~ 28 K (green unfilled triangle). After Ref.[80].

In order to investigate the influence of different laser sources for fabricating $Ba(Fe,Co)_2As_2$ epitaxial thin films, Hiramatsu *et al.*[83] employed four types of PLD wavelengths, the fundamental of Nd:YAG (1064 nm), the second harmonic (532 nm), KrF (248 nm), and ArF (193 nm), for Co-doped Ba-122 thin film growth. They examined the effect of photon energy and several critical factors for PLD-growth of Co-doped Ba-122 films, and some of the results are listed in Table 2-2. It was clarified that the optimal deposition rate is independent of the laser wavelength. The high J_c (over 1 MA/cm^2) obtained from the high quality Co-doped Ba-122 film grown at the optimal pulse energy was obtained irrespective of the laser wavelength. In the case of the KrF excimer laser, high excitation energy is a critical issue for fabricating high-quality films. Furthermore, the authors proposed that a Nd:YAG laser with a low laser power is a better choice for preparing high crystallinity Co-doped Ba-122 thin films with high J_c performance.

Table 2-2. Optimum pulse energies and deposition rates for the lasers (248 nm, 532 nm, and 1064 nm) used to fabricate Co-doped Ba-122 epitaxial films with high J_c and related optical parameters. After Ref.[83].

Laser Wavelength (nm)	248	532	1064
Normal Reflectance (%)	24	34	52
Pulse Width (ns)	20	5	10
Spot area (10^{-2} cm^2)	3.0	3.1	3.1
Optimum Pulse Energy (mJ)	200-300	70-100	40-50
Deposition Rate (Å/s)	3.1-3.6	2.8-3.3	3.5-3.8
Photon Number per Pulse (10^{17}) *	2.5-3.8	1.9-2.7	2.2-2.7
Excitation Energy Density (J/cm^2) **	6.7-10	2.2-3.2	1.3-1.6
Peak Power Density (10^8 W/cm^2) ***	3.3-5.0	4.5-6.4	1.3-1.6

***** Photon number per pulse = Pulse energy (J)/Photon energy (J).

****** Excitation energy density (J/cm^2) = Pulse energy (J)/Spot area (cm^2).

******* Peak power density (W/cm^2) = Pulse energy (J)/Pulse width (s)/Spot area (cm^2).

Through subtle optimization of growth conditions (e.g. raise the phase purity of the target, improve the homogeneity of substrate temperature), Katase *et al.*[84] succeeded in fabricating high-performance Co-doped Ba-122 thin films without any buffer layer. The T_c^{onset} of 22.6 K and J_c (3 K) of 2 - 10 MA/cm^2 are comparable to those for samples grown on STO or *bcc*-Fe buffer layers. It is noteworthy that their work proposed the first demonstration of devices made from iron-based superconductors, including a Josephson junction[84] and DC-SQUID[85] (shown in Fig. 2-17).

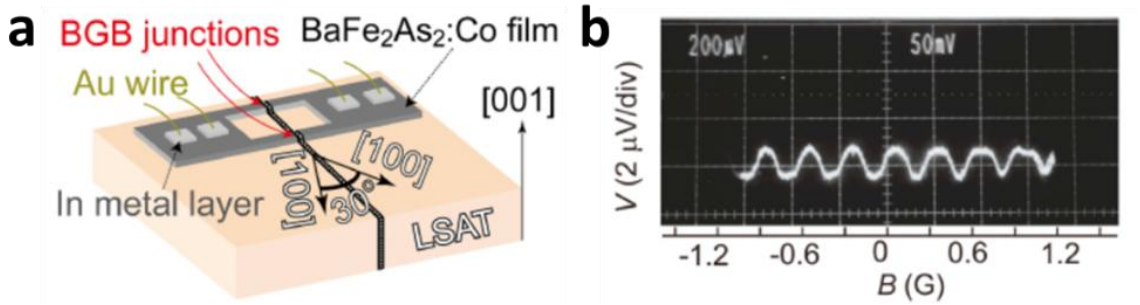

Figure 2-17. (a) Schematic illustration of a DC-SQUID structure fabricated on LSAT bicrystal substrate with θ^{GB} = 30 °. (b) Voltage-flux (V- Φ) characteristics of the DC-SQUID measured at 14 K. After Ref.[85].

2.3.2.3 K-doped Ba-122

For $Ba_{1-x}K_xFe_2As_2$ (K-doped Ba-122) bulk samples, superconductivity can be induced within the range of x = 0.16 – 1, and the highest T_c of 40 K occurs around x = 0.4. In the case of K-doped Ba-122 thin films, systematic research has been conducted

to clarify the influence of different substrates. Similar to the 1111-type thin films, MBE[86-88] and PLD[89] are also suitable for fabricating 122-type thin films. As illustrated in Fig. 2-18, Yamagishi *et al.*[88] reported the detailed K-content dependence of ρ-T curves for MBE-$Ba_{1-x}K_xFe_2As_2$ films. Lee *et al.* [89] obtained a high T_c^{onset} of 40 K and H_{c2} of ~ 155 T (for the $\rho^{90\%}$ criterion) in PLD fabricated K-doped Ba-122 thin film grown on Al_2O_3 substrate. This is comparable with the highest T_c value of a bulk sample of the same compound. Nevertheless, K-doped Ba-122 films are still not developed enough for practical applications due to the difficulty in fabrication resulting from the high vapour pressure of K. Nevertheless, this type of 122-type compound possesses higher T_c[88-89] and low anisotropy[90] compared with its Co-doped Ba-122 counterparts.

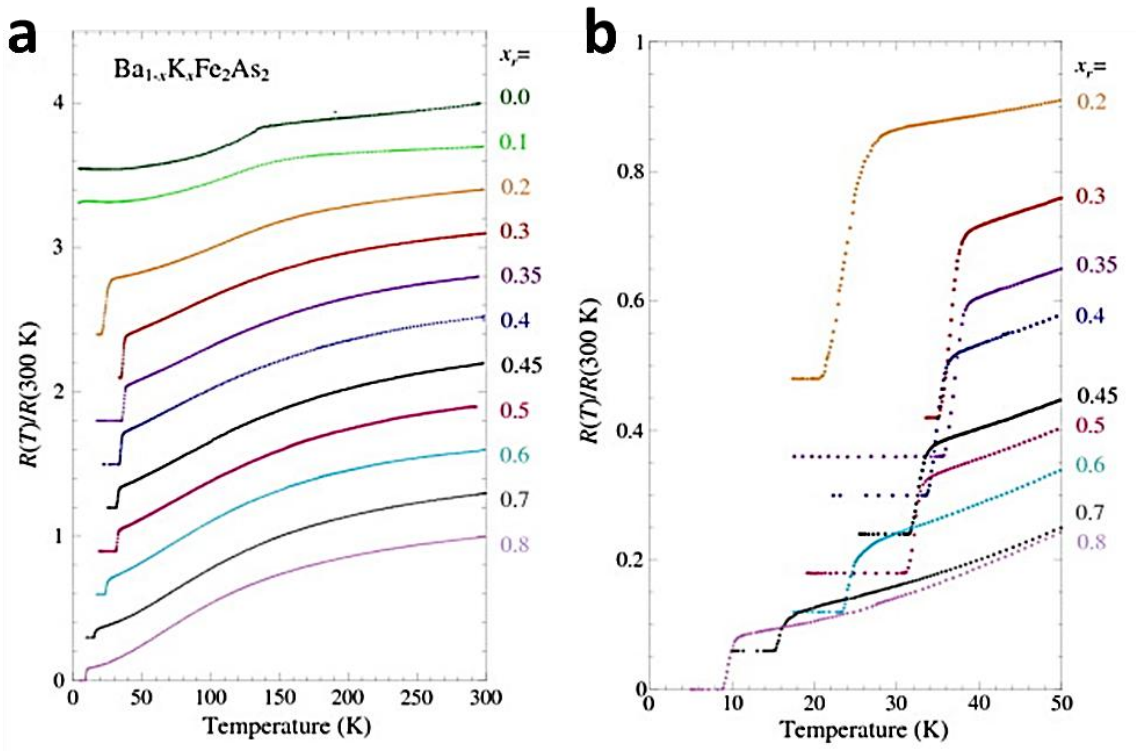

Figure 2-18. Temperature dependence of the normalized resistance (R(T)/R(300 K)) for MBE prepared $Ba_{1-x}K_xFe_2As_2$ films. (a) The whole temperature range, and (b) the magnified view from 0 - 50 K. After Ref.[88].

2.3.2.4 P-doped Ba-122

Jiang *et al.*[91] discovered that the superconductivity can also be induced in the $BaFe_2As_2$ parent phase by a partial substitution of phosphorus for As, which introduces chemical pressure. They studied the $BaFe_2(As_{1-x}P_x)_2$ by tuning the content of P-doping x. Some of the results are shown in Fig. 2-19. Apparently, superconductivity appeared in the range of x' = 0.2 - 0.7, and T_c can be optimized to ~ 31 K around x = 0.32. A similar

result was also reported by Ishida *et al*.[82]

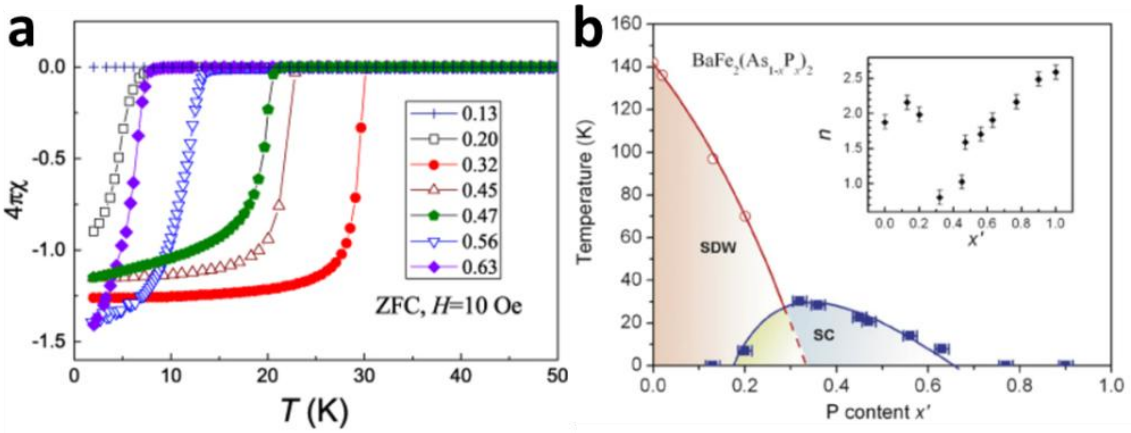

Figure 2-19. (a) Superconducting diamagnetic transitions for $BaFe_2(As_{1-x}P_x)_2$. (b) Phase diagram for $BaFe_2(As_{1-x}P_x)_2$. SDW and SC refer to spin-density-wave and superconducting state, respectively. Inset: the x' dependence on the exponent n in the formula $\rho(T) = \rho_0 + \alpha T^n$. After Ref.[91].

In the case of film fabrication, both the PLD[92-93] and the MBE[94] methods are suitable for fabricating P-doped Ba-122 epitaxial thin films with T_c comparable to those of bulk samples[82, 91]. Intriguingly, the J_c value of P-doped Ba-122 films is found to be extremely high. Sakagami *et al*.[94] reported the strong Ba/Fe ratio dependence of J_c (as shown in Fig. 2-20 (a)). In their work, a thin film sample with Fe-rich conditions generally shows a higher J_c value, which implies that nanoparticles of Fe-related compounds were acting as effective pinning centres. As a result, the highest J_c in self-field at 4.2 K reached 10 MA/cm^2 in this sample. Furthermore, the θ^{GB} dependence of J_c was also investigated (as shown in Fig. 2-20 (b)). The J_c at 4.2 K of a P-doped Ba-122 film grown on MgO bicrystal substrate with a $\theta^{GB} = 24°$ was over 1 MA/cm^2, which, surprisingly, surpassed those of Co-doped Ba-122 films[33] and even YBCO HTS[35]. Therefore, P-doped Ba-122 materials are highly promising for superconducting-related applications in the form of wires or tapes.

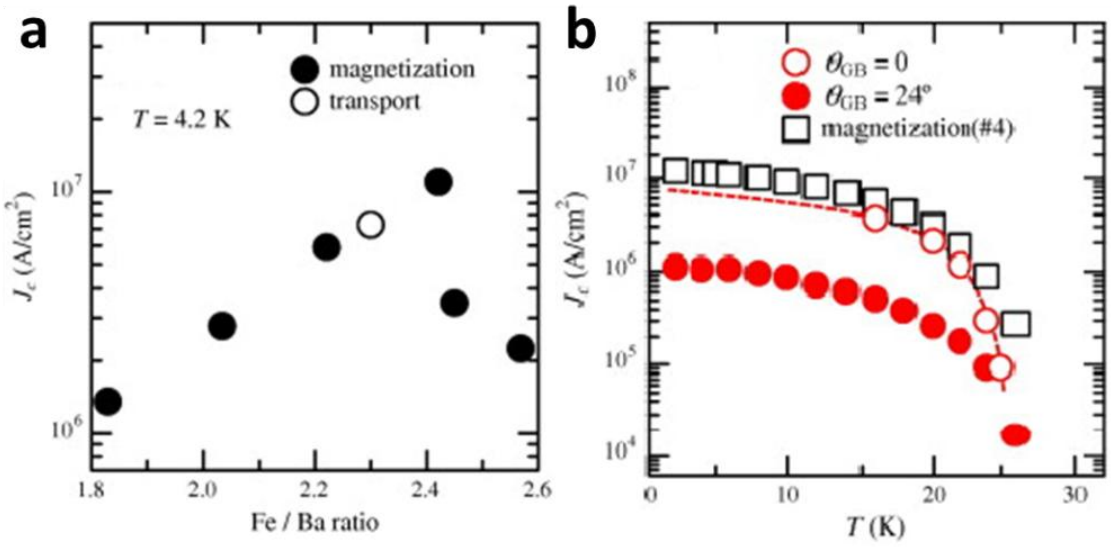

Figure 2-20. (a) Self-field J_c at 4.2 K as a function of the Fe/Ba composition ratio of the $BaFe_2(As,P)_2$ thin films. (b) Temperature dependence of the intra-grain (θ^{GB} = 0°) J_c and inter-grain (θ^{GB} = 24°) J_c. After Ref. [94].

Sato *et al.*[95] fabricated P-doped Ba-122 films with thickness of 150 - 200 nm on MgO substrates by the PLD method (Nd:YAG, 532 nm). The high self-field J_c (4 K) of 7 MA/cm^2 and a high J_c (4 K) of over 1 MA/cm^2 under 9 T obtained in their work broke the J_c record for all types of iron-based superconducting thin films at that time. They pointed out that decreasing the film growth rate would introduce vertical defects along the *c*-axis direction, which would also be able to serve as strong vortex-pinning centres and lead to a low J_c anisotropy. The appearance of the vertical defects is shown below in Fig. 2-21.

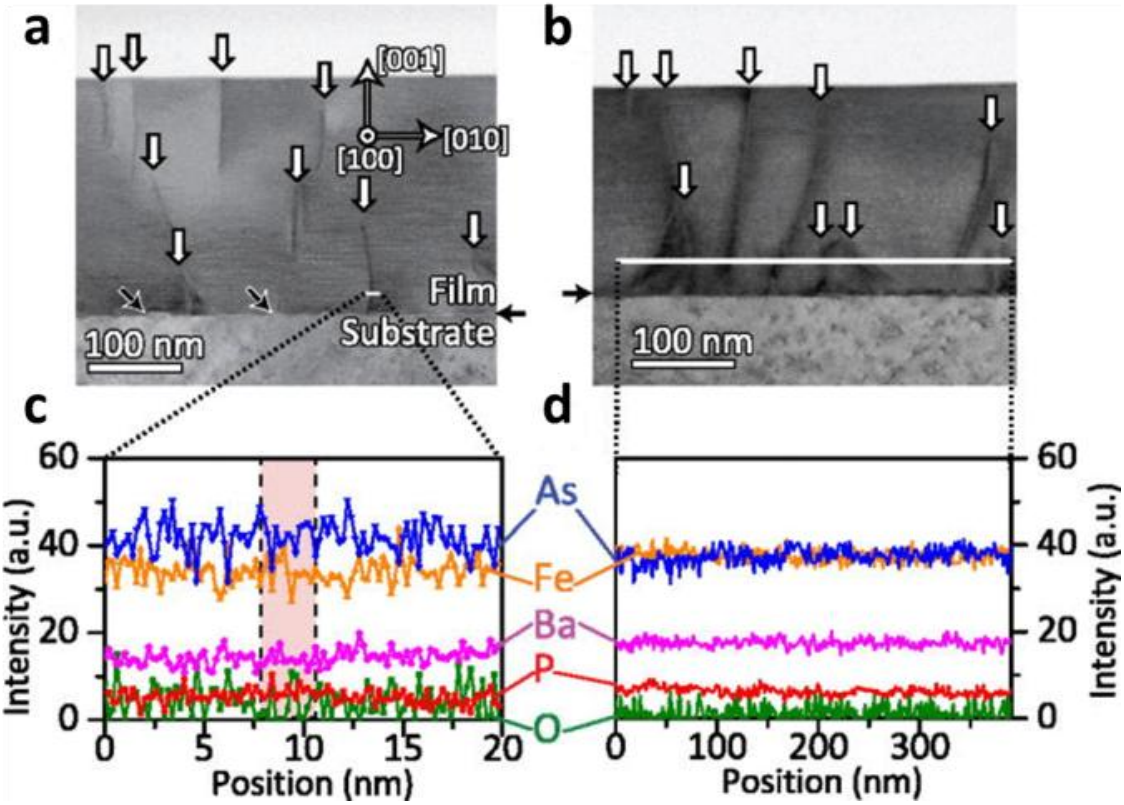

Figure 2-21. Cross-sectional scanning transmission electron microscope (STEM) images for P-doped $BaFe_2As_2$ epitaxial films grown at the growth rates of (a) 2.2 Å/s and (b) 3.9 Å/s. Horizontal black arrows: the heterointerface between the substrate and the film. White arrows: vertical defects. Slanted black arrows: O-rich island structures. (c) & (d): Corresponding STEM-EDS linear scans. Shaded region: corresponding vertical defects in (a). After Ref.[95].

2.3.2.5 Electron-doping & Tensile-strain Induced Superconductivity in Ba-122

Apart from regular chemical replacement, electron-doping and tensile-strain are also useful approaches to induce superconductivity in Ba-122 type compounds.

Due to a unique characteristic of Ba-122 superconductors, superconductivity can be induced by substituting at any of three sites[82]. The substitution on the barium site was always unsuccessful by using conventional solid-state synthesis methods, however, that is to say, in bulk samples. Katase *et al.*[96] accomplished this task by using the PLD method, a nonequilibrium film growth process. In their work, indirect electron-doping into $Ba_{1-x}La_xFe_2As_2$ film was realized by partial element substitution of lanthanum on barium sites, which suppressed the antiferromagnetic transition and then induced superconductivity. The highest T_c^{onset} of 22.4 K was obtained at x = 0.13. Another kind of electron-doping by a direct method was reported by Ni *et al.*[97] in their Co-doped Ba-

122 films by partially replacing cobalt on Fe sites. The electronic phase diagrams for both indirectly and directly electron-doped $BaFe_2As_2$ single crystals are exhibited in Fig. 2-22. More intrinsic evidence of electron-doping was published by Liu *et al.*[98] in their angle-resolved photoemission spectroscopy (ARPES) results. The evolution of the Fermi surface of Co-doped Ba-122 bulks after the doping process was clearly observed.

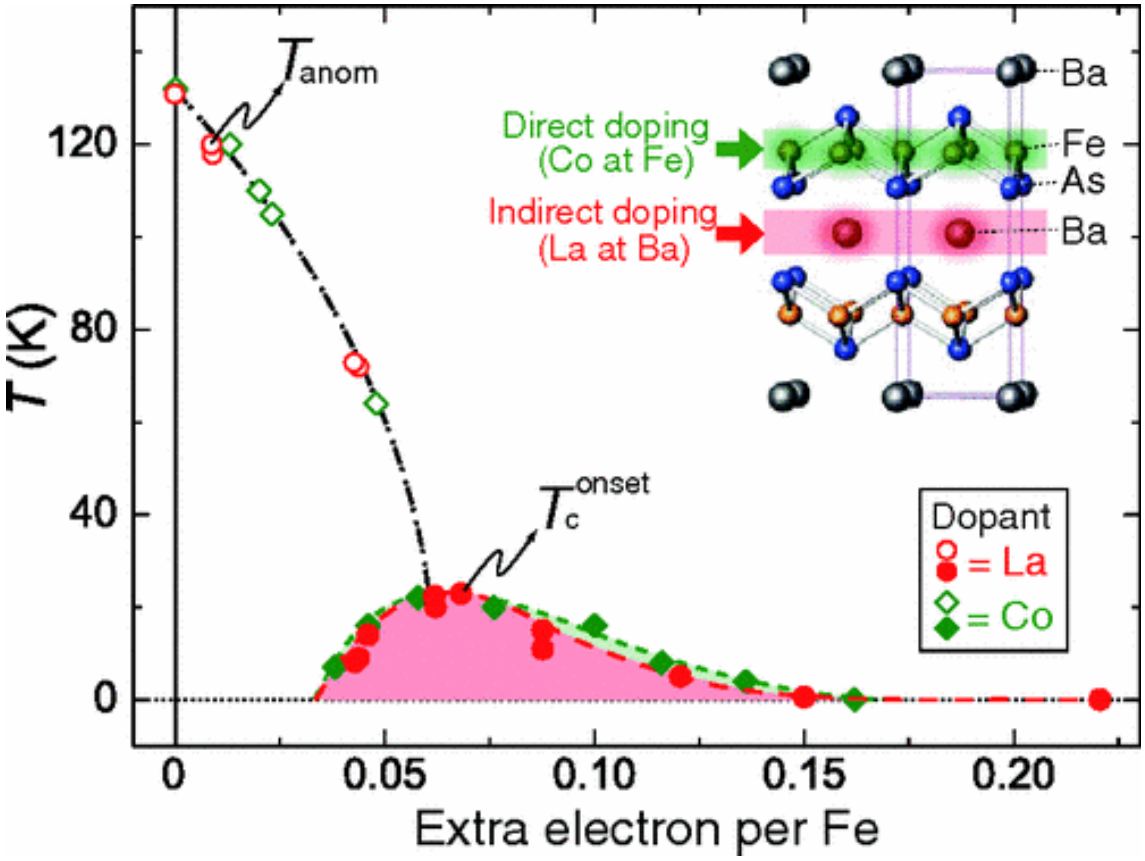

Figure 2-22. Electronic phase diagram of indirectly electron-doped $(Ba_{1-x}La_x)Fe_2As_2$ and directly electron-doped $Ba(Fe_{1-x}Co_x)_2As_2$ single crystals. Inset: the concepts of indirect and direct doping in the $BaFe_2As_2$ crystal. After Ref.[96].

Fig. 2-23 illustrates the J_c-H performance of Co/P-doped Ba-122 thin films together with a Sm-1111 film for comparison. Apparently, the in-field properties of Co-doped Ba-122 films were not promising before the year 2013.Probably due to their high T_c and effective vortex pinning, however, the in-field J_c performance of P-doped Ba-122 films is generally superior to that of Co-doped Ba-122 films. Overall, the Ba-122 type is more promising than the 1111-type for high field applications, not only because of the high T_c and J_c performances, but also because there are much fewer fabrication difficulties.

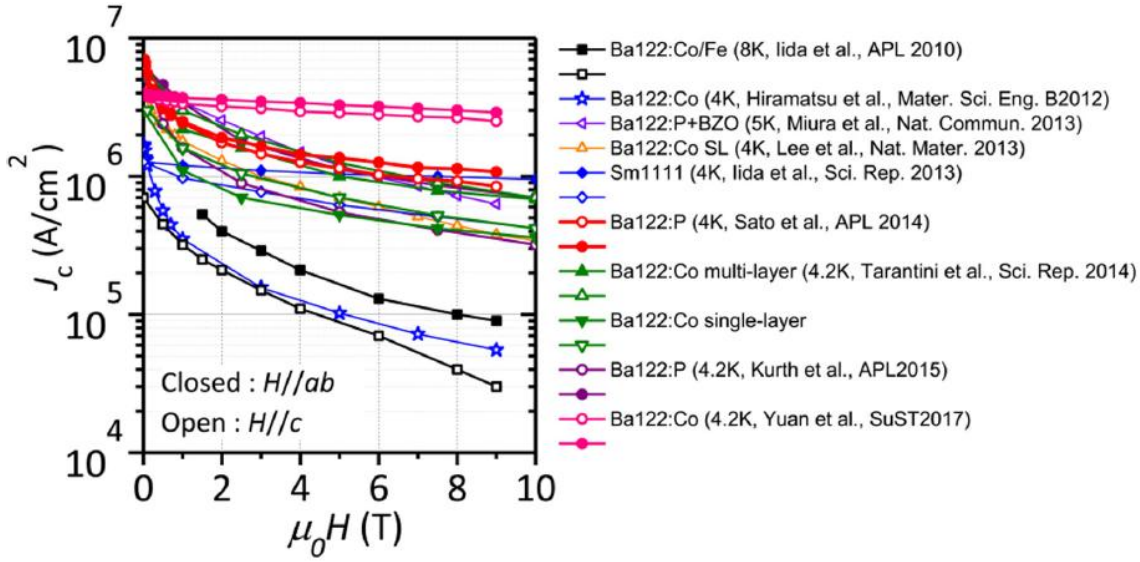

Figure 2-23. J_c-H performance for 1111-type and 122-type epitaxial thin films at low ambient temperatures. After Ref.[29].

2.3.3 11-type

2.3.3.1 A Brief Introduction of 11-type Fe-Ch Bulks

The research done on 11-type bulk samples always has instructional significance for the same compound in the form of thin films. Hence, it is worth first briefly reviewing the highlights in the history of 11-type single crystalline bulks.

Discovery of FeSe Superconductivity

The most obvious distinction between 11-type and other parent phases is that the extremely toxic As is no longer essential, which renders this system less poisonous and much easier to handle. Hsu *et al.*[99] first reported a zero resistance transition at 8 K in the α-FeSe compound. Although FeSe compounds were already being extensively studied in the late 1970s[100-101], Hsu *et al.* pointed out that the key issue in obtaining a clean superconducting phase in this system is fabricating samples with intentional Se deficiency. As displayed in Fig. 2-24 (a), FeSe has the simplest crystal structure among all the iron-based superconductor parent phases, which is classified as the tetragonal "α-PbO" type with the space group *P4/nmm*. Similar to the layered 1111-type quaternary iron oxypnictides (see Fig. 2-24 (b) for a structural comparison between FeSe and LaFeAsO), the tetragonal phase of α-FeSe has a Fe-based layered sublattice as well, consisting of stacked edge-sharing $FeSe_4$-tetrahedra in layers. The zero resistance result for $FeSe_{0.88}$ polycrystalline bulk is shown in Fig. 2-24 (c). T_c monotonically decreases with increasing external field, and the H_{c2} is about 16.3 T, which reflects a coherence

length of $\xi \approx 4.5$ nm.

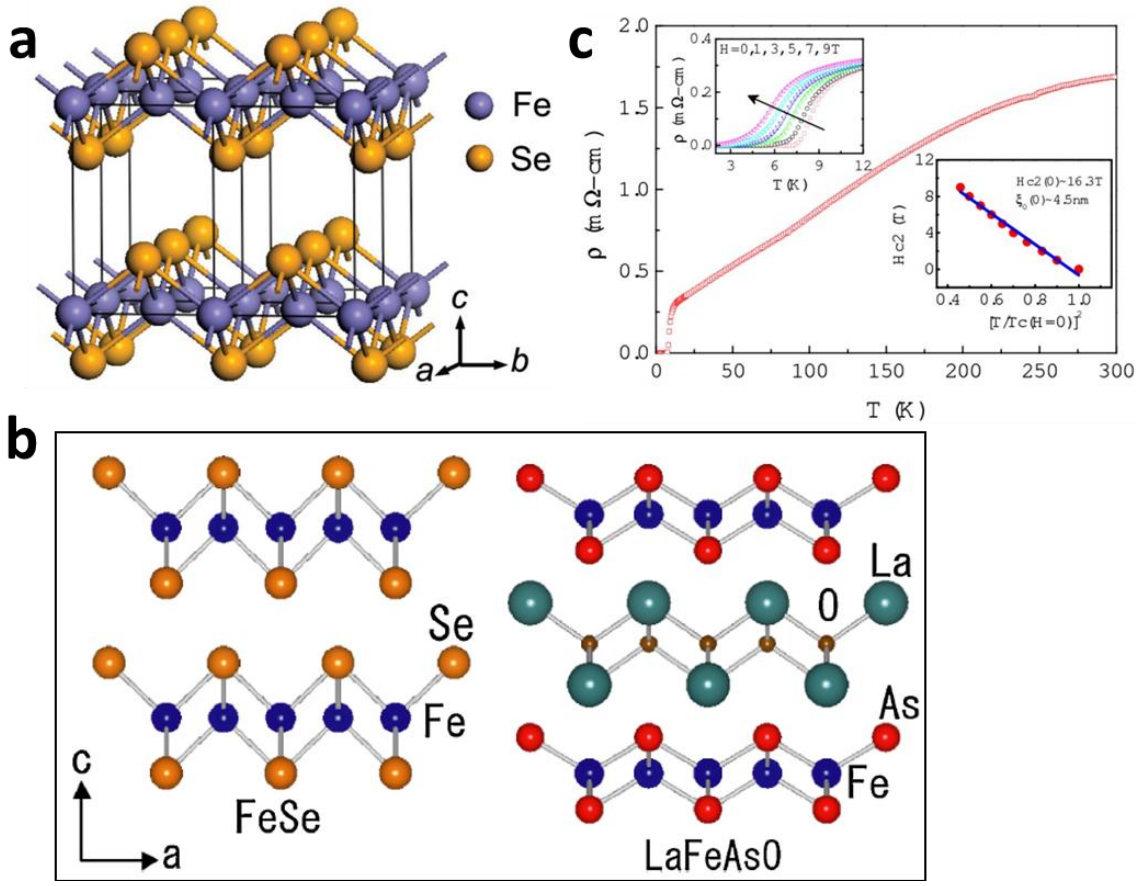

Figure 2-24. (a) Crystal structure of α-FeSe compound[99]. (b) Comparison of the crystal structures of FeSe (left) and LaFeAsO (right)[102]. (c) ρ-T curves of $FeSe_{0.88}$. Left inset: in-field ρ-T curves. Right inset: H_{c2}-T with fitting curve shown in blue[99].

Te-substitution in FeSe

For pursuing higher T_c, chemical substitution in FeSe has been attempted on both Fe and Se sites. Most reports in the literature, however, suggest that substitution on Fe sites often has a negative effect on the superconductivity, or at least exhibits a complex dependence. On the contrary, isoelectronic substitution on Se sites can easily realize T_c enhancement, especially in $FeTe_{1-x}Se_x$ compound.Te, which comes from the same chalcogenide family of elements as Se, was found to be very effective for enhancing the T_c of FeSe compounds by partially substituting on Se sites. T_c was raised from 8 K (in FeSe) to 15 K (in $FeSe_{1-x}Te_x$) at x = 0.5[103]. The improved superconductivity was thought to be due to the higher stability of the spin density wave (SDW) in FeTe than in FeSe. Further investigation found that the increase in T_c was not accompanied by any change in the carrier concentration when Se^{2-} was partially replaced by Te^{2-}[104], which is associated with the structural deformation due to Te-

doping. Apparently, the local symmetry is varied from the average *P4/nmm* (bond angle of Fe-Se-Fe ~ 104 °) to a lower state by substituting Te atoms on Se sites. In addition, the crystal structure of Fe-*Ch* can be further stabilized by the Te-substitution effect. For instance, the tetragonal structure of $Fe_{1+x}Se$ is only stable in the narrow range of $0.011 < x < 0.026$[105] (temperature phase diagram shown in Fig. 2-25 (a)), while a T_c of 15 K can be easily obtained in tetragonal $FeTe_{1-x}Se_x$ over a range of x = 0 - 0.5[106-107] (phase diagram shown in Fig. 2-25 (b)).

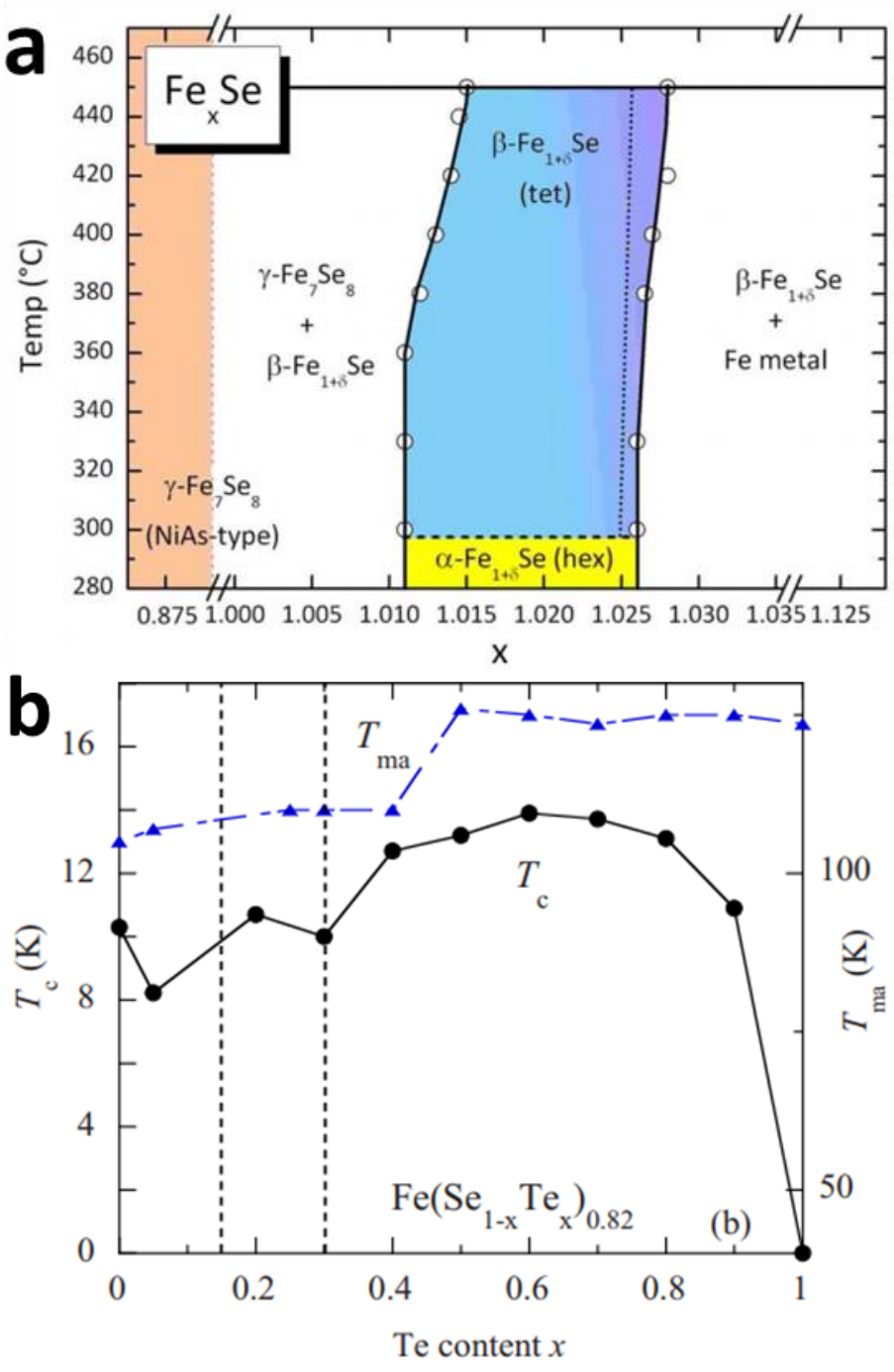

Figure 2-25. (a) Phase diagram for the Fe-Se system near 1:1 stoichiometry[105]. (b) T_c as a function of Te-

content x in the $Fe(Se_{1-x}Te_x)_{0.82}$ series[106].

With an increasing level of Te doping, the structural transition (from tetragonal *P4/nmm* to orthorhombic *Cmma*) is gradually suppressed in $FeSe_{1-x}Te_x$ compounds. The phase diagram of a $Fe_{1+d}Te_{1-x}Se_x$ system with excess-Fe concentration was established by Mizuguchi *et al.*[102], based on experimental results as well as theoretical data, as shown in Fig. 2-26 (a). T_s and T_c refer to the structural transition temperature and the superconducting transition temperature, respectively. The highest T_c can be obtained with x within the range from 0.4 - 0.6 in the tetragonal region. With increasing Te-concentration, T_s is suppressed, T_c decreases, and AFM ordering appears, accompanying the distortion of the tetragonal-monoclinic structure[102]. As the superconductivity can be easily induced by substituting Se[103] or sulfur[108] on Te-site, it is well accepted that FeTe acts as the parent phase of the 11-type Fe-*Ch* superconductors. The fabrication of single crystalline Fe-*Ch* bulk samples is not difficult. By using the flux method, Liu *et al.*[109] obtained a series of $Fe_{1.02}(Te_{1-x}Se_x)$ single crystals and constructed the corresponding electronic and magnetic phase diagram for x within the range of 0 - 0.5. As seen in Fig. 2-26 (b), the Néel temperature (T_N) could be determined by the results of neutron scattering, the susceptibility (χ), the Hall coefficient (R_H), and resistivity (ρ) measurements. Region (I) with $0 \leq x < 0.09$ in pink shows long-range AFM ordering. Region (II) with $0.09 < x < 0.29$ exhibits a non-bulk superconducting state, or the so-called "filamentary superconductivity" with a superconducting volume fraction less than 3 %. Only in Region (III) with $x \geq 0.29$ does bulk superconductivity exist, and the highest $T_c \sim 15$ K appears with about 50 % Se-doping, which is in line with the results on polycrystalline bulks. One of the marked features in the $Fe_{1+d}Te_{1-x}Se_x$ single crystal system is the existence of excess Fe. It appears in both Fe planes and the Se/Te interstitial sites. Excess Fe contains much stronger magnetic moments than Fe in normal sites, which leads to the localization of charge carriers and the complete elimination of superconductivity, even when the amount of excess Fe is as low as 3 - 5 %[105].

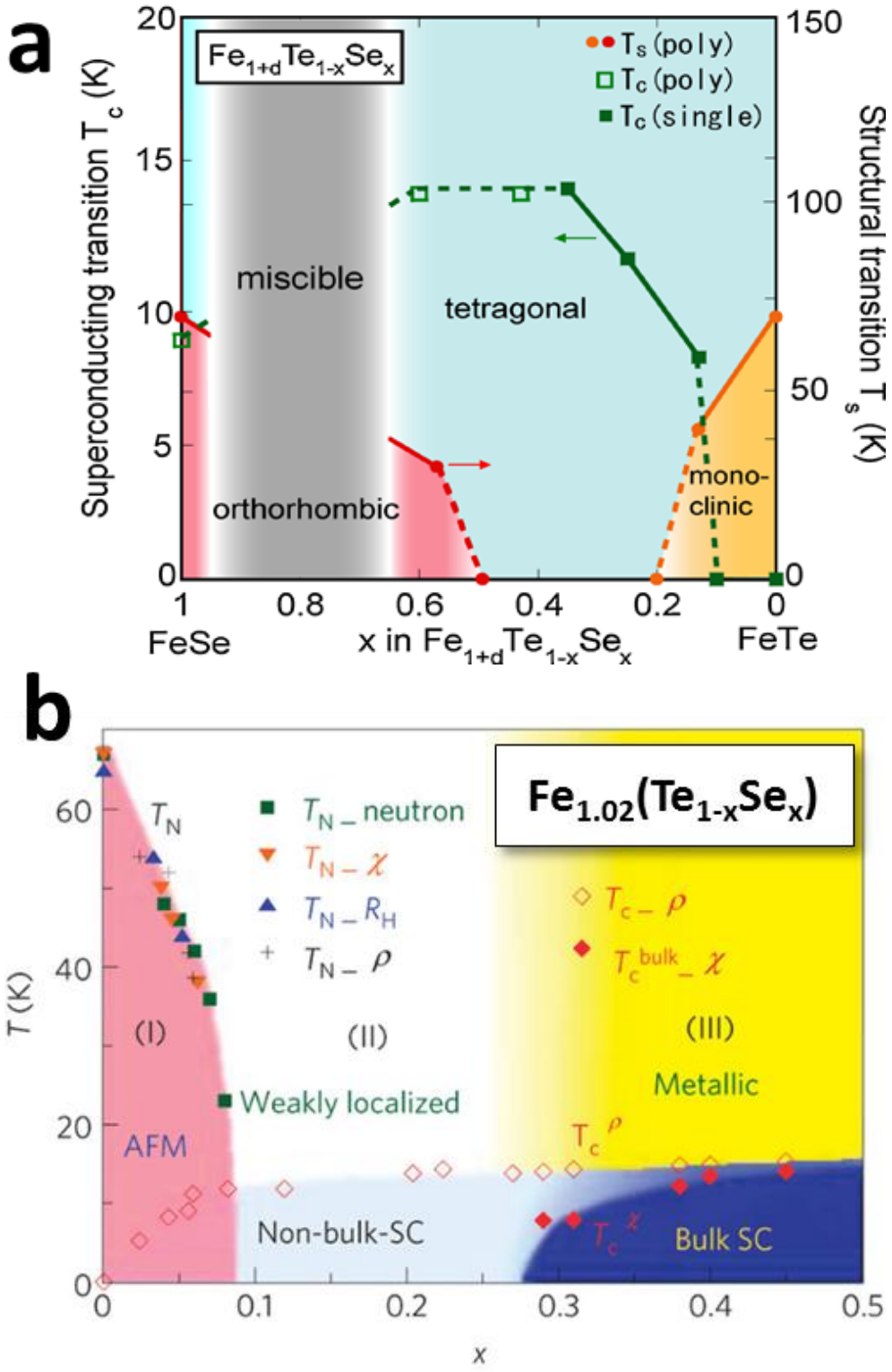

Figure 2-26. (a) Structural phase diagram of $Fe_{1+d}Te_{1-x}Se_x$ with low excess-Fe[102]. (b) Magnetic & electronic phase diagram of $Fe_{1.02}(Te_{1-x}Se_x)$ with x = 0 - 0.5[109].

Pressurization Effect

The pressurization effect on T_c is always of great interest in iron-based superconductors. Similar to most parameter controlled cases, the pressure dependence

of the superconducting T_c of 11-type Fe-*Ch* bulk initially increases up to an optimized level with applied pressure, then decreases once the pressure is too high[110-111]. Among all the iron chalcogenides, FeSe exhibits the most significant T_c enhancement as a result of the pressurization effect. Although pure β-FeSe shows a low T_c ~ 8 K[99], it can be dramatically enhanced to five times higher under high pressure[112]. In detail, Mizuguchi *et al.*[113] published the first observation of the enhanced superconductivity in tetragonal FeSe polycrystalline bulks after a pressurization process in a piston-cylinder cell (shown in Fig. 2-27 (a)). Boosted T_c^{onset} of ~ 27 K and H_{c2} of ~ 72 T were obtained at 1.48 GPa. With the help of diamond-anvil cells, higher pressure was able to be applied. At almost the same time, Medvedev *et al.*[112] and Margadonna *et al.*[110] reported their discoveries of a high T_c of ~ 37 K in pressurized polycrystalline FeSe samples at 8.9 GPa (Fig. 2-27 (b)) and 7 GPa (Fig. 2-27 (c)), respectively. The origin of the significant pressure effect on FeSe was immediately investigated, and its positive linkage with the enhancement of AFM spin fluctuations was proposed by Imai *et al.*[111] based on nuclear magnetic resonance (NMR) results. Garbarino *et al.*[114] studied the structural transition of FeSe under high pressure up to 26 GPa and ascribed the enhanced T_c > 34 K to the greater stabilization of the orthorhombic structure under high pressures than for the tetragonal structure. Margadonna *et al*. summarized the response of bond lengths, bond angles, and anion heights in FeSe to the pressure effect. Moreover, the pressure effect is also correlated with the orientation of the applied pressure[112]. Pressure from different directions can result in variation in structural parameters and consequently break magnetic symmetry.

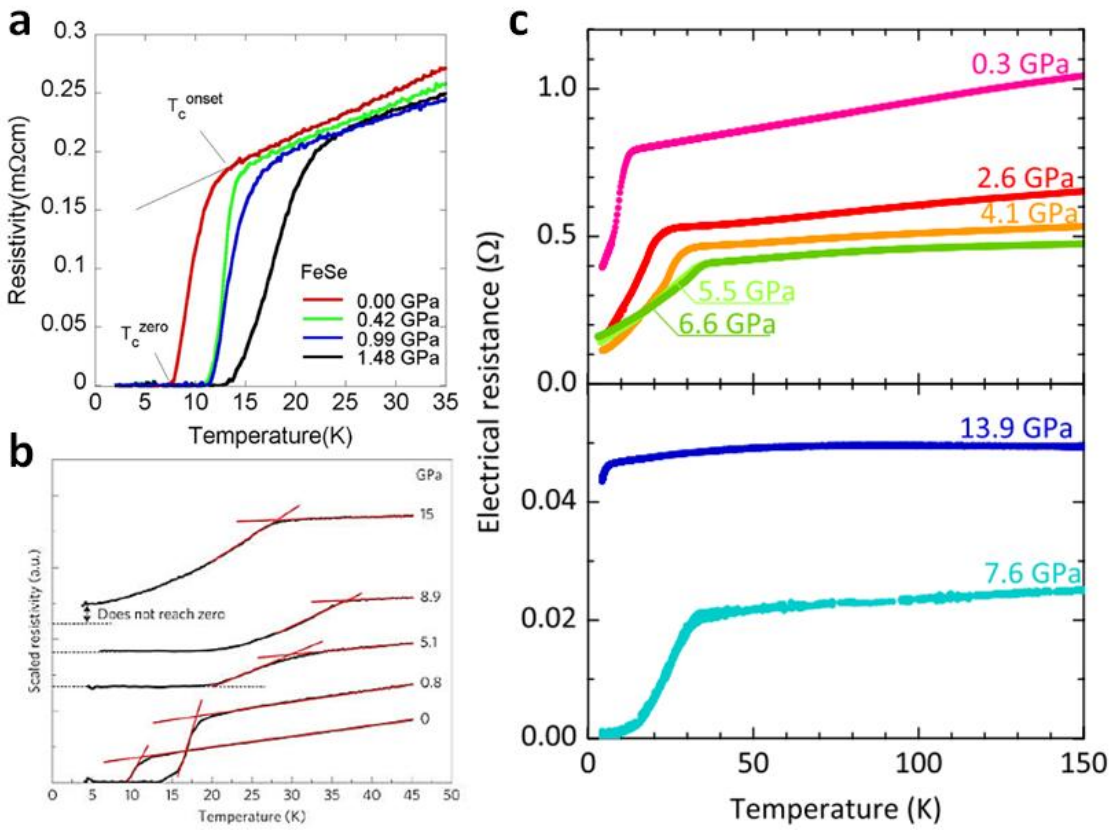

Figure 2-27. *ρ-T* curves of polycrystalline FeSe samples under pressure. After: (a) Ref.[113]. (b) Ref.[112]. (c) Ref.[110].

Se-substituted FeTe ($FeTe_{1-x}Se_x$) shows the highest T_c values among Fe-*Ch* bulks at ambient pressure. The positive pressurization effect on $FeTe_{1-x}Se_x$ resembles that on FeSe mentioned above[115-117]. Three works have been done on this topic and they are separately illustrated in Fig. 2-28. Mizuguchi *et al.*[117] reported a pressure-enhanced T_c in $FeTe_{0.75}Se_{0.25}$ bulk under 0.99 GPa. The highest pressure that was ever tried on $FeTe_{1-x}Se_x$ bulk was 11.9 GPa, and the maximum T_c of 23.3 K was obtained at ~ 3 GPa[115]. A dome-shaped phase diagram indicating the correlation of pressure-temperature for $Fe_{1.03}Te_{0.43}Se_{0.57}$ was also established, showing a clear orthorhombic-monoclinic structural transition around 2 - 3 GPa[115]. Similar T_c vs. pressure behaviour was also found in $FeSe_{0.5}Te_{0.5}$ by Horigane *et al.*[116] The origin of the positive pressure effect in $FeTe_{1-x}Se_x$ was investigated by Shimizu *et al.*[118] based on ^{125}Te NMR measurements. The results supported the scenario that AFM spin fluctuations promote the pairing of electrons for superconductivity, which also works in the case of FeSe. Nevertheless, the non-superconducting property of pure FeTe compound was not changed by applying high pressure[119-120], in spite of the suppression of AFM ordering. Nevertheless, Han *et al.*[121] reported that a superconducting transition was found in

tensile-stressed FeTe films grown on MgO substrates, suggesting the possible importance of uniaxial pressure for inducing superconductivity in the FeTe system. The tensile strain was almost equivalent to a "negative" hydrostatic pressure applied on FeTe compound. Therefore, this work suggests that a pressure effect can be alternatively achieved by interfacial strain introduced by film deposition. Considering that Fe-*Ch* superconductors are quite sensitive to pressure (T_c = 37 K for FeSe bulk under 8.9 GPa[112]), more intriguing findings can reasonably be expected in the research on 11-type thin films by carefully selecting the growth substrates as a source of in-plane strain.

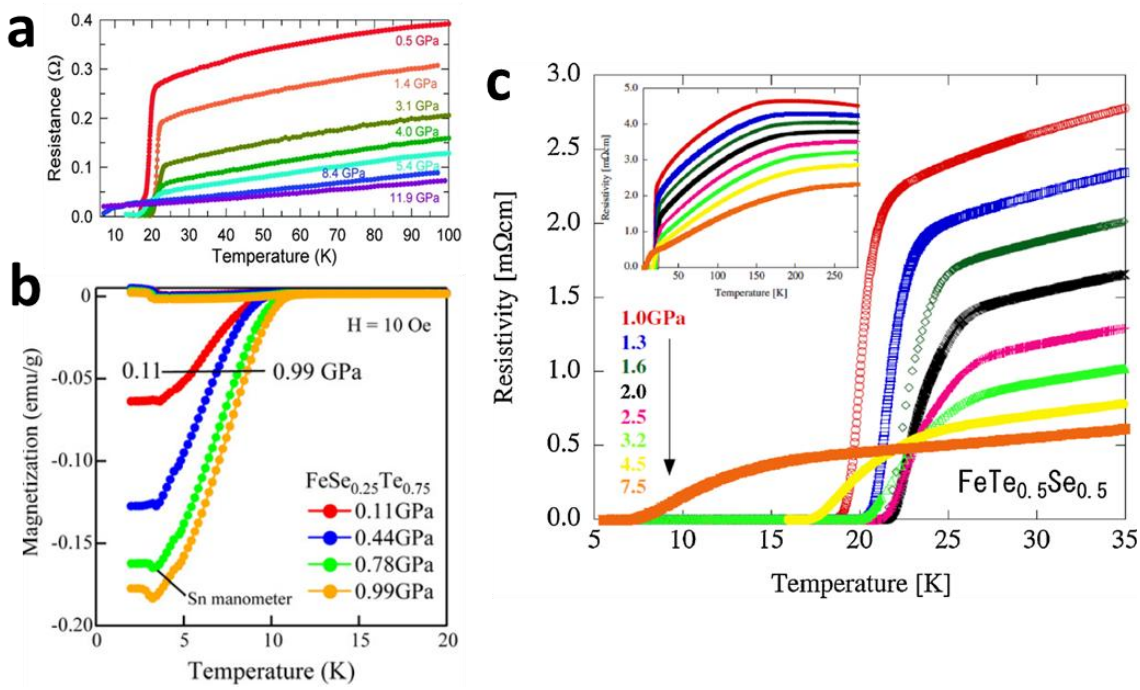

Figure 2-28. Temperature dependence of resistivity/magnetization for $FeTe_{1-x}Se_x$ under different pressures. (a) *R*-*T* curves under pressure up to 11.9 GPa for $Fe_{1.03}Te_{0.43}Se_{0.57}$[115]. (b) *M*-*T* curves under pressure up to 0.99 GPa for $FeTe_{0.75}Se_{0.25}$[117]. (c) *R*-*T* curves under pressure up to 7.5 GPa for $FeTe_{0.5}Se_{0.5}$, with the inset showing a wider temperature range[116].

2.3.3.2 Conventional 11-type Thin Films

Early in 1997, FeSe[122] thin film had already been synthesized, although the characterizations lacked any report on superconductivity. Right after the striking reports on superconducting 122-type thin films, research started to be focused on the superconductivity of the 11-type iron-based compounds. The first observation of superconductivity in a 11-type Fe-*Ch* thin film was by published by Han *et al.*[123] on arXiV (official version: Ref.[37]). Off-stoichiometric $FeSe_x$ (nominal x = 0.92, 0.88, 0.84, and 0.80) polycrystals were used as target materials and STO, LSAT, and LAO as

growth substrates. More than 150 thin films were prepared by varying experimental parameters including substrate temperature and deposition pressure (results shown in Fig. 2-29) in the PLD method. The best T_c^{onset} of 11.8 K and H_{c2} of 14.0 T were obtained in a *c*-axis oriented $FeSe_{0.88}$ film grown on LAO substrate, although T_c^{zero} was only ~ 3.4 K in the optimal sample. The authors also emphasized the difficulty in producing superconducting FeSe thin films, reflecting the narrow window of film growth.

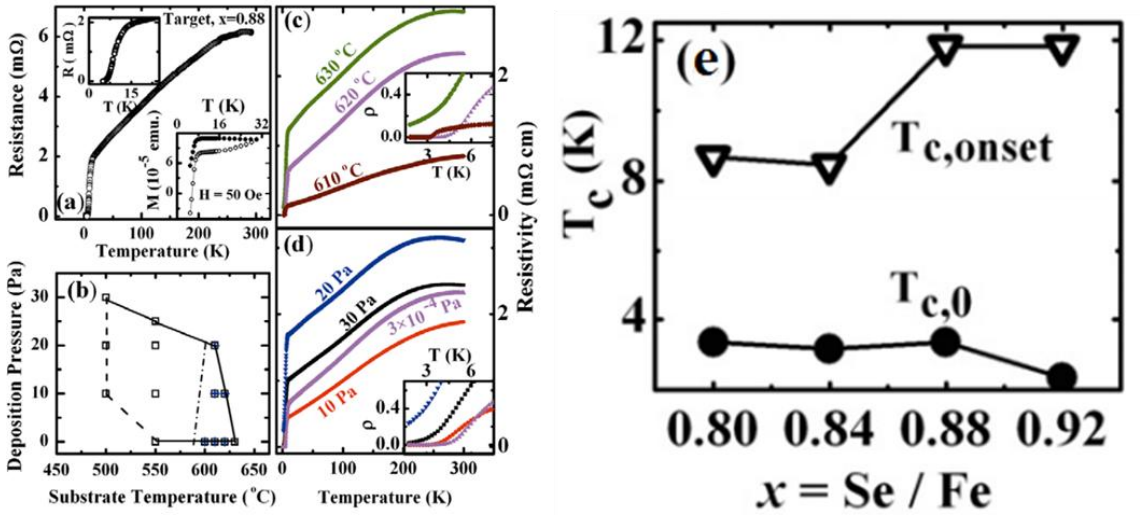

Figure 2-29. The first reported superconductivity in FeSe thin films and the corresponding phase diagram for T_c - "Se content". (a) ρ-T and M-T curves for a $FeSe_{0.88}$ target pellet. (b) Phase diagram for $FeSe_{0.88}$ film deposition parameters. Empty symbols: films were single-phase and epitaxial. Cross symbol: films were superconducting. ρ-T for $FeSe_{0.88}$ films on LAO prepared at different temperatures (c) and pressures (d). (e) Dependence of T_c^{onset} and T_c^{zero} on the Se/Fe ratio for FeSe/LAO films prepared at 620 ℃, 3×10^{-4} Pa. After Ref.[37].

Soon after the work on superconducting FeSe thin films[124], Wu *et al*. reported much improved superconducting performance in FeSe and Te-substituted FeSe ($FeSe_{1-x}Te_x$) thin films. The detailed experimental results are illustrated in Fig. 2-30. Sensitive thickness dependence of T_c in FeSe and $FeSe_{1-x}Te_x$ films has been reported. T_c increases with increasing film thickness, although the detected T_c values were still not in not agreement with that of the bulk sample, even when the thickness of the film was as high as 1 μm. In addition, the chemical doping-effect of β-FeSe, including the substitution of transition metal elements on Fe-sites and Te-sites was also investigated. The superconductivity was found to correlate with structural deformation and the condition of magnetic symmetry. Unfortunately, at the early stage, fabrication of high-quality FeSe and Fe(Se,Te) epitaxial thin films was still not easy, and T_c was often lower than for the corresponding single crystal samples[125-128]. After the improvements in the

fabrication process, T_c enhancement was obtained in some works[129-131], and high-performance 11-type Fe-*Ch* thin films can now be easily prepared. The origin of the enhanced T_c will be discussed in the following section.

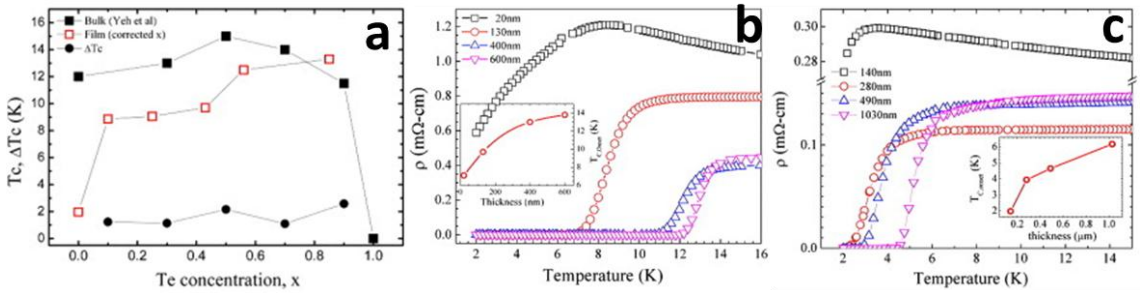

Figure 2-30. (a) Phase diagram of $T_c^{90\%}$ as a function of Te-content. ρ-T curves for b) $FeSe_{0.5}Te_{0.5}$ and c) $FeSe_{1-x}$ thin films. Insets: thickness dependence of T_c^{onset}. After Ref.[124]

Strain-effect

The strain effect originating from film growth is the most prominent factor that determines the physical properties of Fe-*Ch* thin films. Imai *et al.*[128] successfully grew $FeSe_{0.5}Te_{0.5}$ films on MgO substrate by PLD and obtained a T_c^{onset} of 10.6 K, which was considered to be affected by the epitaxial strain. Nie *et al.*[125] fabricated FeSe epitaxial thin films with thickness of 50 nm, 100 nm, and 200 nm on MgO, STO, and LAO substrates (lattice mismatches: 0.64 %, 3.7 %, and 12 %, respectively) and studied the strain effect on the FeSe films. As shown in Fig. 2-31, all the samples exhibited superconducting transitions except for the 50 nm FeSe films grown on MgO and STO substrates, which were attributed to the magnified strain on the relatively thin films. Owing to the strain-relief effect, other FeSe films with higher thicknesses showed a superconducting transition. Thus, the authors pointed out the detrimental effect of tensile strain on the superconductivity in FeSe thin films.

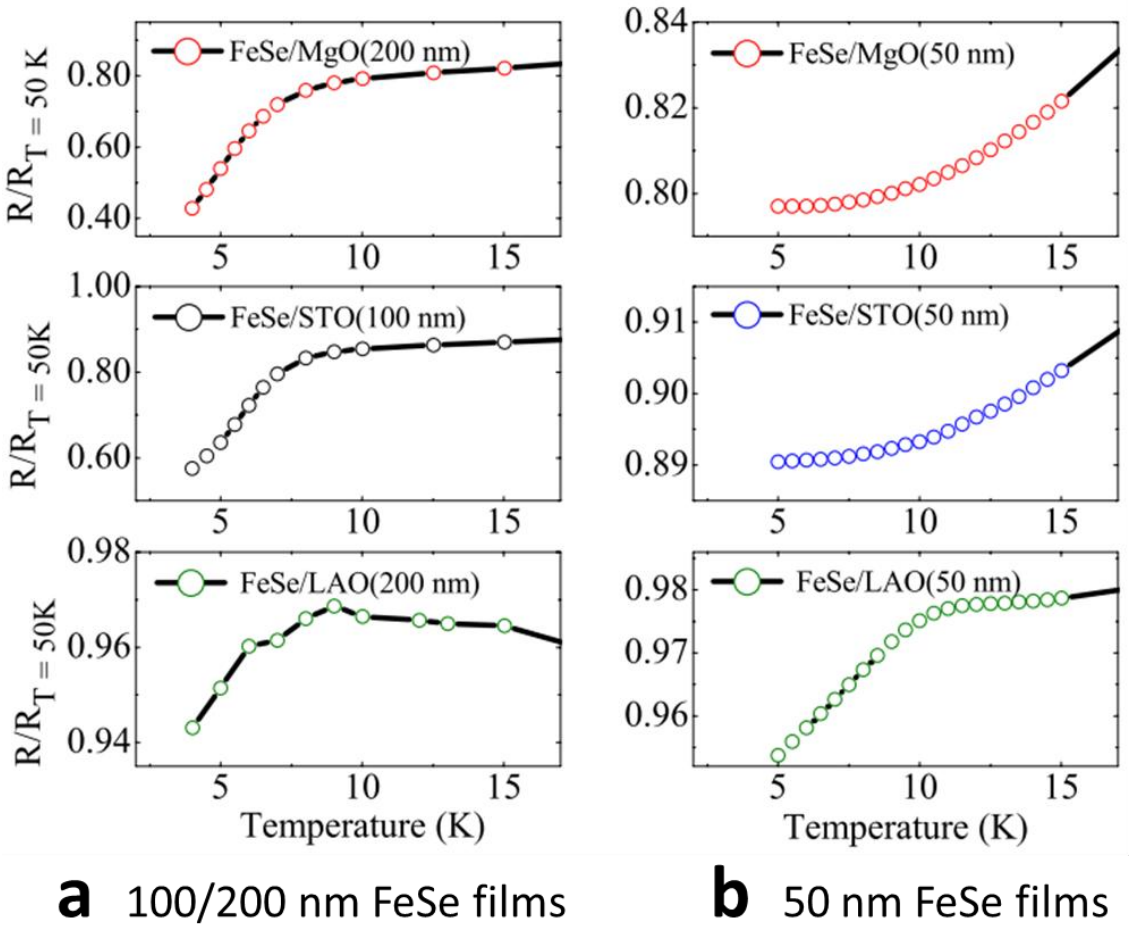

Figure 2-31. Normalized *R-T* curves for FeSe films grown on MgO, STO, and LAO substrates. (a) FeSe films with thickness of 100 or 200 nm. (b) FeSe films with thickness of 50 nm. After Ref.[125]

Bellingeri *et al.*[131] achieved a maximum T_c^{onset} of 21 K in $FeSe_{0.5}Te_{0.5}$ thin films with a significant 30 % increase with respect to a bulk sample. They clearly demonstrated that compressive strain in the *ab*-plane plays a vital role in enhancing the T_c value. The finding that T_c is enhanced after contraction in the *a*-axis length was very similar to the case of FeSe[125, 132] thin films. Furthermore, it was also found that T_c increases to a maximum value once the bond angle and bond length reach the ideal values (109.47 ° and 2.40 Å) to form a regular tetrahedron, as indicated in Fig. 2-32 (a). Another work from the same group further indicated that the in-plane lattice parameters of $FeSe_{0.5}Te_{0.5}$ films show a positive correlation with those of the substrates[133], although Imai *et al.*[134] reported that the T_c and *a*-axis length of $FeSe_{0.5}Te_{0.5}$ films are independent of the in-plane lattice parameters of the substrate because the best T_c was obtained from the films grown on LAO and MgO substrates with a large difference in lattice mismatch (-0.21 % and 9.82 % for LAO and MgO, respectively). Instead of ascribing the enhanced superconductivity to the in-plane length alone, the strong effect of the choice

of eight different substrates on the superconductivity of $FeSe_{0.5}Te_{0.5}$ films was correlated with the in-plane orientation and the *c*/*a* ratio of the $FeSe_{0.5}Te_{0.5}$ lattice (dependences shown in Fig. 2-32 (b)). The distinct discrepancy between the two conclusions might be related to the different growth temperatures. The substrate temperature in Imai *et al*. s' work[134] was set at 573 K (300 ℃), while Bellingeri *et al*.[133] grew the samples at a much higher temperature (550 ℃), which somewhat explained why their films were not strained coherently by the substrates.

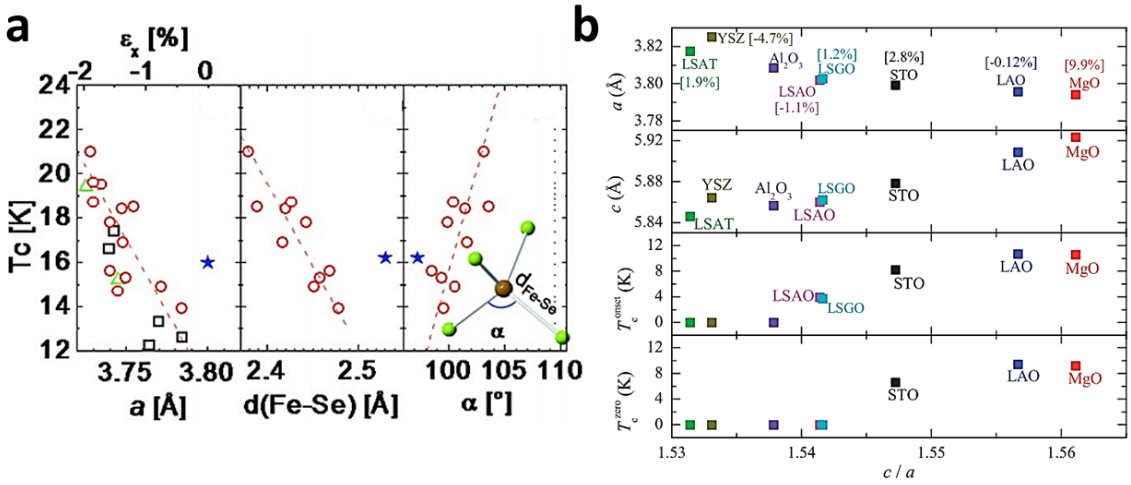

Figure 2-32. T_c as a function of the lattice parameter of $FeSe_{0.5}Te_{0.5}$ thin films. (a) The x-axes refer to the *a*-axis lattice parameter, the Fe-Se/Te bond length, and the Se/Te-Fe-Se/Te bond angle. The stars represent the bulk values. After Ref.[131]. (b) Dependence of T_c on the *c*/*a* ratio. After Ref.[134].

Thickness Effect

The variation of thickness can result in significant change inside epitaxial thin films. An example was given in the last section, that Fe-*Ch* films with low thicknesses experience a massive strain effect originated from the substrate[125]. A few more effects are also believed to be consequences of thickness variation. Nabeshima *et al*.[132] reported that excess-Fe defects appeared near the top surface of FeSe films when their thicknesses were lower than 100 nm. Tensile stress resulting from a Volmer-Weber growth mode (island mechanism), which is detrimental to the superconductivity of Fe-*Ch* films, tends to be induced when the thickness of a $FeSe_{0.5}Te_{0.5}$ thin film is lower than 30 nm[131] (as displayed in Fig. 2-33 (a)). The insulating behaviour at the beginning of growth is due to isolated islands, and they start to coalesce and show a superconducting transition at a thickness of around 30 nm. The superconducting-insulating transition (SIT) is an interesting phenomenon that often can be made to occur by tuning parameters such as the film thickness, magnetic field, charge density, or disorder in superconductors[135-136]. Schneider *et al*.[137-138] studied the SIT in their

sputtering-prepared FeSe films and attributed it to a disorder-driven scenario (as shown in Fig. 2-33 (b)). Our group[139] also reported similar SIT behaviour and ascribed the insulating resistivity behaviour of an 8 nm FeSe film to the severely unbalanced FeSe stoichiometry, which was caused by the CaSe interlayer that universally exists at the FeSe/CaF_2 interface. In addition, it is also well-accepted that severe thermal and quantum fluctuations usually suppress the superconductivity at low dimensionality[140]. Intriguingly, a novel top-down electrochemical-etching approach along with an electric double-layer transistor (EDLT) has been successfully utilized to realize the precise control of $FeSe_{1-x}Te_x$ film thickness[141-143]. As shown in Fig. 2-33 (c, d), the enhanced T_c obtained in etched-FeSe films was comparable to the one made by the *in-situ* MBE technique[144]. Hence, the fine tunability of film thickness should be another effective way to induce high-T_c superconductivity in Fe-*Ch* thin films.

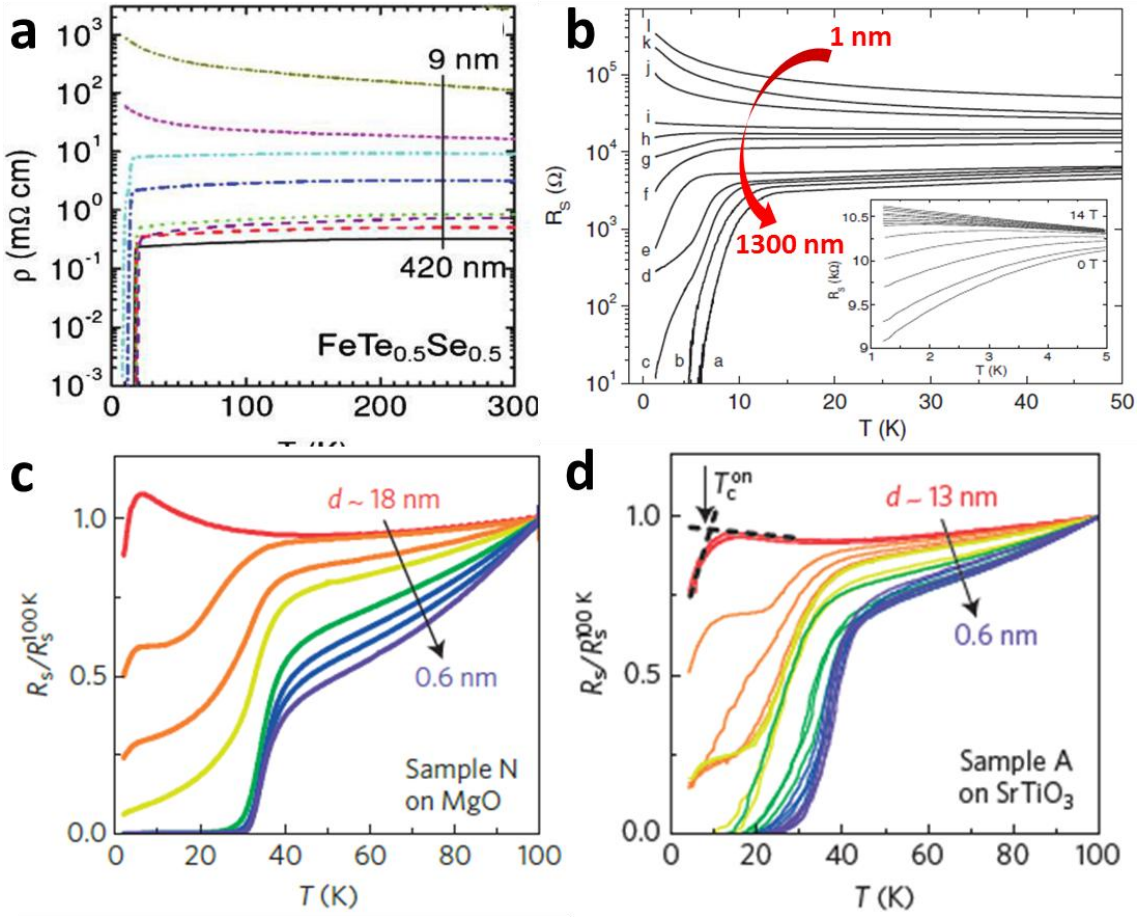

Figure 2-33. ρ-T curves for Fe-*Ch* thin films with different thicknesses. (a) $FeTe_{0.5}Se_{0.5}$ films[131]. (b) FeSe films prepared by sputtering. Inset: In-field performance of a 30 nm FeSe film[138]. FeSe films on c) MgO and d) STO with thickness controlled by electrochemical etching[141].

Temperature Dependence

The substrate temperature always has a strong influence on the growth of

epitaxial thin films, and 11-type Fe-*Ch* films are no exceptions. Wang *et al*.[39] studied the correlation between the growth temperature (LT-320 ℃, HT-500 ℃) and the orientation of FeSe thin films. Pure *c*-axis orientation was observed in the LT-FeSe film, while in HT-FeSe film the (101) orientation was dominant. Further resistivity investigations on LT-FeSe and HT-FeSe films with several thicknesses revealed completely different thickness-dependence behaviours. As displayed in Fig. 2-34 (a), strong T_c suppression in FeSe films with low thicknesses (< 140 nm) was observed in the case of LT-FeSe, while HT-FeSe did not exhibit much difference in T_c when the thickness from varied 140 nm to 1000 nm. By utilizing low-temperature XRD (shown in Fig. 2-34 (b)), a lattice distortion around 80 K was detected in all the samples except for the thinnest LT-FeSe film, which probably hints at the massive strain effect from the underlying substrate, particularly on a very thin film. This research emphasizes the importance of the substrate temperature and the consequent lattice distortion on the superconductivity of FeSe thin films. Similarly, an absence of T_c was also observed in the $Fe_{1+\delta}Se$ bulk samples which did not exhibit structural distortion at low temperature[145].

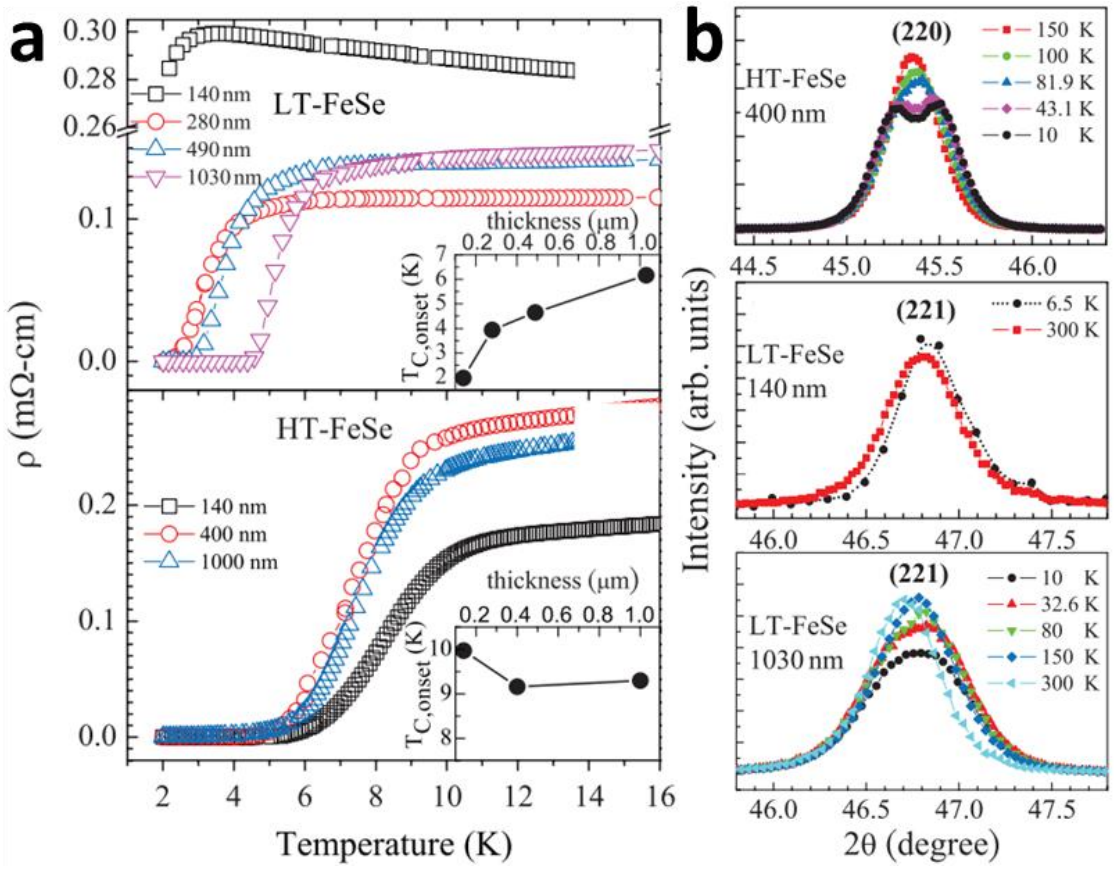

Figure 2-34. (a) *ρ*-*T* curves for LT- and HT-FeSe films with different thicknesses. (b) Low-temperature XRD results. Lattice distortion was only absent in 140 nm LT-FeSe. After Ref.[39].

Huang *et al*.[146] fabricated a batch of $FeSe_{0.5}Te_{0.5}$ films on MgO substrates with a wide range of substrate temperatures from 180 ℃ to 500 ℃. The temperature dependence of the normalized resistance is illustrated in Fig. 2-35 (a). Clearly, films grown at 300 ± 20 ℃ exhibited higher T_c values, while those grown at a temperature higher than 400 ℃ showed semiconductor behaviour. Systematic investigations indicate that the T_c of $FeSe_{0.5}Te_{0.5}$ epitaxial films is quite sensitive to the chalcogen height ($h_{Se/Te}$). As shown in Fig. 2-35 (b), the highest T_c of ~ 10.8 K appeared when $h_{Se/Te}$ was very close to 0. Furthermore, both the *a*-axis lattice parameter and $h_{Se/Te}$ decreased with increasing *c*-axis lattice parameter, with the bond angle remaining almost unchanged at 98 °. DFT calculations[147] for $FeSe_xTe_{1-x}$ indicated that the chalcogen height significantly affects the stability of magnetic phases, and thus gives rise to the fluctuation in iron-based superconductivity. Specifically, the overlap between the Fe 3d and the Te 5p orbitals will be maximized when the chalcogen height decreases (Te atom comes closer to the Fe plane). As a result, the superexchange interaction between the Fe magnetic moments becomes stronger. This theory is in accordance with the strong $h_{Se/Te}$-dependence of T_c found in $FeSe_{0.5}Te_{0.5}$ thin films[146].

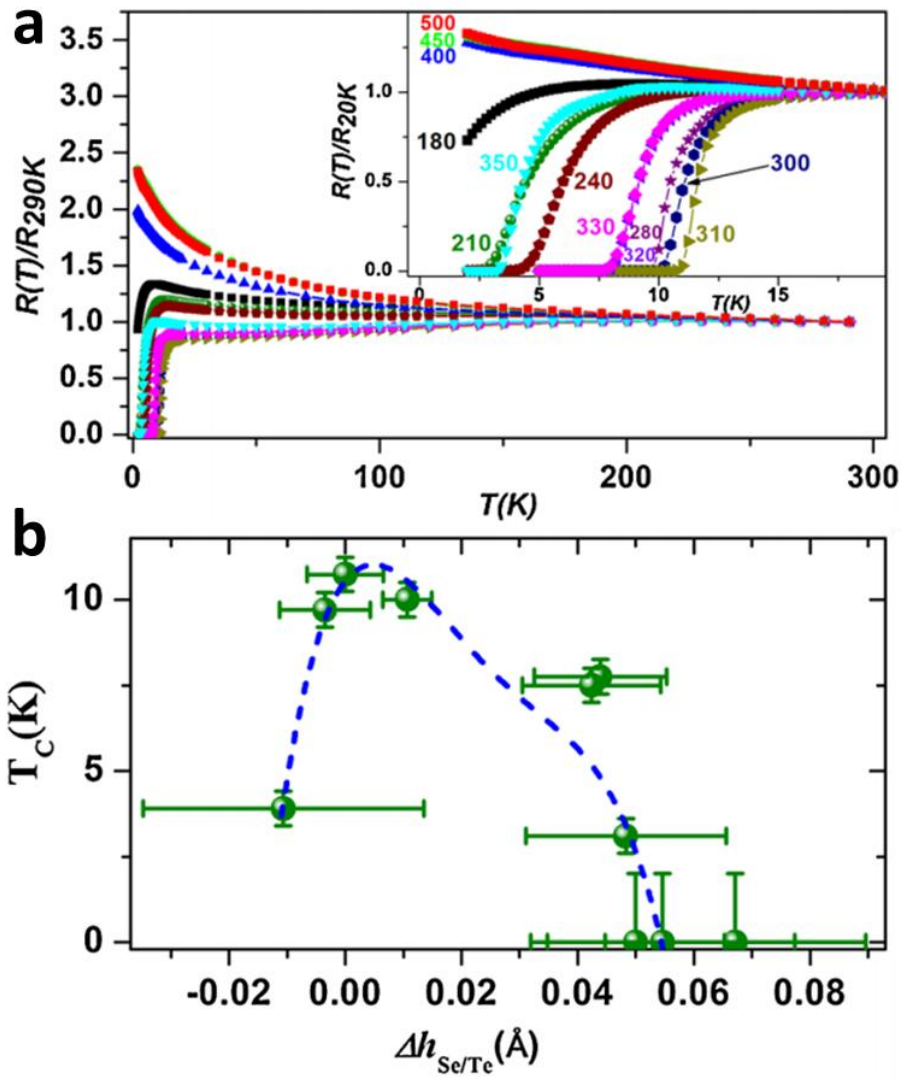

Figure 2-35. (a) Normalized *R*-*T* curves for $FeSe_{0.5}Te_{0.5}$ films with different substrate temperatures. Inset: Enlarged temperature range near T_c. (b) T_c as a function of relative chalcogen height. After Ref.[146].

Substrate Selection for Films: Film-substrate Interface

The choice of substrate is crucial to the growth of high-quality $FeSe_{1-x}Te_x$ thin films. Excluding the special functions of some substrates (e.g. carrier doping, element substitution, artificial strain, etc.), three factors should usually be taken into account: lattice mismatch, thermal expansion, and chemical stability[148]. The relevant specifications of commonly used substrates for growing $FeSe_{1-x}Te_x$ thin films are listed in Table 2-3. First of all, a low lattice mismatch between the film and the underlying substrate is preferred in most cases to ensure an epitaxial film with minimized structural defects or unwanted grain boundaries, which are prone to suppress superconductivity. Generally, the lattice mismatch (*M*) can be defined as:

$$M = 100 \times \frac{a_s - a_f}{a_s}$$

where a_s and a_f refer to the in-plane lattice parameters of the substrate and the film (although sometimes a_s is the lattice constant divided by $\sqrt{2}$, such as for CaF_2). Thus, a positive *M* tends to cause tensile strain, while a negative *M* is expected to bring about compressive strain. According to the Poisson effect, any in-plane tensile/compressive strain in a bulk material would be compensated by contraction/expansion of the out-of-plane lattice. Therefore, the in-plane strain originating from the substrate is partially reflected by the variation in the out-of-plane lattice parameter of the film, although this only works for thin films before the strain is relaxed due to higher thickness[149]. Yeh *et al*.[126] studied the biaxial-stress effect on the superconductivity of FeSe thin films. They observed pure *c*-axis orientation in all FeSe films grown on MgO, LAO, STO, Si, and α-SiO_x substrates and demonstrated that the lattice mismatch did not significantly affect the FeSe superconducting phase. Surprisingly, Imai *et al*.[134] found that a $FeSe_{0.5}Te_{0.5}$ film which was deposited on a hexagonal Al_2O_3 substrate showed strong orientation along the *c*-axis, regardless of the non-structural match between tetragonal Fe-*Ch* and hexagonal Al_2O_3. Hence, a favored 2D growth mode in PLD-prepared $FeSe_{1-x}Te_x$ film was proposed. Speller *et al*.[150] investigated the epitaxial growth of $Fe_ySe_{1-x}Te_x$ thin films by the radio-frequency sputtering method and reported that the in-plane lattice mismatch between the substrate and $Fe_ySe_{1-x}Te_x$ phase played little role in developing the texture. The difference in thermal expansion also needs to be considered. This is because of the huge temperature variation between the film growth conditions (typically hundreds of ℃) and the film measurement or operation conditions (tens of Kelvins in the case of Fe-*Ch* superconducting films), which sometimes causes cracks or other damage to a thin film sample if the coefficient of thermal expansion of the film material is much different from that of the substrate.

Table 2-3. In-plane lattice constant and thermal expansion coefficient of common substrates for $FeSe_{1-x}Te_x$ thin film growth. The substrates are listed in the order of the *in-plane* lattice constant. Partly after Ref.[151]. YSZ: yttrium stabilized zirconia.

Substrate Material	**In-plane lattice constant (Å)**	**Thermal expansion coefficient at 300 K (10^{-6}/K)**	**Oxide substrate or not**
$YAlO_3$	3.716	11	Yes

$LaSrAlO_4$ (LSAO)	3.754	7.55	Yes
LAO	3.793	5.77	Yes
LSAT	3.869	8.22	Yes
STO	3.905	10.3	Yes
MgO	4.211	10.5	Yes
Al_2O_3	4.748	5.6	Yes
YSZ	5.141	11	Yes
CaF_2	5.462	18.9	No

Last but not least, the chemical reactivity of the film and substrate materials is of great importance. For instance, any unexpected impurity resulting from reaction with the substrate is likely to degrade the superconductivity of the FeSe thin film owing to its very narrow growth window[123], although sometimes substrates are specially designed to realize an intentional chemical reaction, such as by F-doping into Sm-1111 thin films[61] and TiO_2-terminated STO substrate for effective electron-doping into FeSe unit-layers[152]. Thus, integrated consideration should be carried out to determine the most suitable substrate for the growth of $FeSe_{1-x}Te_x$ thin films.

Detailed investigations of the chemical reactions at the film/substrate interface have helped to clarify the mystery as to why there is no correlation between the in-plane lattice constants of $FeSe_{1-x}Te_x$ films and those of the substrates. Maeda's group[134, 153-154] performed a series of transmission electron microscopy (TEM) observations on $FeSe_{0.5}Te_{0.5}$/substrate interfacial regions from a cross-sectional viewpoint. The authors found that the $FeSe_{0.5}Te_{0.5}$ films grown on CaF_2, LAO, and MgO substrates, which showed the best superconducting performance, were exhibiting smooth interfaces between the films and the substrates. In contrast, the $FeSe_{0.5}Te_{0.5}$ films grown on yttrium-stabilized zirconia (YSZ) and LSAO showed non-superconducting behaviour and had an amorphous-like appearance at the interface. Comparisons of ρ-T curves and TEM images are shown in Fig. 2-36 (a) and (b), respectively. Further studies on the crystal structure[154] revealed that the amorphous layers were responsible for the lack of correlation between the in-plane lattice parameters of the substrates and the films, which

is in sharp contrast to the immediately formed tetragonal crystals of FeSe films grown on CaF_2, LAO, and MgO substrates. Thus, the presence of the amorphous-like layers on certain kinds of substrates would result in degradation of the crystal structure as well as the superconductivity of $FeSe_{0.5}Te_{0.5}$ thin films. It should be noted that both oxide and non-oxide substrates were used for film growth in this work to clarify the effect of oxygen penetration into the films. As a result, suppression of superconductivity was found in all the films that were experiencing oxygen penetration.

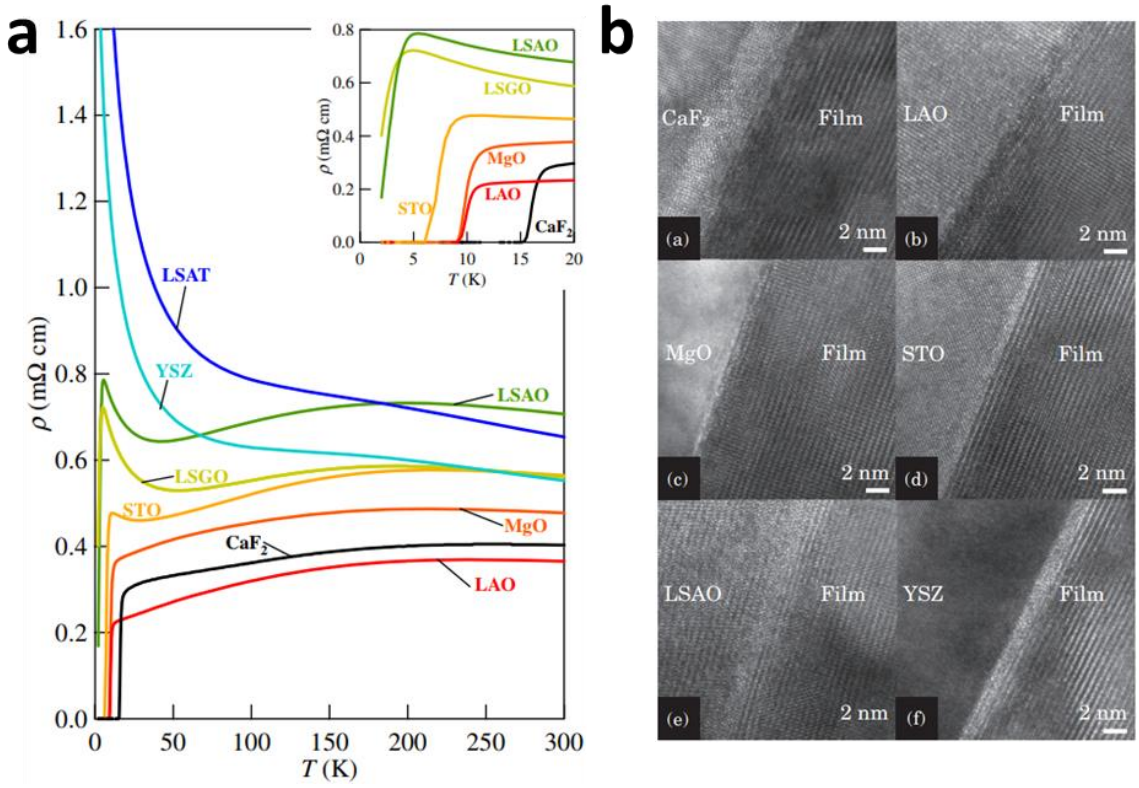

Figure 2-36. (a) ρ-T curves for the $FeSe_{0.5}Te_{0.5}$ films grown on different substrates. Inset: An enlarged view near T_c. (b) Cross-sectional TEM images of $FeSe_{0.5}Te_{0.5}$ films grown on different substrates. After Ref.[153].

In order to avoid the negative influence of oxygen penetration effect on the superconducting properties of Fe-*Ch* films, the selection of a non-oxide substrate is the most straightforward choice. Hanawa *et al.*[154] conducted the first attempt to fabricate 11-type Fe-*Ch* films on CaF_2 substrates. The obtained $FeSe_{0.5}Te_{0.5}$ films showed higher T_c (over 15 K) and a smaller *a*-axis lattice parameter than ones grown on oxide substrates. Considering that the lattice constant of cubic CaF_2 substrate, $a_{CaF2} \approx 3.863$ Å, is larger than a_{film}, the decrease in the in-plane lattice parameter of the film did not result from simple lattice matching. This was further confirmed by systematic TEM and corresponding diffraction characterizations on $FeSe_{1-x}Te_x/CaF_2$ samples over the entire

range of x[155]. (TEM-diffraction results are shown in Fig. 2-37 (a).) The authors demonstrated universal shrinkage of a-axis lattice constants in $FeSe_{1-x}Te_x$, except for the case of FeTe, which had an almost identical a-axis length to that of bulk FeTe, as plotted in Fig. 2-37 (b). A possible scenario was proposed to explain this phenomenon: the first few $FeSe_{1-x}Te_x$ layers initially grown on CaF_2 have a shorter a-axis lattice constant due to the reaction-induced Se-deficiency, and the following layers grow on the initial layers in an epitaxial manner, so that the shrinkage of the a-axis length is inherited. To further understand the reaction at the Fe(Se,Te)/CaF_2 interface, Ichinose *et al.*[156] studied the crystal structure and superconducting properties of Fe(Se,Te) films grown on bare, CaF_2-buffered, and FeSe-buffered CaF_2 substrates. Potential interdiffusion of F and Se elements was revealed by energy dispersive X-ray spectroscopy (EDS) profiles, and the consequent chemical substitution was considered to primarily determine the lattice constants of Fe(Se,Te) films, rather than the lattice mismatches.

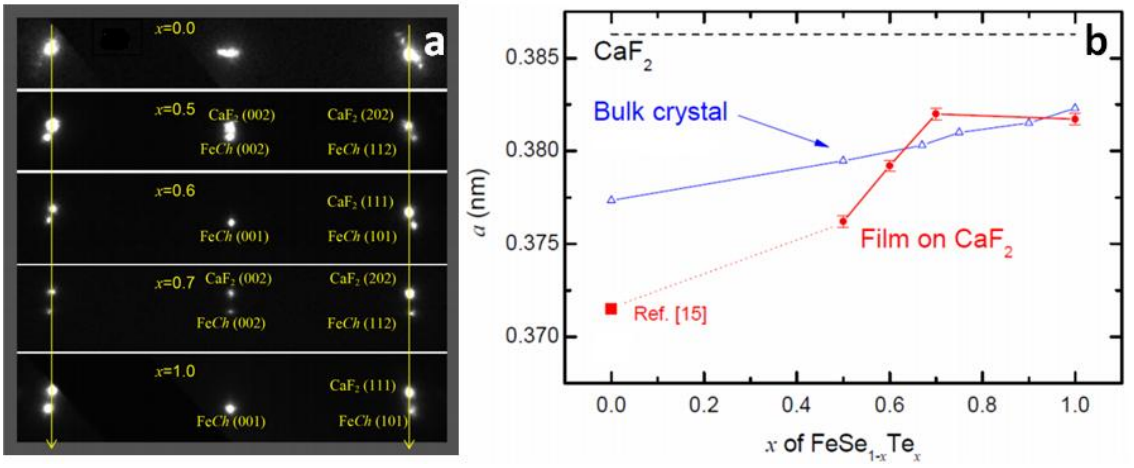

Figure 2-37. (a) The diffraction patterns of $FeSe_{1-x}Te_x$ grown on CaF_2 substrates with different x. (b) a-axis length as a function of x in $FeSe_{1-x}Te_x$ films grown on CaF_2 substrates. After Ref.[155].

The introduction of an appropriate buffer layer is often helpful to simplify growth or improve the ultimate performance of thin films. Iida *et al.*[157] introduced an Fe buffer layer into the $FeSe_{0.5}Te_{0.5}$/MgO structure. They obtained an enhanced T_c^{onset} of 17.7 K in their Fe/$FeSe_{1-x}Te_x$ bilayer with strong intrinsic pinning, which is similar to the case of Fe-buffered Ba-122 thin films[76-78]. A cubic CeO_2 buffer layer with the a-axis lattice constant of $a/\sqrt{2} \approx 3.83$ Å is widely used in the large-scale fabrication of YBCO coated conductors[158-159]. Si *et al.*[160] successfully fabricated high-quality $FeSe_{1-x}Te_x$ (abbreviated as FST in Fig. 2-38 (a)) epitaxial films on CeO_2-buffered YSZ substrate and a standard rolling assisted bi-axially textured substrate (RABiTS) tape with a CeO_2

layer on the top. As shown in Fig. 2-38 (a), both structures exhibited high T_c^{onset}/T_c^{zero}, ~ 20 K/18 K, which is higher than that of FST bulk, FST film on bare YBCO-buffer layers, and FST film on STO substrate. High field characterization (up to 30 T) indicated a nearly isotropic J_c of about 10^5 A/cm^2 at 4.2 K, 30 T. Pinning force analysis (Fig. 2-38 (b)) revealed the superior high-field pinning performance of FST/RABiTS which was only lower than that of YBCO HTSs. The achievement of fabricating $FeSe_{1-x}Te_x$ films on commercial HTS buffer layers with competitive superconducting performances are solid evidence for the promising high-field applications of Fe-*Ch* coated conductors. High-performance $FeSe_{0.5}Te_{0.5}$ films grown on $LaMnO_3$-buffered ion-beam assisted deposition (IBAD) templates were also reported by Xu *et al.*[161] Surprisingly, the highly textured template was found to be no longer essential for fabricating $FeSe_{0.5}Te_{0.5}$ coated conductors, which gives them a great advantage over YBCO coated conductors.

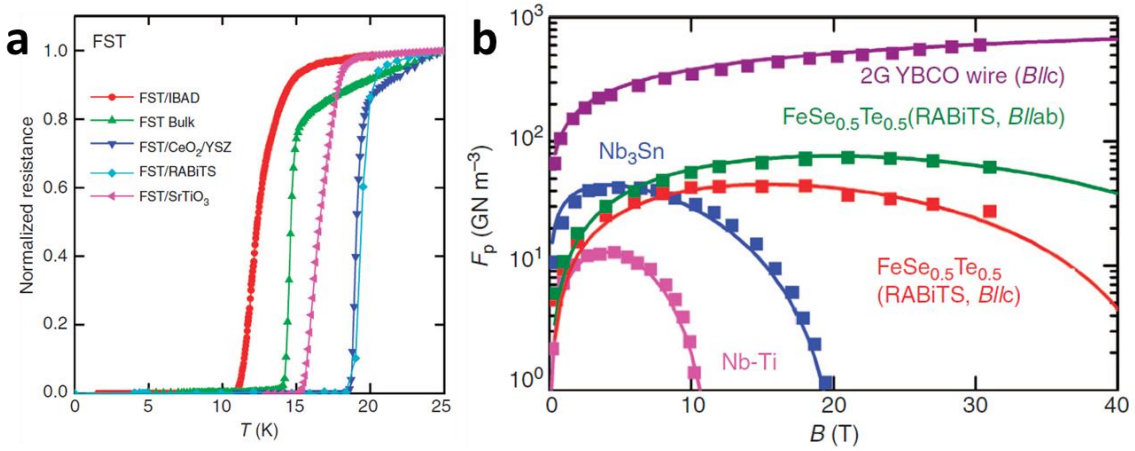

Figure 2-38. Superconducting performance of $FeSe_{1-x}Te_x$ (FST) films grown on CeO_2-buffered substrates. (a) Normalized resistance as a function of temperature. The results for FST bulks and other FST films are also shown for comparison. (b) Pinning force (F_P) of FST/RABiTS films and other counterparts at 4.2 K. After Ref.[160].

Homo-epitaxy is a very effective approach for preparing thin films where it is difficult to realize heteroepitaxy. A good example is can be found in the well-developed IBAD route for fabricating YBCO coated conductors, where a homo-epitaxial MgO buffer layer is deposited on an IBAD-MgO layer[162-163]. Molatta *et al.*[164] reported the homo-epitaxial growth of $FeSe_{1-x}Te_x$ thin films. As illustrated in Fig. 2-39 (a), the reproducibility of homo-epitaxial $FeSe_{1-x}Te_x$ film is much better than that of one without a $FeSe_{1-x}Te_x$ seed layer, which is reflected by the large spread of the resistance curves of the samples grown without a seed layer. Although T_c was not detected in the homo-

epitaxial $FeSe_{1-x}Te_x$ films grown at high temperatures, they do show better texture and highly reproducible T_c values over 17 K as (shown in Fig. 2-39 (b)), which hints at the possibility of implementing this seed-layer technique in the growth process of a variety of iron-based superconducting thin films.

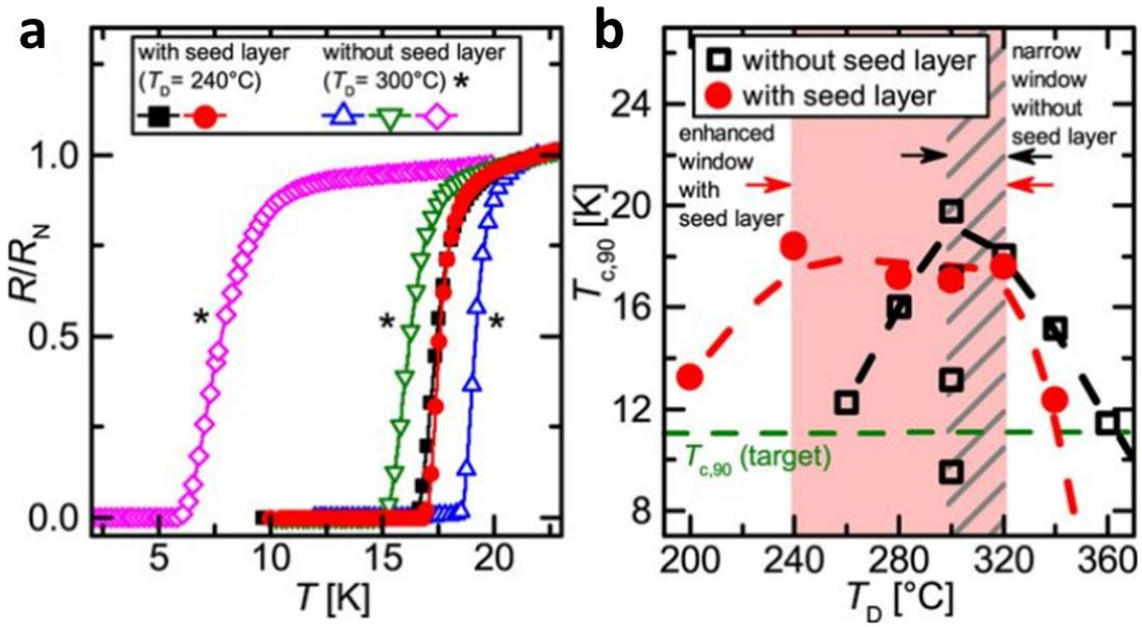

Figure 2-39. (a) Normalized resistance as a function of temperature for the $FeSe_{1-x}Te_x$ films with (240 ℃) or without (300 ℃) a $FeSe_{1-x}Te_x$ seed layer. (b) Comparison of the growth windows of $FeSe_{1-x}Te_x$ films with/without a $FeSe_{1-x}Te_x$ seed layer. After. Ref.[164].

Studies in J_c enhancement

Eisterer *et al.*[165] performed J_c measurements on $FeSe_{0.5}Te_{0.5}$ films grown on LAO substrates. In the films with T_c over 19 K, the magnetic J_c value exceeded 0.1 MA/cm^2 at 4.5 K, 5 T, which was much higher than the J_c values of a stressed FeTe thin film[166], S-doped FeTe thin film[121], and Co-doped Ba-122 film[79]. All samples were found to be intrinsically correlated, with the pinning mechanism parallel to the *ab*-plane. A similar angular J_c dependence was also reported by Iida *et al.*[157, 167] in $FeSe_{1-x}Te_x$ thin films grown on Fe-buffered MgO substrates. Transport measurements and TEM investigations were carefully performed in their work. The intrinsic pinning mechanism was considered to be the origin of the in-field J_c behaviour[167]. In addition, the J_c value can be further improved by the structural defects introduced by specific substrates. Braccini *et al.*[168] compared the J_c performance of $FeSe_{0.5}Te_{0.5}$ thin films grown on CaF_2 and STO substrates. Different types of vortex pinning defects and the corresponding J_c dependence (Fig. 2-40 (a)) were clarified. As shown in Fig. 2-40 (b), the small-scale isotropic point defects (5 - 20 nm) were observed in the films grown on CaF_2, while

columnar nanorods perpendicular to the *ab*-plane existed in the films grown on STO. Apparently, the nanoparticles introduced by the CaF_2 substrates provided effective vortex pinning over a wide range of angles, which resulted in a nearly isotropic high-J_c (over 1 MA/cm^2 at 4 K, self-field) scenario in the system of $FeSe_{1-x}Te_x$ epitaxial thin films. Hence, the proper selection of a growth substrate should be seriously considered as a critical factor that will strongly determine the J_c properties.

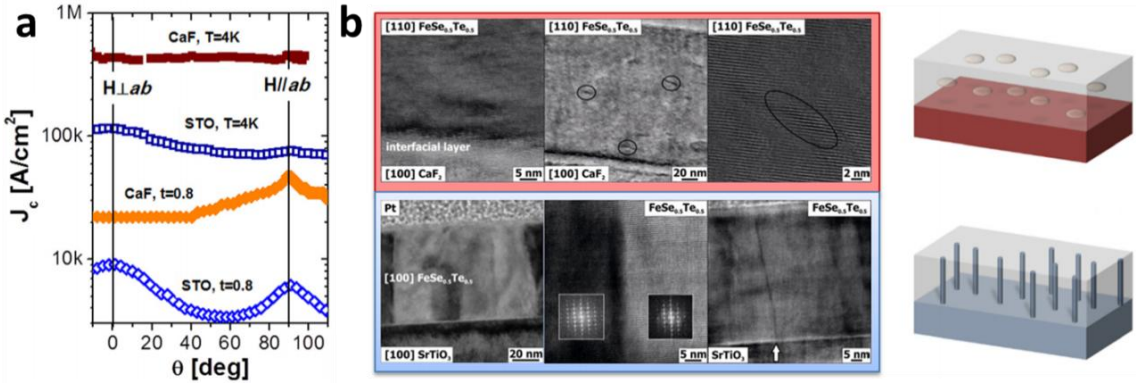

Figure 2-40. The angle dependence of J_c, HRTEM images, and sketches of the defects in $FeSe_{0.5}Te_{0.5}$ thin films grown on CaF_2 and STO, respectively. (a) $J_c(\theta)$ performance at 4 K, 9 T. (b) Cross-sectional HRTEM images and corresponding sketches that show different types of defects in $FeSe_{0.5}Te_{0.5}$ films. Upper pair: thin film grown on CaF_2 with isotropic point defects. Lower pair: thin film grown on STO with nanorod-shaped defects. After Ref.[168].

A more direct way to introduce artificial pinning centres is through the proton irradiation technique. This has been widely utilized in a variety of superconducting systems, including MgB_2[169], YBCO coated conductors[170], and Ba-122 single crystals[171-173]. Ozaki *et al.*[174] intentionally introduced cascade defects into $FeSe_{0.5}Te_{0.5}$ thin films by using low-energy (190 keV) proton irradiation. Fig. 2-41 (a) shows a universal increase in T_c of ~ 0.5 K, which is striking, because a positive effect on T_c by irradiation was never reported before this work for the family of iron-based superconductors[171, 173]. A strong enhancement of the J_c-H performance was also obtained the after irradiation process, and the results are presented in Fig. 2-41 (b). The irradiated samples exhibited a self-field J_c of 1.4 MA/cm^2 at 4.2 K, which was a huge increase by over 50 % compared with that of a pristine sample (0.9 MA/cm^2). A promising cable application for irradiated $FeSe_{1-x}Te_x$ films is indicated based on the outstanding improvement in J_c properties over the entire range of magnetic field. A record high pinning force of about 120 GN/m^3 (H//ab) at 4.2 K, 27 T was obtained in the irradiated sample (Fig. 2-41 (c)). According to the systematic strain analysis shown in Fig. 2-41 (d, e), nanoscale local-strains were clearly distinguished around the cascade defects that were produced by

proton irradiation. The resultant consequence of strong vortex pinning was considered to be the main reason for the significant improvement in the T_c and J_c properties of the irradiated $FeSe_{1-x}Te_x$ thin film samples. Recently, the same group reported the discovery of an enhanced J_c in $FeSe_{0.5}Te_{0.5}$ films by introducing desirable isotropic pinning defects by using Au-ion irradiation[175].

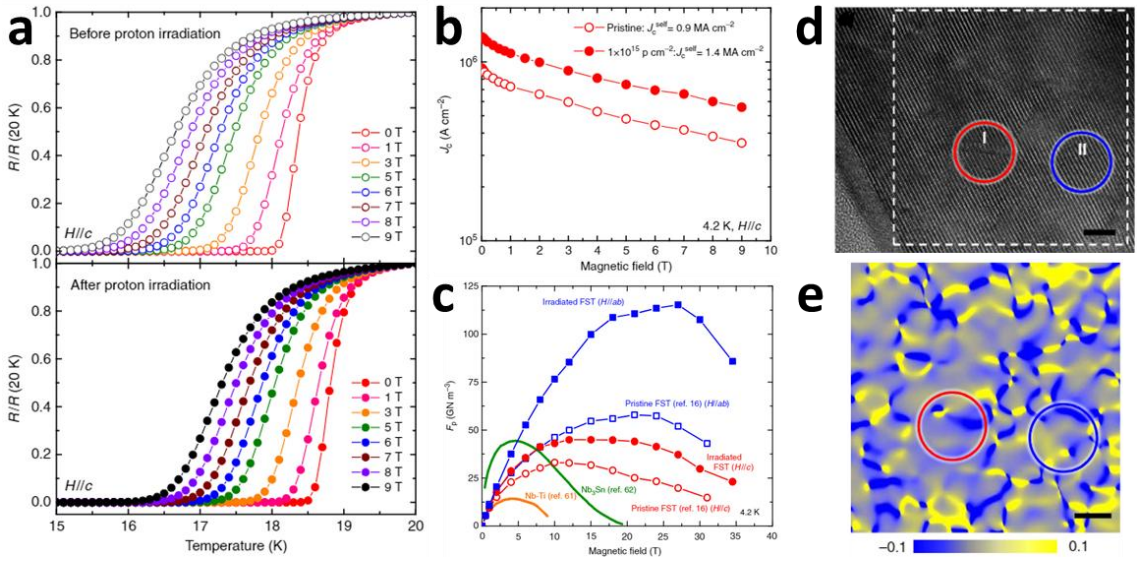

Figure 2-41. Enhanced superconducting performance of $FeSe_{0.5}Te_{0.5}$ thin films before and after proton irradiation and the corresponding strain analysis. (a) Normalized resistance as a function of temperature. (b) J_c as a function of field (parallel to the *c*-axis) at 4.2 K. (c) Comparison of pinning force in different systems. (d) A HRTEM image showing local lattice distortions induced by 190 keV proton irradiation. (e) The in-plane strain mapping for the same area in (d). After Ref.[174].

Superconductivity Induced in FeTe Films.

As the parent phase of "11-type" iron-based superconductors, the realization of superconductivity in the FeTe system used to be considered easily accessible. Subedi *et al.*[16] performed theoretical DFT calculations on iron sulphide (FeS), FeSe, and FeTe compounds and predicted stronger pairing and a higher T_c in FeTe than in FeSe if both of the systems were driven by the same spin-fluctuation pairing mechanism. Due to the unique magnetic properties revealed by Zhang *et al.*[176], FeTe was also thought to exhibit high-T_c superconductivity if the strong SDW is suppressed, although the pristine FeTe bulks never exhibited superconductivity under any circumstances[119, 177-178], even though the other compounds in the 11-type Fe-*Ch* family show exciting superconducting properties in numerous ways. Monni *et al.*[179] carried out DFT investigations on the magnetic ordering behaviour of FeTe compound under pressure and proposed a possible explanation for the absence of superconductivity in FeTe. They found that the ferromagnetic FeTe phase under the pressure range between 2.1 GPa and 17 GPa was in

the ground state, which discriminated FeTe from the other superconducting Fe-*Ch* compounds.

Follow-up research completely changed our belief that FeTe compound was always non-superconducting. Superconductivity in FeTe was finally achieved in the case of FeTe thin films[121, 180-181]. As mentioned above, the first observation of a superconducting transition around 13 K in FeTe thin films was published by Han *et al*.[121] By carrying out careful transport, magnetic, and structural investigations on more than one hundred FeTe specimens, they reached an intriguing conclusion, that superconductivity in FeTe emerged with the softening of the structural phase and first-order magnetic transition. Fig. 2-42 (a, b) shows clear superconducting transitions at about 13.0 K/9 K obtained from DC/AC measurements. Also, an increase in the Fe-Te-Fe bond angles was observed at the same time. The T_c^0 dependence of the bond angle is plotted in Fig. 2-42 (c). Dramatic increases (~ 0.4 ° for Angle 1, ~ 0.75 ° for Angle 2) were found in the Fe-Te-Fe angles of superconducting FeTe film compared to those of $Fe_{1+\delta}Te$ bulk. The authors eventually speculated that tensile strain acted as the essential prerequisite for the superconductivity in FeTe thin films. A work employing thermal expansion measurements also suggested that the lattice of superconducting FeTe is greatly affected by the strain effect[182].

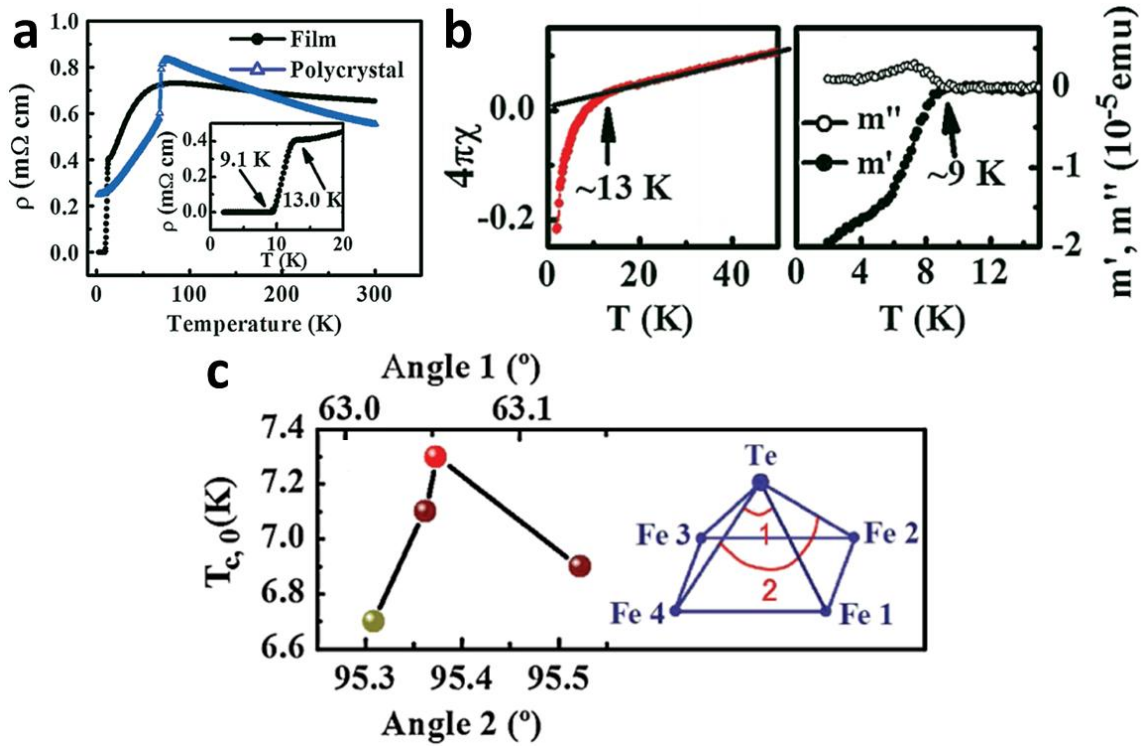

Figure 2-42. (a) *ρ-T* curves of FeTe film with a data on the bulk for reference. Inset: the superconducting transition in an enlarged range of temperature. (b) DC magnetization and AC susceptibility measurements.

(c) T_c^0 as a function of Fe-Te-Fe bond angles. Inset: Definition of the two types of Fe-Te-Fe angles. After Ref.[121].

Soon after the discovery of tensile-induced superconductivity in FeTe was released, Si *et al.*[181] reported a T_c^{onset}/T_c^{zero} of 12 K/8 K in a $Fe_{1.08}Te$ film grown on STO substrate in oxygen-atmosphere (ρ-T curves given in Fig. 2-43 (a)). On comparing the FeTe films deposited in high vacuum (below 1×10^{-6} Torr) and oxygen pressure (below 1×10^{-4} Torr), better superconducting performance was found to exist in the latter situation, which indicated the critical role of oxygen incorporation in inducing the superconductivity of FeTe thin films. The H_{c2} was also predicted to be remarkably high (~ 200 T from T_c^{onset}) due to the moderate degradation of T_c in magnetic field, as shown in Fig. 2-43 (b). Similarly, Nie *et al.*[183] demonstrated that the oxygen-induced superconductivity in FeTe thin films was reversible by an alternative post-annealing order of O_2 gas, vacuum, and O_2 gas again. The normalized resistance as a function of temperature for the FeTe films after different post-annealing treatments is displayed in Fig. 2-43 (c). The superconducting transition in the O_2-annealed FeTe film was first disappeared after annealing in a vacuum chamber, and then was restored (transition was even sharper) with a second oxygen annealing process. Thus, the oxygen-incorporation was strongly evidenced to be the fundamental reason for the superconductivity of FeTe films. Further X-ray absorption characterization (Fig. 2-43 (d)) revealed a nominal 3+ valence of Fe ions in the superconducting state rather than 2+ in the common non-superconducting state. As a result, the superconducting mechanism in oxygen-incorporated FeTe films was supposed to be quite different from that of $FeSe_{1-x}Te_x$, which does not involve any change in the valence of Fe ions. Moreover, Nie *et al.*[183] also commented that the superconducting FeTe films found in Han *et al.*[121]s' work may also be assigned to the scenario of oxygen-incorporation, not only due to the unsatisfactory background vacuum state, but also because of the large amount of (unanalysed) oxygen in their samples (mostly from the oxide substrate). Hence, there is reason to believe that the superconducting FeTe films of Han *et al*. probably absorbed some oxygen as well. Tsukada *et al.*[180] performed detailed Hall effect measurements on both superconducting (but the superconducting transition is not complete) and non-superconducting FeTe thin films. After estimation of the mobility of electron and hole carriers, they proposed the necessity of both itinerant electron- and hole- carriers for the appearance of superconductivity in FeTe thin films.

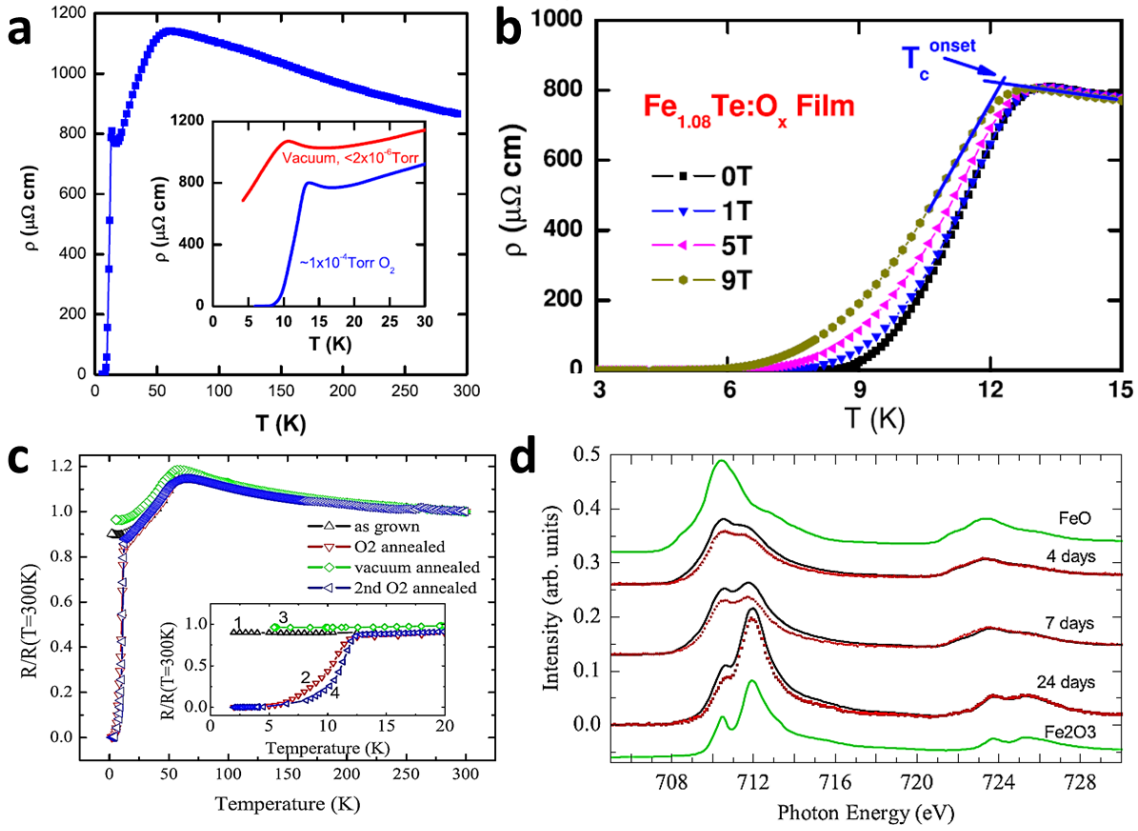

Figure 2-43. Oxygen-incorporation induced superconductivity in FeTe thin films. (a) Self-field ρ-T curves for $Fe_{1.08}Te$ thin films grown on STO in oxygen/vacuum atmosphere. (b) Field-degradation of T_c^{onset} under different magnetic fields. (c) The evolution of resistance behaviour for FeTe thin films after different annealing treatments. (d) X-ray absorption spectroscopy results of FeTe films with the results for Fe_2O_3 and FeO acting as references. (a) & (b) after Ref.[181], (c) & (d) after Ref.[183].

On reviewing the reported superconductivity in the FeTe system, there are several critical issues that need to be mentioned. First of all, superconducting properties were only observed in FeTe samples in the form of thin films, while bulk FeTe crystals never show superconductivity, even after high pressurization treatment or post-annealing in an oxygen atmosphere. This is an interesting phenomenon that suggests thin-film growth as the key to realizing superconductivity in FeTe. In the second place, the superconducting transition in FeTe thin film seems to be derived from multiple factors, including the tensile-strain effect, oxygen-incorporation, variation in ion-valence, the presence of both types of carriers, etc. Moreover, it should also be noted that the superconducting FeTe films resemble $FeSe_{1-x}Te_x$ films in their physical properties. In addition to the significant strain-effect on the the T_c performance[121, 182], the superconductivity is also quite sensitive to the concentration and mobility of charge carriers[180, 184]. These issues suggest that the properties of the superconducting FeTe system are complex and unique, and hint that $FeSe_{1-x}Te_x$ system might be a prospective

breakthrough-point for clarifying the mechanism of the superconductivity in the FeTe system.

2.3.3.3 MonoLayer and Multilayer 11-type Thin Films

In 2012, superconductivity witha strikingly high T_c (possibly over 77 K) was reported by Wang *et al.*[43] in monolayer (also called 1-UC) FeSe films grown by MBE on TiO_2-terminated STO substrates. The T_c value was reflected by a U-shaped superconducting gap which remains open when the superconducting Cooper pairs are correlated. According to BCS theory, the size of the superconducting energy gap Δ reveals the minimum energy for the formation of a Cooper pair, and it shows dependence on the superconducting critical temperature T_c as:

$$\Delta\,(\mathrm{T}=0) = 1.764 k_B T_c$$

where k_B refers to the Boltzmann constant[185]. At 4.2 K, the magnitude of the U-shaped gap of monolayer FeSe was measured to be 40.2 meV, which means that the superconducting gap was half of this value, 20.1 meV. As a result, a corresponding T_c over the boiling point of LN_2 (77 K) can be assumed based on a bulk FeSe scenario. The basic structure in this work is displayed in Fig. 2-44 (a). The growth substrate was Nb-doped STO (001), with a specially designed TiO_2 termination. Fig. 2-44 (b) shows the variation of the *dI*/*dV* spectra of 1-UC FeSe at different temperatures ranging from 4.2 K to 42.9 K. As the size of the superconducting gap was almost unchanged up to 23.6 K, the robust superconductivity in this sample was confirmed. It was interesting that superconducting gaps were absent in the FeSe films with more than one atomic layer, as shown in Fig. 2-44 (c). The tunneling spectrum acquired from a 2-UC FeSe film did not show any sign of superconductivity. This behaviour indicates that the FeSe/STO interface effect plays a vital role in the high-T_c phenomenon in monolayer FeSe films. To further confirm the zero resistance property in this work, measurements of the temperature dependence of the resistance were carried out. Considering that such a monolayer FeSe sample is extremely delicate under the conditions of electrical transport measurements, a 5-UC FeSe film was fabricated on bare STO substrate and finally covered by a 20 nm amorphous silicon film as a protective layer. Non-superconducting FeTe is also widely used for the same purpose[186]. Detailed self-field and in-field transport results are illustrated in Fig. 2-44 (d). A clear superconducting transition occurred near 53 K, and typical degradation of T_c under magnetic field was also observed. Since the non-superconductivity of the 2-UC and thicker FeSe films was

attested, the high-T_c superconductivity shown in transport measurement must have originated from the first FeSe layer adjacent to the STO substrate. Generally, the T_c obtained by *ex-situ* transport or magnetic measurements is lower than indicated by the scanning tunneling microscopy (STM) results, which is due to several reasons, including possible magnetic interference from the FeTe cap[187], dissipation of electron-doping into layers other than FeSe[188], the poor in-plane connection of the monolayer FeSe film, etc.

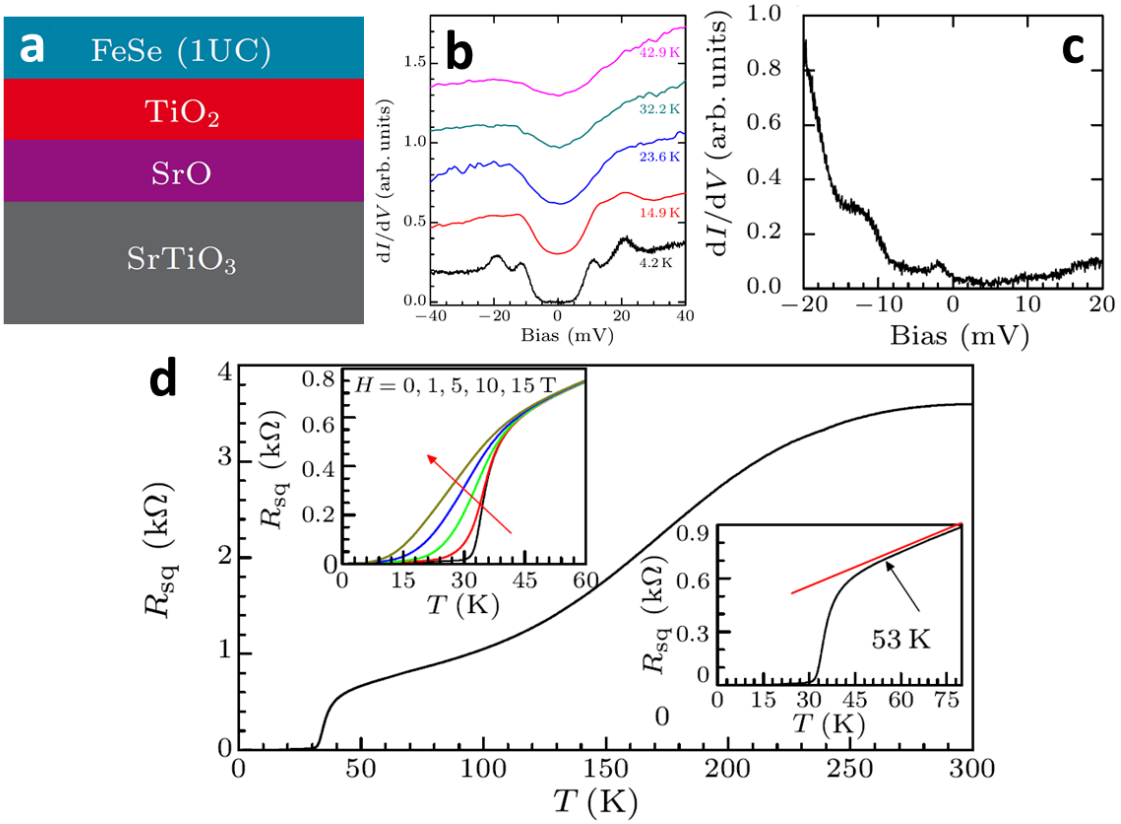

Figure 2-44. Characterization of high-T_c superconductivity in monolayer FeSe film grown on TiO_2-terminated STO substrate. (a) Schematic structure from the cross-sectional view. (b) *dI/dV* tunneling spectra for the surface of a 1-UC FeSe film at different temperatures. (c) *dI/dV* tunneling spectrum of a 2-UC FeSe film at 4.2 K. (d) Square resistivity as a function of temperature for a 5-UC FeSe film. The upper left inset shows the temperature dependence for different magnetic fields, and the lower right is an enlargement of the main panel. After Ref.[43].

The superconducting transition of FeSe thin films can also be characterized by employing the ARPES technique[189-194]. Similar to STM studies, the energy distribution curve (EDC) derived from the ARPES photoemission spectra also contains comprehensive information about the temperature dependence of the superconducting gap. A gap-opening T_c of ~ 65 K in 1-UC FeSe/STO was simultaneously reported by two different groups[190, 195] based on the ARPES technique. The results with respect to

the temperature dependence of the superconducting gap (from EDCs) are shown in Fig. 2-45 (a) and (b), and the corresponding relationship between gap size and the temperature is summarized in Fig. 2-45 (c) and (d). Similar gap-temperature behaviour indicated the non-arbitrary T_c record of 65 ± 5 K at that time.

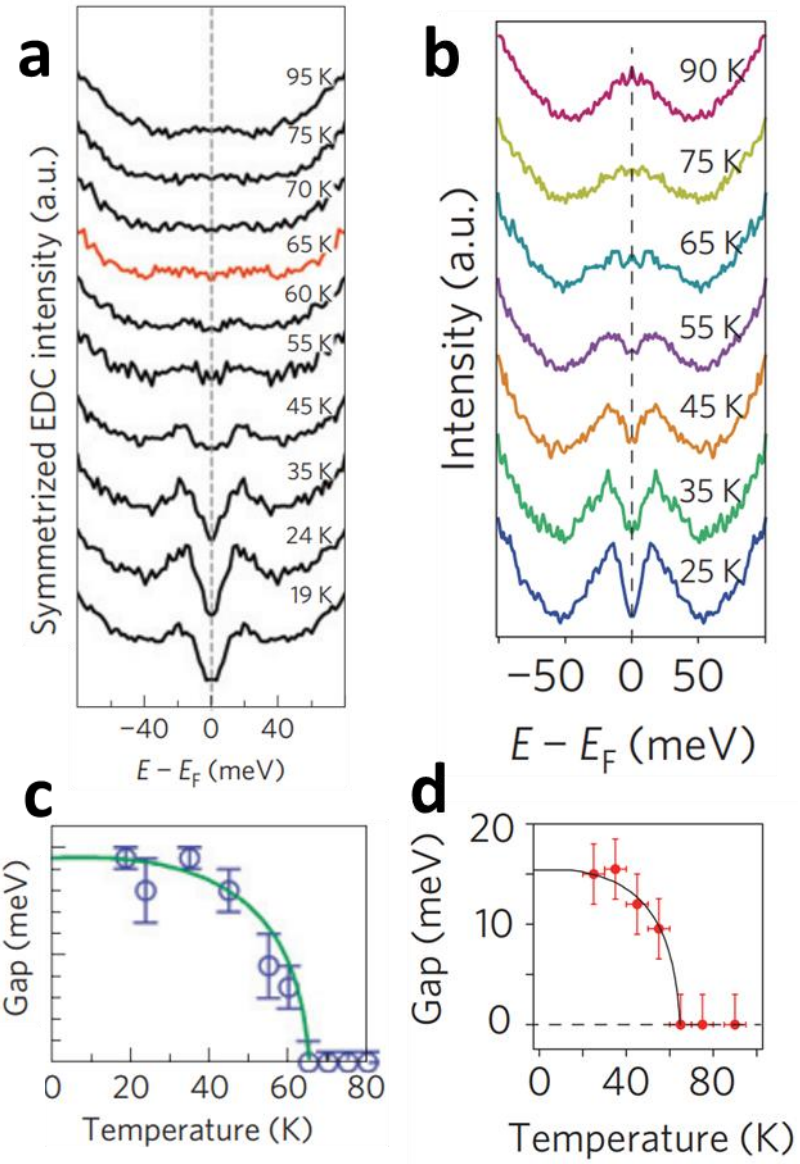

Figure 2-45. Temperature dependence of the energy gap of monolayer FeSe film. The superconducting gap keeps opening up to 65 K. (a, b): Symmetrized EDCs cut near the M point on the Fermi surface. (c, d): The size of the superconducting gap as a function of temperature. The plots are based on the EDC data from (a) and (b). (a) & (c) are after Ref.[190]. (b) & (d) are after Ref.[195].

Actually, ARPES is more than only an alternative way to characterize T_c in studying the superconductivity of the FeSe system. It is very powerful in probing the sophisticated electronic structures near the Fermi level so that information on the direct band structure can be clearly mapped. The electron behaviour in *k*-space and the pairing

mechanism of superconductivity are expected to be clarified by analyzing the results of ARPES. Fig. 2-46 (a) shows the mapping of the band structure of monolayer FeSe at Fermi surface. Only electron pockets around M-points were observed, which resembles the case of $K_xFe_{2-y}Se_2$ single crystals[196], and is in contrast to most of the iron-based superconductors that have a hole-pocket at the centre of Brillouin zone (Γ-point)[197-200]. The absence of a hole-pocket is considered as a signature of heavy electron-doping in the monolayer FeSe/STO system. This also means that the superconductivity in monolayer FeSe/STO is not within the framework of the $s_{\pm}$ pairing scenario[18]. The separate band structures at the Γ- and M- points are shown in Fig. 2-46 (b). The huge energy of 80 meV below the Fermi surface is explained by the absence of the hole-pocket at the Γ-point. A typical Fermi surface of an electron-pocket at the M-point and the corresponding polar diagram are displayed in Fig. 2-46 (c, d). The uniform gap structure with a round and un-nested Fermi surface excludes the possibility that it is induced by SDW-like instabilities[192].

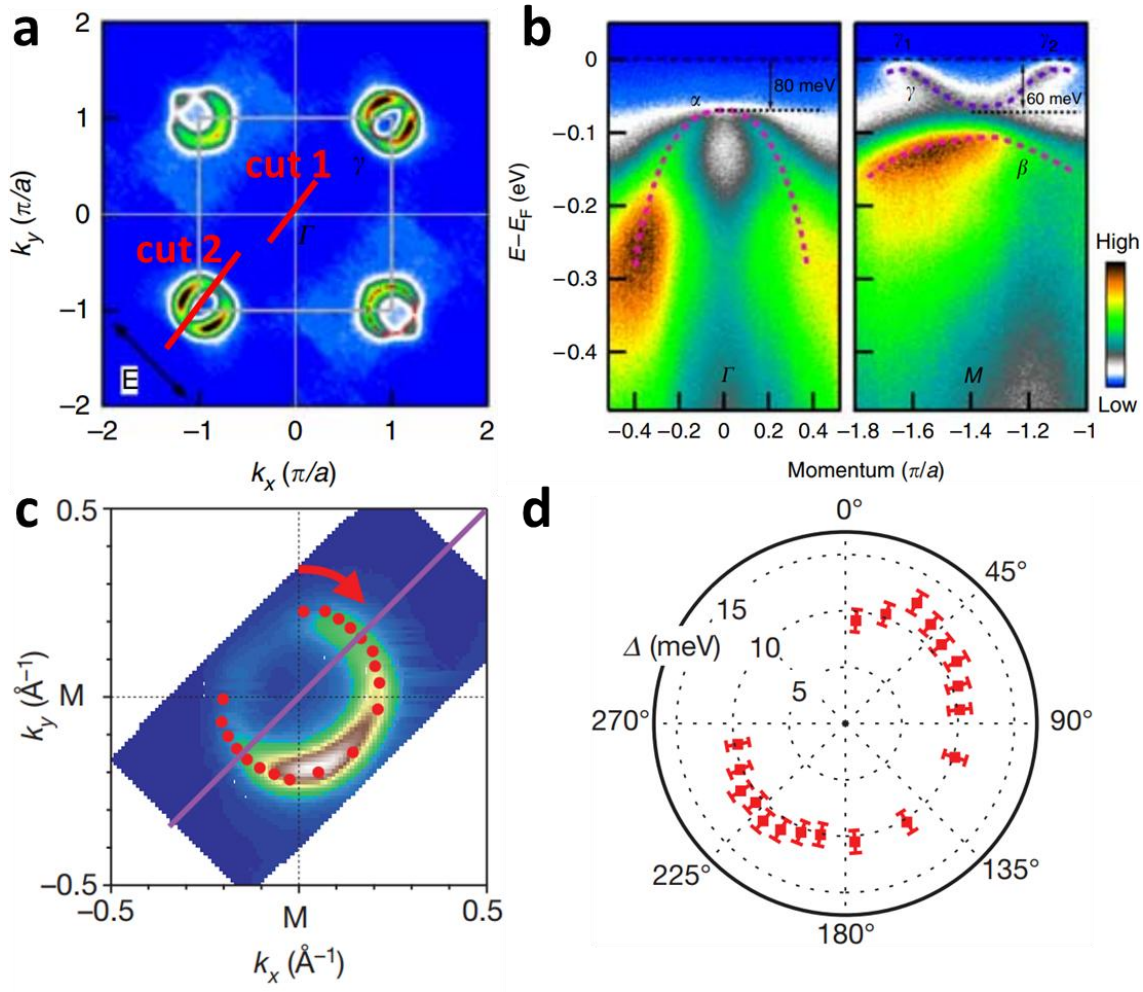

Figure 2-46. The band structure of 1-UC FeSe/STO at the Fermi surface. (a) Mapping of the Fermi surface at 20 K. Only electron pockets are observed at M-points. (b) Band structure along cut 1 (left panel)

and cut 2 (right panel) in (a). (c) A typical electron-pocket at an M-point. (d) Polar diagram of the EDC gaps. Data were extracted from the red dots in (c). (a) & (b) are after Ref.[189]. (c) & (d) are after Ref.[192].

As indicated by the scanning tunneling spectroscopy (STS)[43, 186] and ARPES results[195], the superconducting gap no longer appears from the second FeSe atomic layer. As expected, the Fermi surface of the FeSe film with more than one unit-layer shows a completely different topography compared to that of monolayer FeSe. Specifically, both hole- and electron-pockets are found at the Fermi surfaces of 2-UC or thicker FeSe films, which is quite similar to the case of FeSe bulks. With abundant experimental results showing similar results, the clarification of the underlying mechanism by either material science or condensed matter physics is of great interest. Based on the fact that the enhanced T_c in monolayer FeSe is significantly relevant to the FeSe/STO interface, researchers have proposed three interfacial factors that might be responsible for interface-induced HTS: the tensile-strain owing to the lattice misfit between film and substrate, the electron-doping from the underlying STO substrate or upper alkali metal coating, and the electron-phonon coupling between FeSe electrons and STO phonons. As shown in Fig. 2-47, a linear fit of the T_c vs. the gap was divided into three groups: without any charge transfer or substrate-effect (panel on left), with electron doping but no substrate effect (panel in middle), and with the electron-phonon coupling effect (panel on the right)[201]. Details with respect to the debates on the three possible origins of high-T_c superconductivity in FeSe films will be reviewed one by one in the following part.

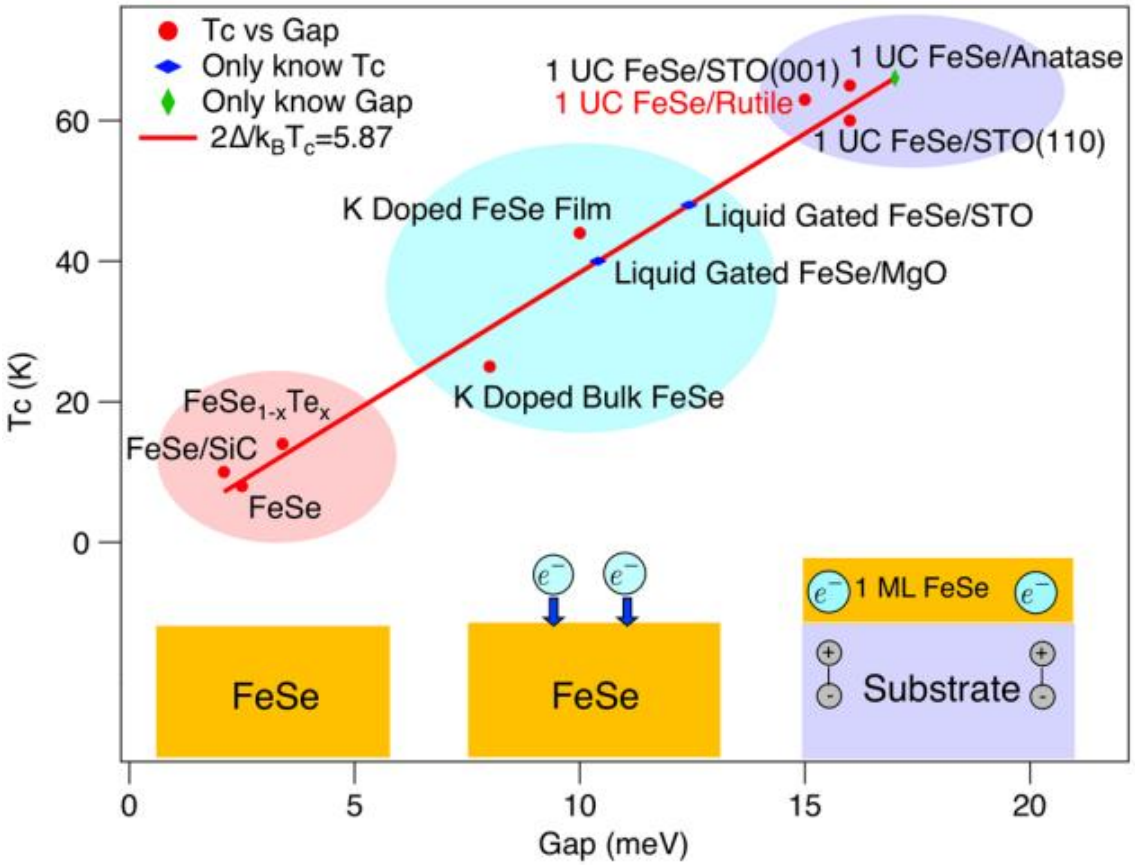

Figure 2-47. Plots showing the T_cs of different superconducting FeSe systems. Bottom panels are three groups with different origins of superconductivity. After Ref.[201].

Firstly, the effect of lattice strain is believed to affect the superconductivity of monolayer FeSe in a similar way to the case of FeSe bulk samples. To figure out the role of different strains from various growth substrates on the T_c enhancement of monolayer FeSe, quite a few investigations[190, 193, 195, 202-203] have been carried out with the corresponding T_c values taken from ARPES results. Table 2-4 lists the dependence of T_c (taken from ARPES results) in monolayer FeSe films grown on various substrates with different in-plane lattice parameters[204]. Although a positive correlation between T_c and tensile-strain seems to be there, an exceptionally high T_c of ~ 70 K was obtained in monolayer FeSe grown on a rotated Nb: $BaTiO_3/KTaO_3$ substrate which only produced a negligible tensile-strain, as low as 0.4 %[202]. Ding *et al.*[205] found a large superconducting gap size of 21 meV in 1-UC $FeSe/TiO_2(001)$, but a strain-free condition was indicated by the fact that both 1-UC and 2-UC FeSe films showed the same in-plane lattice parameter of 3.80 ± 0.05 Å (measured by STM). Thus, the enhanced T_c in 1-UC FeSe cannot be only due to lattice-strain effects.

Table 2-4. Dependence of ARPES T_c of monolayer FeSe films grown on various substrates with different tensile-strain. After Ref.[204].

Substrate	**In-plane lattice parameter (Å)**	**Tensile strain (%)***	**T_c (K)****
Nb: $BaTiO_3/KTaO_3$ (rotated lattice)	3.78	0.4	~ 70
3-UC Nb: STO/LAO	3.79	0.7	~ 55
5-UC Nb: STO/LAO	3.81	1.2	~ 62
Nb: STO	3.91	3.9	~ 65
Nb: $STO/KTaO_3$	3.99	6.0	~ 70
Nb: $BaTiO_3/KTaO_3$	3.99	6.0	~ 75

* Relative values to the FeSe bulk (3.765 Å).

** All the T_c values were taken from ARPES results for consistency.

Charge carrier (electron or hole) doping always plays a significant role in superconductivity. Especially in the BCS weak-coupling limit model[206], superconductivity does not favour a system with an insulating band structure lacking carrier density. Hence, how the carrier doping is affecting the superconductivity of the 1-UC FeSe system has been thoroughly investigated. The ARPES finding that the superconducting gap vanishes in the 2nd FeSe layer while the hole-pocket emerges points out the importance of heavy electron-doping for the superconductivity in monolayer FeSe/STO. T_c of FeSe/STO has been found to be sensitive to the post-annealing effect. Fig. 2-48 (a) summarizes the phase diagram regarding the extensive annealing process for 1-UC FeSe/STO. A competition between two phases (low-doping N phase and superconducting S phase) was demonstrated during the annealing process. Based on the ARPES results, the band structures of *N* and *S* phases are illustrated in Fig. 2-48 (b, c), respectively. Thus, the tunable nature of the electron concentration and the corresponding T_c performance of monolayer FeSe/STO were demonstrated through a mild annealing process. Xue's group[140, 207] studied the effect of post-annealing (various annealing temperatures and periods) on the electrical transport properties of 1-UC and multilayer FeSe films grown on STO substrates. Electron carriers were found to be transferred from the STO substrate into the FeSe film through an annealing process.

Better superconducting performance was present after a higher temperature (Fig. 2-49 (a)) and longer time-period (Fig. 2-49 (b)) of the post-annealing procedure. Hall measurements (Fig. 2-49 (c)) revealed that the sign of R_H of 1-UC FeSe film changed from positive to negative, indicating that the dominant charge carriers changed from holes to electrons after the post-annealing process. Moreover, Wang *et al.*[140] realized enhanced T_c in multilayer FeSe/STO (up to 50-UC) through careful post-annealing control, even though the as-grown sample showed insulating behaviour. The best T_c onset in this work was 39 K in a 5-UC FeSe/STO after a 36-hour post-annealing process (shown in Fig. 2-49 (d)). The corresponding R_H-T curves displayed in Fig. 2-49 (e) suggest a carrier-type reversal from hole- to electron-dominated in the multilayer FeSe/STO system after post-annealing, which probably leads to an insulator-superconductor transition and the occurrence of superconductivity. Hence, it can be concluded that the post-annealing process enables electron charge transfer from the STO substrate to the FeSe film.

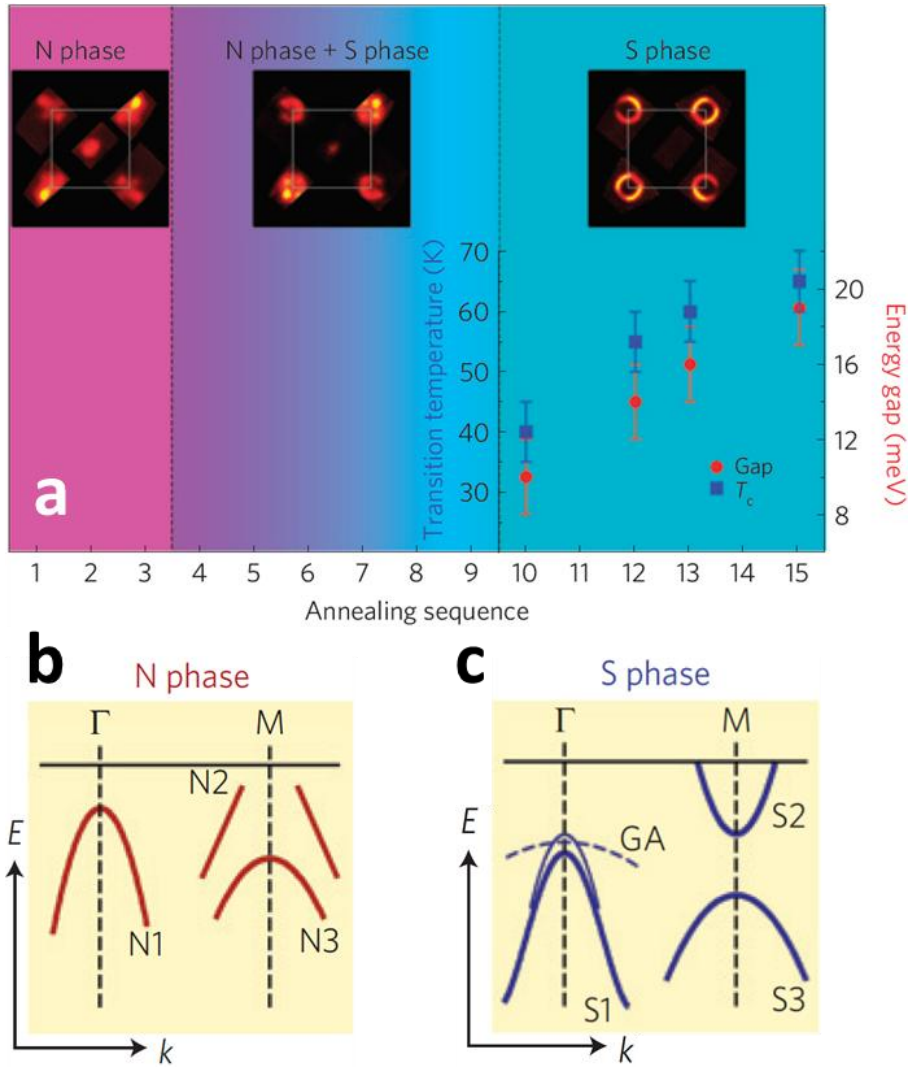

Figure 2-48. The phase diagram of the T_c/gap-size of monolayer FeSe film under different post-annealing processes. (a) The initial *N* phase and superconducting *S* phase are identified at two ends. A combination phase exists in between. Inset: corresponding Fermi surface mappings. Schematic band structures of (b) *N* and (c) *S* phases. After Ref.[190].

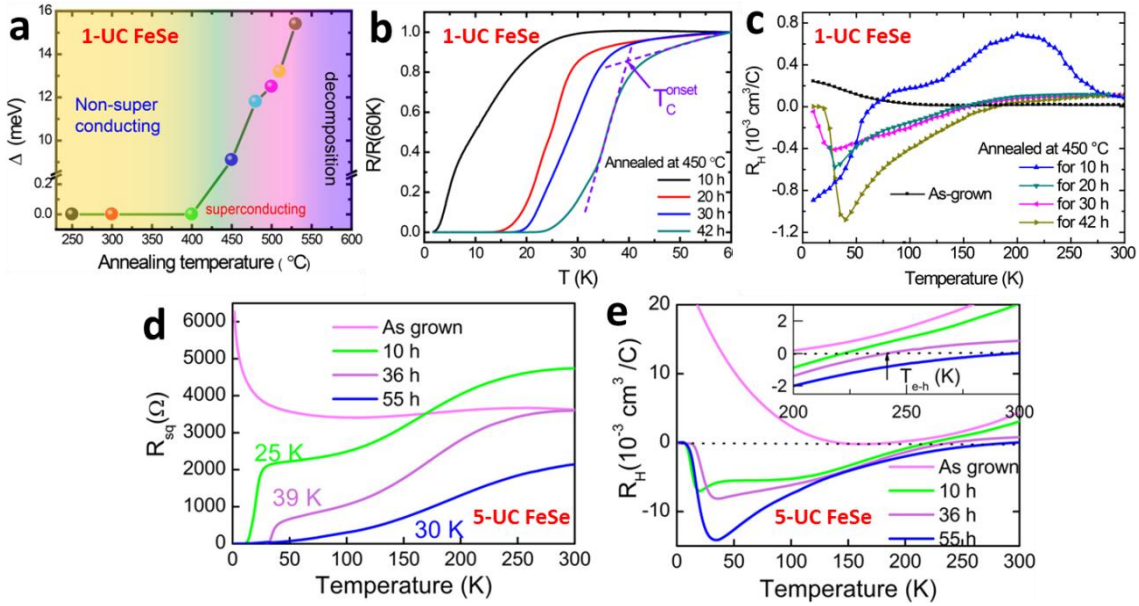

Figure 2-49. Superconducting properties of 1-UC and 5-UC FeSe/STO under different annealing processes. (a) The superconducting gap of 1-UC FeSe/STO as a function of annealing temperature. Higher temperature results in a larger gap size. (b) The normalized resistance of 1-UC FeSe/STO annealed for various time periods. (c) The Hall coefficient as a function of temperature for 1-UC FeSe/STO films annealed for different numbers of hours. (d) Temperature dependence of the sheet resistance of 5-UC FeSe/STO with different annealing times. (e) The corresponding Hall coefficients for the samples in (d) vs. temperature. Inset: the point where electron carriers become dominant. (a) - (c) are after Ref.[207]. (d) & (e) are after Ref.[140].

K-coating of the top surface was found to be effective for introducing extra electron carriers into multilayer FeSe films, which apparently lack enough electron doping. Miyata *et al.*[208] first published the finding of an enhanced T_c as high as 48 K in an originally non-superconducting multilayer (3-UC) FeSe film on STO substrate, which was by depositing K on the film surface. In Fig. 2-50 (a), the ARPES results show a significant suppression of the hole-pocket at the Γ-point after K was deposited on a 3-UC FeSe film, suggesting the effective electron-doping introduced by the K-coating process. Follow-up works[209-213] further confirmed the electron-dominated nature of the Fermi surface and the high T_c of multilayer FeSe films coated by K, even for a 50-UC FeSe film[210]. Two graphs showing the K-coverage effect on the superconducting gap are presented in Fig. 2-50 (b) and (c). The dome-shaped dependence indicates that an optimized dopant concentration is required for high-T_c superconductivity in

multilayer FeSe films. Unconventional superconductivity in the K-doped FeSe film was also deduced, based on the dome-shaped temperature-doping phase diagram[208].

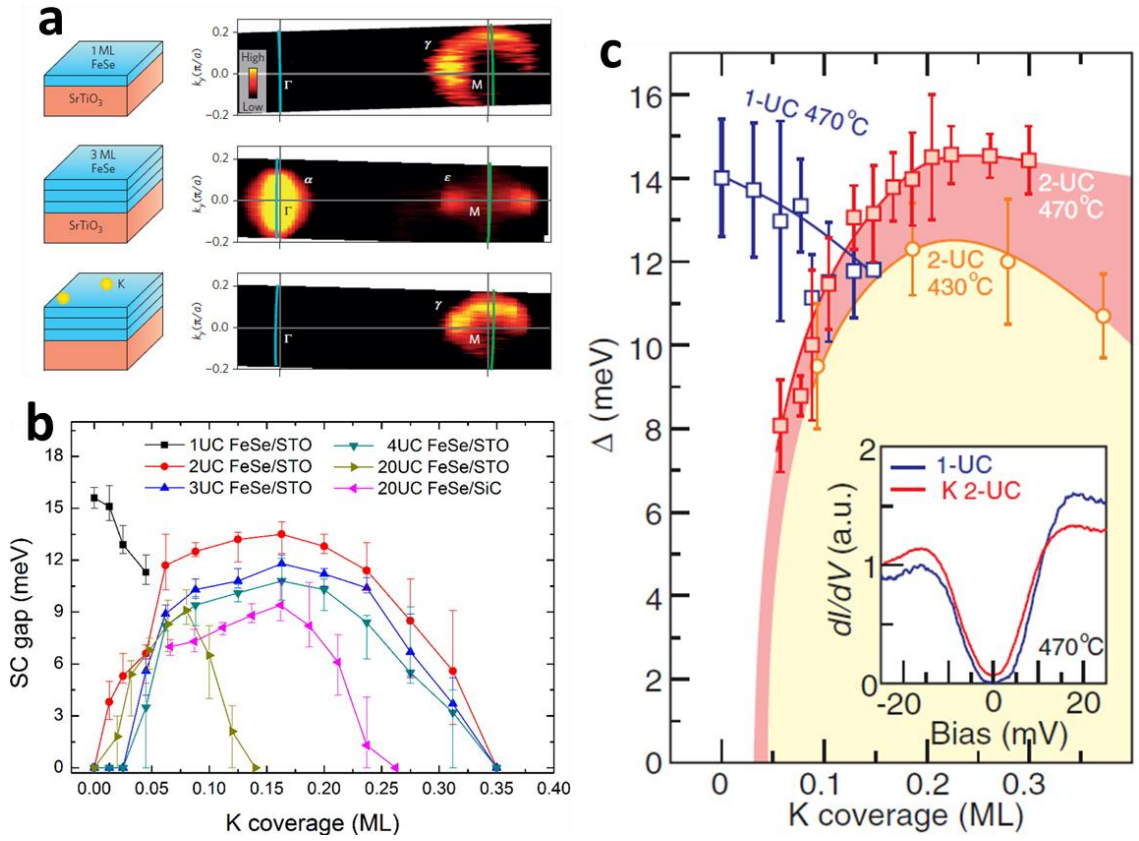

Figure 2-50. K-coating effect on multilayer FeSe films grown on STO. (a) Left panels: schematic structures of different samples with FeSe layers (blue sheets) and K-deposition (yellow circles); right panels: corresponding ARPES results[208]. (b) Dependence of superconducting gap size on K-coverage. The thickness of the FeSe layer is up to 20-UC[213]. (c) Dependence of gap-size of 1-UC and 2-UC FeSe films on K-coverage.[209]

Direct electron-carrier doping can also be realized by an EDLT technique. This was first demonstrated by Shiogai *et al.*[141] in FeSe/STO and FeSe/MgO thick films, and T_c^{onset} was over 40 K for both structures. An electrochemical etching technique was employed for investigating the thickness dependence of T_c. A quick follow-up work from the same group[142] showed a similar high-T_c result for a FeSe/$KTaO_3$ structure (results are shown in Fig. 2-51 (a)). The results of Hall measurements proved the electrostatic carrier doping by EDLT. Therefore, a unified mechanism for high-T_c superconductivity in FeSe films was proposed to be a specific electron-doped band structure rather than an interfacial effect, such as the strong coupling between the monolayer FeSe film and the STO substrate[43]. Hanzawa *et al.*[214] achieved a maximum T_c of 35 K in a 10-nm-thick FeSe film grown on STO substrate with the help of EDLT-induced electric fields. As shown in Fig. 2-51 (b), a superconducting transition

gradually appeared with increasing applied bias up to 5.5 V. The accumulation of electron-carriers near the channel surface of FeSe was revealed by Hall measurements. Fig. 2-51 (c) shows the results of the EDLT technique on FeSe single-crystal flakes in work conducted by Lei *et al.*[215] With increasing gate voltage, a T_c of ~ 40 K was obtained with a simultaneous sign-reversal of R_H, indicating the occurrence of a Lifshitz Transition[216] in the HTS state due to the disappearance of the hole-pocket Fermi surface. The significant enhancement of T_c from ~ 8 K in FeSe bulk to ~ 40 K in EDLT-FeSe films or thin flakes firmly indicates the huge contribution of electron-doping to the high-T_c superconductivity in this system.

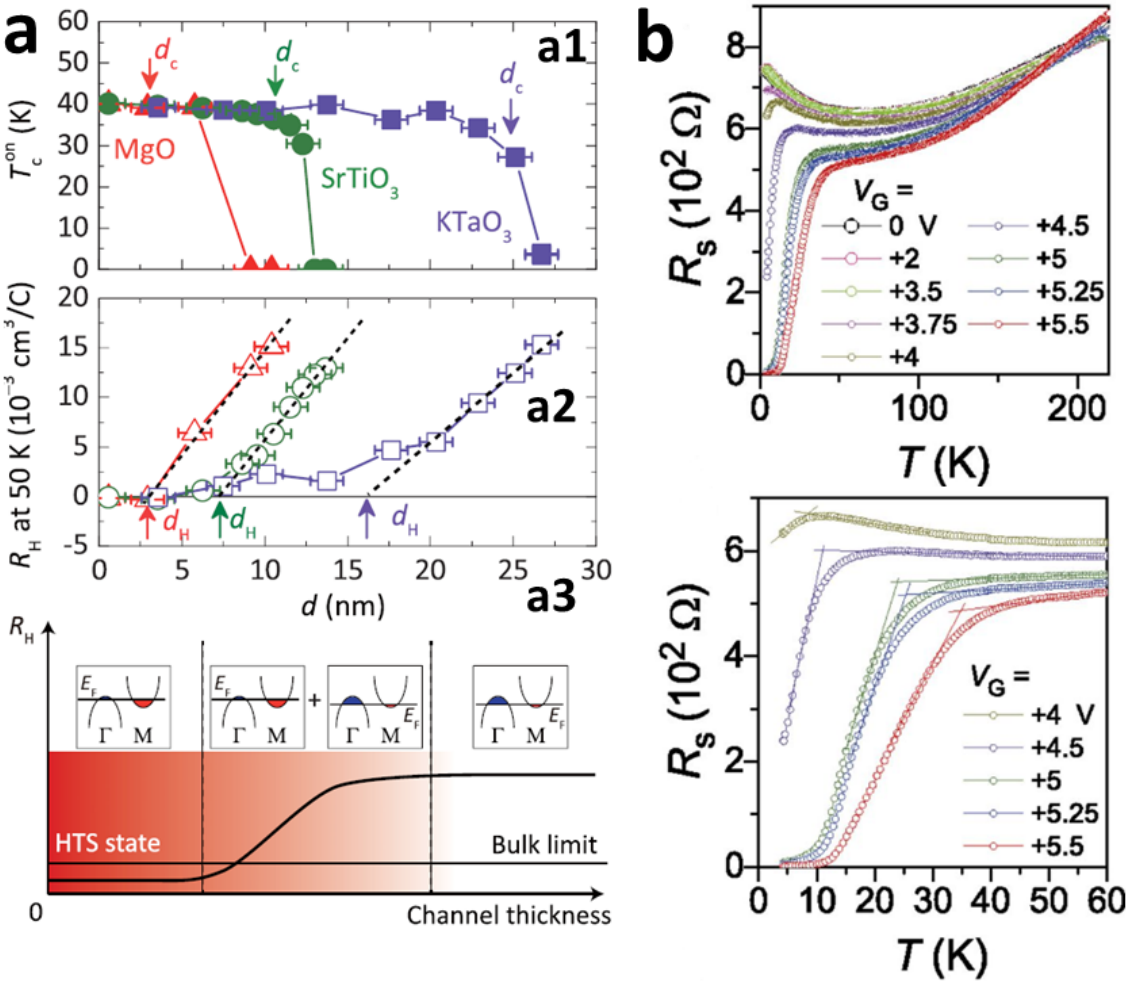

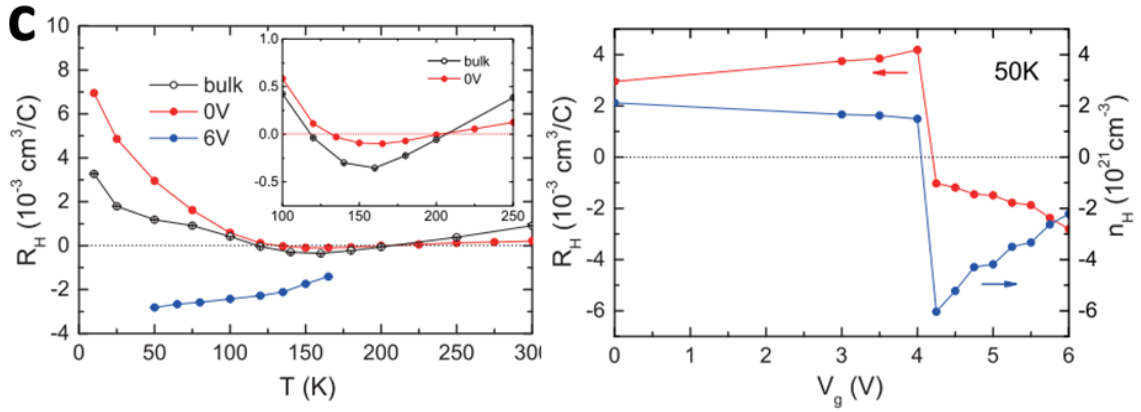

Figure 2-51. Effect of EDLT technique towards inducing high-T_c superconductivity in FeSe. (a) Thickness dependence of T_c^{onset} and R_H (50 K) for FeSe films grown on STO, MgO, and $KTaO_3$ substrates. A schematic image is shown in the bottom, showing how electron-doping induces HTS of FeSe in this work[142]. (b) R_s-T curves of the FeSe film (~ 10 nm in thickness) under different biases V_G[214]. (c) Temperature and gate-voltage dependence of R_H and the carrier density of FeSe flake[215].

Electron-phonon coupling is considered as one of the most intrinsic origins of the enhanced superconductivity in monolayer FeSe films[217]. Li *et al.*[218] studied the unique electronic structure and phonon properties of the FeSe/STO interface by DFT calculations. Fig. 2-52 (a) illustrates the higher frequency-dependence of the phonon density of states (DOS) in FeSe/STO than in bulk FeSe. In order to quantify the strength of electron-phonon coupling, an electron-phonon coupling constant $\lambda(\omega)$, defined as

$$\lambda_\omega = 2\int_0^\omega dv[\alpha^2F(v)/v]$$

was introduced, where $\alpha^2F(\omega)$ refers to the Eliashberg spectral function. The frequency-dependence of $\lambda(\omega)$ and $\alpha^2F(\omega)$ in nonmagnetic and antiferromagnetic states is shown in Fig. 2-52 (b) and (c). A higher electron-phonon coupling strength $\lambda(\omega)$ of 0.30 was obtained in FeSe/STO, which is nearly 1.7 times the $\lambda(\omega)$ of 0.18 for bulk FeSe. Hence, the authors proposed that the ferroelectric phonons in the TiO_2 plane were mainly for the increased $\lambda(\omega)$, and their coupling with the Fe-3d electrons from the FeSe layer would promote Cooper pairing in the interfacial region of FeSe/STO. Similar experimental phenomena, relating to large electron-phonon coupling at the FeSe/STO interface, were also reported[192, 212, 219-220].

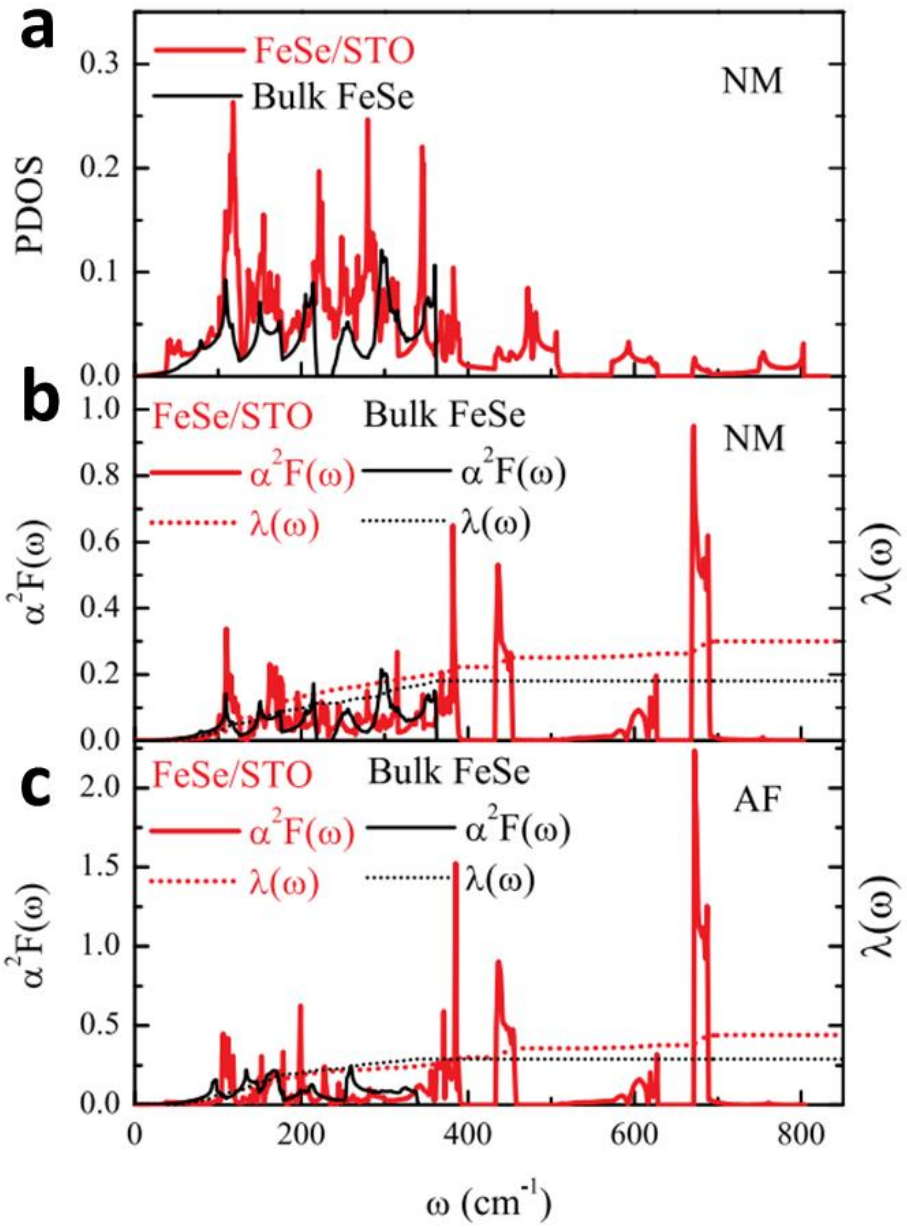

Figure 2-52. Calculation results for the phonon-DOS and $\alpha^2F(\omega)$ (Eliashberg spectral function) of the FeSe/STO interface and bulk FeSe. (a) Comparison of the phonon-DOS with the bulk in the nonmagnetic state. Comparison of $\alpha^2F(\omega)$ for (b) nonmagnetic and (c) antiferromagnetic states. After Ref.[218].

A "replica band" is a dispersed band structure with a similar shape to the real band, and it locates at ~ 100 meV lower than the true one[192]. Lee *et al.*[192] first published their observation of replica bands at the interface of a 1-UC FeSe film and its STO substrate. The electron-phonon coupling constant λ in this work was estimated to be 0.5 based on the intensity ratio of replica bands, signaling the fact that the replica band can be taken as an indication of the strong electron-phonon coupling at the FeSe/STO interface. Moreover, the replica bands were found to only exist in 1-UC FeSe/STO and not in 2-UC or thicker FeSe films[192]. As displayed in Fig. 2-53, Wang *et al.*[204] compared

the Fermi surfaces and band structures of four representative superconducting FeSe systems, including pristine multilayer-FeSe/STO, K-doped multilayer-FeSe/STO, monolayer-FeSe/STO, and monolayer-FeSe/TiO_2. The hole-pocket Fermi surface at Γ-point was only detected in 60-UC FeSe/STO, which showed the lowest T_c of < 20 K. The higher T_c of ~ 40 K in K-doped 3-UC FeSe/STO was correlated with the absence of the hole-pocket at the Γ-point. No replica band was observed in Fig. 2-53 (a) or (b), however. Evidently, a much enhanced T_c of ~ 60 K can only be obtained in the FeSe system in the case where a replica band is observed in the second derivative image, such as 1-UC FeSe films grown on STO and TiO_2 substrates (Fig. 2-53 (c, d)). This is reminiscent of the proposal of Lee *et al.*[192] that the coincidental emergence of a much enhanced T_c and replica bands emphasizes the important role of the interfacial electron-phonon coupling in the T_c enhancement in monolayer FeSe systems. Currently, no experimental results can demonstrate a direct correlation between the significantly enhanced superconductivity and the electron-phonon coupling. Nevertheless, the similar interface-induced superconductivity reported in other FeSe-related materials, such as FeSeTe/STO[221], FeSe/$BaTiO_3$[202], KFe_2Se_2/STO[209], and FeSe/TiO_2[205], suggests a universal mechanism for comprehensively understanding the HTS in the FeSe system, especially the interface-induced superconductivity.

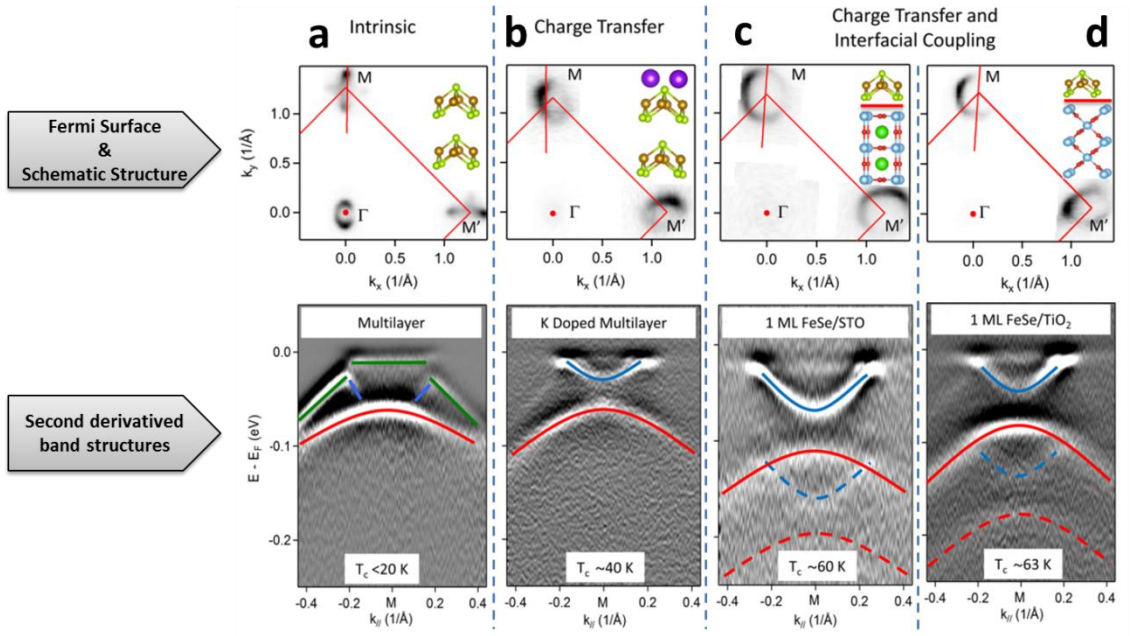

Figure 2-53. Comparison of the Fermi surface and band structures of four superconducting FeSe systems. (a) 60-UC FeSe grown on STO. (b) K-doped 3-UC FeSe grown on STO. (c) 1-UC FeSe grown on STO. (d) 1-UC FeSe grown on TiO_2. Upper panels: Fermi surface and schematic structure. Lower panels: Second derivative images of the corresponding band structures. After Ref.[204].

In summary, 11-type iron-based superconductors (Fe-*Ch*) have been carefully reviewed in the above section. Since its recognition as an iron-based superconductor with the simplest binary structure, FeSe superconductor keeps rejuvenating through novel paradigms, such as the distinct improvement in T_c by Te-substitution or pressurization. More breakthroughs were discovered in the landscape of thin film growth. Not only higher superconducting performance, but also unique properties have been continuously reported with respect to the FeSe-related thin films, including the effects of lattice strain and film thickness, synthesis temperature dependence, growth substrate selection, enhancement of the critical current density, inducing superconductivity in non-superconducting FeTe parent phase, etc. On the other hand, the significantly enhanced T_c with the potential to exceed the boiling point of liquid nitrogen that was discovered in monolayer FeSe film grown on STO substrate has triggered a huge research upsurge in condensed matter physics. Hot debates on the intrinsic mechanism of this special system have offered three popular proposals, in which the mechanism is due to a massive strain-effect, heavy electron doping, or interfacial coupling between electrons (FeSe) and phonons (STO). The latter two factors are now believed to be more likely to reveal the mechanism of high T_c in 1-UC FeSe/STO and other HTS cases in regard to interface superconductivity. Further investigations focusing on the interfacial and Mg-coating effects on the PLD-FeSe thin films are carried out in this thesis work to unveil the mechanism of the enhanced superconductivity.

2.4 References

(1) "“Nobel Lecture: On Superconductivity and Superfluidity”." *Ginzburg, V. L.* Nobel Media AB 2014. Web.: http://www.nobelprize.org/nobel_prizes/physics/laureates/2003/ginzburg-lecture.pdf.
(2) Bednorz, J. G.; Müller, K. A. Possible high T_c superconductivity in the Ba−La−Cu−O system. *Zeitschrift für Physik B Condensed Matter* **1986,** *64*, 189-193.
(3) Wu, M. K.; Ashburn, J. R.; Torng, C. J.; Hor, P. H.; Meng, R. L.; Gao, L.; Huang, Z. J.; Wang, Y. Q.; Chu, C. W. Superconductivity at 93 K in a new mixed-phase Y-Ba-Cu-O compound system at ambient pressure. *Phys. Rev. Lett.* **1987,** *58*, 908-910.
(4) Schilling, A.; Cantoni, M.; Guo, J. D.; Ott, H. R. Superconductivity above 130 K in the Hg-Ba-Ca-Cu-O system. *Nature* **1993,** *363*, 56-58.
(5) Gao, L.; Xue, Y. Y.; Chen, F.; Xiong, Q.; Meng, R. L.; Ramirez, D.; Chu, C. W.; Eggert, J. H.; Mao, H. K. Superconductivity up to 164 K in $HgBa_2Ca_{m-1}Cu_mO_{2m+2+\delta}$ (m=1, 2, and 3) under quasihydrostatic pressures. *Phys. Rev. B* **1994,** *50*, 4260-4263.
(6) Takahashi, H.; Igawa, K.; Arii, K.; Kamihara, Y.; Hirano, M.; Hosono, H. Superconductivity at 43 K in an iron-based layered compound $LaO_{1-x}F_xFeAs$. *Nature* **2008,** *453*, 376-378.
(7) Ren, Z.-A.; Che, G.-C.; Dong, X.-L.; Yang, J.; Lu, W.; Yi, W.; Shen, X.-L.; Li, Z.-C.; Sun, L.-L.; Zhou, F.; Zhao, Z.-X. Superconductivity and phase diagram in iron-based arsenic-oxides $ReFeAsO_{1-\delta}$ (Re = rare-earth metal) without fluorine doping. *EPL* **2008,** *83*, 17002.
(8) Kamihara, Y.; Watanabe, T.; Hirano, M.; Hosono, H. Iron-based Layered Superconductor $La[O_{1-x}F_x]FeAs$ (x = 0.05-0.12) with T_c = 26 K. *J. Am. Chem. Soc.* **2008,** *130*, 3296-3297.
(9) Li, Y.; Hao, J.; Liu, H.; Li, Y.; Ma, Y. The metallization and superconductivity of dense hydrogen sulfide. *J. Chem. Phys.* **2014,** *140*, 174712.
(10) Drozdov, A. P.; Eremets, M. I.; Troyan, I. A.; Ksenofontov, V.; Shylin, S. I. Conventional superconductivity at 203 kelvin at high pressures in the sulfur hydride system. *Nature* **2015,** *525*, 73-76.
(11) Hosono, H.; Kuroki, K. Iron-based superconductors: Current status of materials and pairing mechanism. *Phys. C* **2015,** *514*, 399-422.
(12) Ray, P. J., Figure 2.4 in Master's thesis, "Structural investigation of La(2-x)Sr(x)CuO(4+y) - Following staging as a function of temperature". In *Niels Bohr Institute, Faculty of Science*, University of Copenhagen: Copenhagen, Denmark, 2015.
(13) Kamihara, Y.; Hiramatsu, H.; Hirano, M.; Kawamura, R.; Yanagi, H.; Kamiya, T.; Hosono, H. Iron-Based Layered Superconductor: LaOFeP. *J. Am. Chem. Soc.* **2006,** *128*, 10012-10013.
(14) Ren, Z.-A.; Lu, W.; Yang, J.; Yi, W.; Shen, X.-L.; Zheng, C.; Che, G.-C.; Dong, X.-L.; Sun, L.-L.; Zhou, F.; Zhao, Z.-X. Superconductivity at 55 K in Iron-Based F-Doped Layered Quaternary Compound $Sm[O_{1-x}F_x]$ FeAs. *Chin. Phys. Lett.* **2008,** *25*, 2215.
(15) Singh, D. J.; Du, M. H. Density Functional Study of $LaFeAsO_{1-x}F_x$: A Low Carrier Density Superconductor Near Itinerant Magnetism. *Phys. Rev. Lett.* **2008,** *100*, 237003.
(16) Subedi, A.; Zhang, L.; Singh, D. J.; Du, M. H. Density functional study of FeS, FeSe, and FeTe: Electronic structure, magnetism, phonons, and superconductivity. *Phys. Rev. B* **2008,** *78*, 134514.
(17) Ishibashi, S.; Terakura, K.; Hosono, H. A Possible Ground State and Its Electronic Structure of a Mother Material (LaOFeAs) of New Superconductors. *J Phys. Soc. Jpn.* **2008,** *77*, 053709.
(18) Mazin, I. I.; Singh, D. J.; Johannes, M. D.; Du, M. H. Unconventional Superconductivity with a Sign Reversal in the Order Parameter of $LaFeAsO_{1-x}F_x$. *Phys. Rev. Lett.* **2008,** *101*, 057003.
(19) Kuroki, K.; Onari, S.; Arita, R.; Usui, H.; Tanaka, Y.; Kontani, H.; Aoki, H. Unconventional Pairing Originating from the Disconnected Fermi Surfaces of Superconducting $LaFeAsO_{1-x}F_x$. *Phys. Rev. Lett.* **2008,** *101*, 087004.
(20) Yanagi, Y.; Yamakawa, Y.; Adachi, N.; Ōno, Y. Orbital Order, Structural Transition, and

Superconductivity in Iron Pnictides. *J. Phys. Soc. Jpn.* **2010,** *79*, 123707.
(21) Kontani, H.; Onari, S. Orbital-Fluctuation-Mediated Superconductivity in Iron Pnictides: Analysis of the Five-Orbital Hubbard-Holstein Model. *Phys. Rev. Lett.* **2010,** *104*, 157001.
(22) Yanagi, Y.; Yamakawa, Y.; Ōno, Y. Two types of *s*-wave pairing due to magnetic and orbital fluctuations in the two-dimensional 16-band *d-p* model for iron-based superconductors. *Phys. Rev. B* **2010,** *81*, 054518.
(23) Hosono, H.; Kuroki, K. Iron-based superconductors: Current status of materials and pairing mechanism. *Physica C* **2015,** *514*, 399-422.
(24) Sun, Y.; Zhang, W.; Xing, Y.; Li, F.; Zhao, Y.; Xia, Z.; Wang, L.; Ma, X.; Xue, Q. K.; Wang, J. High temperature superconducting FeSe films on SrTiO3 substrates. *Sci. Rep.* **2014,** *4*, 6040.
(25) Ge, J.; Liu, Z.; Liu, C.; Gao, C.; Qian, D.; Xue, Q.-K.; Liu, Y.; Jia, J. Superconductivity Above 100 K in Single-layer FeSe Films on Doped $SrTiO_3$. *Nat. Mater.* **2015,** *14*, 285-289.
(26) Wang, Z.-S.; Luo, H.-Q.; Ren, C.; Wen, H.-H. Upper critical field, anisotropy, and superconducting properties of $Ba_{1-x}K_xFe_2As_2$ single crystals. *Phys. Rev. B* **2008,** *78*, 140501.
(27) Kalenyuk, A. A.; Pagliero, A.; Borodianskyi, E. A.; Aswartham, S.; Wurmehl, S.; Büchner, B.; Chareev, D. A.; Kordyuk, A. A.; Krasnov, V. M. Unusual two-dimensional behavior of iron-based superconductors with low anisotropy. *Phys. Rev. B* **2017,** *96*, 134512.
(28) Huang, Y.; Feng, Z.; Ni, S.; Li, J.; Hu, W.; Liu, S.; Mao, Y.; Zhou, H.; Zhou, F.; Jin, K.; Wang, H.; Yuan, J.; Dong, X.; Zhao, Z. Superconducting (Li,Fe)OHFeSe Film of High Quality and High Critical Parameters. *Chin. Phys. Lett.* **2017,** *34*, 077404.
(29) Hosono, H.; Yamamoto, A.; Hiramatsu, H.; Ma, Y. Recent advances in iron-based superconductors toward applications. *Mater. Today* **2018,** *21*, 278-302.
(30) Ling, J.; Voccio, J. P.; Hahn, S.; Kim, Y.; Song, J.; Bascuñán, J.; Iwasa, Y. Construction and Persistent-Mode Operation of MgB_2 Coils in the Range 10-15 K for a 0.5-T/240-mm Cold Bore MRI Magnet. *IEEE Trans. Appl. Supercond.* **2015,** *25*, 1-5.
(31) Kim, H. S.; Kovacs, C.; Rindfleisch, M.; Yue, J.; Doll, D.; Tomsic, M.; Sumption, M. D.; Collings, E. W. Demonstration of a Conduction Cooled React and Wind <roman>MgB_2 Coil Segment for MRI Applications. *IEEE Trans. Appl. Supercond.* **2016,** *26*, 1-5.
(32) Iwasa, Y. HTS and NMR/MRI magnets: Unique features, opportunities, and challenges. *Physica C* **2006,** *445-448*, 1088-1094.
(33) Katase, T.; Ishimaru, Y.; Tsukamoto, A.; Hiramatsu, H.; Kamiya, T.; Tanabe, K.; Hosono, H. Advantageous grain boundaries in iron pnictide superconductors. *Nat. Commun.* **2011,** *2*, 409.
(34) Holzapfel, B.; Verebelyi, D.; Cantoni, C.; Paranthaman, M.; Sales, B.; Feenstra, R.; Christen, D.; Norton, D. P. Low angle grain boundary transport properties of undoped and doped Y123 thin film bicrystals. *Physica C* **2000,** *341-348*, 1431-1434.
(35) Hilgenkamp, H.; Mannhart, J. Grain boundaries in high-T_c superconductors. *Rev. Mod. Phys.* **2002,** *74*, 485-549.
(36) Aswathy, P. M.; Anooja, J. B.; Sarun, P. M.; Syamaprasad, U. An overview on iron based superconductors. *Supercond. Sci. Technol.* **2010,** *23*, 073001.
(37) Han, Y.; Li, W. Y.; Cao, L. X.; Zhang, S.; Xu, B.; Zhao, B. R. Preparation and Superconductivity of Iron Selenide Thin Films. *J. Phys.: Condens. Matter*. **2009,** *21*, 235702.
(38) Wu, M. K.; Hsu, F. C.; Yeh, K. W.; Huang, T. W.; Luo, J. Y.; Wang, M. J.; Chang, H. H.; Chen, T. K.; Rao, S. M.; Mok, B. H.; Chen, C. L.; Huang, Y. L.; Ke, C. T.; Wu, P. M.; Chang, A. M.; Wu, C. T.; Perng, T. P. The development of the superconducting PbO-type β-FeSe and related compounds. *Physica C: Supercond.* **2009,** *469*, 340-349.
(39) Wang, M. J.; Luo, J. Y.; Huang, T. W.; Chang, H. H.; Chen, T. K.; Hsu, F. C.; Wu, C. T.; Wu, P. M.; Chang, A. M.; Wu, M. K. Crystal Orientation and Thickness Dependence of the Superconducting Transition Temperature of Tetragonal $FeSe_{1-x}$ Thin Films. *Phys. Rev. Lett.* **2009,** *103*, 117002.
(40) Jung, S.-G.; Lee, N. H.; Choi, E.-M.; Kang, W. N.; Lee, S.-I.; Hwang, T.-J.; Kim, D. H. Fabrication of FeSe1−x superconducting films with bulk properties. *Physica C: Supercond.* **2010,** *470*, 1977-1980.
(41) Agatsuma, S.; Yamagishi, T.; Takeda, S.; Naito, M. MBE growth of FeSe and Sr1−xKxFe2As2. *Physica C: Supercond.* **2010,** *470*, 1468-1472.

(42) Jourdan, M.; ten Haaf, S. Preparation, characterization, and upper critical field of epitaxial FeSe thin films. *J. Appl. Phys.* **2010,** *108*, 023913.
(43) Wang, Q.; Li, Z.; Zhang, W.; Zhang, Z.; Zhang, J.; Li, W.; Ding, H.; Ou, Y.; Deng, P.; Chang, K.; Wen, J.; Song, C.; He, K.; Jia, J.; Ji, S.; Wang, Y.; Wang, L.; Chen, X.; Ma, X.; Xue, Q.-K. Interface-Induced High-Temperature Superconductivity in Single Unit-Cell FeSe Films on $SrTiO_3$. *Chin. Phys. Lett.* **2012,** *29*, 037402.
(44) Li, L.; Yang, Z. R.; Sun, Y. P.; Zhang, J. Y.; Shen, D. Z.; Zhang, Y. H. Superconductivity and magnetism in FeSe thin films grown by metal–organic chemical vapor deposition. *Supercond. Sci. Technol.* **2011,** *24*, 015010.
(45) Qi, X.; Wang, J.-Y.; Kuo, J.-C.; Yates, K. A.; Cohen, L. F. Superconducting property and Fe valence state of FeSe thick films grown from high temperature solution. *J. Alloys Compd.* **2011,** *509*, 6350-6353.
(46) Singh, D. J. Electronic structure and doping in $BaFe_2As_2$ and LiFeAs: Density functional calculations. *Phys. Rev. B* **2008,** *78*, 094511.
(47) Chen, X. H.; Wu, T.; Wu, G.; Liu, R. H.; Chen, H.; Fang, D. F. Superconductivity at 43 K in $SmFeAsO_{1-x}F_x$. *Nature* **2008,** *453*, 761-762.
(48) Hiramatsu, H.; Katase, T.; Kamiya, T.; Hirano, M.; Hosono, H. Heteroepitaxial growth and optoelectronic properties of layered iron oxyarsenide, LaFeAsO. *Appl. Phys. Lett.* **2008,** *93*, 162504.
(49) Hiramatsu, H.; Katase, T.; Kamiya, T.; Hirano, M.; Hosono, H. Superconductivity in Epitaxial Thin Films of Co-Doped $SrFe_2As_2$ with Bilayered FeAs Structures and their Magnetic Anisotropy. *Appl. Phys. Expr.* **2008,** *1*, 101702.
(50) Backen, E.; Haindl, S.; Niemeier, T.; Hühne, R.; Freudenberg, T.; Werner, J.; Behr, G.; Schultz, L.; Holzapfel, B. Growth and anisotropy of La(O, F)FeAs thin films deposited by pulsed laser deposition. *Supercond. Sci. Technol.* **2008,** *21*, 122001.
(51) Haindl, S.; Kidszun, M.; Kauffmann, A.; Nenkov, K.; Kozlova, N.; Freudenberger, J.; Thersleff, T.; Hänisch, J.; Werner, J.; Reich, E.; Schultz, L.; Holzapfel, B. High Upper Critical Fields and Evidence of Weak-Link Behavior in Superconducting $LaFeAsO_{1-x}F_x$ Thin Films. *Phys. Rev. Lett.* **2010,** *104*, 077001.
(52) Kidszun, M.; Haindl, S.; Reich, E.; Hänisch, J.; Iida, K.; Schultz, L.; Holzapfel, B. Epitaxial $LaFeAsO_{1-x}F_x$ thin films grown by pulsed laser deposition. *Supercond. Sci. Technol.* **2010,** *23*, 022002.
(53) Kidszun, M.; Haindl, S.; Thersleff, T.; Hänisch, J.; Kauffmann, A.; Iida, K.; Freudenberger, J.; Schultz, L.; Holzapfel, B. Critical Current Scaling and Anisotropy in Oxypnictide Superconductors. *Phys. Rev. Lett.* **2011,** *106*, 137001.
(54) Silvia, H.; Martin, K.; Erik, K. Iron pnictide thin films: Synthesis and physics. *Phys. Status Solidi B* **2017,** *254*, 1600341.
(55) Kidszun, M.; Haindl, S.; Thersleff, T.; Werner, J.; Langer, M.; Hänisch, J.; Iida, K.; Reich, E.; Schultz, L.; Holzapfel, B. Fabrication of superconducting oxypnictide thin films. *EPL* **2010,** *90*, 57005.
(56) Haindl, S.; Hanzawa, K.; Sato, H.; Hiramatsu, H.; Hosono, H. In-situ growth of superconducting $SmO_{1-x}F_xFeAs$ thin films by pulsed laser deposition. *Sci. Rep.* **2016,** *6*, 35797.
(57) Ueda, S.; Takeda, S.; Takano, S.; Yamamoto, A.; Naito, M. High-T_c and high-J_c SmFeAs(O,F) films on fluoride substrates grown by molecular beam epitaxy. *Appl. Phys. Lett.* **2011,** *99*, 232505.
(58) Kawaguchi, T.; Uemura, H.; Ohno, T.; Tabuchi, M.; Ujihara, T.; Takenaka, K.; Takeda, Y.; Ikuta, H. In situ growth of superconducting NdFeAs(O,F) thin films by molecular beam epitaxy. *Appl. Phys. Lett.* **2010,** *97*, 042509.
(59) Takahiko, K.; Hiroki, U.; Toshiya, O.; Ryotaro, W.; Masao, T.; Toru, U.; Koshi, T.; Yoshikazu, T.; Hiroshi, I. Epitaxial Growth of NdFeAsO Thin Films by Molecular Beam Epitaxy. *Appl. Phys. Expr.* **2009,** *2*, 093002.
(60) Kawaguchi, T.; Uemura, H.; Ohno, T.; Tabuchi, M.; Ujihara, T.; Takeda, Y.; Ikuta, H. Molecular Beam Epitaxy Growth of Superconducting NdFeAs(O,F) Thin Films Using a F-Getter and a Novel F-Doping Method. *Appl. Phys. Expr.* **2011,** *4*, 083102.
(61) Ueda, S.; Takeda, S.; Takano, S.; Naito, M. As-Grown Superconducting SmFeAs(O,F)

Thin Films by Molecular Beam Epitaxy. *Appl. Phys. Expr.* **2012,** *5*, 053101.
(62) Sugawara, H.; Tsuneki, T.; Watanabe, D.; Yamamoto, A.; Sakoda, M.; Naito, M. One-step growth of SmFeAs(O,F) films by molecular beam epitaxy using FeF_2 as a fluorine source. *Supercond. Sci. Technol.* **2015,** *28*, 015005.
(63) Sakoda, M.; Ishii, A.; Takinaka, K.; Naito, M. Molecular beam epitaxy growth of SmFeAs(O,F) films with $T_c = 55$ K using the new fluorine source FeF_3. *J. Appl. Phys.* **2017,** *122*, 015306.
(64) Iida, K.; Kurth, F.; Chihara, M.; Sumiya, N.; Grinenko, V.; Ichinose, A.; Tsukada, I.; Hänisch, J.; Matias, V.; Hatano, T.; Holzapfel, B.; Ikuta, H. Highly textured oxypnictide superconducting thin films on metal substrates. *Appl. Phys. Lett.* **2014,** *105*, 172602.
(65) Iida, K.; Hänisch, J.; Tarantini, C.; Kurth, F.; Jaroszynski, J.; Ueda, S.; Naito, M.; Ichinose, A.; Tsukada, I.; Reich, E.; Grinenko, V.; Schultz, L.; Holzapfel, B. Oxypnictide SmFeAs(O,F) superconductor: a candidate for high–field magnet applications. *Sci. Rep.* **2013,** *3*, 2139.
(66) Werthamer, N. R.; Helfand, E.; Hohenberg, P. C. Temperature and Purity Dependence of the Superconducting Critical Field,H_{c2}. III. Electron Spin and Spin-Orbit Effects. *Phys. Rev.* **1966,** *147*, 295-302.
(67) Clogston, A. M. Upper Limit for the Critical Field in Hard Superconductors. *Phys. Rev. Lett.* **1962,** *9*, 266-267.
(68) Matsuishi, S.; Inoue, Y.; Nomura, T.; Yanagi, H.; Hirano, M.; Hosono, H. Superconductivity Induced by Co-Doping in Quaternary Fluoroarsenide CaFeAsF. *J. Am. Chem. Soc.* **2008,** *130*, 14428-14429.
(69) Fujitsu, S.; Matsuishi, S.; Hosono, H. Iron based superconductors processing and properties. *Int. Mater. Rev.* **2012,** *57*, 311-327.
(70) Choi, E.-M.; Jung, S.-G.; Lee, N. H.; Kwon, Y.-S.; Kang, W. N.; Kim, D. H.; Jung, M.-H.; Lee, S.-I.; Sun, L. In situ fabrication of cobalt-doped $SrFe_2As_2$ thin films by using pulsed laser deposition with excimer laser. *Appl. Phys. Lett.* **2009,** *95*, 062507.
(71) Hiramatsu, H.; Katase, T.; Kamiya, T.; Hirano, M.; Hosono, H. Water-induced superconductivity in $SrFe_2As_2$. *Phys. Rev. B* **2009,** *80*, 052501.
(72) Katase, T.; Hiramatsu, H.; Yanagi, H.; Kamiya, T.; Hirano, M.; Hosono, H. Atomically-flat, chemically-stable, superconducting epitaxial thin film of iron-based superconductor, cobalt-doped $BaFe_2As_2$. *Solid State Commun.* **2009,** *149*, 2121-2124.
(73) Lee, S.; Jiang, J.; Weiss, J. D.; Folkman, C. M.; Bark, C. W.; Tarantini, C.; Xu, A.; Abraimov, D.; Polyanskii, A.; Nelson, C. T.; Zhang, Y.; Baek, S. H.; Jang, H. W.; Yamamoto, A.; Kametani, F.; Pan, X. Q.; Hellstrom, E. E.; Gurevich, A.; Eom, C. B.; Larbalestier, D. C. Weak-link behavior of grain boundaries in superconducting $Ba(Fe_{1-x}Co_x)_2As_2$ bicrystals. *Appl. Phys. Lett.* **2009,** *95*, 212505.
(74) Iida, K.; Hänisch, J.; Hühne, R.; Kurth, F.; Kidszun, M.; Haindl, S.; Werner, J.; Schultz, L.; Holzapfel, B. Strong Tc dependence for strained epitaxial $Ba(Fe_{1-x}Co_x)_2As_2$ thin films. *Appl. Phys. Lett.* **2009,** *95*, 192501.
(75) Lee, S.; Jiang, J.; Zhang, Y.; Bark, C. W.; Weiss, J. D.; Tarantini, C.; Nelson, C. T.; Jang, H. W.; Folkman, C. M.; Baek, S. H.; Polyanskii, A.; Abraimov, D.; Yamamoto, A.; Park, J. W.; Pan, X. Q.; Hellstrom, E. E.; Larbalestier, D. C.; Eom, C. B. Template engineering of Co-doped $BaFe_2As_2$ single-crystal thin films. *Nat. Mater.* **2010,** *9*, 397.
(76) Iida, K.; Haindl, S.; Thersleff, T.; Hänisch, J.; Kurth, F.; Kidszun, M.; Hühne, R.; Mönch, I.; Schultz, L.; Holzapfel, B.; Heller, R. Influence of Fe buffer thickness on the crystalline quality and the transport properties of $Fe/Ba(Fe_{1-x}Co_x)_2As_2$ bilayers. *Appl. Phys. Lett.* **2010,** *97*, 172507.
(77) Thersleff, T.; Iida, K.; Haindl, S.; Kidszun, M.; Pohl, D.; Hartmann, A.; Kurth, F.; Hänisch, J.; Hühne, R.; Rellinghaus, B.; Schultz, L.; Holzapfel, B. Coherent interfacial bonding on the FeAs tetrahedron in $Fe/Ba(Fe_{1-x}Co_x)_2As_2$ bilayers. *Appl. Phys. Lett.* **2010,** *97*, 022506.
(78) Iida, K.; Hänisch, J.; Trommler, S.; Haindl, S.; Kurth, F.; Hühne, R.; Schultz, L.; Holzapfel, B. Thickness dependence of structural and transport properties of Co-doped $BaFe_2As_2$ on Fe buffered MgO substrates. *Supercond. Sci. Technol.* **2011,** *24*, 125009.
(79) Iida, K.; Hänisch, J.; Thersleff, T.; Kurth, F.; Kidszun, M.; Haindl, S.; Hühne, R.; Schultz, L.; Holzapfel, B. Scaling behavior of the critical current in clean epitaxial $Ba(Fe_{1-x}Co_x)_2As_2$ thin

films. *Phys. Rev. B* **2010,** *81*, 100507.
(80) Kurth, F.; Reich, E.; Hänisch, J.; Ichinose, A.; Tsukada, I.; Hühne, R.; Trommler, S.; Engelmann, J.; Schultz, L.; Holzapfel, B.; Iida, K. Versatile fluoride substrates for Fe-based superconducting thin films. *Appl. Phys. Lett.* **2013,** *102*, 142601.
(81) Sefat, A. S.; Jin, R.; McGuire, M. A.; Sales, B. C.; Singh, D. J.; Mandrus, D. Superconductivity at 22 K in Co-doped $BaFe_2As_2$ crystals. *Phys. Rev. Lett.* **2008,** *101*, 117004.
(82) Ishida, S.; Nakajima, M.; Liang, T.; Kihou, K.; Lee, C.-H.; Iyo, A.; Eisaki, H.; Kakeshita, T.; Tomioka, Y.; Ito, T.; Uchida, S.-i. Effect of Doping on the Magnetostructural Ordered Phase of Iron Arsenides: A Comparative Study of the Resistivity Anisotropy in Doped $BaFe_2As_2$ with Doping into Three Different Sites. *J. Am. Chem. Soc.* **2013,** *135*, 3158-3163.
(83) Hiramatsu, H.; Sato, H.; Katase, T.; Kamiya, T.; Hosono, H. Critical factor for epitaxial growth of cobalt-doped $BaFe_2As_2$ films by pulsed laser deposition. *Appl. Phys. Lett.* **2014,** *104*, 172602.
(84) Katase, T.; Ishimaru, Y.; Tsukamoto, A.; Hiramatsu, H.; Kamiya, T.; Tanabe, K.; Hosono, H. Josephson junction in cobalt-doped $BaFe_2As_2$ epitaxial thin films on $(La,Sr)(Al,Ta)O_3$ bicrystal substrates. *Appl. Phys. Lett.* **2010,** *96*, 142507.
(85) Katase, T.; Ishimaru, Y.; Tsukamoto, A.; Hiramatsu, H.; Kamiya, T.; Tanabe, K.; Hosono, H. DC superconducting quantum interference devices fabricated using bicrystal grain boundary junctions in Co-doped $BaFe_2As_2$ epitaxial films. *Supercond. Sci. Technol.* **2010,** *23*, 082001.
(86) Takeda, S.; Ueda, S.; Yamagishi, T.; Agatsuma, S.; Takano, S.; Mitsuda, A.; Naito, M. Molecular Beam Epitaxy Growth of Superconducting $Sr_{1-x}K_xFe_2As_2$ and $Ba_{1-x}K_xFe_2As_2$. *Appl. Phys. Lett.* **2010,** *3*, 093101.
(87) Agatsuma, S.; Yamagishi, T.; Takeda, S.; Naito, M. MBE growth of FeSe and $Sr_{1-x}K_xFe_2As_2$. *Physica C* **2010,** *470*, 1468-1472.
(88) Yamagishi, T.; Ueda, S.; Takeda, S.; Takano, S.; Mitsuda, A.; Naito, M. A study of the doping dependence of T_c in $Ba_{1-x}K_xFe_2As_2$ and $Sr_{1-x}K_xFe_2As_2$ films grown by molecular beam epitaxy. *Physica C* **2011,** *471*, 1177-1180.
(89) Lee, N. H.; Jung, S.-G.; Kim, D. H.; Kang, W. N. Potassium-doped $BaFe_2As_2$ superconducting thin films with a transition temperature of 40 K. *Appl. Phys. Lett.* **2010,** *96*, 202505.
(90) Yuan, H. Q.; Singleton, J.; Balakirev, F. F.; Baily, S. A.; Chen, G. F.; Luo, J. L.; Wang, N. L. Nearly isotropic superconductivity in $(Ba,K)Fe_2As_2$. *Nature* **2009,** *457*, 565.
(91) Jiang, S.; Xing, H.; Xuan, G.; Wang, C.; Ren, Z.; Feng, C.; Dai, J.; Xu, Z. a.; Cao, G. Superconductivity up to 30 K in the vicinity of the quantum critical point in $BaFe_2(As_{1-x}P_x)_2$. *J. Phys.: Condens. Matter* **2009,** *21*, 382203.
(92) Adachi, S.; Shimode, T.; Miura, M.; Chikumoto, N.; Takemori, A.; Nakao, K.; Oshikubo, Y.; Tanabe, K. Pulsed laser deposition of $BaFe_2(As,P)_2$ superconducting thin films with high critical current density. *Supercond. Sci. Technol.* **2012,** *25*, 105015.
(93) Miura, M.; Maiorov, B.; Kato, T.; Shimode, T.; Wada, K.; Adachi, S.; Tanabe, K. Strongly enhanced flux pinning in one-step deposition of $BaFe_2(As_{0.66}P_{0.33})_2$ superconductor films with uniformly dispersed $BaZrO_3$ nanoparticles. *Nat. Commun.* **2013,** *4*, 2499.
(94) Sakagami, A.; Kawaguchi, T.; Tabuchi, M.; Ujihara, T.; Takeda, Y.; Ikuta, H. Critical current density and grain boundary property of $BaFe_2(As,P)_2$ thin films. *Physica C* **2013,** *494*, 181-184.
(95) Sato, H.; Hiramatsu, H.; Kamiya, T.; Hosono, H. High critical-current density with less anisotropy in $BaFe_2(As,P)_2$ epitaxial thin films: Effect of intentionally grown c-axis vortex-pinning centers. *Appl. Phys. Lett.* **2014,** *104*, 182603.
(96) Katase, T.; Iimura, S.; Hiramatsu, H.; Kamiya, T.; Hosono, H. Identical effects of indirect and direct electron doping of superconducting $BaFe_2As_2$ thin films. *Phys. Rev. B* **2012,** *85*, 140516.
(97) Ni, N.; Tillman, M. E.; Yan, J. Q.; Kracher, A.; Hannahs, S. T.; Bud'ko, S. L.; Canfield, P. C. Effects of Co substitution on thermodynamic and transport properties and anisotropic H_{c2} in $Ba(Fe_{1-x}Co_x)_2As_2$ single crystals. *Phys. Rev. B* **2008,** *78*, 214515.
(98) Liu, C.; Kondo, T.; Fernandes, R. M.; Palczewski, A. D.; Mun, E. D.; Ni, N.; Thaler, A. N.; Bostwick, A.; Rotenberg, E.; Schmalian, J.; Bud'ko, S. L.; Canfield, P. C.; Kaminski, A.

Evidence for a Lifshitz transition in electron-doped iron arsenic superconductors at the onset of superconductivity. *Nat. Phys.* **2010,** *6*, 419.
(99) Hsu, F. C.; Luo, J. Y.; Yeh, K. W.; Chen, T. K.; Huang, T. W.; Wu, P. M.; Lee, Y. C.; Huang, Y. L.; Chu, Y. Y.; Yan, D. C.; Wu, M. K. Superconductivity in the PbO-type structure alpha-FeSe. *Proc. Natl. Acad. Sci. USA* **2008,** *105*, 14262-14264.
(100) Terzieff, P.; Komarek, K. L. The paramagnetic properties of iron selenides with NiAs-type structure. *Monats. Chem.* **1978,** *109*, 651-659.
(101) Schuster, W.; Mikler, H.; Komarek, K. L. Transition metal-chalcogen systems, VII.: The iron-selenium phase diagram. *Monats. Chem.* **1979,** *110*, 1153-1170.
(102) Mizuguchi, Y.; Takano, Y. Review of Fe Chalcogenides as the Simplest Fe-Based Superconductor. *J. Phys. Soc. Jpn.* **2010,** *79*, 102001.
(103) Yeh, K.-W.; Huang, T.-W.; Huang, Y.-l.; Chen, T.-K.; Hsu, F.-C.; Wu, P. M.; Lee, Y.-C.; Chu, Y.-Y.; Chen, C.-L.; Luo, J.-Y.; Yan, D.-C.; Wu, M.-K. Tellurium Substitution Effect on Superconductivity of the α-phase Iron Selenide. *EPL* **2008,** *84*, 37002.
(104) Horigane, K.; Hiraka, H.; Ohoyama, K. Relationship between Structure and Superconductivity in $FeSe_{1-x}Te_x$. *J. Phys. Soc. Jpn.* **2009,** *78*, 074718.
(105) McQueen, T. M.; Huang, Q.; Ksenofontov, V.; Felser, C.; Xu, Q.; Zandbergen, H.; Hor, Y. S.; Allred, J.; Williams, A. J.; Qu, D.; Checkelsky, J.; Ong, N. P.; Cava, R. J. Extreme Sensitivity of Superconductivity to Stoichiometry in $Fe_{1+\delta}Se$. *Phys. Rev. B* **2009,** *79*, 014522.
(106) Fang, M. H.; Pham, H. M.; Qian, B.; Liu, T. J.; Vehstedt, E. K.; Liu, Y.; Spinu, L.; Mao, Z. Q. Superconductivity close to magnetic instability in$Fe(Se_{1-x}Te_x)_{0.82}$. *Phys. Rev. B* **2008,** *78*, 224503.
(107) Sales, B. C.; Sefat, A. S.; McGuire, M. A.; Jin, R. Y.; Mandrus, D.; Mozharivskyj, Y. Bulk superconductivity at 14 K in single crystals of $Fe_{1+y}Te_xSe_{1-x}$. *Phys. Rev. B* **2009,** *79*, 094521.
(108) Mizuguchi, Y.; Tomioka, F.; Tsuda, S.; Yamaguchi, T.; Takano, Y. Superconductivity in S-substituted FeTe. *Appl. Phys. Lett.* **2009,** *94*, 012503.
(109) Liu, T. J.; Hu, J.; Qian, B.; Fobes, D.; Mao, Z. Q.; Bao, W.; Reehuis, M.; Kimber, S. A. J.; Prokeš, K.; Matas, S.; Argyriou, D. N.; Hiess, A.; Rotaru, A.; Pham, H.; Spinu, L.; Qiu, Y.; Thampy, V.; Savici, A. T.; Rodriguez, J. A.; Broholm, C. From (π,0) magnetic order to superconductivity with (π,π) magnetic resonance in $Fe_{1.02}Te_{1-x}Se_x$. *Nat. Mater.* **2010,** *9*, 718.
(110) Margadonna, S.; Takabayashi, Y.; Ohishi, Y.; Mizuguchi, Y.; Takano, Y.; Kagayama, T.; Nakagawa, T.; Takata, M.; Prassides, K. Pressure Evolution of the Low-temperature Crystal Structure and Bonding of the Superconductor FeSe (T_c = 37 K). *Phys. Rev. B* **2009,** *80*, 064506.
(111) Imai, T.; Ahilan, K.; Ning, F. L.; McQueen, T. M.; Cava, R. J. Why Does Undoped FeSe Become a High-T_c Superconductor under Pressure? *Phys. Rev. Lett.* **2009,** *102*, 177005.
(112) Medvedev, S.; McQueen, T. M.; Troyan, I. A.; Palasyuk, T.; Eremets, M. I.; Cava, R. J.; Naghavi, S.; Casper, F.; Ksenofontov, V.; Wortmann, G.; Felser, C. Electronic and Magnetic Phase Diagram of beta-$Fe_{1.01}Se$ with Superconductivity at 36.7 K Under Pressure. *Nat. Mater.* **2009,** *8*, 630-633.
(113) Mizuguchi, Y.; Tomioka, F.; Tsuda, S.; Yamaguchi, T.; Takano, Y. Superconductivity at 27K in Tetragonal FeSe Under High Pressure. *Appl. Phys. Lett.* **2008,** *93*, 152505.
(114) Garbarino, G.; Sow, A.; Lejay, P.; Sulpice, A.; Toulemonde, P.; Mezouar, M.; Núñez-Regueiro, M. High-temperature superconductivity (T_c onset at 34 K) in the high-pressure orthorhombic phase of FeSe. *EPL* **2009,** *86*, 27001.
(115) Gresty, N. C.; Takabayashi, Y.; Ganin, A. Y.; McDonald, M. T.; Claridge, J. B.; Giap, D.; Mizuguchi, Y.; Takano, Y.; Kagayama, T.; Ohishi, Y.; Takata, M.; Rosseinsky, M. J.; Margadonna, S.; Prassides, K. Structural Phase Transitions and Superconductivity in $Fe_{1+\delta}Se_{0.57}Te_{0.43}$ at Ambient and Elevated Pressures. *J. Am. Chem. Soc.* **2009,** *131*, 16944-16952.
(116) Horigane, K.; Takeshita, N.; Lee, C.-H.; Hiraka, H.; Yamada, K. First Investigation of Pressure Effects on Transition from Superconductive to Metallic Phase in $FeSe_{0.5}Te_{0.5}$. *J. Phys. Soc. Jpn.* **2009,** *78*, 063705.
(117) Mizuguchi, Y.; Tomioka, F.; Deguchi, K.; Tsuda, S.; Yamaguchi, T.; Takano, Y. Pressure effects on FeSe family superconductors. *Physica C* **2010,** *470*, S353-S355.
(118) Shimizu, Y.; Yamada, T.; Takami, T.; Niitaka, S.; Takagi, H.; Itoh, M. Pressure-Induced

Antiferromagnetic Fluctuations in the Pnictide Superconductor $FeSe_{0.5}Te_{0.5}$: ^{125}Te NMR Study. *J. Phys. Soc. Jpn.* **2009,** *78*, 123709.
(119) Zhang, C.; Yi, W.; Sun, L.; Chen, X.-J.; Hemley, R. J.; Mao, H.-k.; Lu, W.; Dong, X.; Bai, L.; Liu, J.; Moreira Dos Santos, A. F.; Molaison, J. J.; Tulk, C. A.; Chen, G.; Wang, N.; Zhao, Z. Pressure-induced lattice collapse in the tetragonal phase of single-crystalline $Fe_{1.05}Te$. *Phys. Rev. B* **2009,** *80*, 144519.
(120) Okada, H.; Takahashi, H.; Mizuguchi, Y.; Takano, Y.; Takahashi, H. Successive Phase Transitions under High Pressure in $FeTe_{0.92}$. *J. Phys. Soc. Jpn.* **2009,** *78*, 083709.
(121) Han, Y.; Li, W. Y.; Cao, L. X.; Wang, X. Y.; Xu, B.; Zhao, B. R.; Guo, Y. Q.; Yang, J. L. Superconductivity in iron telluride thin films under tensile stress. *Phys. Rev. Lett.* **2010,** *104*, 017003.
(122) Takemura, Y.; Suto, H.; Honda, N.; Kakuno, K.; Saito, K. Characterization of FeSe thin films prepared on GaAs substrate by selenization technique. *J. Appl. Phys* **1997,** *81*, 5177-5179.
(123) Han, Y.; Li, W. Y.; Cao, L. X.; Zhang, S.; Xu, B.; Zhao, B. R. Preparation and superconductivity of iron selenide thin films. *arXiv:0904.4731* **2009**.
(124) Wu, M. K.; Hsu, F. C.; Yeh, K. W.; Huang, T. W.; Luo, J. Y.; Wang, M. J.; Chang, H. H.; Chen, T. K.; Rao, S. M.; Mok, B. H.; Chen, C. L.; Huang, Y. L.; Ke, C. T.; Wu, P. M.; Chang, A. M.; Wu, C. T.; Perng, T. P. The development of the superconducting PbO-type β-FeSe and related compounds. *Physica C* **2009,** *469*, 340-349.
(125) Nie, Y. F.; Brahimi, E.; Budnick, J. I.; Hines, W. A.; Jain, M.; Wells, B. O. Suppression of superconductivity in FeSe films under tensile strain. *Appl. Phys. Lett.* **2009,** *94*, 242505.
(126) Chen, T.-K.; Luo, J.-Y.; Ke, C.-T.; Chang, H.-H.; Huang, T.-W.; Yeh, K.-W.; Chang, C.-C.; Hsu, P.-C.; Wu, C.-T.; Wang, M.-J.; Wu, M.-K. Low-temperature fabrication of superconducting FeSe thin films by pulsed laser deposition. *Thin Solid Films* **2010,** *519*, 1540-1545.
(127) Kumary, T. G.; Baisnab, D. K.; Janaki, J.; Mani, A.; Satya, A. T.; Sarguna, R. M.; Ajikumar, P. K.; Tyagi, A. K.; Bharathi, A. Superconducting $Fe_{1+\delta}Se_{1-x}Te_x$ thin films: growth, characterization and properties. *Supercond. Sci. Technol.* **2009,** *22*, 095018.
(128) Imai, Y.; Tanaka, R.; Akiike, T.; Hanawa, M.; Tsukada, I.; Maeda, A. Superconductivity of $FeSe_{0.5}Te_{0.5}$ Thin Films Grown by Pulsed Laser Deposition. *Jpn. J. Appl. Phys.* **2010,** *49*, 023101.
(129) Bellingeri, E.; Buzio, R.; Gerbi, A.; Marrè, D.; Congiu, S.; Cimberle, M. R.; Tropeano, M.; Siri, A. S.; Palenzona, A.; Ferdeghini, C. High quality epitaxial $FeSe_{0.5}Te_{0.5}$ thin films grown on $SrTiO_3$ substrates by pulsed laser deposition. *Supercond. Sci. Technol.* **2009,** *22*, 105007.
(130) Si, W.; Lin, Z.-W.; Jie, Q.; Yin, W.-G.; Zhou, J.; Gu, G.; Johnson, P. D.; Li, Q. Enhanced superconducting transition temperature in $FeSe_{0.5}Te_{0.5}$ thin films. *Appl. Phys. Lett.* **2009,** *95*, 052504.
(131) Bellingeri, E.; Pallecchi, I.; Buzio, R.; Gerbi, A.; Marrè, D.; Cimberle, M. R.; Tropeano, M.; Putti, M.; Palenzona, A.; Ferdeghini, C. T_c=21K in epitaxial $FeSe_{0.5}Te_{0.5}$ thin films with biaxial compressive strain. *Appl. Phys. Lett.* **2010,** *96*, 102512.
(132) Nabeshima, F.; Imai, Y.; Hanawa, M.; Tsukada, I.; Maeda, A. Enhancement of the Superconducting Transition Temperature in FeSe Epitaxial Thin Films by Anisotropic Compression. *Appl. Phys. Lett.* **2013,** *103*, 172602.
(133) Bellingeri, E.; Kawale, S.; Braccini, V.; Buzio, R.; Gerbi, A.; Martinelli, A.; Putti, M.; Pallecchi, I.; Balestrino, G.; Tebano, A.; Ferdeghini, C. Tuning of the superconducting properties of $FeSe_{0.5}Te_{0.5}$ thin films through the substrate effect. *Supercond. Sci. Technol.* **2012,** *25*, 084022.
(134) Imai, Y.; Akiike, T.; Hanawa, M.; Tsukada, I.; Ichinose, A.; Maeda, A.; Hikage, T.; Kawaguchi, T.; Ikuta, H. Systematic Comparison of Eight Substrates in the Growth of $FeSe_{0.5}Te_{0.5}$ Superconducting Thin Films. *Appl. Phys. Express* **2010,** *3*, 043102.
(135) Leng, X.; Garcia-Barriocanal, J.; Bose, S.; Lee, Y.; Goldman, A. M. Electrostatic Control of the Evolution from a Superconducting Phase to an Insulating Phase in Ultrathin $YBa_2Cu_3O_{7-x}$ Films. *Phys. Rev. Lett.* **2011,** *107*, 027001.
(136) Hebard, A. F.; Paalanen, M. A. Magnetic-field-tuned superconductor-insulator transition

in two-dimensional films. *Phys. Rev. Lett.* **1990,** *65*, 927-930.
(137) Schneider, R.; Zaitsev, A. G.; Fuchs, D.; v. Löhneysen, H. Superconducting and Insulating Phases of Disordered FeSe Thin Films. *Eur. Phys. J. B* **2015,** *88*, 14.
(138) Schneider, R.; Zaitsev, A. G.; Fuchs, D.; H, V. L. Superconductor-insulator Quantum Phase Transition in Disordered FeSe Thin Films. *Phys. Rev. Lett.* **2012,** *108*, 257003.
(139) Qiu, W.; Ma, Z.; Patel, D.; Sang, L.; Cai, C.; Shahriar Al Hossain, M.; Cheng, Z.; Wang, X.; Dou, S. X. The Interface Structure of FeSe Thin Film on CaF_2 Substrate and its Influence on the Superconducting Performance. *ACS Appl. Mater. Interfaces* **2017,** *9*, 37446-37453.
(140) Wang, Q. Y.; Zhang, W. H.; Zhang, Z. C.; Sun, Y.; Xing, Y.; Wang, Y. Y.; Wang, L. L.; Ma, X. C.; Xue, Q. K.; Wang, J. Thickness dependence of superconductivity and superconductor–insulator transition in ultrathin FeSe films on $SrTiO_3$ (001) substrate. *2D Mater.* **2015,** *2*, 044012.
(141) Shiogai, J.; Ito, Y.; Mitsuhashi, T.; Nojima, T.; Tsukazaki, A. Electric-field-induced superconductivity in electrochemically etched ultrathin FeSe films on $SrTiO_3$ and MgO. *Nat. Phys.* **2016,** *12*, 42-46.
(142) Shiogai, J.; Miyakawa, T.; Ito, Y.; Nojima, T.; Tsukazaki, A. Unified trend of superconducting transition temperature versus Hall coefficient for ultrathin FeSe films prepared on different oxide substrates. *Phys. Rev. B* **2017,** *95*, 115101.
(143) Kouno, S.; Sato, Y.; Katayama, Y.; Ichinose, A.; Asami, D.; Nabeshima, F.; Imai, Y.; Maeda, A.; Ueno, K. Superconductivity at 38 K in an electrochemical interface between ionic liquid and Fe($Se_{0.8}Te_{0.2}$) on various substrates. *arXiv:1805.02380* **2018**.
(144) Wang, Q.-Y.; Li, Z.; Zhang, W.-H.; Zhang, Z.-C.; Zhang, J.-S.; Li, W.; Ding, H.; Ou, Y.-B.; Deng, P.; Chang, K.; Wen, J.; Song, C.-L.; He, K.; Jia, J.-F.; Ji, S.-H.; Wang, Y.-Y.; Wang, L.-L.; Chen, X.; Ma, X.-C.; Xue, Q.-K. Interface-Induced High-Temperature Superconductivity in Single Unit-Cell FeSe Films on SrTiO3. *Chin. Phys. Lett.* **2012,** *29*, 037402.
(145) McQueen, T. M.; Williams, A. J.; Stephens, P. W.; Tao, J.; Zhu, Y.; Ksenofontov, V.; Casper, F.; Felser, C.; Cava, R. J. Tetragonal-to-Orthorhombic Structural Phase Transition at 90 K in the Superconductor $Fe_{1.01}Se$. *Phys. Rev. Lett.* **2009,** *103*, 057002.
(146) Huang, S. X.; Chien, C. L.; Thampy, V.; Broholm, C. Control of Tetrahedral Coordination and Superconductivity in $FeSe_{0.5}Te_{0.5}$ Thin Films. *Phys. Rev. Lett.* **2010,** *104*, 217002.
(147) Moon, C.-Y.; Choi, H. J. Chalcogen-Height Dependent Magnetic Interactions and Magnetic Order Switching in $FeSe_xTe_{1-x}$. *Phys. Rev. Lett.* **2010,** *104*, 057003.
(148) Speller, S. *Microstructural development and control in $Ti_2Ba_2CaCu_2O_8$, Materials Department report*; Oxford University, UK: 2004.
(149) Haindl, S.; Kidszun, M.; Oswald, S.; Hess, C.; Buchner, B.; Kolling, S.; Wilde, L.; Thersleff, T.; Yurchenko, V. V.; Jourdan, M.; Hiramatsu, H.; Hosono, H. Thin Film Growth of Fe-based Superconductors: from Fundamental Properties to Functional Devices. A Comparative Review. *Rep. Prog. Phys.* **2014,** *77*, 046502.
(150) Speller, S. C.; Aksoy, C.; Saydam, M.; Taylor, H.; Burnell, G.; Boothroyd, A. T.; Grovenor, C. R. M. Analysis of $Fe_ySe_{1-x}Te_x$ thin films grown by radio frequency sputtering. *Supercond. Sci. Technol.* **2011,** *24*, 075023.
(151) Imai, Y.; Nabeshima, F.; Maeda, A. Comparative Review on Thin Film Growth of Iron-Based Superconductors. *Condens. Matter* **2017,** *2*, 25.
(152) Zou, K.; Mandal, S.; Albright, S. D.; Peng, R.; Pu, Y.; Kumah, D.; Lau, C.; Simon, G. H.; Dagdeviren, O. E.; He, X.; Božović, I.; Schwarz, U. D.; Altman, E. I.; Feng, D.; Walker, F. J.; Ismail-Beigi, S.; Ahn, C. H. Role of double TiO_2 layers at the interface of FeSe/$SrTiO_3$ superconductors. *Phys. Rev. B* **2016,** *93*, 180506.
(153) Hanawa, M.; Ichinose, A.; Komiya, S.; Tsukada, I.; Imai, Y.; Maeda, A. Empirical Selection Rule of Substrate Materials for Iron Chalcogenide Superconducting Thin Films. *Jpn. J. Appl. Phys.* **2012,** *51*, 010104.
(154) Hanawa, M.; Ichinose, A.; Komiya, S.; Tsukada, I.; Akiike, T.; Imai, Y.; Hikage, T.; Kawaguchi, T.; Ikuta, H.; Maeda, A. Substrate Dependence of Structural and Transport Properties in $FeSe_{0.5}Te_{0.5}$ Thin Films. *Jpn. J. Appl. Phys.* **2011,** *50*, 053101.
(155) Tsukada, I.; Ichinose, A.; Nabeshima, F.; Imai, Y.; Maeda, A. Origin of Lattice

Compression of $FeSe_{1-x}Te_x$ Thin Films on CaF_2 Substrates. *AIP Adv.* **2016,** *6*, 095314.
(156) Ichinose, A.; Nabeshima, F.; Tsukada, I.; Hanawa, M.; Seiki, K.; Akiike, T.; Imai, Y.; Maeda, A. Microscopic Analysis of the Chemical Reaction Between Fe(Te, Se) Thin Films and Underlying CaF_2. *Supercond. Sci. Technol.* **2013,** *26*, 075002.
(157) Iida, K.; Hänisch, J.; Schulze, M.; Aswartham, S.; Wurmehl, S.; Büchner, B.; Schultz, L.; Holzapfel, B. Generic Fe buffer layers for Fe-based superconductors: Epitaxial $FeSe_{1-x}Te_x$ thin films. *Appl. Phys. Lett.* **2011,** *99*, 202503.
(158) Goyal, A.; Norton, D. P.; Budai, J. D.; Paranthaman, M.; Specht, E. D.; Kroeger, D. M.; Christen, D. K.; He, Q.; Saffian, B.; List, F. A.; Lee, D. F.; Martin, P. M.; Klabunde, C. E.; Hartfield, E.; Sikka, V. K. High critical current density superconducting tapes by epitaxial deposition of $YBa_2Cu_3O_x$ thick films on biaxially textured metals. *Appl. Phys. Lett.* **1996,** *69*, 1795-1797.
(159) Bhuiyan, M. S.; Paranthaman, M.; Sathyamurthy, S.; Aytug, T.; Kang, S.; Lee, D. F.; Goyal, A.; Payzant, E. A.; Salama, K. MOD approach for the growth of epitaxial CeO_2 buffer layers on biaxially textured Ni–W substrates for YBCO coated conductors. *Supercond. Sci. Technol.* **2003,** *16*, 1305.
(160) Si, W.; Han, S. J.; Shi, X.; Ehrlich, S. N.; Jaroszynski, J.; Goyal, A.; Li, Q. High current superconductivity in $FeSe_{0.5}Te_{0.5}$-coated conductors at 30 tesla. *Nat. Commun.* **2013,** *4*, 1347.
(161) Xu, Z.; Yuan, P.; Ma, Y.; Cai, C. High-performance $FeSe_{0.5}Te_{0.5}$ thin films fabricated on less-well-textured flexible coated conductor templates. *Supercond. Sci. Technol.* **2017,** *30*, 035003.
(162) Wang, W.; Liu, L.-F.; Yao, Y.-J.; Lu, S.-D.; Wu, X.; Zheng, T.; Liu, S.-F.; Li, Y.-J. Growth dynamics controllable deposition of homoepitaxial MgO films on the IBAD-MgO substrates. *Appl. Surf. Sci.* **2018,** *435*, 225-228.
(163) Lu, R.; Wu, J. Z.; Varanasi, C.; Burke, J.; Maartense, I.; Barnes, P. N. Textured Ion-Beam Assisted Deposition: Mg Oxide Template on Non-Metallic Flexible Ceraflex for Epitaxial Growth of Perovskite Films. *J. Electron. Mater.* **2007,** *36*, 1258-1264.
(164) Molatta, S.; Haindl, S.; Trommler, S.; Schulze, M.; Wurmehl, S.; Hühne, R. Interface control by homoepitaxial growth in pulsed laser deposited iron chalcogenide thin films. *Sci. Rep.* **2015,** *5*, 16334.
(165) Eisterer, M.; Raunicher, R.; Weber, H. W.; Bellingeri, E.; Cimberle, M. R.; Pallecchi, I.; Putti, M.; Ferdeghini, C. Anisotropic critical currents in $FeSe_{0.5}Te_{0.5}$ films and the influence of neutron irradiation. *Supercond. Sci. Technol.* **2011,** *24*, 065016.
(166) Mele, P.; Matsumoto, K.; Haruyama, Y.; Mukaida, M.; Yoshida, Y.; Ichino, Y.; Kiss, T.; Ichinose, A. In-field characterization of $FeTe_{0.8}S_{0.2}$ epitaxial thin films with enhanced superconducting properties. *Supercond. Sci. Technol.* **2010,** *23*, 052001.
(167) Iida, K.; Hänisch, J.; Reich, E.; Kurth, F.; Hühne, R.; Schultz, L.; Holzapfel, B.; Ichinose, A.; Hanawa, M.; Tsukada, I.; Schulze, M.; Aswartham, S.; Wurmehl, S.; Büchner, B. Intrinsic pinning and the critical current scaling of clean epitaxial Fe(Se,Te) thin films. *Phys. Rev. B* **2013,** *87*, 104510.
(168) Braccini, V.; Kawale, S.; Reich, E.; Bellingeri, E.; Pellegrino, L.; Sala, A.; Putti, M.; Higashikawa, K.; Kiss, T.; Holzapfel, B.; Ferdeghini, C. Highly Effective and Isotropic Pinning in Epitaxial Fe(Se,Te) Thin Films Grown on CaF_2 Substrates. *Appl. Phys. Lett.* **2013,** *103*, 172601.
(169) Bugoslavsky, Y.; Cohen, L. F.; Perkins, G. K.; Polichetti, M.; Tate, T. J.; Gwilliam, R.; Caplin, A. D. Enhancement of the high-magnetic-field critical current density of superconducting MgB_2 by proton irradiation. *Nature* **2001,** *411*, 561.
(170) Jia, Y.; LeRoux, M.; Miller, D. J.; Wen, J. G.; Kwok, W. K.; Welp, U.; Rupich, M. W.; Li, X.; Sathyamurthy, S.; Fleshler, S.; Malozemoff, A. P.; Kayani, A.; Ayala-Valenzuela, O.; Civale, L. Doubling the critical current density of high temperature superconducting coated conductors through proton irradiation. *Appl. Phys. Lett.* **2013,** *103*, 122601.
(171) Taen, T.; Ohtake, F.; Pyon, S.; Tamegai, T.; Kitamura, H. Critical current density and vortex dynamics in pristine and proton-irradiated $Ba_{0.6}K_{0.4}Fe_2As_2$. *Supercond. Sci. Technol.* **2015,** *28*, 085003.
(172) Fang, L.; Jia, Y.; Schlueter, J. A.; Kayani, A.; Xiao, Z. L.; Claus, H.; Welp, U.; Koshelev,

A. E.; Crabtree, G. W.; Kwok, W. K. Doping- and irradiation-controlled pinning of vortices in $BaFe_2(As_{1-x}P_x)_2$ single crystals. *Phys. Rev. B* **2011,** *84*, 140504.
(173) Nakajima, Y.; Taen, T.; Tsuchiya, Y.; Tamegai, T.; Kitamura, H.; Murakami, T. Suppression of the critical temperature of superconducting $Ba(Fe_{1-x}Co_x)_2As_2$ by point defects from proton irradiation. *Phys. Rev. B* **2010,** *82*, 220504.
(174) Ozaki, T.; Wu, L.; Zhang, C.; Jaroszynski, J.; Si, W.; Zhou, J.; Zhu, Y.; Li, Q. A route for a strong increase of critical current in nanostrained iron-based superconductors. *Nat. Commun.* **2016,** *7*, 13036.
(175) Ozaki, T.; Wu, L.; Zhang, C.; Si, W.; Jie, Q.; Li, Q. Enhanced critical current in superconducting $FeSe_{0.5}Te_{0.5}$ films at all magnetic field orientations by scalable gold ion irradiation. *Supercond. Sci. Technol.* **2018,** *31*, 024002.
(176) Zhang, L.; Singh, D. J.; Du, M. H. Density functional study of excess Fe in $Fe_{1+x}Te$: Magnetism and doping. *Phys. Rev. B* **2009,** *79*, 012506.
(177) Chen, G. F.; Chen, Z. G.; Dong, J.; Hu, W. Z.; Li, G.; Zhang, X. D.; Zheng, P.; Luo, J. L.; Wang, N. L. Electronic properties of single-crystalline $Fe_{1.05}Te$ and $Fe_{1.03}Se_{0.30}Te_{0.70}$. *Phys. Rev. B* **2009,** *79*, 140509.
(178) Mizuguchi, Y.; Tomioka, F.; Tsuda, S.; Yamaguchi, T.; Takano, Y. FeTe as a candidate material for new iron-based superconductor. *Physica C* **2009,** *469*, 1027-1029.
(179) Monni, M.; Bernardini, F.; Profeta, G.; Massidda, S. Theoretical investigation of FeTe magnetic ordering under hydrostatic pressure. *Phys. Rev. B* **2013,** *87*, 094516.
(180) Tsukada, I.; Hanawa, M.; Komiya, S.; Ichinose, A.; Akiike, T.; Imai, Y.; Maeda, A. Mobility Analysis of FeTe Thin Films. *J. Phys. Soc. Jpn.* **2011,** *80*, 023712.
(181) Si, W.; Jie, Q.; Wu, L.; Zhou, J.; Gu, G.; Johnson, P. D.; Li, Q. Superconductivity in epitaxial thin films of $Fe_{1.08}Te{:}O_x$. *Phys. Rev. B* **2010,** *81*, 092506.
(182) Narangammana, L. K.; Liu, X.; Nie, Y. F.; Rueckert, F. J.; Budnick, J. I.; Hines, W. A.; Gu, G.; Wells, B. O. Low temperature crystal structure and large lattice discontinuity at T_c in superconducting $FeTeO_x$ films. *Appl. Phys. Lett.* **2013,** *103*, 102604.
(183) Nie, Y. F.; Telesca, D.; Budnick, J. I.; Sinkovic, B.; Wells, B. O. Superconductivity induced in iron telluride films by low-temperature oxygen incorporation. *Phys. Rev. B* **2010,** *82*, 020508.
(184) Tsukada, I.; Hanawa, M.; Komiya, S.; Akiike, T.; Tanaka, R.; Imai, Y.; Maeda, A. Hall effect in superconducting $Fe(Se_{0.5}Te_{0.5})$ thin films. *Phys. Rev. B* **2010,** *81*, 054515.
(185) Tinkham, M. *Introduction to Superconductivity*, 2nd ed.; McGraw-Hill: New York, 1996.
(186) Zhang, W.; Sun, Y.; Zhang, J.; Li, F.; Guo, M.; Zhao, Y.; Zhang, H.; Peng, J.; Xing, Y.; Wang, H.; Fujita, T.; Hirata, A.; Li, Z.; Ding, H.; Tang, C.; Wang, M.; Wang, Q.; He, K.; Ji, S.; Chen, X.; Wang, J.; Xia, Z.; Li, L.; Wang, Y.; Wang, J.; Wang, L.; Chen, M.; Xue, Q.-K.; Ma, X. Direct Observation of High-Temperature Superconductivity in One-Unit-Cell FeSe Films. *Chin. Phys. Lett.* **2014,** *31*, 017401.
(187) Ma, F.; Ji, W.; Hu, J.; Lu, Z.-Y.; Xiang, T. First-Principles Calculations of the Electronic Structure of Tetragonal α-FeTe and α-FeSe Crystals: Evidence for a Bicollinear Antiferromagnetic Order. *Phys. Rev. Lett.* **2009,** *102*, 177003.
(188) Liu, X.; Liu, D.; Zhang, W.; He, J.; Zhao, L.; He, S.; Mou, D.; Li, F.; Tang, C.; Li, Z.; Wang, L.; Peng, Y.; Liu, Y.; Chen, C.; Yu, L.; Liu, G.; Dong, X.; Zhang, J.; Chen, C.; Xu, Z.; Chen, X.; Ma, X.; Xue, Q.; Zhou, X. J. Dichotomy of the electronic structure and superconductivity between single-layer and double-layer $FeSe/SrTiO_3$ films. *Nat. Commun.* **2014,** *5*, 5047.
(189) Liu, D.; Zhang, W.; Mou, D.; He, J.; Ou, Y.-B.; Wang, Q.-Y.; Li, Z.; Wang, L.; Zhao, L.; He, S.; Peng, Y.; Liu, X.; Chen, C.; Yu, L.; Liu, G.; Dong, X.; Zhang, J.; Chen, C.; Xu, Z.; Hu, J.; Chen, X.; Ma, X.; Xue, Q.; Zhou, X. J. Electronic Origin of High-temperature Superconductivity in Single-layer FeSe Superconductor. *Nat. Commun.* **2012,** *3*, 931.
(190) He, S.; He, J.; Zhang, W.; Zhao, L.; Liu, D.; Liu, X.; Mou, D.; Ou, Y.-B.; Wang, Q.-Y.; Li, Z.; Wang, L.; Peng, Y.; Liu, Y.; Chen, C.; Yu, L.; Liu, G.; Dong, X.; Zhang, J.; Chen, C.; Xu, Z.; Chen, X.; Ma, X.; Xue, Q.; Zhou, X. J. Phase diagram and electronic indication of high-temperature superconductivity at 65 K in single-layer FeSe films. *Nat. Mater.* **2013,** *12*, 605-610.
(191) He, J.; Liu, X.; Zhang, W.; Zhao, L.; Liu, D.; He, S.; Mou, D.; Li, F.; Tang, C.; Li, Z.;

Wang, L.; Peng, Y.; Liu, Y.; Chen, C.; Yu, L.; Liu, G.; Dong, X.; Zhang, J.; Chen, C.; Xu, Z.; Chen, X.; Ma, X.; Xue, Q.; Zhou, X. J. Electronic evidence of an insulator–superconductor crossover in single-layer FeSe/SrTiO3 films. *Proc. Natl. Acad. Sci. U.S.A.* **2014,** *111*, 18501-18506.
(192) Lee, J. J.; Schmitt, F. T.; Moore, R. G.; Johnston, S.; Cui, Y. T.; Li, W.; Yi, M.; Liu, Z. K.; Hashimoto, M.; Zhang, Y.; Lu, D. H.; Devereaux, T. P.; Lee, D. H.; Shen, Z. X. Interfacial mode coupling as the origin of the enhancement of Tc in FeSe films on $SrTiO_3$. *Nature* **2014,** *515*, 245.
(193) Peng, R.; Shen, X. P.; Xie, X.; Xu, H. C.; Tan, S. Y.; Xia, M.; Zhang, T.; Cao, H. Y.; Gong, X. G.; Hu, J. P.; Xie, B. P.; Feng, D. L. Measurement of an Enhanced Superconducting Phase and a Pronounced Anisotropy of the Energy Gap of a Strained FeSe Single Layer in FeSe/Nb: $SrTiO_3$/$KTaO_3$ Heterostructures Using Photoemission Spectroscopy. *Phys. Rev. Lett.* **2014,** *112*, 107001.
(194) Shen, B.; Feng, Z.-P.; Huang, J.-W.; Hu, Y.; Gao, Q.; Li, C.; Yu, X.; Liu, G.-D.; Yu, L.; Zhao, L.; Jin, K.; Zhou, X. J. Electronic structure and nematic phase transition in superconducting multiple-layer FeSe films grown by pulsed laser deposition method. *Chin. Phys. B* **2017,** *26*, 077402.
(195) Tan, S.; Zhang, Y.; Xia, M.; Ye, Z.; Chen, F.; Xie, X.; Peng, R.; Xu, D.; Fan, Q.; Xu, H.; Jiang, J.; Zhang, T.; Lai, X.; Xiang, T.; Hu, J.; Xie, B.; Feng, D. Interface-induced Superconductivity and Strain-dependent Spin Density Waves in FeSe/$SrTiO_3$ Thin Films. *Nat. Mater.* **2013,** *12*, 634-640.
(196) Qian, T.; Wang, X. P.; Jin, W. C.; Zhang, P.; Richard, P.; Xu, G.; Dai, X.; Fang, Z.; Guo, J. G.; Chen, X. L.; Ding, H. Absence of a Holelike Fermi Surface for the Iron-Based K0.8Fe1.7Se2 Superconductor Revealed by Angle-Resolved Photoemission Spectroscopy. *Phys. Rev. Lett.* **2011,** *106*, 187001.
(197) Ding, H.; Richard, P.; Nakayama, K.; Sugawara, K.; Arakane, T.; Sekiba, Y.; Takayama, A.; Souma, S.; Sato, T.; Takahashi, T.; Wang, Z.; Dai, X.; Fang, Z.; Chen, G. F.; Luo, J. L.; Wang, N. L. Observation of Fermi-surface–dependent nodeless superconducting gaps in $Ba_{0.6}K_{0.4}Fe_2As_2$. *EPL* **2008,** *83*, 47001.
(198) Nakayama, K.; Miyata, Y.; Phan, G. N.; Sato, T.; Tanabe, Y.; Urata, T.; Tanigaki, K.; Takahashi, T. Reconstruction of Band Structure Induced by Electronic Nematicity in an FeSe Superconductor. *Phys. Rev. Lett.* **2014,** *113*, 237001.
(199) Maletz, J.; Zabolotnyy, V. B.; Evtushinsky, D. V.; Thirupathaiah, S.; Wolter, A. U. B.; Harnagea, L.; Yaresko, A. N.; Vasiliev, A. N.; Chareev, D. A.; Böhmer, A. E.; Hardy, F.; Wolf, T.; Meingast, C.; Rienks, E. D. L.; Büchner, B.; Borisenko, S. V. Unusual band renormalization in the simplest iron-based superconductor $FeSe_{1-x}$. *Phys. Rev. B* **2014,** *89*, 220506.
(200) Seo, J. J.; Kim, B. Y.; Kim, B. S.; Jeong, J. K.; Ok, J. M.; Kim, J. S.; Denlinger, J. D.; Mo, S. K.; Kim, C.; Kim, Y. K. Superconductivity below 20 K in heavily electron-doped surface layer of FeSe bulk crystal. *Nat. Commun.* **2016,** *7*, 11116.
(201) Rebec, S. N.; Jia, T.; Zhang, C.; Hashimoto, M.; Lu, D. H.; Moore, R. G.; Shen, Z. X. Coexistence of Replica Bands and Superconductivity in FeSe Monolayer Films. *Phys. Rev. Lett.* **2017,** *118*, 067002.
(202) Peng, R.; Xu, H. C.; Tan, S. Y.; Cao, H. Y.; Xia, M.; Shen, X. P.; Huang, Z. C.; Wen, C. H. P.; Song, Q.; Zhang, T.; Xie, B. P.; Gong, X. G.; Feng, D. L. Tuning the Band Structure and Superconductivity in Single-layer FeSe by Interface Engineering. *Nat. Commun.* **2014,** *5*, 5044.
(203) Huang, Z. C.; Pu, Y. J.; Xu, H. C.; Xu, D. F.; Song, Q.; Lou, X.; Wen, C. H. P.; Peng, R.; Feng, D. L. Electronic structure and superconductivity of single-layer FeSe on Nb:$SrTi_3$/$LaAlO_3$ with varied tensile strain. *2D Mater.* **2016,** *3*, 014005.
(204) Wang, Z.; Liu, C.; Liu, Y.; Wang, J. High-temperature superconductivity in one-unit-cell FeSe films. *J. Phys.: Condens. Matter* **2017,** *29*, 153001.
(205) Ding, H.; Lv, Y.-F.; Zhao, K.; Wang, W.-L.; Wang, L.; Song, C.-L.; Chen, X.; Ma, X.-C.; Xue, Q.-K. High-Temperature Superconductivity in Single-Unit-Cell FeSe Films on Anatase TiO_2 (001). *Phys. Rev. Lett.* **2016,** *117*, 067001.
(206) Bardeen, J.; Cooper, L. N.; Schrieffer, J. R. Theory of superconductivity. *Phys. Rev.* **1957,** *108*, 1175-1204.

(207) Zhang, W.; Li, Z.; Li, F.; Zhang, H.; Peng, J.; Tang, C.; Wang, Q.; He, K.; Chen, X.; Wang, L.; Ma, X.; Xue, Q.-K. Interface Charge Doping Effects on Superconductivity of Single-unit-cell FeSe Films on $SrTiO_3$ Substrates. *Phys. Rev. B* **2014,** *89*, 060506(R).
(208) Miyata, Y.; Nakayama, K.; Sugawara, K.; Sato, T.; Takahashi, T. High-temperature Superconductivity in Potassium-coated Multilayer FeSe Thin Films. *Nat. Mater.* **2015,** *14*, 775-779.
(209) Tang, C.; Zhang, D.; Zang, Y.; Liu, C.; Zhou, G.; Li, Z.; Zheng, C.; Hu, X.; Song, C.; Ji, S.; He, K.; Chen, X.; Wang, L.; Ma, X.; Xue, Q.-K. Superconductivity Dichotomy in K-coated Single and Double Unit Cell FeSe Films on $SrTiO_3$. *Phys. Rev. B* **2015,** *92*, 180507.
(210) Wen, C. H. P.; Xu, H. C.; Chen, C.; Huang, Z. C.; Lou, X.; Pu, Y. J.; Song, Q.; Xie, B. P.; Abdel-Hafiez, M.; Chareev, D. A.; Vasiliev, A. N.; Peng, R.; Feng, D. L. Anomalous Correlation Effects and Unique Phase Diagram of Electron-doped FeSe Revealed by Photoemission Spectroscopy. *Nat. Commun.* **2016,** *7*, 10840.
(211) Song, C.; Zhang, H.; Zhong, Y.; Hu, X.; Ji, S.; Wang, L.; He, K.; Ma, X.; Xue, Q.-K. Observation of Double-Dome Superconductivity in Potassium-Doped FeSe Thin Films. *Phys. Rev. Lett.* **2016,** *116*, 157001.
(212) Tang, C.; Liu, C.; Zhou, G.; Li, F.; Ding, H.; Li, Z.; Zhang, D.; Li, Z.; Song, C.; Ji, S.; He, K.; Wang, L.; Ma, X.; Xue, Q.-K. Interface-enhanced Electron-phonon Coupling and High-temperature Superconductivity in Potassium-coated Ultrathin FeSe Films on $SrTiO_3$. *Phys. Rev. B* **2016,** *93*, 020507.
(213) Zhang, W. H.; Liu, X.; Wen, C. H. P.; Peng, R.; Tan, S. Y.; Xie, B. P.; Zhang, T.; Feng, D. L. Effects of Surface Electron Doping and Substrate on the Superconductivity of Epitaxial FeSe Films. *Nano Lett.* **2016,** *16*, 1969-1973.
(214) Hanzawa, K.; Sato, H.; Hiramatsu, H.; Kamiya, T.; Hosono, H. Electric Field-induced Superconducting Transition of Insulating FeSe Thin Film at 35 K. *Proc. Natl. Acad. Sci. U.S.A.* **2016,** *113*, 3986-3990.
(215) Lei, B.; Cui, J. H.; Xiang, Z. J.; Shang, C.; Wang, N. Z.; Ye, G. J.; Luo, X. G.; Wu, T.; Sun, Z.; Chen, X. H. Evolution of High-Temperature Superconductivity from a Low-T_c Phase Tuned by Carrier Concentration in FeSe Thin Flakes. *Phys. Rev. Lett.* **2016,** *116*, 077002.
(216) Lifshitz, I. M. Anomalies of Electron Characteristics of a Metal in the High Pressure Region. *JETP* **1960,** *11*, 1130.
(217) Lee, D.-H. What makes the T_c of FeSe/$SrTiO_3$ so high? *Chin. Phys. B* **2015,** *24*, 117405.
(218) Li, B.; Xing, Z. W.; Huang, G. Q.; Xing, D. Y. Electron-phonon coupling enhanced by the FeSe/$SrTiO_3$ interface. *J. Appl. Phys.* **2014,** *115*, 193907.
(219) Tian, Y. C.; Zhang, W. H.; Li, F. S.; Wu, Y. L.; Wu, Q.; Sun, F.; Zhou, G. Y.; Wang, L.; Ma, X.; Xue, Q.-K.; Zhao, J. Ultrafast Dynamics Evidence of High Temperature Superconductivity in Single Unit Cell FeSe on $SrTiO_3$. *Phys. Rev. Lett.* **2016,** *116*, 107001.
(220) Zhang, S.; Guan, J.; Jia, X.; Liu, B.; Wang, W.; Li, F.; Wang, L.; Ma, X.; Xue, Q.; Zhang, J.; Plummer, E. W.; Zhu, X.; Guo, J. Role of $SrTiO_3$ phonon penetrating into thin FeSe films in the enhancement of superconductivity. *Phys. Rev. B* **2016,** *94*, 081116.
(221) Li, F.; Ding, H.; Tang, C.; Peng, J.; Zhang, Q.; Zhang, W.; Zhou, G.; Zhang, D.; Song, C.-L.; He, K.; Ji, S.; Chen, X.; Gu, L.; Wang, L.; Ma, X.-C.; Xue, Q.-K. Interface-enhanced high-temperature superconductivity in single-unit-cell $FeTe_{1-x}Se_x$ films on $SrTiO_3$. *Phys. Rev. B* **2015,** *91*, 220503.

Chapter 3

3 Experimental Procedures

In this work, pulsed laser deposition (PLD) was used as the primary sample fabrication method. PLD is a physical vapour deposition (PVD) technique for thin film growth. During the whole period of the experiment, a polycrystalline target as the material source was prepared by a standard two-step solid-phase reaction method prior to the deposition process, and various types of substrates (commercially available) can be used as growth surfaces for the film material. The detailed fabrication procedures are listed in this section, including the synthesis of target materials and the parameters of PLD deposition. After sample preparation, a variety of follow-up measurements are carried out to characterize the performance and properties of the as-grown samples. The characterizations involve the analysis of superconducting performance, macroscopic/microscopic crystal structures, chemical compositions, electrical/magnetic properties, etc. The acquired data are supposed to scientifically explain the experimental phenomena and support our discussion on the possible mechanism.

3.1 Fabrication Methods

3.1.1 Synthesis of Polycrystalline Targets

All the $FeSe_{1-x}Te_x$ targets involved in this thesis work were home-made polycrystalline pellets fabricated by a standard two-step solid-phase reaction method. The precursory powders were purchased from commercial suppliers, including Fe powder (Alfa Aesar, -200 mesh, 99+ %), Se powder (Aldrich, -100 mesh, 99.99 %), and Te powder (Aldrich, -200 mesh, 99.8 %). The fabrication process of a nominal $FeSe_{0.93}$ target pellet will be described in detail as an example.

The precursors (Fe and Se powders) were separately weighed (nominal molar ratio of Fe: Se = 1: 0.93) and poured into a ceramic mortar. The entire assembly was then transferred into a glove box filled with an argon atmosphere. Inside the glove box, the powder materials were fully ground for 30 minutes. The fully-mixed powder was immediately pressed into a disc ($\Phi \approx 12.7$ mm, thickness ≈ 5 mm) and sealed in a evacuated quartz tube by using an oxyacetylene flame. Then, the sealed quartz tube was

pushed into a tube furnace for the first-stage heat treatment (650 ℃ for 48 hours, ramp rate 5 ℃/min, furnace cooling) to allow the complete reaction of Fe and Se powders. Afterwards, the resultant bulk was taken out of the quartz tube, reground, and pressed again into a disc. The pellet was placed in a tube furnace with a constant argon flow for the second-stage heat treatment (400 ℃ for 15 hours, ramp rate of 5 ℃/min, furnace cooling). The second-stage sintering effectively improved the mechanical strength and crystallization of the bulk crystal. A schematic illustration is presented in Fig. 3-1.

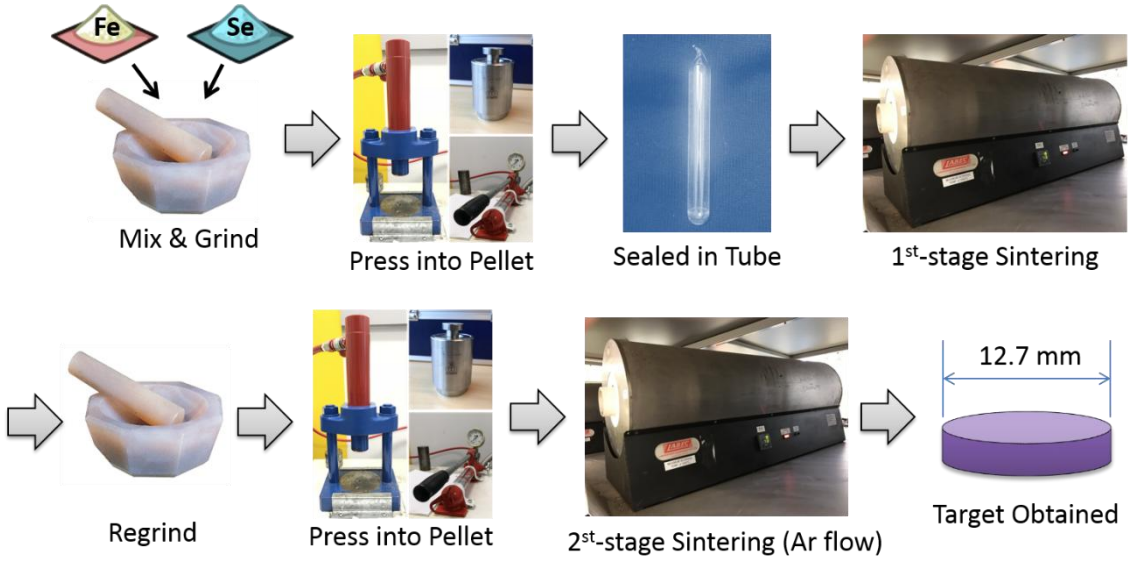

Figure 3-1. Schematic illustration of the fabrication process for a polycrystalline FeSe target.

3.1.2 Pulsed Laser Deposition (PLD) for Thin Film Preparation

PLD is a PVD technique widely used for depositing high-quality thin film samples[1], such as metals, semiconductors, ceramics, oxides, etc. An excimer laser source for melting the raw materials is the most outstanding feature of the PLD technique. A basic demonstration is depicted in Fig. 3-2 to provide a basic idea of how the laser works in a PLD system. First of all, the high-energy laser beam enters into the chamber and strikes the target. Due to the extremely high energy density on the laser spot, materials on the target surface are melted and vaporized within a finite volume, inducing a plasma plume, which encloses the ions, electrons, molecules, and clusters bombarded from the target materials. Actually, the real interaction between the laser and target is a non-equilibrium process. Once the target absorbs the incident laser light, the energy is first transformed into electron excitation energy, then heat is produced to induce chemical reaction energy, and mechanical energy is finally obtained. The

complex process successively results in the evaporation and melting of the target materials, and the formation and exfoliation of plasma plumes. As a result, the thin film is eventually formed at the growth temperature. The final nuclear growth and crystallization of the thin film are realized by the heat-treatment function supplied on the sample holder. One of the advantages of PLD is its ability to grow materials with an extremely high melting point or thermodynamically unstable structures. The non-equilibrium property of the plasma plume enables several degrees of freedom during film growth, so that the quality of the film can be further improved via the optimization of deposition conditions, such as the substrate temperature, the pressure of the atmosphere, etc.

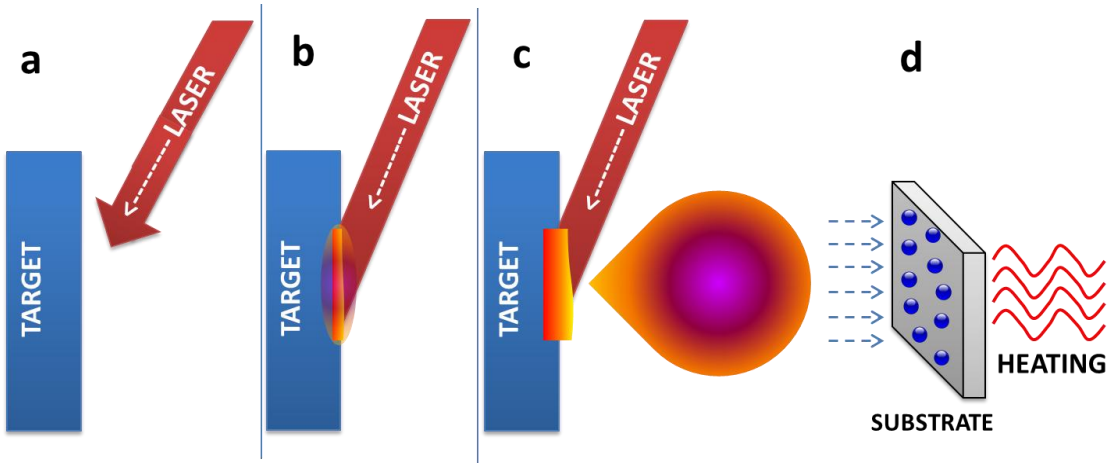

Figure 3-2. Schematic diagram showing laser ablation in a PLD system. (a) Laser enters the chamber. (b) Laser hits the target. Some materials start melting and evaporating. (c) Bombarded target materials give rise to a plasma plume. (d) Thin film sample is formed on the substrate. The heating function is available for final nuclear growth and crystallization.

Five years after the first realization of laser generation, Smith and Turner deposited the first thin film by employing a ruby laser[2] in 1965. The most significant breakthrough in the history of PLD application was the successful growth[3] of YBCO superconducting thin film which contains multi-cations with different evaporation properties. Nowadays, PLD has been developed as a modern fabrication method, even for industrial production requirements. As shown in Fig. 3-3, a standard PLD system consists of three major parts: the laser and optical system, the vacuum section, and the main chamber. The laser and optical system determines the type of laser wavelength and the ultimate energy density of the laser that hits the target material. By adjusting the light path, the spot size and spot location on the target can be changed as required. The vacuum section generally refers to the evacuation system combined with a low-vacuum

backing pump (usually a mechanical pump), a high-vacuum pump (usually a molecular pump), and the corresponding valves and gas lines. The pressure and atmosphere can be freely controlled for any desired deposition rate. The main chamber is a confined space where the deposition process takes place. Both the target and substrate holder are in-plane rotatable for better homogeneity and quality of thin film samples. Furthermore, additional accessories can also be attached for additional purposes. For example, an assistant Kaufmann ion source near the sample holder is helpful to improve the surface quality of the growth substrate, the *in-situ* reflection high-energy electron diffraction (RHEED) provides microstructural information about the top few atomic layers of the thin film sample, etc.

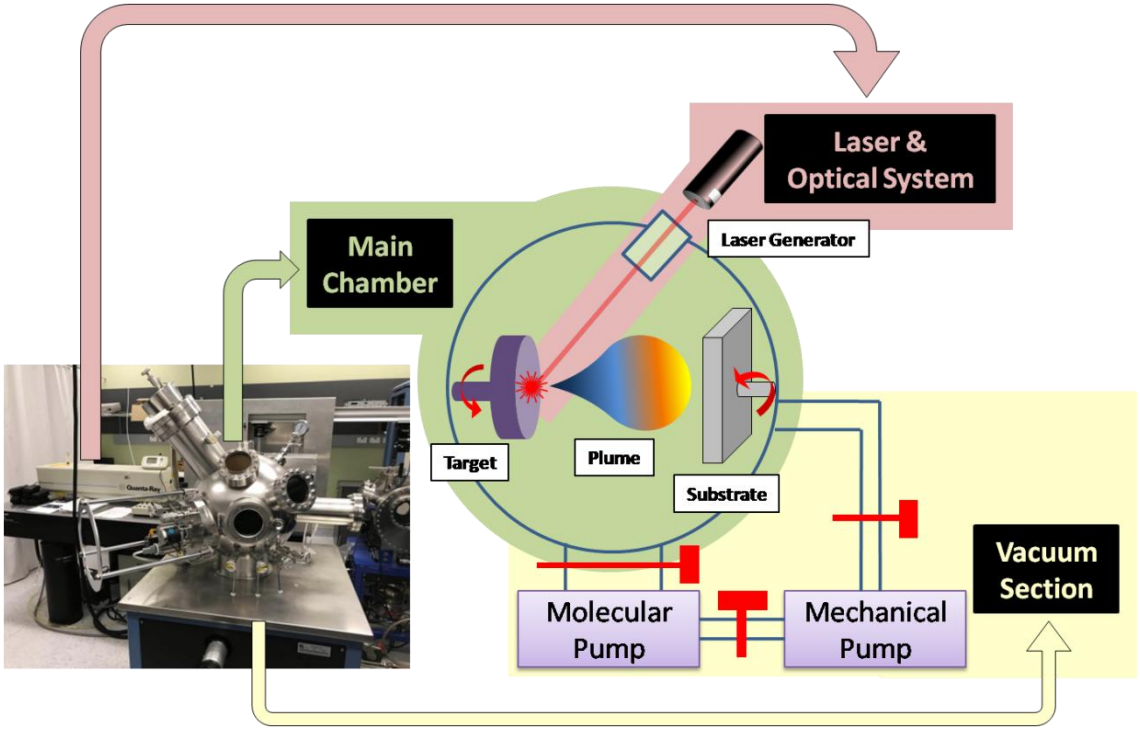

Figure 3-3. Schematic illustration of a typical PLD system. The PLD-450 system used in this thesis work is shown on left.

In this thesis work, a **neodymium**-doped yttrium aluminum garnet (Nd:YAG) laser (Quanta-Ray®, 355 nm, 10 Hz) was used as the laser source. The output power of the laser beam was set at 200 mJ per pulse (2.0 W). The main chamber (PLD-450) and corresponding accessories were fabricated by SKY Technology Development Co., Ltd, CAS®. The sample holder is able to produce a substrate temperature up to 800 ℃, and the stabilization is controlled by automatic Proportional-integral-derivative (PID). A maximum of 4 targets can be loaded at the same time. Targets can be switched in a

revolution motion. The target-sample distance is fixed at 40 mm. Before starting deposition, the entire system is kept under a vacuum better than 4×10^{-6} Torr. A 2D scanning mechanical platform provides a 2-degrees of freedom laser scanning option. Commercial single crystal CaF_2 (001) substrate (lattice constants: $a = c = 5.462$ Å) was selected as the growth template in this work. The oxygen-free property of CaF_2 substrate can avoid oxygen diffusion into the superconducting layer, which has been proved to be detrimental to the superconductivity of "11-type" thin films.

3.2 Characterization Techniques

All the samples produced in this thesis work (including thin films as well as target materials) were characterized by a variety of measurements. The identification of phase was detected by using X-ray diffraction (XRD), energy dispersive spectroscopy (EDS), and electron energy loss spectroscopy (EELS). The surface morphology and structural information were investigated by scanning and transmission electron microscopy (SEM and TEM). The lamellae of thin film samples for TEM observation were prepared by focused ion beam (FIB). The physical properties were measured in a Physical Properties Measurement System (PPMS). These characterization techniques will be briefly introduced in the following section.

3.2.1 Phase and Structure Identification

3.2.1.1 X-Ray Diffraction (XRD)

XRD is a common analytical method for phase identification in the material sciences. Due to the comparable wavelength between the radiation that is used (0.01 - 10 nm) and the inter-atomic distances (nanoscale) within crystal lattices, the results of XRD are quite sensitive to aspects of the crystal structure, such as lattice constants, grain size, crystallographic orientation, etc. The high penetration depth of X-rays (several μm) provides integral information rather than localized features, especially in the case of thin films grown on oriented substrates.

When X-rays are generated and incident on the sample, they will be scattered by the atoms within the lattice. Most of the scattering results compensate each other owing to the destructive interference, also called elastic scattering. The principle of the XRD technique is based on another kind of scattering result, which is called constructive interference. It can be described by Bragg's law:

$$2d_{hkl} \sin\theta = n\lambda$$

where d_{hkl} is the lattice inter-planar spacing of the crystal, θ is the X-ray incidence angle (Bragg angle), n is an integer, and λ refers to the wavelength of the characteristic X-ray beam. As illustrated in Fig. 3-4 (a), featured diffraction only occurs when the product of $2d_{hkl}$ and $sin\theta$ is identical to an integral multiple of the wavelength of incident X-rays. As a result, the Bragg's law will be satisfied, and distinct enhancement in scattering can be detected at certain 2θ angles.

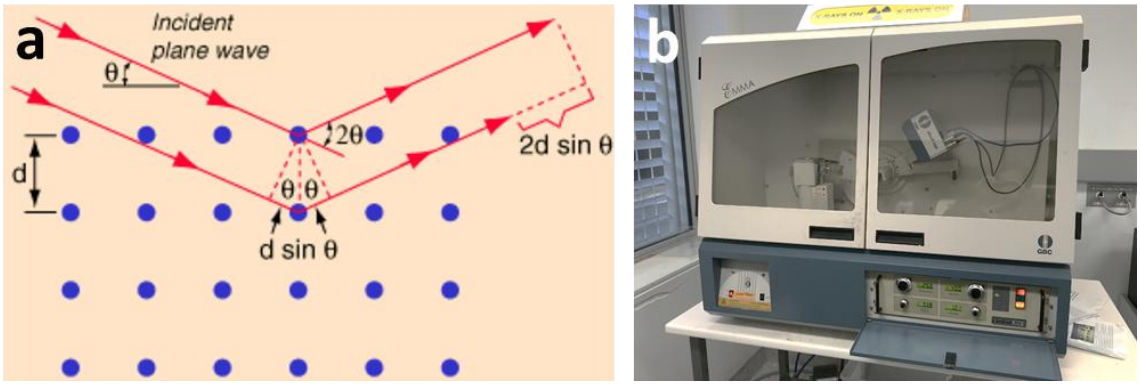

Figure 3-4. (a) Schematic diagram of Bragg's law. (b) The GBC-MMA facility utilized for XRD characterization in this work.

The XRD device utilized in the current work was a GBC-MMA Mini-materials Analyzer (GBC Scientific Equipment, USA). A picture of the real instrument is displayed in Fig. 3-4 (b). The X-ray source is Cu-Kα (λ = 1.54056 Å) radiation. The standard θ - 2θ scanning mode was used, with 2θ ranging from 10 °to 70 °. The scanning rate was set at 1 - 4 °/min and the step size was fixed at 0.02 °. In order to acquire better XRD results from thin films grown on single crystal substrates, additional actions should be taken into account to make sure that the film surface is in perfect alignment with the base level, which is indicated by the outer terrace of the concave-shaped sample holder. Fig. 3-5 shows the operational procedures involved in performing an XRD measurement on a thin film sample step-by-step. The sample is placed on an amorphous glass slide during measurement. Flexible plasticine acts as an adhesive medium to firmly hold the glass on the resin holder as well as the sample on the glass. With the assistance of weighing paper (to avoid contamination) and a glass slide, the thin film sample is finally placed for XRD θ - 2θ characterization under optimal conditions, and the possible peak shifting due to the altitude difference is restrained to a minimum level.

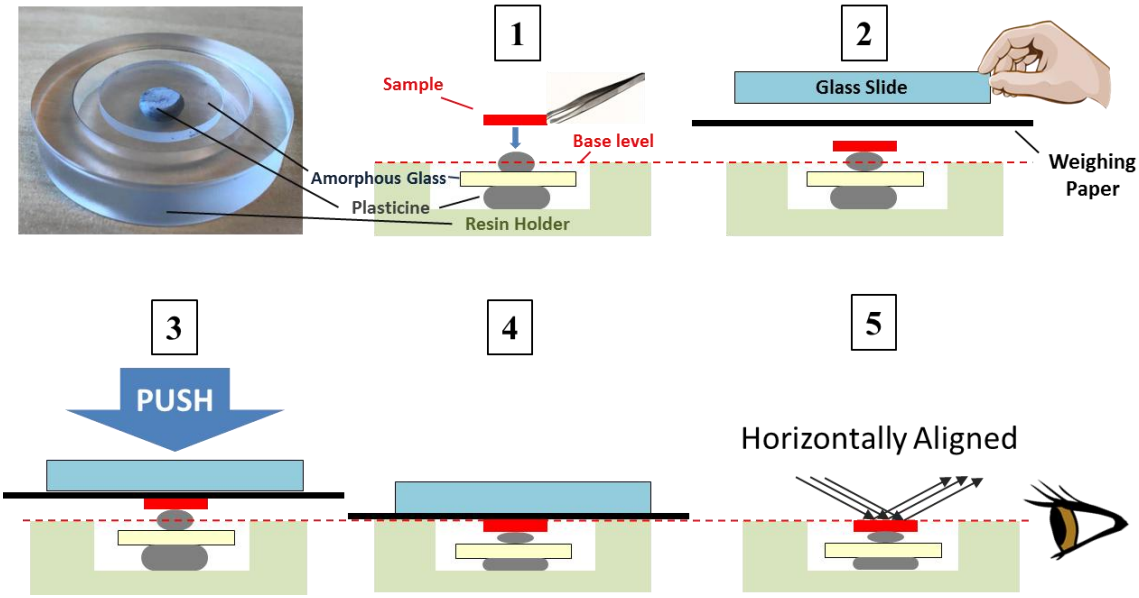

Figure 3-5. Photo: The resin holder and amorphous glass for XRD measurements. Schematic diagrams: operational procedures involved in performing an XRD measurement for a thin film sample from a cross-sectional view. The surface of the thin film is kept horizontally align with the base level to minimize the error resulting from peak shifting.

3.2.1.2 X-ray Photoelectron Spectroscopy (XPS)

XPS is a well-developed spectroscopic technique for characterizing chemical information in a sample. It can provide quantitative results in regard to chemical state, elemental composition and electronic state. However, it is very surface-sensitive, which means only the information of the top few layers are detected by XPS. In detail, a specimen is irradiated by a X-ray beam during XPS measurement. The number of the electrons that escape from the top few nanometers of the material are collected and the corresponding kinetic energy are measured. According to the obtained XPS spectra, one can identify the valence states of the involved elements and estimate the elemental ratio of each state. The XPS measurement in this thesis work was conducted by using VG Scientific ESCALAB 2201XL, equipped with a Thermo Scientific Sigma Probe instrument in KETI using Al Kα X-ray radiation and a fixed analyzer transmission mode.

3.2.1.3 Electron Microscopes (EM)

Scanning Electron Microscope (SEM)

The electron microscope is a type of microscope that uses accelerated electrons as the illumination source. SEM acquires specific types of electrons after their interaction with the atoms on the surface of the sample and converts the information

into detailed surface topography. Fig. 3-6 (a) illustrates the typical set-up of an SEM system. From top to bottom, there are the electron gun, anode, sets of different lenses, and the sample stage with signal detectors. The secondary electrons (SE) and backscattered electrons (BSE) are the most used electron signals. The former (~ 1 nm penetration depth) are dominated by surface features or edges, while the latter (~ 1 μm penetration depth) are more sensitive to the atomic number *Z*. Hence, SE mode is preferred for observing details of the morphology, and BSE mode is more suitable for distinguishing areas with different chemical compositions[4].

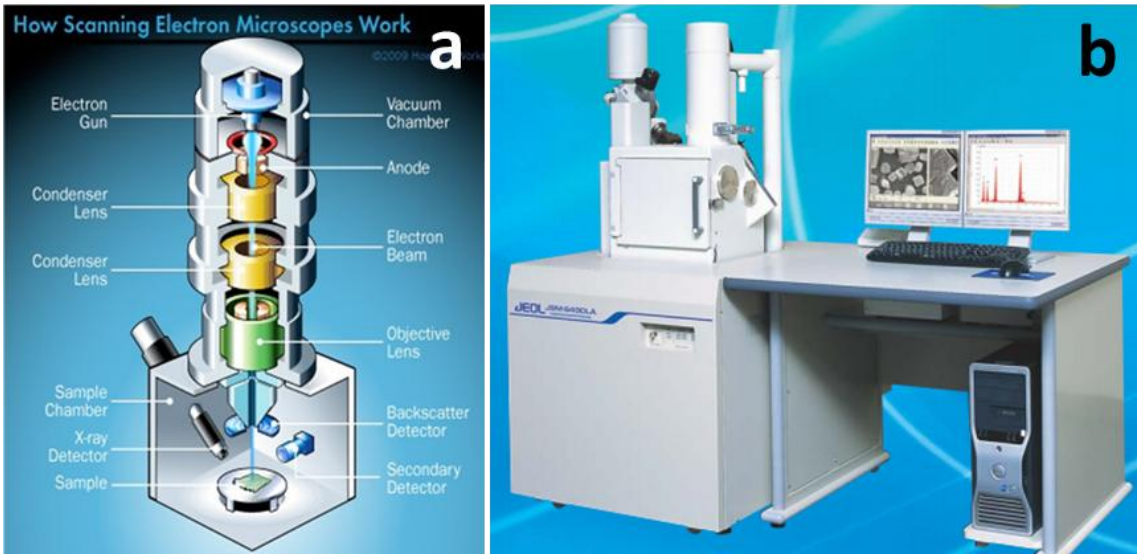

Figure 3-6. (a) Basic set-up of SEM facility[5]. (b) The SEM facility (JEOL-6490LV) used in this work.

A JEOL-6490LV was used in this thesis work (see Fig. 3-6 (b)). The electrons are generated by a 30 kV tungsten filament. Either SE or BSE can be chosen as the signal. A powerful EDS detector is supplied for rapid elemental mapping and quantitative analysis. Detailed information on the EDS technique will be discussed separately.

Transmission Electron Microscope (TEM)

TEM like SEM also uses electrons as the interactive medium with the sample, although the information acquired from TEM and the corresponding imaging mechanism is significantly different from those of SEM. Table 3-1 lists some major difference between SEM and TEM. In contrast to the case of SEM, where the scattered electrons are collected as the imaging information, TEM utilizes the high-energy electrons that pass through the specimen. Hence, the thickness of the sample must be smaller than their mean free path (MFP), which is the distance that an electron can

travels through a solid before being inelastically scattered, usually no more than 100 nm. The acceleration voltage of the electrons and the atomic number of materials will affect the MFP. Due to the unique projection feature of TEM imaging, a thinner specimen will bring about less energy loss and effectively reduces the possibility of blurring and pile-up circumstances that can occur with a thick specimen. The typical resolution for a 200 kV TEM system is about 2 Å, which is an order of magnitude higher than that of an SEM. Four types of electrons are generally used in TEM and TEM-related techniques: transmitted electrons, diffracted electrons, energy loss electrons, and Rutherford scattered electrons. The transmitted electrons, which never lose energy or change phase after passing through the specimen are used for the basic imaging process. The diffracted electrons change phase coherently and are sensitive to crystal orientation and thickness. Both energy loss and phase change occur in the energy loss electrons (phonons, plasmons, bremsstrahlung, and core loss), which provide chemical and bonding information on the material based on the EELS technique. As a result, although the interpretation and analysis of TEM results are not quite straightforward, they do contain abundant information about the internal microstructure and lattice behaviour which are unavailable in SEM.

Table 3-1. Feature comparison between SEM and TEM.

Feature	**SEM** 	**TEM** 
Information	Surface Morphology 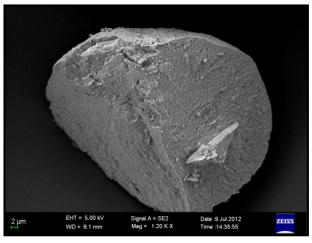	Projection 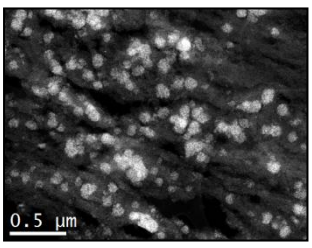

Specimen	no Specific Requirement 	Lamella or Powder (*e*-transparent) 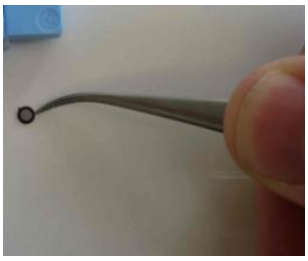
Voltage (kV)	≤ 30	120 - 400
Advanced Microanalysis	EDS (μm scale) 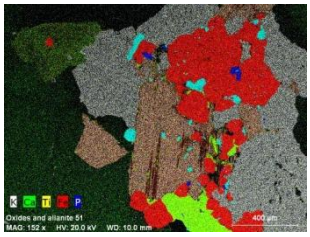	EDS, EELS (nm scale) 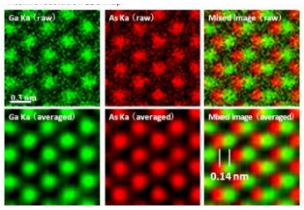
Resolution	~ 20 Å	~ 2 Å
Diffraction Availability	Typically no	Yes
Interpretability	Direct	2D projection, Diffraction, Phase contrast

The basic structure of a standard TEM is shown in Fig. 3-7. The key components of a TEM have the same nomenclature as optical microscopes. The source of illumination in a TEM is a source of electrons (Tungsten, LaB_6, hot/cold field emission gun, etc.). The generated electron beam can be considered as an electron laser with a single wavelength and identical phase. The condenser lenses control the spot size of the electron beam on the specimen as desired. The specimen is mounted on a sample insert with a 3-axis motor and double-tilt function. The objective lens brings the scattered electrons to a focus after their interaction with the specimen. The magnification control of the image is realized by the intermediate lenses and the projector lens, similar to the function of focusing knobs on optical microscopes. The ultimate image is shown on a fluorescent screen like a projector, and the camera on the bottom can be employed to record the information for generating images.

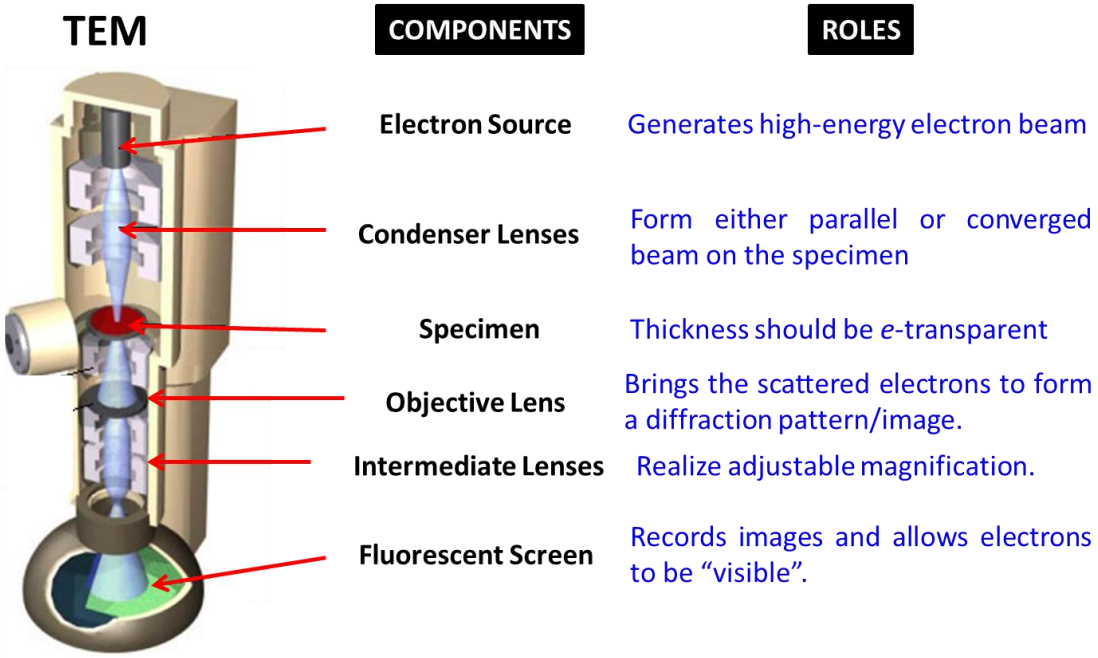

Figure 3-7. The major components and the corresponding functions in a TEM system.

In this thesis work, a JEOL JEM-ARM200F scanning transmission electron microscope (STEM) was used to carry out the TEM-related work (shown in Fig. 3-8 (a)). The measurement tasks included atomic-resolution TEM imaging, selected-area electron diffraction (SAED), micro-region EDS analysis, EELS, etc. This system is equipped with an aberration correction, which enables imaging down to single-atom scale and atomic-resolution mapping. The electrons are generated by a cold field emission gun with a low resolution of 0.3 eV. The most fundamental feature of a STEM is the serial scanning acquisition mode rather than the parallel mode in a conventional TEM, which eliminates the difficulty in imaging thick samples in TEM due to the chromatic aberration. Additionally, high-angle annular dark-field[6] (HAADF) imaging is available in a STEM system. In HAADF mode, only those electrons incoherently scattered at a very high angle (θ > 50 mrad) are collected to contribute to the imaging (illustrated in Fig. 3-8 (b)). It is also called *Z*-contrast imaging due to its high sensitivity to the variations in atomic number. The HAADF detector is able to collect many more scattered electrons than in regular dark-field imaging, which spares the main beam for simultaneous bright-field (BF) imaging as well as further analysis, such as by EELS or EDS.

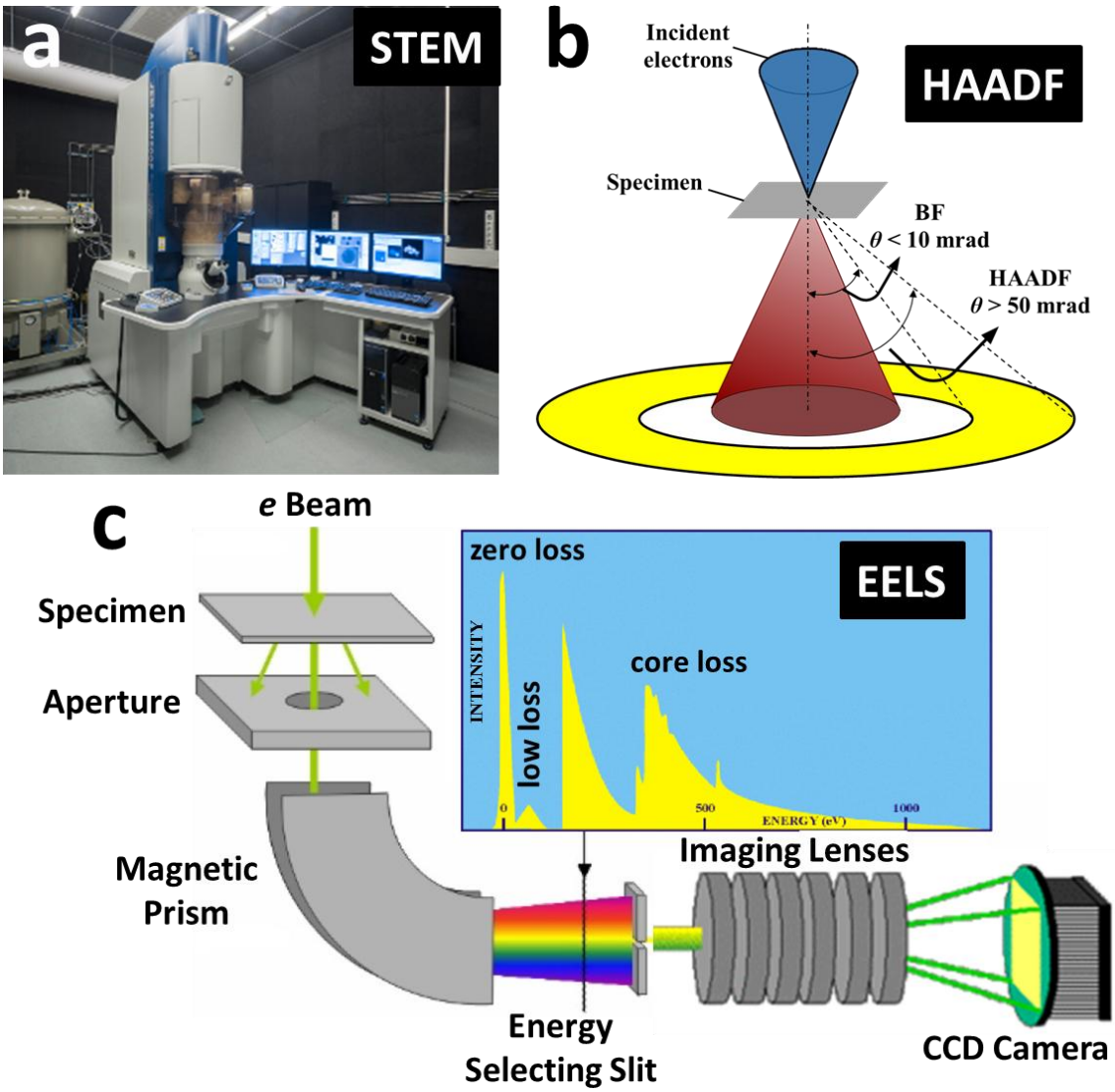

Figure 3-8. The JEOL-ARM200F STEM system and the corresponding HAADF and EELS functions. (a) The STEM facility used in this work. (b) Schematic diagram of HAADF imaging. (c) Schematic illustration of EELS system. The zero-loss, low-loss, and core-loss edges reflect the electrons that are elastically scattered, have weakly interacted with outer shells, and have intensively interacted with inner shells, respectively.

EELS is the abbreviation for electron energy loss spectroscopy. It is based on the loss of energy of the electron beam after the interaction with the specimen. Fig. 3-8 (c) displays a schematic illustration showing how an EELS spectrum is generated. The focused electron beam interacts with the sample and loses energy due to excitation of the electrons in the specimen material. The residual electrons pass through the magnetic prism and are dispersed by the electron spectrometer for energy selecting. The ultimate energy-loss spectrum is recorded on a charge-coupled device (CCD) camera. The type of energy loss can be interpreted in terms of how the electrons lose energy. The zero loss edges come from the elastically scattered electrons. Inelastic interactions result in

low losses (≤ ~30 eV, also called plasmon losses) and core loss edges (> ~ 50 eV, also called ionization edges). The core loss electrons in EELS provide abundant chemical composition and bonding information on the material. Compared to the conventional EDS technique, EELS provides higher accuracy for analyzing light elements, better spatial resolution, and additional bonding information about the sample, although a high-quality specimen and advanced knowledge are required for quantifying complicated EELS results. The detailed mechanisms regarding how the energy edges form will be discussed in Chapter 5 with the Fe-$L_{3,2}$ edges as an example.

Energy Dispersive X-Ray Spectroscopy (EDS)

EDS (or EDX) is a microanalytical technique mainly focusing on the chemical composition and the elemental distribution layout in a sample. Either SEM or TEM is an applicable platform for carrying out EDS work. Although the spatial resolution of EDS analysis is much higher in TEM due to the different forms of specimens and the accelerating voltages, the basic principles for the generation and detection of EDS in SEM and TEM are the same. Fig. 3-9 shows a schematic illustration of how an EDS spectrum is processed. After the interaction between the incident beam and the specimen, two types of X-rays are generated: Bremsstrahlung X-rays and characteristic X-rays. The Bremsstrahlung X-rays are the radiation that is emitted when electrons are experiencing a sudden braking force due to interaction with the sample. They will be presented as the background in an EDS spectrum. The other type of radiation, the characteristic X-rays, acts as a unique signature for each element. Because each element possesses specific ionization energies, the differences in the energy position and intensity act as a signature for every element, except for H, He, and Li, with atomic numbers Z that are equal to or less than three.

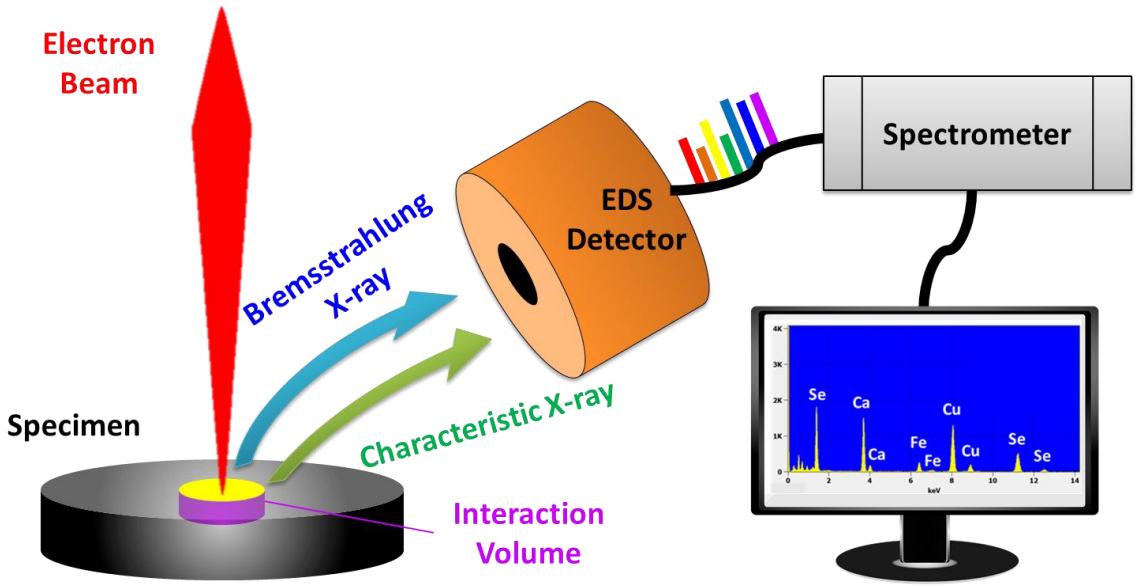

Figure 3-9. Schematic illustration showing the generation of an EDS spectrum.

The EDS equipment supplied with SEM (JEOL-6490LV) and STEM (JEOL JEM-ARM200F) was employed to characterize the chemical composition and element distribution of the thin films involved in this work. The Oxford Instruments X-Max 123 eV SDD EDS detector was utilized during SEM sessions for elemental tracing and mapping on a µm scale. The Centurio SDD EDS detector supplied with the STEM enables precise composition-microanalysis and elemental mapping with an atomic resolution.

Focused Ion Beam (FIB) for *in-situ* Lift-out

In fact, the ultimate quality of a TEM image mostly depends on the quality of the TEM-specimen. In contrast to the straightforward TEM process for the preparation of powder (dispersion) or bulk samples (ion-milling), the preparation of lamellae of the thin films grown on single crystal substrates in this thesis work had to be fulfilled in a more sophisticated way due to the unique 2D property and low thickness (< 200 nm) required. The FIB technique is the most reliable method to prepare high-quality lamellas of thin films in a nondestructive way. Relying on precise mechanical transmission in all directions and the availability of multiple monitors, FIB is capable of performing of milling, processing, and assembling operations in 3D coordinates.

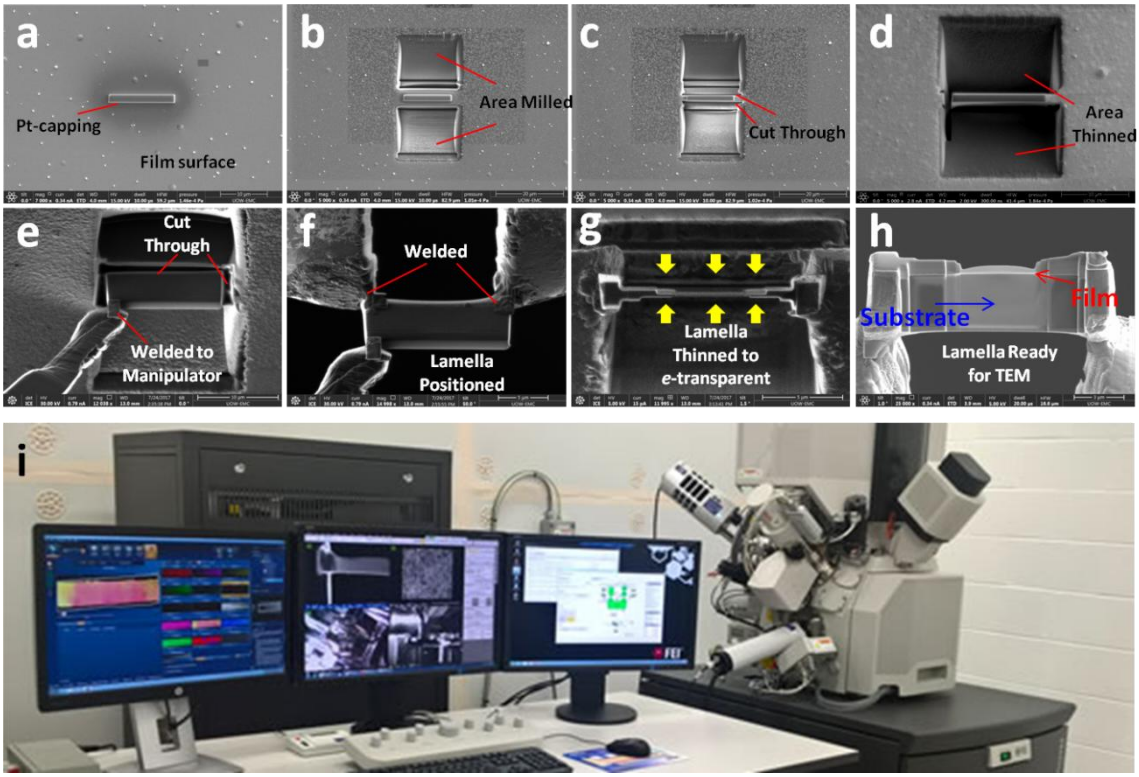

Figure 3-10. (a) – (h) Process diagrams showing an *in-situ* lift-out FIB session for preparing a lamella for TEM observation. (i) The FIB facility used in this work.

Most of the TEM lamellae in this thesis work were carefully prepared by using a state-of-the-art FIB system (FEI Helios NanoLab G3 CX). Platinum, carbon and nitrogen gas injections are available in the chamber. Platinum and carbon materials can be coated on the designated area as a capping layer or welding solder. A high-energy gallium ion beam is employed to realize precise cutting and thinning operations. Fig. 3-10 provides a series of screenshots taken during an *in-situ* lift-out FIB session. Here, *in-situ* means that the entire process, including cutting, lift-out, welding, and thinning, was operated inside the FIB chamber. It is much more efficient and the quality of such lamellae is no doubt better than for the lamellae fabricated *ex-situ* considering that the vacuum state is never broken until the lamella is ready to use.

3.2.2 Physical Property Measurement System (PPMS)

A Quantum Design PPMS® (PPMS-9T, DynaCool™-9T) was employed for characterizing the magnetic and electrical properties of our thin film samples. Fig. 3-11 shows a photograph of a PPMS system. The vibrating sample magnetometer (VSM) option is currently activated with the VSM module installed on top. No LHe is required for running this system, as a two-stage pulse tube cooler is able to cool down both the sample temperature and the superconducting magnet. External helium gas flow allows

accurate temperature control.

Figure 3-11. The Quantum Design PPMS® DynaCool™ instrument used in this work. The VSM option is activated with a VSM module installed on top.

Magnetic Measurements

In this work, the magnetization information was collected by using the VSM option, in which the genuine signal is able to be filtered out, even it is weaker than the noise. The root-mean-square sensitivity is better than 10^{-6} emu with per second averaging. The Meissner effect (complete diamagnetism) of a superconductor can be demonstrated by the diamagnetic signal detected below T_c. By utilizing the VSM mode, a standard "Zero-field Cooling (ZFC) & Field Cooling (FC)" measurement process is effective for determining the magnetic T_c (T_c^{mag}). As the name implies, ZFC means that the sample was cooled down from the initial state (room temperature) without any external magnetic field, while FC means that there was an additional field applied onto the sample prior to the variation of temperature.

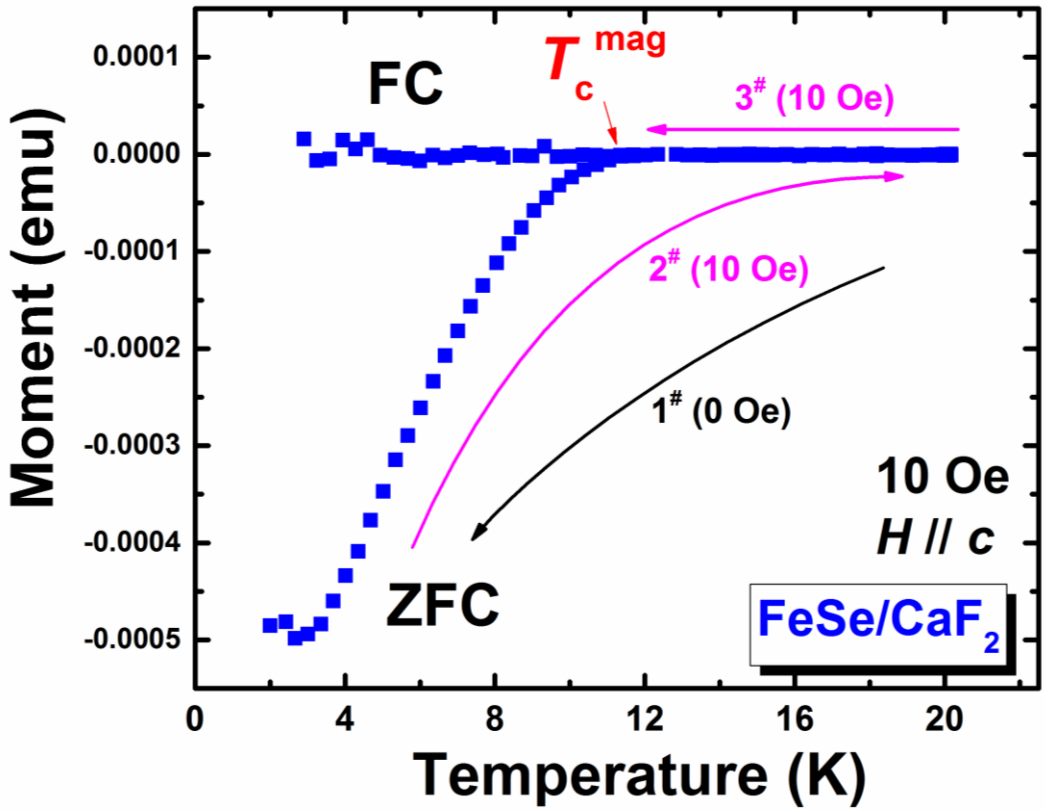

Figure 3-12. An example showing how the magnetic T_c is determined in a "ZFC & FC" measurement by using the VSM mode. The excitation magnetic field was set at 10 Oe (parallel to *c*-axis).

Fig. 3-12 illustrates a standard "ZFC & FC" measurement process for a FeSe thin film grown on a CaF_2 substrate in this work. Three steps are included in this measurement to acquire the T_c^{mag}. Firstly, the sample was cooled down to 2 K without any field applied (aka, ZFC). Due to the Meissner effect, a repulsive field is spontaneously generated to compensate for the flux penetration inside the superconducting sample as long as the temperature is below T_c. For the second step, an external excitation magnetic field of 10 Oe is applied parallel to the *c*-axis of the film plane. Then, the data acquisition starts with warming up the temperature (aka, FC Warming). During this stage, the diamagnetic signal gradually degrades due to the increasing flux penetration. The sample becomes a normal state above T_c and is fully penetrated by external flux. The final step is the cooling sample with the excitation field (aka, FC Cooling). Considering the existence of the "Vortex Phase" in type-II superconductors, part of the flux is pinned inside the superconductor, which leads to the different temperature-moment dependences between FC Cooling (3rd step) and FC Warming (2nd step). As a result, the resultant crossing-point is defined as the temperature where the superconducting transition occurs. The general temperature range

for a “ZFC & FC” measurement in this work was set at 2 - 25 K with a ramp rate of 0.5 K/min.

Electrical Transport Measurements

In electrical transport measurements, the “Resistivity” mode was usually activated in PPMS for data acquisition. In most cases, the electrodes were manually prepared. Conductive silver paste (Electron Microscopy Sciences®) and pure gold wires (99.99 %, 25 μm diameter, Surepure Chemetals®) were utilized in the preparation procedures to reduce the error from contact resistance. Two types of electrical transport measurements, resistance measurement and Hall measurement, were involved in this thesis work. Fig. 3-13 displays the models for resistance as well as Hall measurements, with the prepared electrodes shown on the side. The strips in grey refer to the areas coated by silver paste. Each silver strip is made to straight and firmly adhere to the sample surface. The purpose of applying silver strips across the entire width of the sample is to improve the homogeneity of the current passing through. The electrical resistivity (ρ) can be calculated according to the equation:

$$\rho = R\frac{S}{L}$$

where R is the electrical resistance obtained by the method shown above, and S and L stand for the distance between two voltage electrodes, and the cross-sectional area of the sample, respectively. Different selections of L and S for resistance and Hall measurements are also illustrated in the figure. For the resistance measurements, the entire temperature range (2 K - 300 K) is divided into two parts, 2 K - 20 K and 20 K - 300 K. The ramp rate of the low-temperature region is set at ~ 0.18 K/min to get an accurate T_c transition, while for the high-temperature region, it is about 4 K/min. Each resistance is averaged based on 25 data points taken under the same conditions.

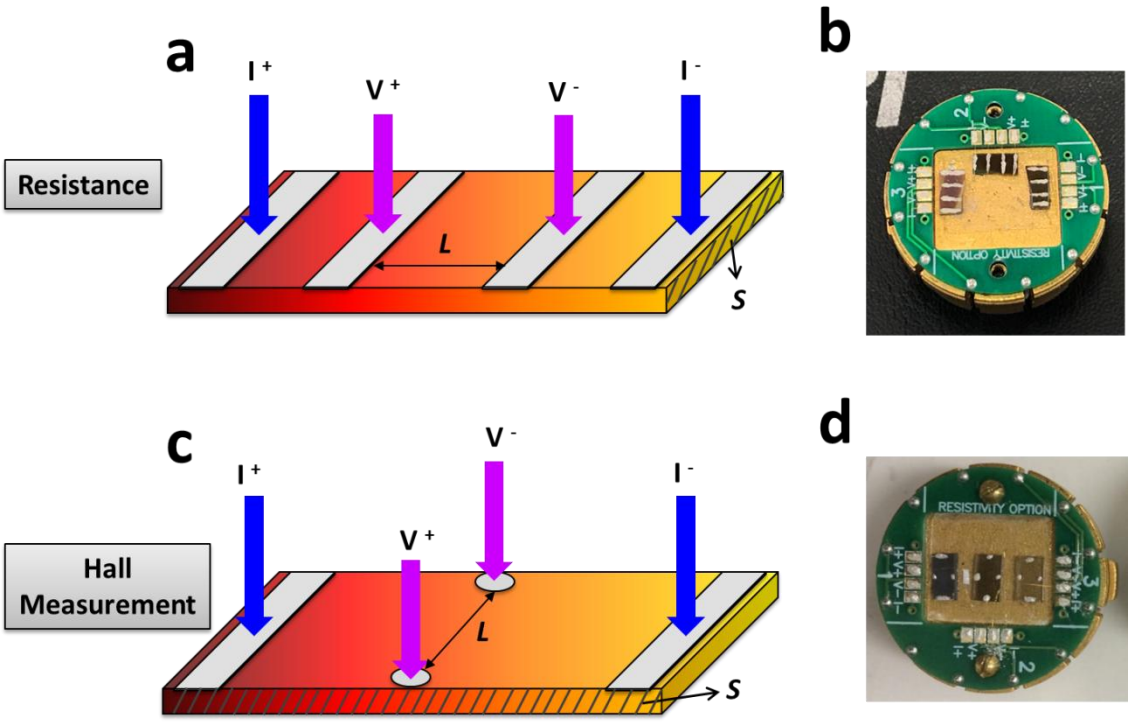

Figure 3-13. Models (left) and photographs of prepared samples (right) for the two kinds of electrical transport measurements used in this work. (a, b) Standard four-probe layout for resistance measurements. (c, d) Cross-type layout for Hall measurements. Grey strips indicate the areas that are coated with the conductive silver paste.

Hall measurements are very useful for studying the charge carrier type and also the concentration of carriers in the sample. The voltage electrodes in Hall measurements are placed on the vertical sides of the specimen, so that the Hall voltage due to the carrier accumulation can be detected. For preparing Hall probes, however, the size of the voltage electrodes was made as small as possible to minimize the effect of longitudinal resistance (magnetoresistance, MR) owing to misalignment, as shown in Fig. 3-13 (c). In addition, the error introduced by MR was also effectively reduced by averaging the Hall resistance (R_{xy}) obtained from the two opposite directions of external magnetic fields. The R_{xy} was acquired in both positive and negative fields and then calculated the difference, i.e.,

$$R_{xy}(H) = \left[R_{xy}(+H) - R_{xy}(-H)\right]/2$$

3.3 References

(1) Chrisey, D. B.; Hubler, G. K. *Pulsed Laser Deposition of Thin Films*, John Wiley & Sons: New York, 1994.
(2) Smith, H. M.; Turner, A. F. Vacuum Deposited Thin Films Using a Ruby Laser. *Appl. Opt.* **1965,** *4*, 147-148.
(3) Dijkkamp, D.; Venkatesan, T.; Wu, X. D.; Shaheen, S. A.; Jisrawi, N.; Min-Lee, Y. H.; McLean, W. L.; Croft, M. Preparation of Y-Ba-Cu oxide superconductor thin films using pulsed laser evaporation from high T_c bulk material. *Appl. Phys. Lett.* **1987,** *51*, 619-621.
(4) Goldstein, G. I.; Newbury, D. E.; Echlin, P. J., D. C.; Fiori, C.; Lifshin, E. *Scanning electron microscopy and x-ray microanalysis.*, Springer US: New York, 1981.
(5) http://emicroscope.blogspot.com/2011/03/scanning-electron-microscope-sem-how-it.html?view=snapshot.
(6) Jesson, D. E.; Pennycook, S. J. Incoherent imaging of crystals using thermally scattered electrons. *Proc. Roy. Soc. A* **1995,** *449*, 273-293.

Chapter 4

4 The Interlayer Structure of FeSe Thin Film on CaF_2 Substrate and its Influence on the Superconducting Performance

4.1 Introduction

Soon after the discovery of superconductivity in $LaFeAsO_{1-x}F_x$, the survival of superconductivity in Fe-based compounds ignited worldwide enthusiasm for exploring this novel type of superconductor[1-4]. The binary compound iron selenide (FeSe), with superconducting transition temperature (T_c) = 8 K[4], has the simplest crystal structure among the Fe-based superconductors. Pressurization[5-9] and elemental substitution[10-12] have been proved very effective for improving the superconducting performance of FeSe crystalline bulks. Generally, FeSe in the form of thin film shows more enhancement of T_c than the bulk[13], and it is expected to be further enhanced by methods such as electron doping[14-18] or interface engineering[19-25]. Since 2012, growing two-dimensional (2D) thin films by molecular beam epitaxy (MBE) has become a highly popular research topic for pursuing high T_c superconductivity in the FeSe system. T_c can be significantly enhanced in unit-cell[19-29] or K-doped multi-cell[15-17, 30] FeSe grown on pre-treated strontium titanate ($SrTiO_3$, STO) substrate. Neither the stability nor the superconducting performance of the FeSe/STO structure is satisfactory, however, if the thickness of the FeSe layer is increased to make it suitable for large-scale applications (tens to hundreds of nanometers). Systematic work was also conducted on FeSe thin films grown on Mg oxide (MgO) substrate[31-34] but the highest T_c^{zero} was still less than 10 K. In the case of mono/multi-layer FeSe thin film grown by MBE method on STO substrate, the strong electron-phonon coupling effect is considered as one of the most intrinsic mechanism for the much enhanced T_c found in this system. It is believed that oxygen contamination is a possible negative factor for obtaining high-quality Fe-chalcogenide thin films[35-36] on oxide substrates. Calcium fluoride (CaF_2) is considered

as one of the best growth substrates[37-40] due to its oxygen-free nature, as well as its ability to introduce in-plane lattice compression on the FeSe film above, which can obviously enhance superconducting properties. Considering the success of exceptional T_c enhancement in FeSe/STO structure, the clarification of FeSe/CaF_2 interface is believed helpful to pave the way to understanding the growth mechanism of FeSe from a different aspect, and even achieve a better superconducting performance.

In this work, FeSe thin films were fabricated with various thicknesses on CaF_2 substrates and studied the evolution of superconductivity. Both superconductor-insulator transition (SIT) and suppression in Tc are observed, and the origins are investigated. With the assistance of high-resolution scanning transmission electron microscope (STEM) facilities, the interfaces between FeSe and CaF_2 substrate are carefully characterized. It is worth mentioning that a calcium selenide (CaSe) interlayer has been distinctly observed and identified. Furthermore, the formation mechanism of this CaSe interlayer is also studied. The results in this thesis work can provide constructive guidance for carrying out further interface engineering in the FeSe/CaF_2 structure.

4.2 Experimental Details

FeSe thin films were deposited by pulsed laser deposition (PLD) (Nd: YAG, λ = 355 nm, 10 Hz, 2 W) under a high vacuum better than 5×10^{-6} Torr. A home-made FeSe pellet served as the target. CaF_2 (100) single crystal with lattice parameter a = 5.462 Å ($a/\sqrt{2}$ = 3.862 Å) was chosen as the growth substrate considering the absence of O element and its negligible lattice mismatch with FeSe. During the deposition, the temperature of substrate was kept at 300 ˚C, and a series of FeSe films were obtained by varying the deposition time. As shown in Fig. 4-1, The FeSe layers can be clearly distinguished in the images. The thickness of the FeSe layers is 8 nm, 60 nm, 127 nm, and 160 nm, respectively (denoted as #FS1, #FS2, #FS3, and #FS4). Electron-transparent lamellae were prepared through the *in-situ* lift-out technique in a focused-ion-beam (FIB, FEI Helios 600 NanoLab) system for cross-sectional observations. STEM (JEOL ARM-200F) equipped with an energy dispersive X-ray detector (EDS, Centurio SDD) was employed for obtaining high-resolution micrographs as well as determining the elemental distributions at an atomic level from the thin films. When analyzing EDS results, principal component analysis (PCA) was used to separate different phases when they are highly overlapped or superimposed on large

backgrounds. The phase identification was carried out by conventional X-ray diffraction (XRD) with Cu Kα radiation. The surface morphology of the specimens was observed with a field emission scanning electron microscope (FESEM, JEOL JSM-7500). The transport measurements were conducted with a 9 T physical properties measurement system (PPMS, Quantum Design). The X-ray Photoelectron Spectroscopy (XPS) measurement in this work was conducted by using VG Scientific ESCALAB 2201XL, equipped with a Thermo Scientific Sigma Probe instrument in KETI using Al Kα X-ray radiation and a fixed analyzer transmission mode.

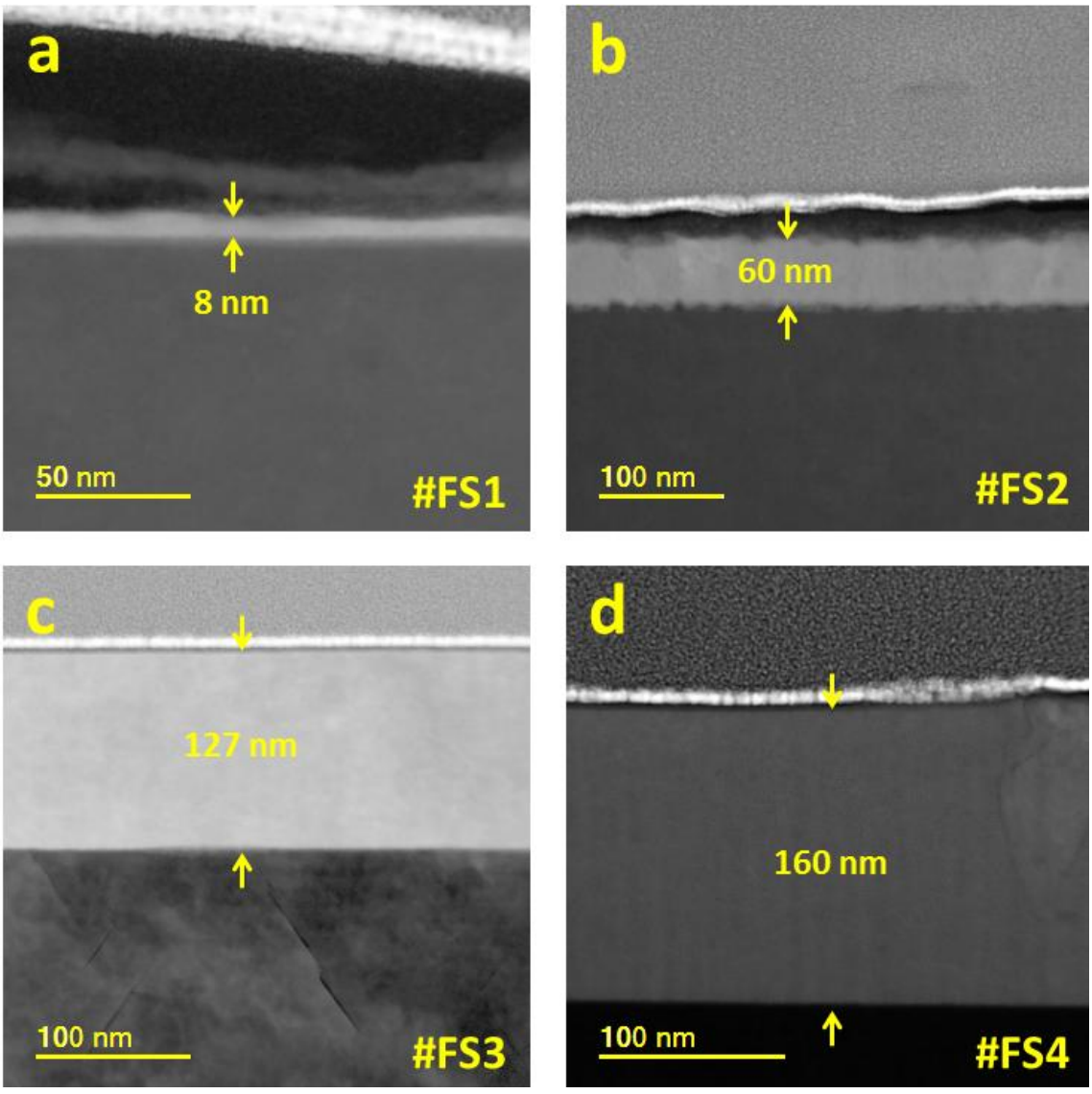

Figure 4-1. Cross-sectional STEM images for (a) #FS1; (b) #FS2; (c) #FS3; and (d) #FS4.

4.3 Results and Discussion

Good quality *c*-axis texture in all the FeSe thin films was revealed by XRD

results which are provided in Fig. 4-2 (a). The diffraction peaks for FeSe are marked by their Miller indices (hkl), Pure *c*-axis oriented FeSe phases were detected in the results except for one unidentified phase (2θ ~ 15 °). It is estimated to be a FeSe-related composition or a secondary phase considering the intensity is in direct proportion to the thickness of FeSe layer. From Fig. 4-2 (b), the peaks which exist before depositing FeSe layer can be distinguished by comparing the spectra of #FS3 and CaF_2. Generally, these impurities in CaF_2 substrate seem not result in negative effect on the following FeSe thin films. Further investigation will be continued to clear the confusions in unidentified peaks.

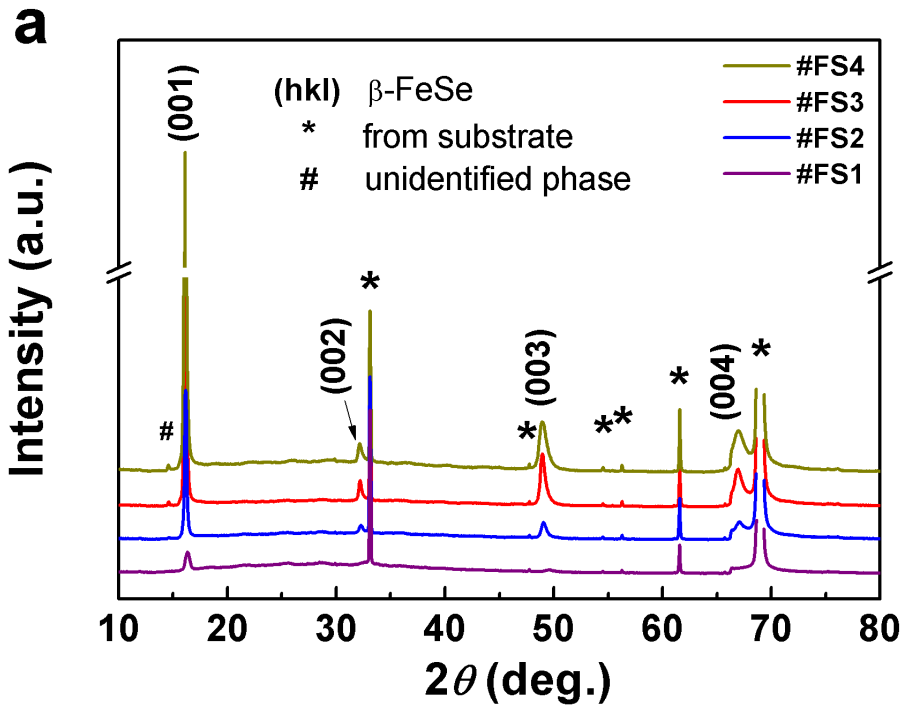

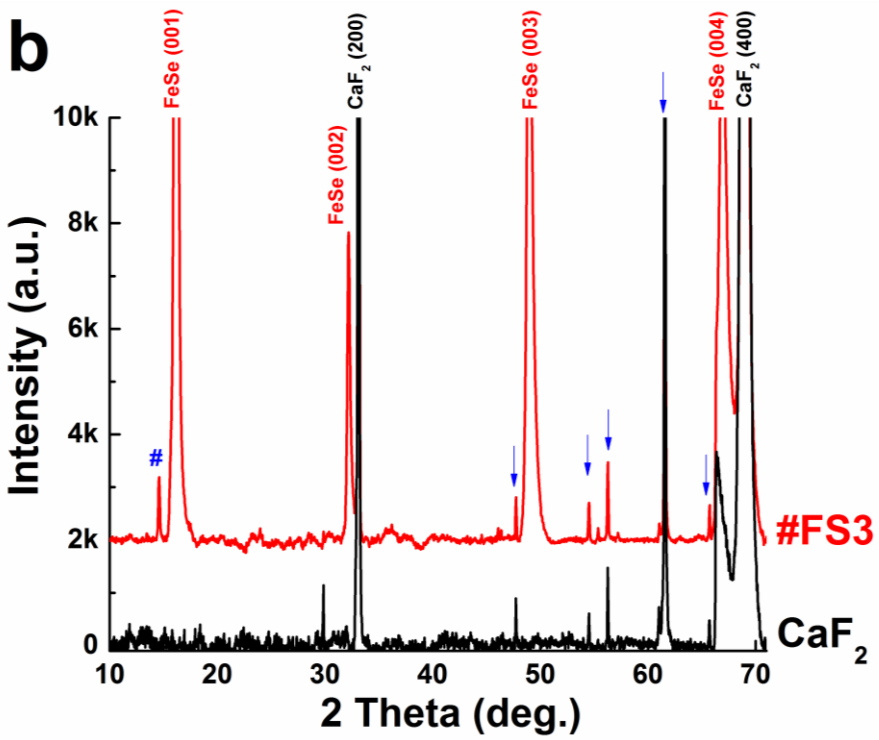

Figure 4-2. XRD *θ-2θ* patterns for the samples in this work. (a) XRD *θ-2θ* patterns for the four FeSe thin films ranging from 10 °to 80 °. Asterisks indicate the peaks originating from the substrate. (b) Comparison of XRD *2θ* patterns for #FS3 and CaF_2 substrate. Arrows mark the peaks which were detected before depositing FeSe layer.

From XRD *2θ* results, the *c*-axis lattice parameters of four FeSe samples were calculated as 5.5189 Å, 5.5667 Å, 5.5767 Å and 5.5748 Å for #FS1, #FS2, #FS3 and #FS4, respectively. Furthermore, lattice information from high-resolution STEM images was also acquired. An example is given in Fig. 4-3 (a), showing how *a* and *c* lattice parameters were measured based on line profile results from STEM images for #FS1. In order to minimize the error, the lattice parameters of CaF_2 were measured first. The difference (scale factors for *a* and *c*, respectively) between the measured ones ($a/\sqrt{2}$ = 3.6416 Å, *c* = 5.3372 Å) and the standard ones ($a/\sqrt{2}$ = 3.862 Å, *c* = 5.462 Å) of CaF_2 reflects how dimensions varies proportionally inside a single image. Based on that, the dimensions of FeSe layers in the same image were measured and normalized subject to the case of CaF_2 substrate. Fig. 4-3 (b) illustrates the line profile corresponding to the blue rectangle in Fig. 4-3 (a). Almost steady *c*-axis parameters of FeSe layer is observed regardless of the position of the unit-layer. The corresponding *c*-axis lattice parameters based on the XRD 2*θ* results are plotted in Fig. 4-3 (c) together with those from STEM images for comparison. Two sets of data show a similar trend: the *c*-axis lattice parameter of FeSe first keeps increasing along with the film thickness till the case of

#FS3 which shows the highest T_c, then, it shrinks a little in #FS4 with a small T_c degradation. Considering that the films have only *(001)* orientation, one can only get the information of *a*–axis lattice parameter by the XRD diffractometer with a five-axis sample stage. Unfortunately, the specific facility was not available during this thesis work. However, the two sets of data (*c*-axis lattice parameter) have only ~ 2 % difference, which indicates a quite good consistency between the results of XRD and STEM. Hence, the *a* & *c*-axis lattice parameters obtained from STEM results should be fairly reliable.

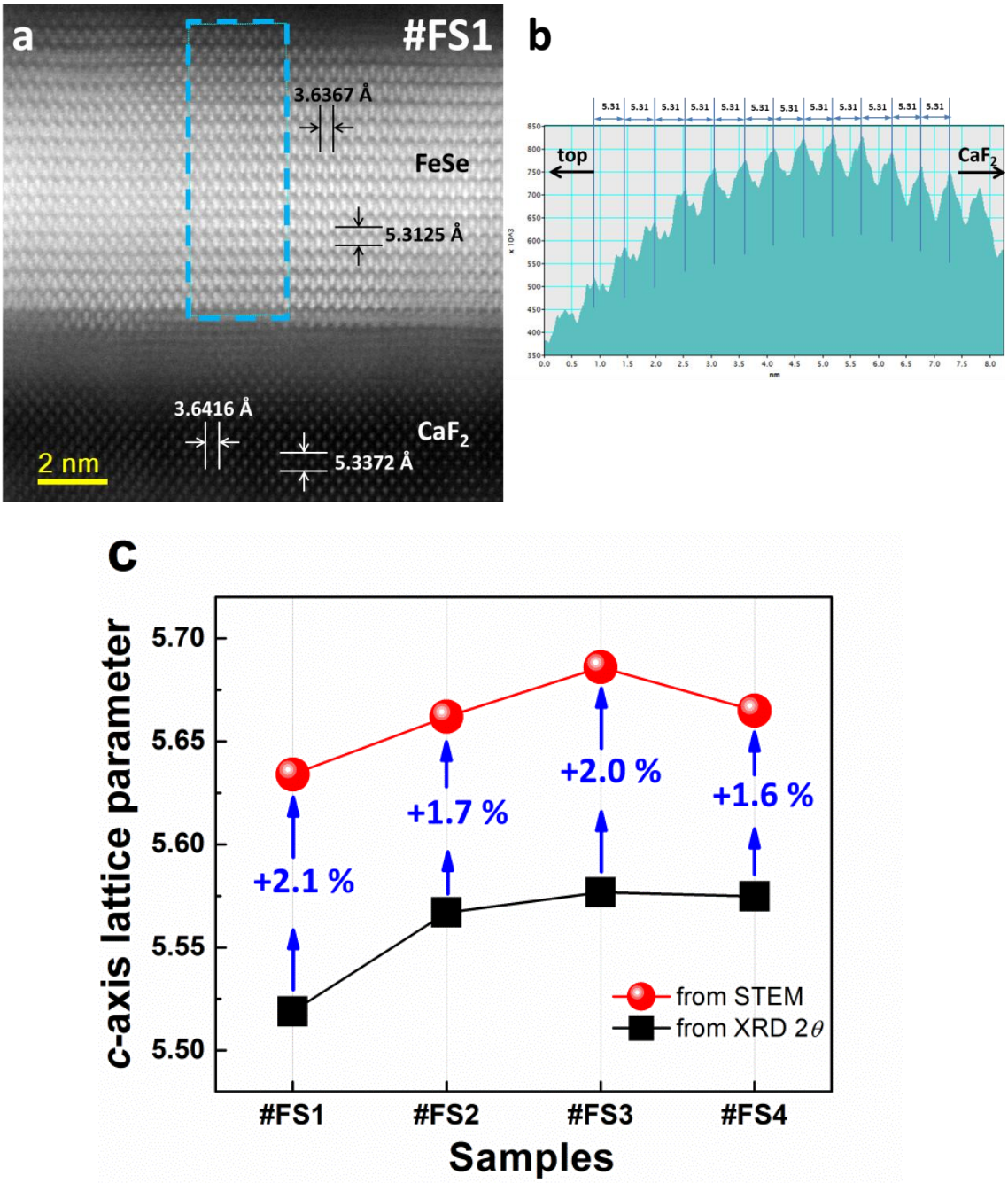

Figure 4-3. An example showing how lattice parameters are measured in STEM images. (a) A STEM

image for #FS1. Lattice of FeSe and CaF_2 are clearly seen. (b) The line profile corresponding to the blue rectangle in (a). (c) The comparison of *c*-axis lattice parameters calculated by STEM (red circles) and XRD 2θ (black squares). The percentages indicate the difference.

The detailed specifications of the FeSe films in this work are listed in Table 4-1. The data marked with asterisks were acquired from high-resolution STEM images. In this work, T_c^{onset} is defined as the temperature at which the resistivity starts to drop, and T_c^{zero} refers to the point where the resistivity is very close to zero. The results for chemical composition were acquired from several different areas to ensure the reliability. It is noticed that the pristine FeSe thin films in this work show negligible degradation in ambient atmosphere even after various characterizations (as shown in Fig. 4-4), which is a prerequisite for further post-treatments, such as chemical doping[16-18], liquid gating technique[14], post-annealing[41], or external electrical field[42-43]. The chemical stability is thought to be a prominent advantage for both experimental accessibility and device fabrications[44].

Table 4-1. Detailed specifications of FeSe thin films in this work.

	Thickness (nm)*	***a*-axis (Å)***	***c*-axis (Å)***	***c*/*a***	**T_c^{onset} (K)**	**T_c^{zero} (K)**	**ΔT_c (K)**	**H_{c2} (T)**	**Fe/Se (at.%)**
#FS1	8	3.722	5.634	1.514	n/a	n/a	n/a	n/a	1.38:1.00
#FS2	60	3.738	5.662	1.515	10.7	8.1	2.6	27.8	1.14:1.00
#FS3	127	3.727	5.686	1.525	15.1	13.4	1.7	35.5	1.05:1.00
#FS4	160	3.734	5.665	1.517	13.3	11.2	2.1	31.5	>1.15:1.00**

(For reference, the lattice constants of FeSe bulk are a = 3.765 Å, c = 5.518 Å.)

* Data acquired from high-resolution STEM images;

** Considering that only areas that were homogeneous and free of Fe-rich phase were selected, the amount of excess Fe could be higher than 15 at. % if the Fe-rich phase is included.

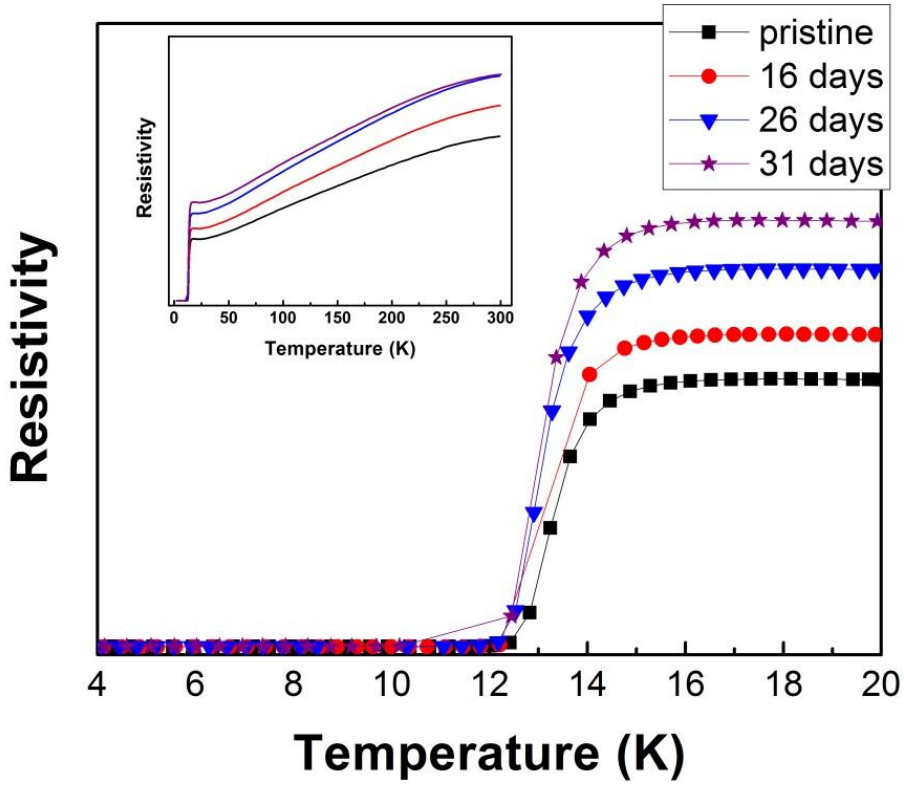

Figure 4-4. An example showing the aging degradation of resistivity for #FS3. Inset shows the results in a temperature range up to room temperature.

The temperature dependence of the electronic resistivity is shown in Fig. 4-5 (a). With increasing thickness from 8 nm to 127 nm, a clear SIT and gradual enhancement of T_c are observed. The superconductivity is suppressed, however, when the thickness of the FeSe film is further increased from 127 nm to 160 nm. The highest T_c^{onset} and T_c^{zero} (up to 15.1 K and 13.4 K) are obtained for the film with a thickness of 127 nm (#FS3), which is more than double that in FeSe polycrystalline bulks. Full range ρ-T data from room temperature to 4.2 K is also given in the inset of Fig. 4-5 (a), showing completely different temperature dependences: insulator-like behaviour with a negative temperature coefficient appears in ultra-thin #FS1, while the other samples behave in a metallic way. The temperature dependence of the upper critical magnetic field $H_{c2}(T)$ is plotted in Fig. 4-5 (b), with the linear extrapolations to T = 0 K shown in the inset. H_{c2} is determined as a function of T_c^{mid} (defined as the temperature at which the resistivity has dropped to one-half of the normal state (at onset) value). The estimated H_{c2} values of #FS2, #FS3, and #FS4 are 27.8 T, 35.5 T, and 31.5 T, respectively. So far, the T_c and H_{c2} values in this work are the highest among the reported pure FeSe thin films with practical thickness.

There is an empirical principle that a large ratio of lattice constants, c/a,

generally accompanies high T_c values in the Fe-chalcogenide system. The c/a values together with the corresponding T_c^{zero} in this work have been added to the results from Nabeshima *et al.*'s work[45] and plotted in Fig. 4-5 (c). Our FeSe thin films basically coincide with the monotonically increasing T_c dependence on c/a (shown as a dashed line) except for #FS2. It is speculated that relatively low thickness of FeSe layer might contribute to the deviation from the empirical c/a - T_c^{zero} dependence. When the film gets thicker, it gradually resembles like a bulk material, which is well fitted with the dashed line. The potential for obtaining higher superconducting T_c in the FeSe system with a larger c/a ratio is well reflected in this work. The follow-up research will be focused on clarifying the reason of SIT and the suppressed superconductivity in overly-thick #FS4. The clarification on either of the above issues can provide valuable hints for further enhancing the superconducting performance in the atmosphere-stable FeSe thin films.

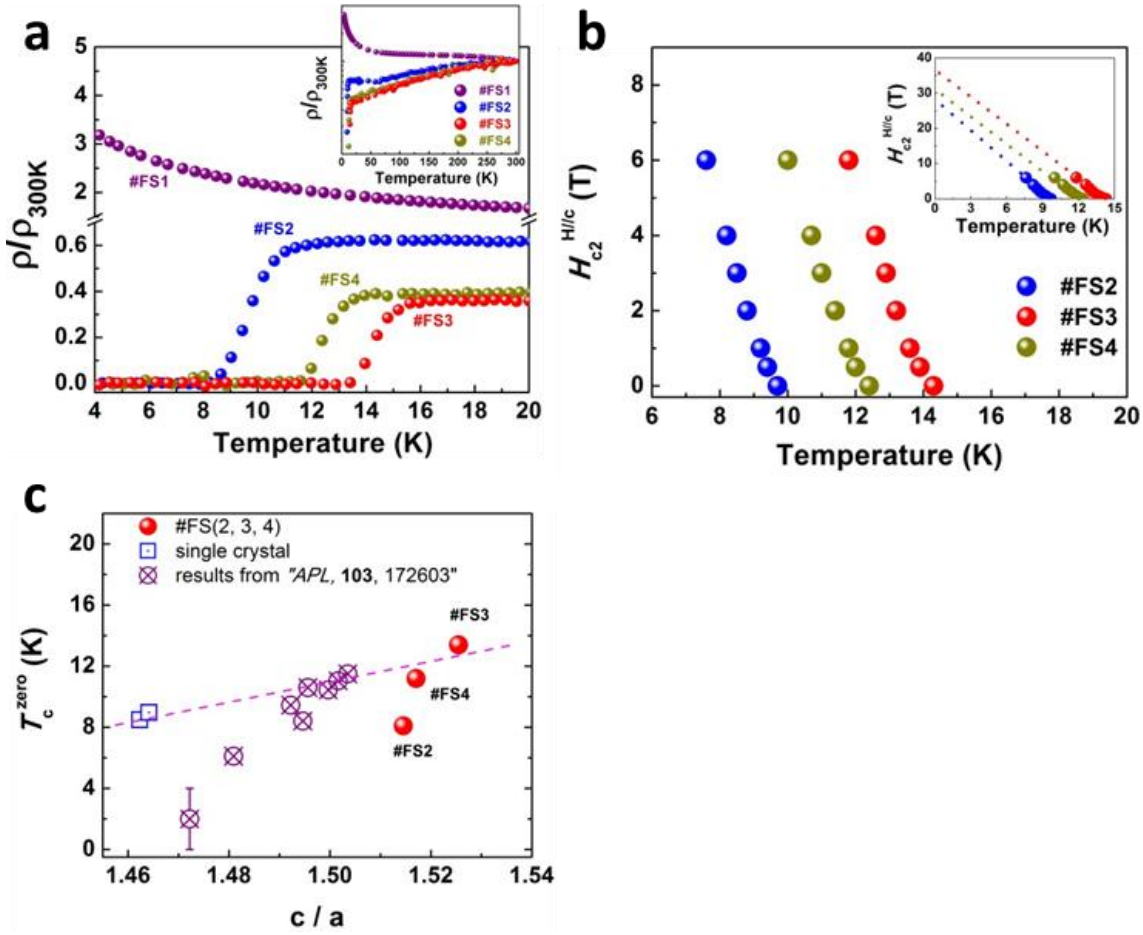

Figure 4-5. ρ via T, H_{c2} via T, and T_c^{zero} via c/a results. (a) Temperature dependence of the resistivity at self-field for FeSe films with different thicknesses from 4 K to 20 K. Inset is the full range ρ-T data from 300 K to 4.2 K. (b) Plots of the upper critical field (H_{c2}) as a function of T_c^{mid} for the three FeSe films

showing superconductivity. The linear extrapolations to T = 0 K are shown in the inset. (c) T_c^{zero} values as a function of c/a. The values for the superconducting FeSe films in this work (#FS2, #FS3, and #FS4) are added into the previous results from Ref. [45].

It has been proved that significant deviation from the 1:1 ratio of Fe:Se might give rise to suppression of superconductivity[46-47]. The superconductivity of $Fe_{1+\delta}Se$ bulks can be easily destroyed by tiny changes (< 5 at. %) in Fe:Se stoichiometry[46]. The chemical compositions of all the samples were acquired by using STEM-EDS technology. For better universality, only the regions that can cover the entire FeSe layer as much as possible were selected as the characterizing area (in the case of #FS4, the areas free of Fe-rich phases were selected). The analyzed Fe/Se ratios are illustrated by the green columns in Fig. 4-6. The stoichiometric deviation is simplified as the amount of excess Fe (at. %) with respect to Fe:Se = 1:1. In accordance with the previous scenario, #FS3, which has the smallest stoichiometric deviation compared to the other samples, therefore exhibits the best superconductivity. In #FS2 and #FS4, T_c^{onset} deteriorates due to the deviation from 1:1 FeSe stoichiometry. In the ultra-thin #FS1, however, no superconducting transition is detected down to 2 K. Although the abundant amount of excess Fe (about 38 at. %) brings about a huge stoichiometric deviation, there is no significant change in the c/a ratio of #FS1 compared with other samples (shown in Table 4-1). Apparently, the chemical composition is impacted by some other reasons. Considering the thickness of #FS1 is only 8 nm (< 20 unit cells), the interface issue might play a vital role in the absence of superconductivity.

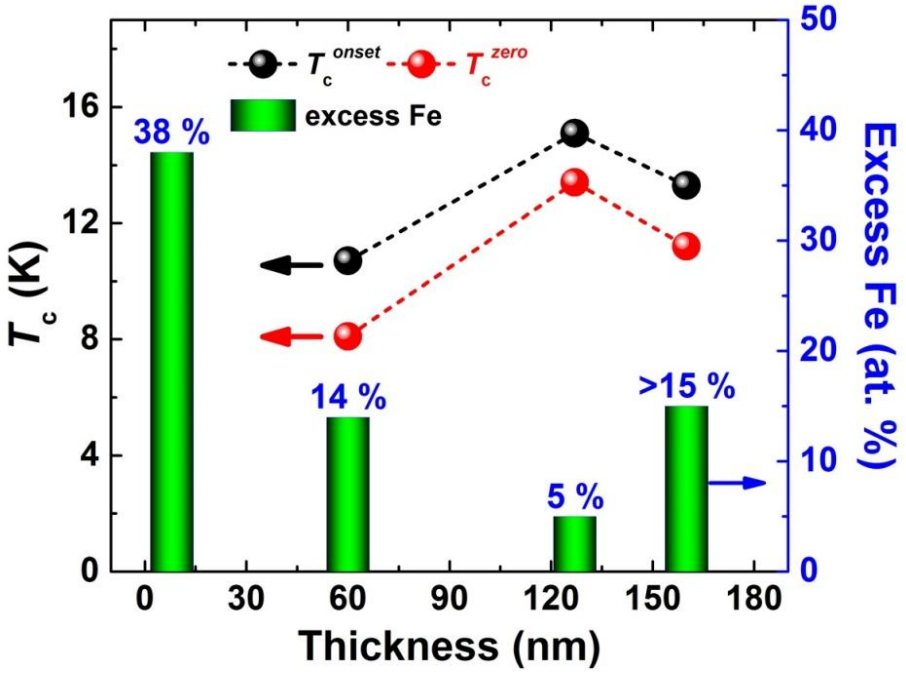

Figure 4-6. Thickness dependence of T_c^{onset} and the amount of excess Fe (at. %). Left y-axis: the dependence of T_c^{onset} on FeSe thickness. No superconductivity is detected in #FS1. Right y-axis: the ratio of Fe:Se is simplified as the amount of excess Fe over the stoichiometric ratio and illustrated in the form of columns.

In the field of Fe-based superconductors, research on the interface has been one of the most exciting topics since the superconducting gap was found to be open at 43 K in the unit-cell FeSe/STO system[19]. The record value for the highest temperature at which the superconducting gap remains open (T_{SC}) has been broken several times recently through elaborate interface engineering[22, 24, 28, 48] on STO substrate. In this case, CaF_2 was used as the growth substrate rather than STO. Therefore, research on the FeSe/CaF_2 interface is urgently needed for follow-up work. Atomic-resolution micrographs provide the most outstanding way to visualize the microstructure of crystalline objects. In this work, cross-sectional STEM micrographs were collected from all the samples. One typical STEM image (viewed along [101] direction) captured on #FS1 is shown in Fig. 4-7 (a). While taking this image, the adjacent area between the FeSe layer and the substrate was intentionally targeted in order to acquire as much the detailed information about FeSe/CaF_2 interface as possible. From the cross-sectional image, three different layers can be clearly distinguished. FeSe with the standard layered structure (Se-Fe-Se) is observed on the top of the image. Cubic CaF_2 substrate is located at the bottom. In addition, a crystalline interlayer with the cubic structure is found between the FeSe layer and the CaF_2 substrate. Interestingly, same form of interlayer exists in all four FeSe specimens in this work and its thickness (≈ 3 nm) has nothing to do with the upper FeSe layer. Similar interlayer has already been observed by Braccini *et al.*[39], Hanawa *et al.*[36], Mele *et al.*[49], Ichinose *et al.*[50], and Horide *et al.*[51] in Fe(Te, Se)/CaF_2 structure, but neither the resolution nor the composition was clear enough for phase identification. Local FFT pattern for an area covering both lattices of interlayer and CaF_2 substrate is shown in Fig. 4-7 (b). Two sets of pattern with the same crystal structure are clearly observed and marked out by red (smaller lattice) and purple (bigger lattice) circles.

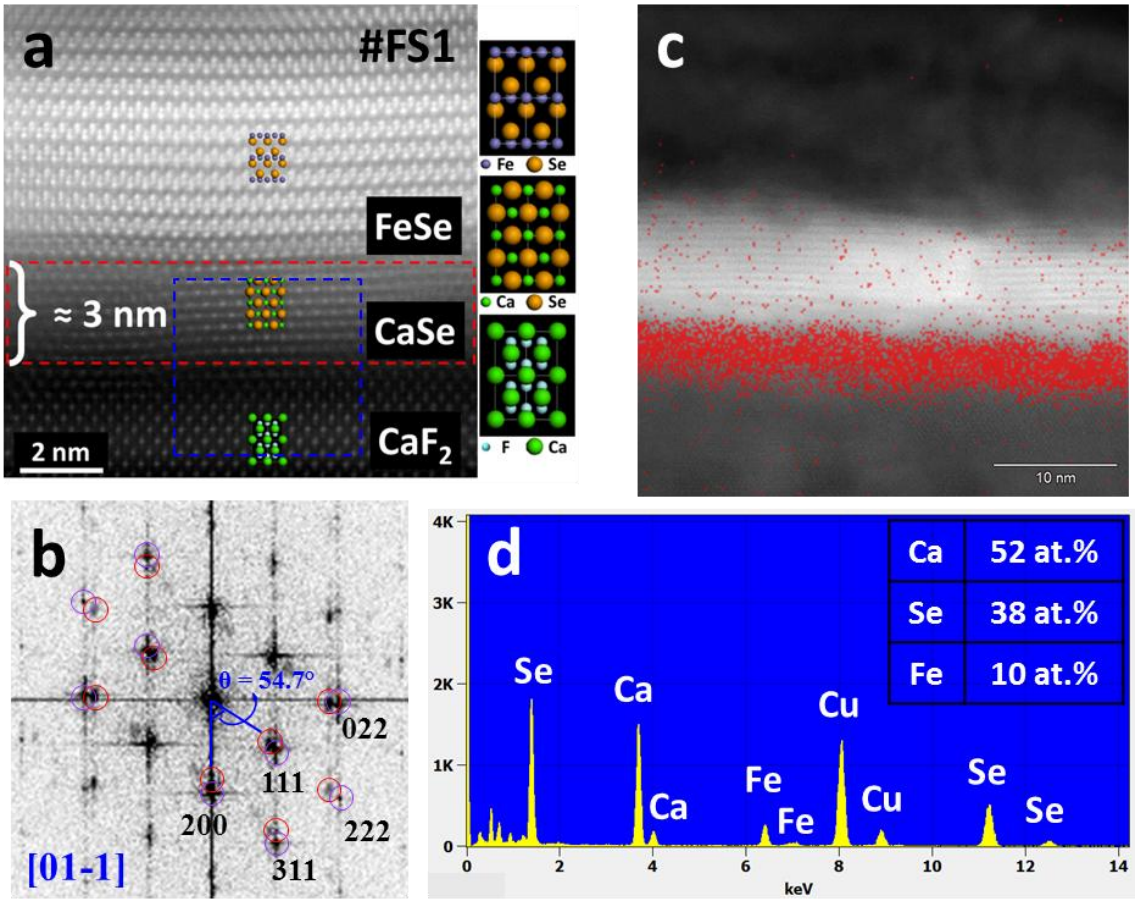

Figure 4-7. The identification of CaSe resulting from STEM results. (a) Cross-sectional view on a FeSe/CaF_2 interfacial region in #FS1. A crystalline interlayer (highlighted with red rectangle) is identified in middle part. The corresponding 2 unit-cells crystal models of FeSe, CaSe, and CaF_2 are provided on the right side. (b) Two sets of diffraction patterns are observed in the FFT pattern for an area (blue square in (a)) containing both the interlayer and CaF_2. (c) The chemical composition of the interlayer (red strip) is identified by PCA method based on EDS results. The corresponding spectrum and calculated atomic percentages of Ca, Se and Fe elements are provided in (d).

EDS analysis is carried out afterwards on the same area. According to the PCA results, an interlayer with a specific element composition is confirmed to lie between FeSe layer and CaF_2 substrate (red strip in Fig. 4-7 (c)). Fig. 4-7 (d) provides the corresponding spectrum, from which the atomic percentages of Ca (≈ 52 at. %), Se (≈ 48 at. %) and Fe (≈ 10 at. %) elements in the interlayer are determined. Obviously, Ca and Se are the major elements in this region, while little Fe is also detected. The portion of Fe element results from free Fe phases which occupy almost same area as CaSe interlayer, which will be discussed later. By measuring the lattice constant in Fig. 4-7 (a) (error are minimized by a normalization subject to CaF_2 lattice), the lattice parameter is found as $a \approx 5.908$ Å, which has only a tiny difference (-0.07 %) compared with the standard CaSe (group: *Fm-3m*, $a_0 \approx 5.912$ Å). Similar results are also obtained from the

other samples with larger thickness. As a result, it is speculated that CaSe is the principal phase in FeSe/CaF_2 interlayer. This is the first time that the interface between FeSe and CaF_2 substrate has been distinctly observed and identified. Further investigation might reveal more about the nature of CaSe interlayer and its influence on the superconducting performance of upper FeSe thin films. In addition, the corresponding 2 unit-cell crystal models for FeSe, CaSe, and CaF_2 are illustrated on the ride side of Fig. 4-7 (a). Purple, orange, green, and aqua spheres refer to Fe, Se, Ca, and F atoms, respectively. Apparently, the CaSe crystal model is well fitted with the realistic lattice of the interlayer.

A series of schematics are illustrated in Fig. 4-8 (a) – (c) to describe the possible formation mechanism of a CaSe interlayer in the FeSe/CaF_2 structure. Fig. 4-8 (a) shows the first stage in the preparation procedure of FeSe films. Generally, Se and Fe which are simultaneously bombarded out of the target material are supposed to form FeSe composite on the CaF_2 substrate. However in fact, some F-vacancies exist in the top few layers of CaF_2 substrate, which is revealed by the X-ray Photoelectron Spectroscopy (XPS) results (shown in Fig. 4-9). In order to investigate the chemical concentration of Ca and F elements, F 1s and Ca 2s are chosen as the characteristic peaks. According to the calculation, the atomic concentration for Ca and F are 37.69 at. % and 62.31 at.%, respectively, which shows a slight F-deficiency as 13.07 at. % subject to the standard stoichiometric ratio of CaF_2 composite (Ca : F = 1:2). This is one of the evidences that indicate a slight deficiency in F element subject to the standard stoichiometric ratio of Ca : F = 1:2. Considering that XPS only reveals the top few atomic layers of the specimen, some F-vacancies are supposed to exist near the surface of CaF_2 substrate. Furthermore, from the thermodynamic point of view, the Gibbs energy of formation of CaSe is lower than that of FeSe, which means Se is prone to react with Ca first rather than with Fe. Hence, in this case, the deposited Se prefers to occupy the F-vacancies in the top few layers of CaF_2 substrate, and then react with Ca forming CaSe interlayer prior to the formation of FeSe layer. Similar cubic CaSe lattices are also found in #FS3 and #FS4, as shown in Fig. 4-8 (d) and (e), respectively.

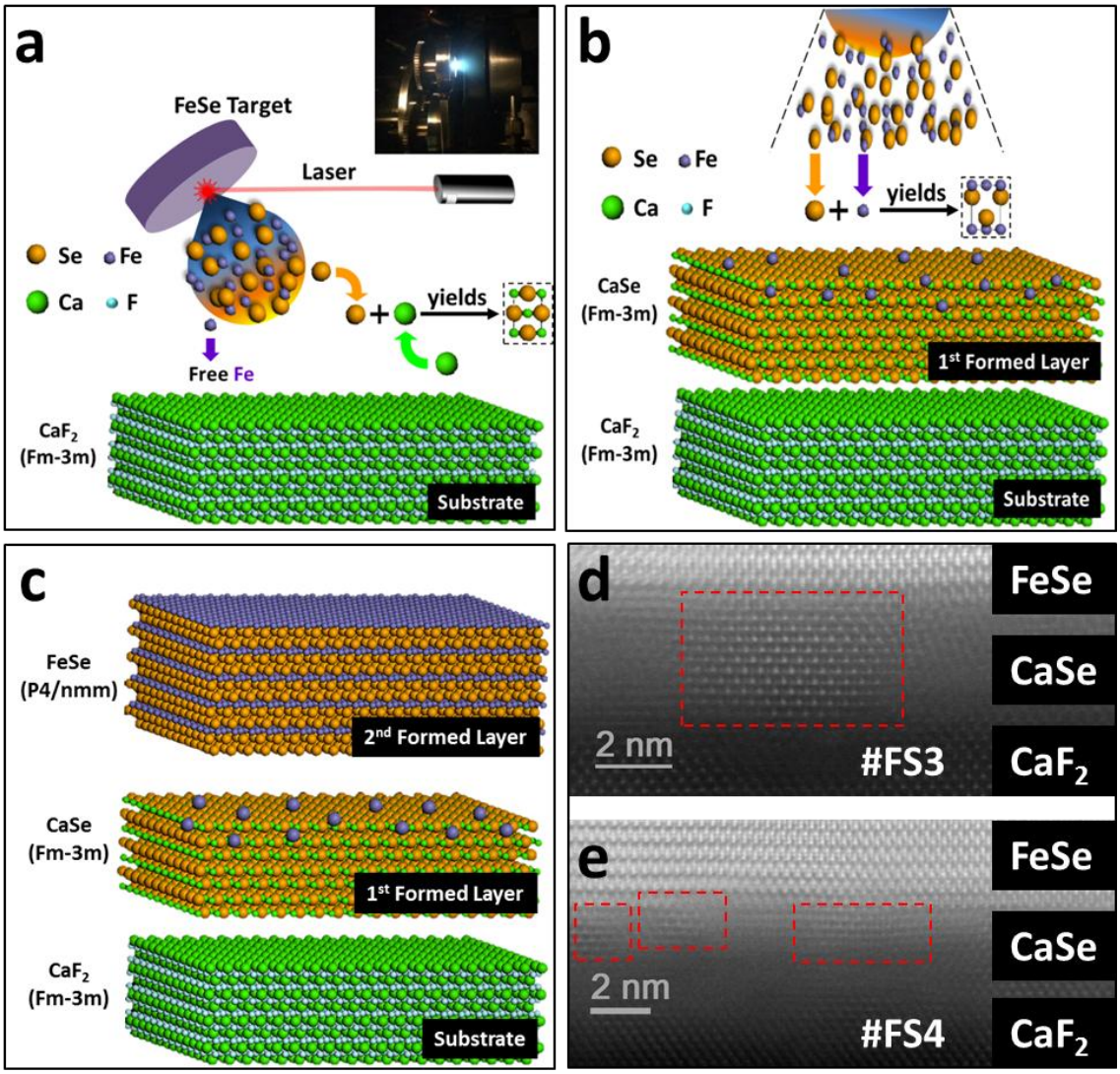

Figure 4-8. The schematic for the FeSe/CaSe layered structure on CaF_2 substrate in this work. (a) At the first stage, Se and Fe are bombarded out of the target. CaSe layer combined with Se and Ca (from the substrate) is formed prior to FeSe composite, leaving free Fe distributes near FeSe/CaSe interface. A photograph showing the real deposition process in the PLD chamber is given on the top right corner. (b) Once the CaSe layer reaches to a certain thickness (≈ 3 nm), the follow-up Se can no longer react with Ca so that FeSe starts to form. (c) The schematic model for a FeSe/CaSe/CaF_2 tri-layer structure. (d) & (e) Similar CaSe lattices found in #FS3 and #FS4 (red rectangles) by cross-sectional STEM.

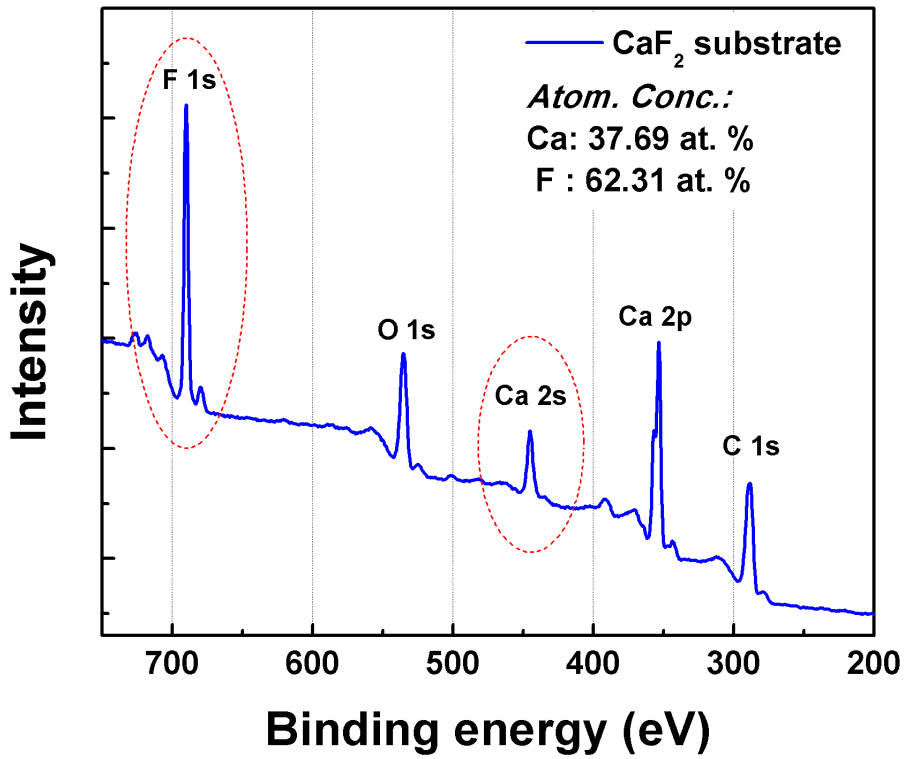

Figure 4-9. XPS spectrum for a CaF_2 (100) single-crystal substrate. Dashed oval indicates the characteristic peaks used to calculate the atomic concentration of Ca and F elements.

If the reaction between Ca and Se happens, there must be excess Fe elements left somewhere at the interfacial region. The speculation is demonstrated by the regional HRTEM and EDS results given in Fig. 4-10. The HRTEM image was taken along [101] direction so that typical structures of tetragonal FeSe and cubic CaF_2 can be distinguished. Apart from CaSe lattice, another set of bright phases (highlighted by dashed black circles) is observed to distribute sporadically close to the top side of CaSe region. The lattice of CaSe is blurry here because the bright areas are being focused. A line EDS profile scan is carried out along the horizontal direction to collect the statistical net counts of Fe and Se elements from this area. Consequently, the bright areas are found to be rich in Fe element, while lack of Se element in the same region. Considering the EDS results are acquired as a sum of projection, the yield for Se element should be the contribution of CaSe from the same column. The wave-shaped line profile indicates interval emergence of Fe-rich areas and CaSe phases.

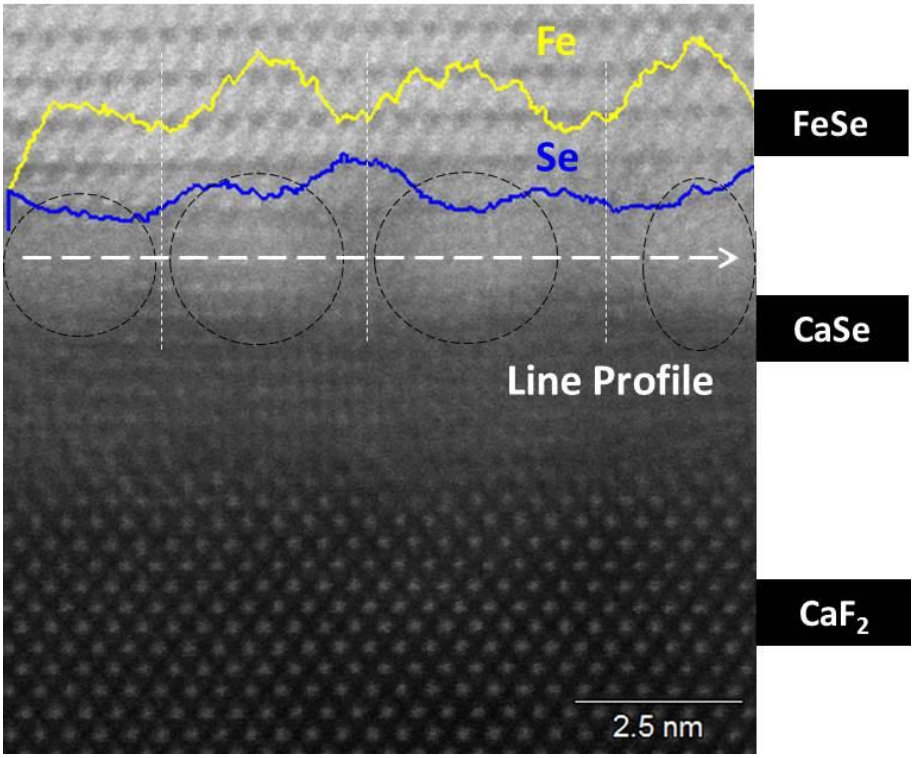

Figure 4-10. EDS results on the cross-sectional high resolution STEM image for one FeSe/CaF_2 interfacial area. The relative net counts for Fe and Se elements are exhibited as yellow and blue lines, respectively (the dashed white arrow indicates the scanning direction of the EDS line profile). Black circles marked out the regions with relatively high Fe net counts. Vertical dashed lines are guide for the eyes.

Due to the periodical distribution of Fe-rich phases discussed above, CaSe interlayers are generally not homogeneous along the horizontal direction. Further investigation discovered that most of the CaSe phases are in the shape of inverted-trapezoids from a cross-sectional view, as shown in Fig. 4-11. In this case, CaF_2 substrate is the only Ca source for CaSe composition. It is extremely difficult for Se to substitute Ca from CaF_2 which is formed by ionically-bonded Ca and F at the temperature as low as 300 ℃. F-vacancies (verified by XPS result in Fig. 4-9) are thought to be the best possible way through which Se might have a chance to react with Ca. In addition, it is easy to infer that the density of F-vacancies has a descending gradient downwards. Thus, CaSe phases eventually form into inverted-trapezoid shape in cross-sectional view (marked by white dashed lines in Fig. 4-11. Based on this phenomenon, the CaSe phases are considered to form in the F-vacancy areas which distribute dispersedly on *ab* plane and diminish in density along *c* plane. The shape of CaSe phases is closed to frustum of a cone in 3-dimension. With the increment of the thickness of CaSe interlayer, it gets harder for Se to further interact with the Ca from the

substrate. As a result, typical tetragonal FeSe composite starts to form once CaSe interlayer reaches a certain thickness (≈ 3 nm), regardless of the thickness of the upper FeSe layer.

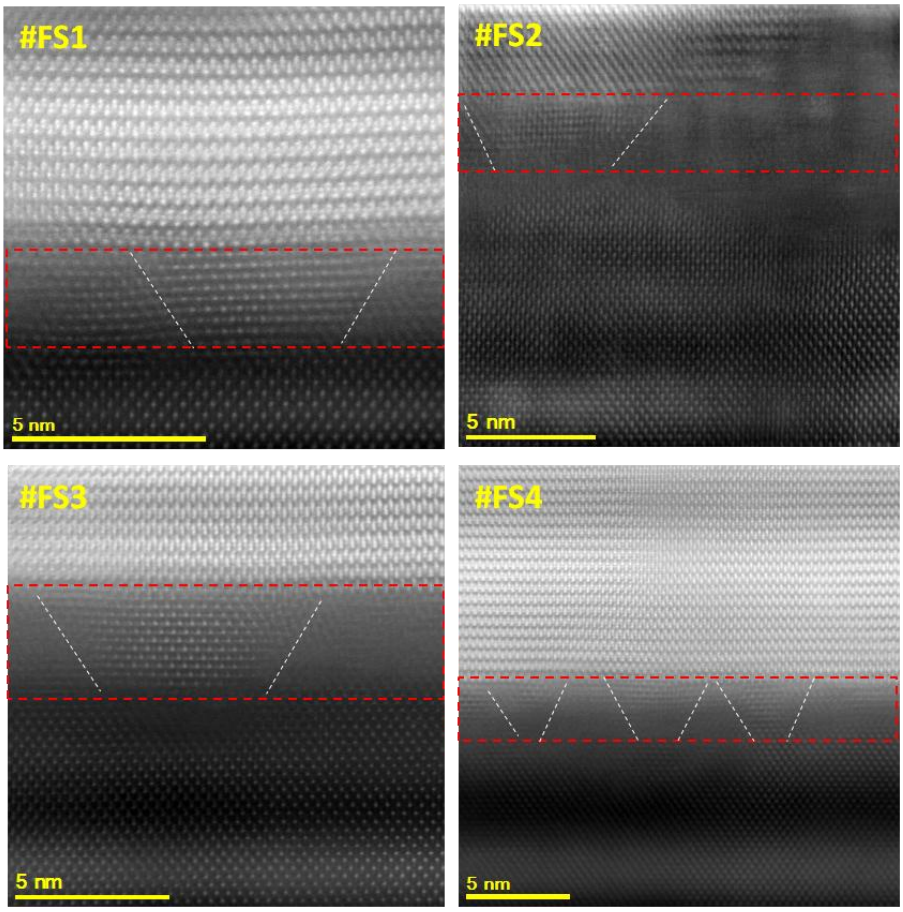

Figure 4-11. Cross-sectional high-resolution STEM images for the FeSe/CaF_2 interfacial areas of all four film samples. The CaSe interlayers are highlighted with dashed rectangles. A general shape of CaSe sites as inverted-trapezoid is recognized and marked by white dashed lines.

Obviously, the prerequisite of forming CaSe interlayer is that part of Se was seized at the interface of FeSe/CaF_2 . That is to say, a stoichiometric deviation occurs in the FeSe layer as a compensation for the formation of CaSe interlayer. Especially in the case of #FS1, which has a comparable thickness (8 nm) to the CaSe layer (≈ 3 nm), the negative effect is significantly amplified (about 38 at. % Fe excess). The severe Se deficiency is considered as the main factor that might lead to the insulator-like behaviour in #FS1. Based on the results and discussions above, put an additional Se pre-deposition procedure is put forward to restore the superconductivity in this case. The Se-deficiency in the ultra-thin FeSe film is expected to be compensated by intentionally growing a CaSe layer prior to the deposition of FeSe material. Nevertheless, whether the texture and roughness of the growth surface is still good enough for subsequent

FeSe growth is elusive and needs to be clarified in further work.

It is also noticed that localized bending exists in FeSe layers in Fig. 4-7 (a). It might be another negative factor that renders the absence of superconductivity in thin films, especially for the case of ultra-thin #FS1 (≈ 8 nm / 15 unit cells). Similar case of strain-induced T_c suppression is also reported in La-based cuprates[52-54]. Few more cross-sectional images on #FS1 were photographed with the results shown in Fig. 4-12 (a) - (d) (the area shown in Fig. 4-12 (a) is same as that in Fig. 4-7 (a)). Similar "bending" features are also found in Fig. 4-12 (b) but absent in Fig. 4-12 (c) & (d), indicating that this bending issue is a localized phenomenon rather than a general one. Through careful observation, the "bending" feature is attributed to the different out-of-plane orientations of FeSe atomic layers which are interlacing with each other at small angles. The inferred formation mechanism is illustrated in Fig. 4-12 (e). As FeSe film grows on CaF_2 substrate in a highly epitaxial way, any defect (such as steep step) on the surface of CaF_2 will be inherited and duplicated into FeSe layers. As a result, the FeSe layers above CaF_2 defects exhibit the observed local "bending" features. However, the rough facial defect from CaF_2 substrate can be weaken with the CaSe interlayer serving as an intermediate buffer, and the roughness gets further alleviated when the thickness of FeSe layer increases.

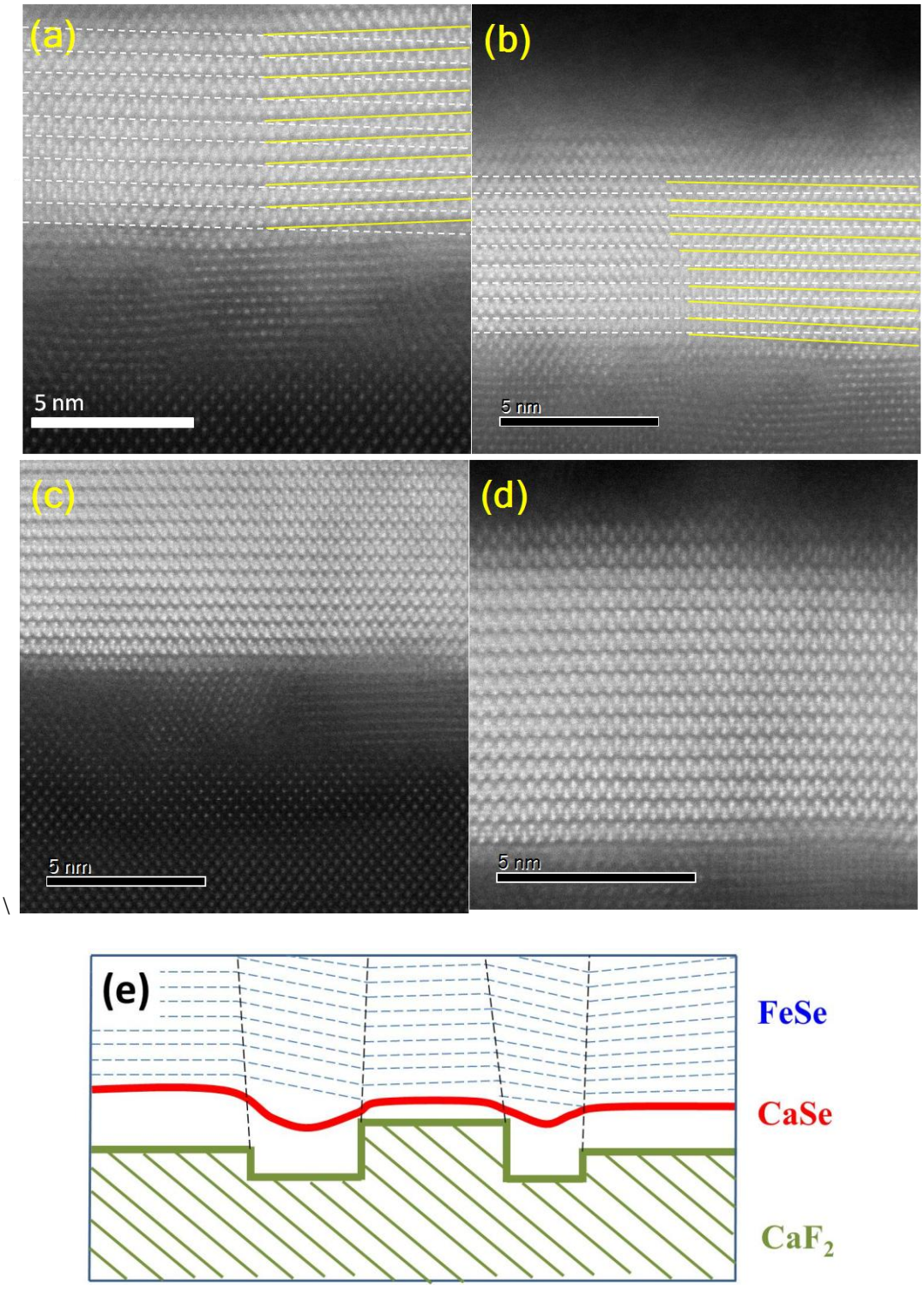

Figure 4-12. Cross-sectional STEM images on different areas of #FS1. Localized lattice distortions are found in (a) and (b), while well aligned FeSe layers exist in (c) and (d). Different orientations of FeSe layers are indicated by white and yellow lines. (e) A schematic diagram showing the evolution of lattice distortion from CaF_2 substrate, through CaSe interlayer, to FeSe layers.

Although the existence of a CaSe interlayer is universal and has nothing to do with the thickness of upper FeSe layer, its influence on varying the stoichiometry of

FeSe becomes gradually negligible when the film thickness increases. Eventually, superconductivity emerges in thicker FeSe thin films with much smaller Se-deficiency / Fe-excess (Fig. 4-6).

As seen in Table 4-1, the T_c of #FS4, which has the thickest FeSe layer, shifts to a lower temperature than that of #FS3. It is speculated that some other factor results in the degradation of superconductivity. When investigating the morphologies of the FeSe thin films by FESEM (shown in Fig. 4-13), massive particles (about 100 – 200 nm in size) were found homogeneously distributing in #FS4, while the other samples show much better surface quality. The images were collected by FESEM at 5.0 kV. Similar lumps recognized as Fe phases were also reported by Jung *et al.*[55] in their $FeSe_{1-x}$/STO and $FeSe_{1-x}$/LAO thin films.

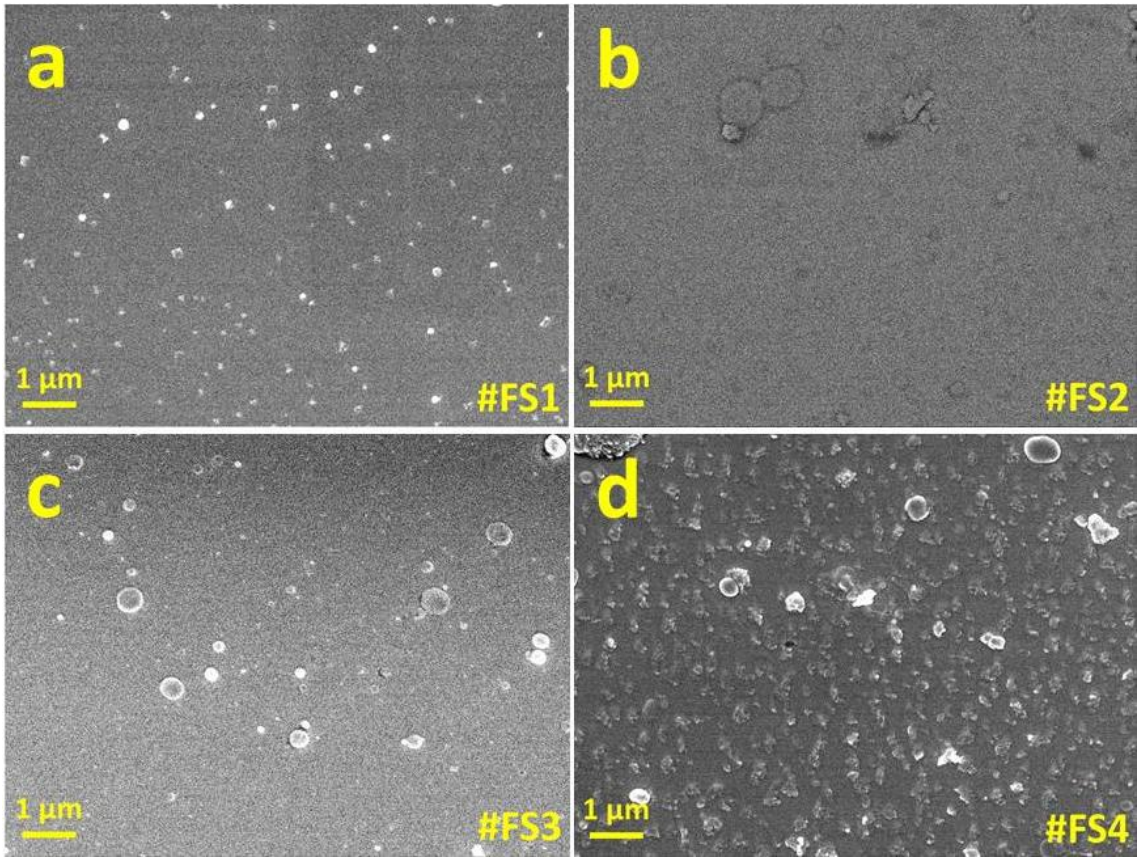

Figure 4-13. Surface morphologies of the four FeSe thin films in this work taken by FESEM : (a) #FS1; (b) #FS2; (c) #FS3; (d) #FS4. Massive amounts of particles were only found in #FS4.

In Fig. 4-14, detailed STEM characterizations were carried out to clarify the nature of the massive precipitates. In Fig. 4-14 (a1), one precipitate is captured inside FeSe layer in #FS4. EDS PCA results for the corresponding area are shown in Fig. 4-14 (b1), (c1) and (d1) with the corresponding spectra given in Fig. 4-14 (b2), (c2) and (d2). Apart from FeSe phase (Fe: Se = 51:48 at. %) and CaF_2, another phase with exactly the

same shape as the precipitate in Fig. 4-14 (a1) is distinguished. Fe is the major element consisting in this phase with the atomic percentage as high as 83 % (while for Se is only 17 at. %), which indicating it to be rich in Fe element. To further confirm the speculation, In Fig. 4-14 (a2), SAED pattern was acquired targeting the nearby area in Fig. 4-14 (a1). Along [010] zone axis, a batch of planes is indexed as a result of α-Fe. A high-resolution STEM image for the precipitate is taken and shown in Fig. 4-14 (a3). α-Fe (200) planes are clearly observed with a *d*-spacing measured as 1.47 Å, which is very close to the standard one as 1.4340 Å (*Im-3m*). Furthermore, the corresponding FFT pattern in the inset is assigned and well matched with the typical α-Fe pattern from $[10\bar{2}]$ direction. Therefore, the numerous precipitates in #FS4 are proved to be Fe-rich phases with α-Fe as the main component, which is ferromagnetic and could lead to the suppression of superconductivity the FeSe layer[56]. Nabeshima *et al.*[45] reported the disorder from the excess Fe forms near the surface of the FeSe layer due to the high vapour pressure of Se in thick films. Inspired by the work of Schneider *et al.*[57], an additional Se target or higher Se fraction in the FeSe target is expected to be helpful in reducing the Se deficiency during the deposition process. Further investigation is needed to determine the formation mechanism of the Fe-rich phase.

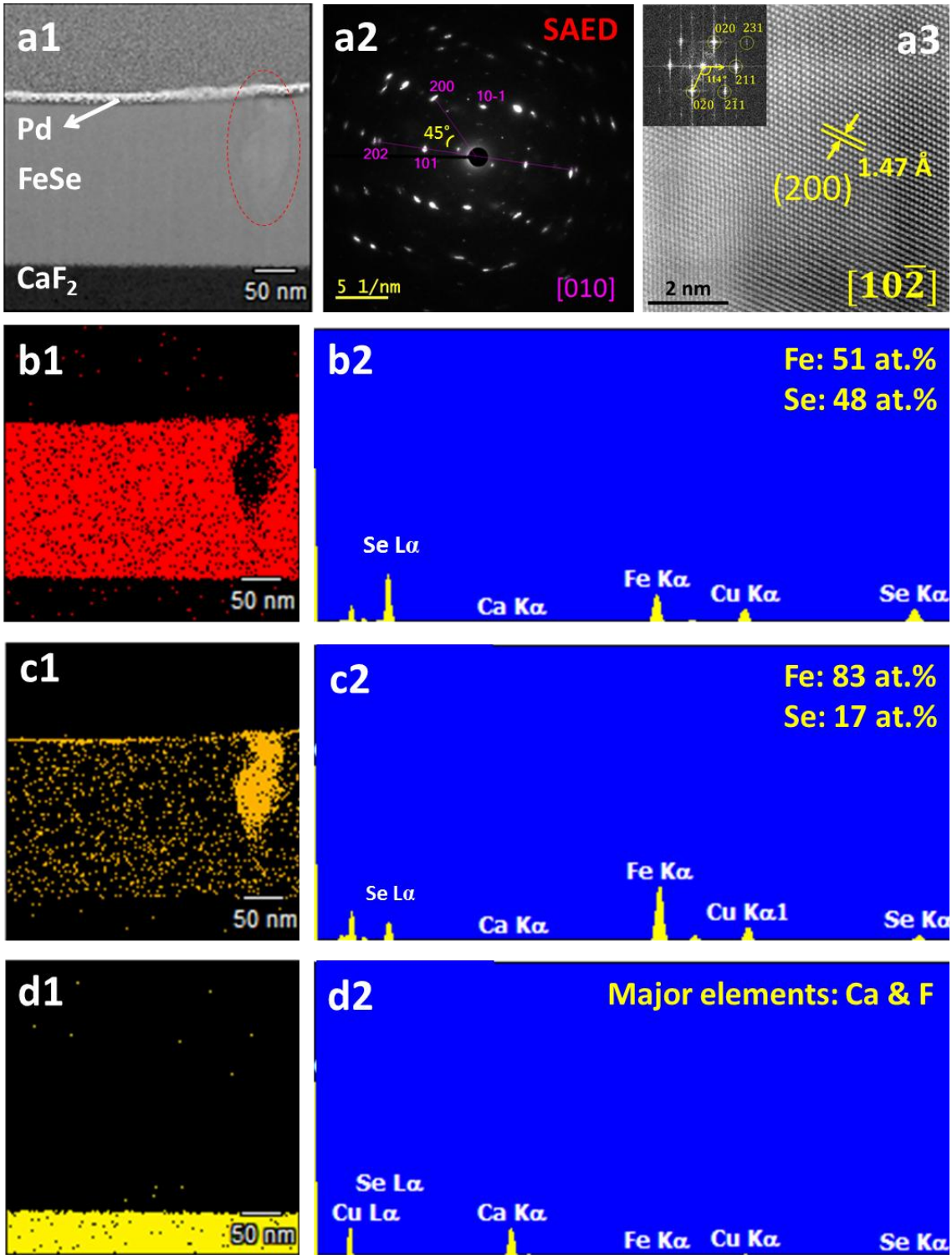

Figure 4-14. Identification of the massive precipitates found in #FS4. (a1) A cross-sectional STEM image for #FS4 with a secondary phase marked by red oval. (b1), (c1) & (d1) For the same area as in (a1), three main phases (FeSe (b1), Fe-rich phase (c1), and CaF_2 (d1)) are distinguished by PCA. The corresponding EDS spectra are given in (b2), (c2) and (d2) with the composition of major elements given on the corner. (a2) SAED pattern targeting the nearby area in (a1). The Miller Indices are indexed α-Fe planes. (a3) High-resolution STEM image for one Fe-rich phase. The corresponding FFT pattern is shown in the inset.

4.4 Conclusions

In summary, high quality and atmosphere-stable FeSe thin films on CaF_2 (100) substrate have been fabricated by PLD technique. Via increasing film thickness, the evolution of superconductivity, including the SIT phenomenon, the highest T_c^{zero} reported, up to 13.4 K, and the degradation in superconductivity in an overly-thick FeSe thin film are observed. The T_c value in this work is the highest reported to date in the class of FeSe thin films with practical thickness. According to the STEM investigations, a CaSe interlayer around 3 nm thick universally exists between FeSe and CaF_2, regardless of the thickness of the FeSe layer. The ultra-thin (8 nm) FeSe thin film exhibits insulating ρ-T behaviour with the excess Fe amounting to 38 at. %, which mainly results from the severe Se deficiency caused by this CaSe interlayer. Although the influence of CaSe becomes negligible as the FeSe layer becomes thicker, the superconductivity is suppressed in the overly-thick (160 nm) FeSe film as a result of the emergence of massive Fe-rich precipitates. In addition, a pre-deposition of Se and the simultaneous deposition of Se with FeSe are proposed for the purpose of compensating the Se deficiency in the FeSe layer. The results not only clarify the existence of the CaSe interlayer, but also prove the feasibility of exploring the mechanism of the FeSe superconducting thin films on the atomic level via the STEM technique.

4.5 References

(1) Chen, X. H.; Wu, T.; Wu, G.; Liu, R. H.; Chen, H.; Fang, D. F. Superconductivity at 43 K in $SmFeAsO_{1-x}F_x$. *Nature* **2008,** *453*, 761-762.
(2) Rotter, M.; Tegel, M.; Johrendt, D. Superconductivity at 38 K in the Iron Arsenide $(Ba_{1-x}K_x)Fe_2As_2$. *Phys. Rev. Lett.* **2008,** *101*, 107006.
(3) Wang, X. C.; Liu, Q. Q.; Lv, Y. X.; Gao, W. B.; Yang, L. X.; Yu, R. C.; Li, F. Y.; Jin, C. Q. The Superconductivity at 18 K in LiFeAs System. *Solid State Commun.* **2008,** *148*, 538-540.
(4) Hsu, F.-C.; Luo, J.-Y.; Yeh, K.-W.; Chen, T.-K.; Huang, T.-W.; Wu, P. M.; Lee, Y.-C.; Huang, Y.-L.; Chu, Y.-Y.; Yan, D.-C.; Wu, M.-K. Superconductivity in the PbO-type Structure Alpha-FeSe. *Proc. Natl. Acad. Sci. U.S.A.* **2008,** *105*, 14262-14264.
(5) Mizuguchi, Y.; Tomioka, F.; Tsuda, S.; Yamaguchi, T.; Takano, Y. Superconductivity at 27K in Tetragonal FeSe Under High Pressure. *Appl. Phys. Lett.* **2008,** *93*, 152505.
(6) Margadonna, S.; Takabayashi, Y.; Ohishi, Y.; Mizuguchi, Y.; Takano, Y.; Kagayama, T.; Nakagawa, T.; Takata, M.; Prassides, K. Pressure Evolution of the Low-temperature Crystal Structure and Bonding of the Superconductor FeSe (T_c = 37 K). *Phys. Rev. B* **2009,** *80*, 064506.
(7) Medvedev, S.; McQueen, T. M.; Troyan, I. A.; Palasyuk, T.; Eremets, M. I.; Cava, R. J.; Naghavi, S.; Casper, F.; Ksenofontov, V.; Wortmann, G.; Felser, C. Electronic and Magnetic Phase Diagram of beta-$Fe_{1.01}Se$ with Superconductivity at 36.7 K Under Pressure. *Nat. Mater.* **2009,** *8*, 630-633.
(8) Millican, J. N.; Phelan, D.; Thomas, E. L.; Leão, J. B.; Carpenter, E. Pressure-induced Effects on the Structure of the FeSe Superconductor. *Solid State Commun.* **2009,** *149*, 707-710.
(9) Bendele, M.; Ichsanow, A.; Pashkevich, Y.; Keller, L.; Strässle, T.; Gusev, A.; Pomjakushina, E.; Conder, K.; Khasanov, R.; Keller, H. Coexistence of Superconductivity and Magnetism in $FeSe_{1-x}$ Under Pressure. *Phys. Rev. B* **2012,** *85*, 064517.
(10) Yeh, K.-W.; Huang, T.-W.; Huang, Y.-l.; Chen, T.-K.; Hsu, F.-C.; Wu, P. M.; Lee, Y.-C.; Chu, Y.-Y.; Chen, C.-L.; Luo, J.-Y.; Yan, D.-C.; Wu, M.-K. Tellurium Substitution Effect on Superconductivity of the α-phase Iron Selenide. *EPL* **2008,** *84*, 37002.
(11) Liu, T. J.; Hu, J.; Qian, B.; Fobes, D.; Mao, Z. Q.; Bao, W.; Reehuis, M.; Kimber, S. A.; Prokes, K.; Matas, S.; Argyriou, D. N.; Hiess, A.; Rotaru, A.; Pham, H.; Spinu, L.; Qiu, Y.; Thampy, V.; Savici, A. T.; Rodriguez, J. A.; Broholm, C. From (pi,0) Magnetic Order to Superconductivity with (pi,pi) Magnetic Resonance in $Fe_{1.02}Te_{1-x}Se_x$. *Nat. Mater.* **2010,** *9*, 716-720.
(12) Mizuguchi, Y.; Tomioka, F.; Tsuda, S.; Yamaguchi, T.; Takano, Y. Superconductivity in S-substituted FeTe. *Appl. Phys. Lett.* **2009,** *94*, 012503.
(13) Han, Y.; Li, W. Y.; Cao, L. X.; Zhang, S.; Xu, B.; Zhao, B. R. Preparation and Superconductivity of Iron Selenide Thin Films. *J. Phys.: Condens. Matter.* **2009,** *21*, 235702.
(14) Lei, B.; Cui, J. H.; Xiang, Z. J.; Shang, C.; Wang, N. Z.; Ye, G. J.; Luo, X. G.; Wu, T.; Sun, Z.; Chen, X. H. Evolution of High-Temperature Superconductivity from a Low-T_c Phase Tuned by Carrier Concentration in FeSe Thin Flakes. *Phys. Rev. Lett.* **2016,** *116*, 077002.
(15) Tang, C.; Liu, C.; Zhou, G.; Li, F.; Ding, H.; Li, Z.; Zhang, D.; Li, Z.; Song, C.; Ji, S.; He, K.; Wang, L.; Ma, X.; Xue, Q.-K. Interface-enhanced Electron-phonon Coupling and High-temperature Superconductivity in Potassium-coated Ultrathin FeSe Films on $SrTiO_3$. *Phys. Rev. B* **2016,** *93*, 020507.
(16) Song, C.; Zhang, H.; Zhong, Y.; Hu, X.; Ji, S.; Wang, L.; He, K.; Ma, X.; Xue, Q.-K. Observation of Double-Dome Superconductivity in Potassium-Doped FeSe Thin Films. *Phys. Rev. Lett.* **2016,** *116*, 157001.
(17) Miyata, Y.; Nakayama, K.; Sugawara, K.; Sato, T.; Takahashi, T. High-temperature Superconductivity in Potassium-coated Multilayer FeSe Thin Films. *Nat. Mater.* **2015,** *14*, 775-779.
(18) Qiu, W.; Ma, Z.; Liu, Y.; Hossain, M. S. A.; Wang, X.; Cai, C.; Dou, S. X. Tuning Superconductivity in FeSe Thin Films via Mg Doping. *ACS Appl. Mater. Interfaces* **2016,** *8*,

7891-7896.
(19) Wang, Q.; Li, Z.; Zhang, W.; Zhang, Z.; Zhang, J.; Li, W.; Ding, H.; Ou, Y.; Deng, P.; Chang, K.; Wen, J.; Song, C.; He, K.; Jia, J.; Ji, S.; Wang, Y.; Wang, L.; Chen, X.; Ma, X.; Xue, Q.-K. Interface-Induced High-Temperature Superconductivity in Single Unit-Cell FeSe Films on $SrTiO_3$. *Chin. Phys. Lett.* **2012,** *29*, 037402.
(20) He, S.; He, J.; Zhang, W.; Zhao, L.; Liu, D.; Liu, X.; Mou, D.; Ou, Y. B.; Wang, Q. Y.; Li, Z.; Wang, L.; Peng, Y.; Liu, Y.; Chen, C.; Yu, L.; Liu, G.; Dong, X.; Zhang, J.; Chen, C.; Xu, Z.; Chen, X.; Ma, X.; Xue, Q.; Zhou, X. J. Phase Diagram and Electronic Indication of High-temperature Superconductivity at 65 K in Single-layer FeSe Films. *Nat. Mater.* **2013,** *12*, 605-610.
(21) Liu, D.; Zhang, W.; Mou, D.; He, J.; Ou, Y.-B.; Wang, Q.-Y.; Li, Z.; Wang, L.; Zhao, L.; He, S.; Peng, Y.; Liu, X.; Chen, C.; Yu, L.; Liu, G.; Dong, X.; Zhang, J.; Chen, C.; Xu, Z.; Hu, J.; Chen, X.; Ma, X.; Xue, Q.; Zhou, X. J. Electronic Origin of High-temperature Superconductivity in Single-layer FeSe Superconductor. *Nat. Commun.* **2012,** *3*, 931.
(22) Tan, S.; Zhang, Y.; Xia, M.; Ye, Z.; Chen, F.; Xie, X.; Peng, R.; Xu, D.; Fan, Q.; Xu, H.; Jiang, J.; Zhang, T.; Lai, X.; Xiang, T.; Hu, J.; Xie, B.; Feng, D. Interface-induced Superconductivity and Strain-dependent Spin Density Waves in FeSe/$SrTiO_3$ Thin Films. *Nat. Mater.* **2013,** *12*, 634-640.
(23) Cui, Y. T.; Moore, R. G.; Zhang, A. M.; Tian, Y.; Lee, J. J.; Schmitt, F. T.; Zhang, W. H.; Li, W.; Yi, M.; Liu, Z. K.; Hashimoto, M.; Zhang, Y.; Lu, D. H.; Devereaux, T. P.; Wang, L. L.; Ma, X. C.; Zhang, Q. M.; Xue, Q. K.; Lee, D. H.; Shen, Z. X. Interface Ferroelectric Transition near the Gap-Opening Temperature in a Single-Unit-Cell FeSe Film Grown on Nb-Doped $SrTiO_3$ Substrate. *Phys. Rev. Lett.* **2015,** *114*, 037002.
(24) Ge, J.; Liu, Z.; Liu, C.; Gao, C.; Qian, D.; Xue, Q.-K.; Liu, Y.; Jia, J. Superconductivity Above 100 K in Single-layer FeSe Films on Doped $SrTiO_3$. *Nat. Mater.* **2015,** *14*, 285-289.
(25) Wang, Z. F.; Zhang, H.; Liu, D.; Liu, C.; Tang, C.; Song, C.; Zhong, Y.; Peng, J.; Li, F.; Nie, C.; Wang, L.; Zhou, X. J.; Ma, X.; Xue, Q. K.; Liu, F. Topological Edge States in a High-temperature Superconductor FeSe/$SrTiO_3$(001) Film. *Nat. Mater.* **2016,** *15*, 968-973.
(26) Zhang, W.; Sun, Y.; Zhang, J.; Li, F.; Guo, M.; Zhao, Y.; Zhang, H.; Peng, J.; Xing, Y.; Wang, H.; Fujita, T.; Hirata, A.; Li, Z.; Ding, H.; Tang, C.; Wang, M.; Wang, Q.; He, K.; Ji, S.; Chen, X.; Wang, J.; Xia, Z.; Li, L.; Wang, Y.; Wang, J.; Wang, L.; Chen, M.; Xue, Q.-K.; Ma, X. Direct Observation of High-Temperature Superconductivity in One-Unit-Cell FeSe Films. *Chin. Phys. Lett.* **2014,** *31*, 017401.
(27) Lee, J. J.; Schmitt, F. T.; Moore, R. G.; Johnston, S.; Cui, Y. T.; Li, W.; Yi, M.; Liu, Z. K.; Hashimoto, M.; Zhang, Y.; Lu, D. H.; Devereaux, T. P.; Lee, D. H.; Shen, Z. X. Interfacial Mode Coupling as the Origin of the Enhancement of T_c in FeSe Films on $SrTiO_3$. *Nature* **2014,** *515*, 245-248.
(28) Zhang, Z.; Wang, Y.; Song, Q.; Liu, C.; Peng, R.; Moler, K. A.; Feng, D.; Wang, Y. Onset of the Meissner Effect at 65 K in FeSe Thin Film Grown on Nb-doped $SrTiO_3$ Substrate. *Sci. Bull.* **2015,** *60*, 1301-1304.
(29) Zhou, G.; Zhang, D.; Liu, C.; Tang, C.; Wang, X.; Li, Z.; Song, C.; Ji, S.; He, K.; Wang, L.; Ma, X.; Xue, Q.-K. Interface Induced High Temperature Superconductivity in Single Unit-cell FeSe on $SrTiO_3$(110). *Appl. Phys. Lett.* **2016,** *108*, 202603.
(30) Tang, C.; Zhang, D.; Zang, Y.; Liu, C.; Zhou, G.; Li, Z.; Zheng, C.; Hu, X.; Song, C.; Ji, S.; He, K.; Chen, X.; Wang, L.; Ma, X.; Xue, Q.-K. Superconductivity Dichotomy in K-coated Single and Double Unit Cell FeSe Films on $SrTiO_3$. *Phys. Rev. B* **2015,** *92*, 180507.
(31) Wen, C. H. P.; Xu, H. C.; Chen, C.; Huang, Z. C.; Lou, X.; Pu, Y. J.; Song, Q.; Xie, B. P.; Abdel-Hafiez, M.; Chareev, D. A.; Vasiliev, A. N.; Peng, R.; Feng, D. L. Anomalous Correlation Effects and Unique Phase Diagram of Electron-doped FeSe Revealed by Photoemission Spectroscopy. *Nat. Commun.* **2016,** *7*, 10840.
(32) Wang, M. J.; Luo, J. Y.; Huang, T. W.; Chang, H. H.; Chen, T. K.; Hsu, F. C.; Wu, C. T.; Wu, P. M.; Chang, A. M.; Wu, M. K. Crystal Orientation and Thickness Dependence of the Superconducting Transition Temperature of Tetragonal $FeSe_{1-x}$ Thin Films. *Phys. Rev. Lett.* **2009,** *103*, 117002.
(33) Schneider, R.; Zaitsev, A. G.; Fuchs, D.; H, V. L. Superconductor-insulator Quantum

Phase Transition in Disordered FeSe Thin Films. *Phys. Rev. Lett.* **2012,** *108*, 257003.
(34) Schneider, R.; Zaitsev, A. G.; Fuchs, D.; v. Löhneysen, H. Superconducting and Insulating Phases of Disordered FeSe Thin Films. *Eur. Phys. J. B* **2015,** *88*, 14.
(35) Imai, Y.; Akiike, T.; Hanawa, M.; Tsukada, I.; Ichinose, A.; Maeda, A.; Hikage, T.; Kawaguchi, T.; Ikuta, H. Systematic Comparison of Eight Substrates in the Growth of $FeSe_{0.5}Te_{0.5}$ Superconducting Thin Films. *Appl. Phys. Express* **2010,** *3*, 043102.
(36) Hanawa, M.; Ichinose, A.; Komiya, S.; Tsukada, I.; Akiike, T.; Imai, Y.; Hikage, T.; Kawaguchi, T.; Ikuta, H.; Maeda, A. Substrate Dependence of Structural and Transport Properties in $FeSe_{0.5}Te_{0.5}$ Thin Films. *Jpn. J. Appl. Phys.* **2011,** *50*, 053101.
(37) Ichiro, T.; Masafumi, H.; Takanori, A.; Fuyuki, N.; Yoshinori, I.; Ataru, I.; Seiki, K.; Tatsuo, H.; Takahiko, K.; Hiroshi, I.; Atsutaka, M. Epitaxial Growth of $FeSe_{0.5}Te_{0.5}$ Thin Films on CaF_2 Substrates with High Critical Current Density. *Appl. Phys. Express* **2011,** *4*, 053101.
(38) Kawale, S.; Bellingeri, E.; Braccini, V.; Pallecchi, I.; Putti, M.; Grimaldi, G.; Leo, A.; Guarino, A.; Nigro, A.; Ferdeghini, C. Comparison of Superconducting Properties of $FeSe_{0.5}Te_{0.5}$ Thin Films Grown on Different Substrates. *IEEE Trans. Appl. Supercond.* **2013,** *23*, 7500704.
(39) Braccini, V.; Kawale, S.; Reich, E.; Bellingeri, E.; Pellegrino, L.; Sala, A.; Putti, M.; Higashikawa, K.; Kiss, T.; Holzapfel, B.; Ferdeghini, C. Highly Effective and Isotropic Pinning in Epitaxial Fe(Se,Te) Thin Films Grown on CaF_2 Substrates. *Appl. Phys. Lett.* **2013,** *103*, 172601.
(40) Tsukada, I.; Ichinose, A.; Nabeshima, F.; Imai, Y.; Maeda, A. Origin of Lattice Compression of $FeSe_{1-x}Te_x$ Thin Films on CaF_2 Substrates. *AIP Adv.* **2016,** *6*, 095314.
(41) Zhang, W.; Li, Z.; Li, F.; Zhang, H.; Peng, J.; Tang, C.; Wang, Q.; He, K.; Chen, X.; Wang, L.; Ma, X.; Xue, Q.-K. Interface Charge Doping Effects on Superconductivity of Single-unit-cell FeSe Films on $SrTiO_3$ Substrates. *Phys. Rev. B* **2014,** *89*, 060506(R).
(42) Hanzawa, K.; Sato, H.; Hiramatsu, H.; Kamiya, T.; Hosono, H. Electric Field-induced Superconducting Transition of Insulating FeSe Thin Film at 35 K. *Proc. Natl. Acad. Sci. U.S.A.* **2016,** *113*, 3986-3990.
(43) Hanzawa, K.; Sato, H.; Hiramatsu, H.; Kamiya, T.; Hosono, H. Key Factors for Insulator-Superconductor Transition in FeSe Thin Films by Electric Field. *IEEE Trans. Appl. Supercond.* **2017,** *27*, 1-5.
(44) Haindl, S.; Kidszun, M.; Oswald, S.; Hess, C.; Buchner, B.; Kolling, S.; Wilde, L.; Thersleff, T.; Yurchenko, V. V.; Jourdan, M.; Hiramatsu, H.; Hosono, H. Thin Film Growth of Fe-based Superconductors: from Fundamental Properties to Functional Devices. A Comparative Review. *Rep. Prog. Phys.* **2014,** *77*, 046502.
(45) Nabeshima, F.; Imai, Y.; Hanawa, M.; Tsukada, I.; Maeda, A. Enhancement of the Superconducting Transition Temperature in FeSe Epitaxial Thin Films by Anisotropic Compression. *Appl. Phys. Lett.* **2013,** *103*, 172602.
(46) McQueen, T. M.; Huang, Q.; Ksenofontov, V.; Felser, C.; Xu, Q.; Zandbergen, H.; Hor, Y. S.; Allred, J.; Williams, A. J.; Qu, D.; Checkelsky, J.; Ong, N. P.; Cava, R. J. Extreme Sensitivity of Superconductivity to Stoichiometry in $Fe_{1+\delta}Se$. *Phys. Rev. B* **2009,** *79*, 014522.
(47) Williams, A. J.; McQueen, T. M.; Cava, R. J. The Stoichiometry of FeSe. *Solid State Commun.* **2009,** *149*, 1507-1509.
(48) Peng, R.; Xu, H. C.; Tan, S. Y.; Cao, H. Y.; Xia, M.; Shen, X. P.; Huang, Z. C.; Wen, C. H. P.; Song, Q.; Zhang, T.; Xie, B. P.; Gong, X. G.; Feng, D. L. Tuning the Band Structure and Superconductivity in Single-layer FeSe by Interface Engineering. *Nat. Commun.* **2014,** *5*, 5044.
(49) Paolo, M.; Kaname, M.; Kouhei, F.; Yutaka, Y.; Takanobu, K.; Ataru, I.; Masashi, M. Fe–Te–Se Epitaxial Thin Films with Enhanced Superconducting Properties. *Supercond. Sci. Technol.* **2012,** *25*, 084021.
(50) Ichinose, A.; Nabeshima, F.; Tsukada, I.; Hanawa, M.; Seiki, K.; Akiike, T.; Imai, Y.; Maeda, A. Microscopic Analysis of the Chemical Reaction Between Fe(Te, Se) Thin Films and Underlying CaF_2. *Supercond. Sci. Technol.* **2013,** *26*, 075002.
(51) Horide, T.; Sanyoushi, M.; Ichinose, A.; Matsumoto, K. Influence of Strain and Composition on T_c in $FeSe_{1-x}Te_x$ Films. *J. Appl. Phys.* **2014,** *116*, 213906.
(52) Tranquada, J. M.; Axe, J. D.; Ichikawa, N.; Moodenbaugh, A. R.; Nakamura, Y.; Uchida, S.

Coexistence of, and Competition between, Superconductivity and Charge-Stripe Order in $La_{1.6-x}Nd_{0.4}Sr_xCuO_4$. *Phys. Rev. Lett.* **1997,** *78*, 338-341.
(53) Ding, J. F.; Xiang, X. Q.; Zhang, Y. Q.; Liu, H.; Li, X. G. Two-dimensional Superconductivity in Stripe-ordered $La_{1.6-x}Nd_{0.4}Sr_xCuO_4$ Single Crystals. *Phys. Rev. B* **2008,** *77*, 214524.
(54) Zhang, Y. Q.; Ding, J. F.; Xiang, X. Q.; Li, X. G.; Chen, Q. H. Effect of Stripe Order on the Vortex Phase Transition in $La_{1.44}Nd_{0.4}Sr_{0.16}CuO_4$ Films. *Supercond. Sci. Technol.* **2009,** *22*, 085010.
(55) Jung, S.-G.; Lee, N. H.; Choi, E.-M.; Kang, W. N.; Lee, S.-I.; Hwang, T.-J.; Kim, D. H. Fabrication of $FeSe_{1-x}$ Superconducting Films with Bulk Properties. *Phys. C* **2010,** *470*, 1977-1980.
(56) Buzdin, A. I. Proximity Effects in Superconductor-ferromagnet Heterostructures. *Rev. Mod. Phys.* **2005,** *77*, 935-976.
(57) Schneider, R.; Zaitsev, A. G.; Fuchs, D.; Fromknecht, R. Analysis of Superconducting FeSe Thin Films Deposited by a Sputtering Technique. *Supercond. Sci. Technol.* **2013,** *26*, 055014.

4.6 Note: Chapter Publication and Text Usage Detail

Part of his Chapter has been published in *ACS Applied Materials and Interfaces* as a paper (see below reference). Part of the written text in this chapter has been taken from my published paper, as shown below.

- **W. Qiu**, Z. Ma, D. Patel, L. Sang, C. Cai, M. S. A. Hossain, Z. Cheng, X. Wang, & S. X. Dou, The Interface Structure of FeSe Thin Film on CaF_2 Substrate and its Influence on the Superconducting Performance. *ACS Appl. Mater. Interfaces* 2017, **9,** 37446-37453.

Chapter 5

5 Superconductivity Induced by FeTe/FeSe Interface

5.1 Introduction

Considering that the mechanism of high-temperature superconductivity still remains unsolved[1-2] since its discovery 3 decades ago[3], scientists are seeking for inspiration from novel superconductors, for instance, Fe-based superconductors. Intense debate has been triggered since the survival of superconductivity was found in Fe-based compounds[4] in 2008. Among the numerous types of Fe-based superconductors[4-10], iron selenide[10-11] (FeSe) with the simplest binary structure is an appropriate candidate for investigating the intrinsic mechanism of unconventional superconductivity. Through applying high pressure[12-16], elemental substitution[17-19]/intercalation[20-22], or a liquid-gating technique[23-25], the superconducting transition temperature (T_c) of FeSe crystals can be substantially raised despite the low T_c of ~ 8 K[10] in the original bulk FeSe. More surprisingly, FeSe compound in the form of thin films or multilayers has attracted considerable attentions in the past few years due to its potential for achieving significantly high T_c and unique electronic properties.

By employing molecular beam epitaxy[26-35] (MBE), a dramatic enhancement in superconductivity (T_c^{onset} over 40 K/60 K shown by transport/scanning tunneling spectroscopy measurements) was realized in 1 unit-cell FeSe on pretreated $SrTiO_3$ (STO) substrate. High-T_c superconductivity (HTS) no longer survives, however, if the film has more than one atomic layer[32, 36-37]. The only way to revive superconductivity in multi-layer Fe-Chalcogenide (Fe-*Ch*) thin film is through post-engineering for electron-doping or enhancing the electron-phonon coupling. For example, an alkali-metal-coating (Li, K) process[36-41] was found promising for introducing massive electron-doping into multilayer FeSe films on STO. Wang *et al.*[42] reported that a post-annealing procedure is another effective way to introduce electron charge carriers into multilayer FeSe system and realize an insulator-superconductor transition. A novel method was also proposed by Shiogai *et al.*[43-44]. They reported their achievements in tuning the

thickness and corresponding superconductivity of ultrathin FeSe films on oxide substrates through subtly controlled electrochemical etching and electric field application. Nevertheless, the STO substrate is a prerequisite in this HTS Fe-*Ch* system, as it transfers massive electron doping into the first Fe-*Ch* unit cell[26, 45].

On the other hand, undoped Fe-*Ch*[46-52] thick films grown on a non-STO substrate showed superconducting behaviour that is significantly different from the case of monolayer or electron-doped multilayer FeSe. Even though the T_c is currently not comparable with the T_c record achieved in ultrathin FeSe thin films, a deep investigation into the Fe-*Ch* thick film is still of great importance to reveal the universal mechanism behind the superconductivity in Fe-*Ch* and similar systems. Using the pulsed laser deposition (PLD) method, Fe-*Ch* films with T_c^{onset} over 15 K[53] in FeSe, or 21 K[54] in $FeSe_{0.5}Te_{0.5}$, can be easily prepared without external electron doping, although there is a minimum thickness for this system to exhibit superconductivity, empirically over 20 nm for FeSe[51, 55-56] and over 30 nm for Fe-Se-Te[43, 51, 56-60]. Films with less thickness are generally non-superconducting or even insulating. Quite a few works have explained the disappearance of superconductivity in ultra-thin Fe-*Ch* films. For instance, it is well accepted that severe thermal and quantum fluctuations at low dimensionality usually suppress the T_c of a superconducting film[42]. Tensile stress, which is detrimental to the superconductivity of Fe-Chalcogenide films[57], tends to be induced when the thickness of $FeSe_{0.5}Te_{0.5}$ is lower than 30 nm[54]. Nabeshima *et al.*[51] demonstrated that low T_c in FeSe films thinner than 100 nm was due to the excess-Fe disorder near the surface of the films. The superconducting-insulating transition (SIT) was ascribed to a disorder-driven effect by Schneider *et al.*[55-56] in their FeSe films prepared by a sputtering technique. More recently, we reported similar SIT behaviour and ascribed the insulating resistivity behaviour of an 8 nm FeSe film to the severely unbalanced FeSe stoichiometry, which is caused by the calcium selenide (CaSe) interlayer that universally exists at FeSe/CaF_2 interfaces[53]. Despite the various viewpoints, the intrinsic reason for the suppression of superconductivity in undoped ultrathin Fe-*Ch* films still remains elusive, which is preventing the discovery of HTS in this system. A very recent work published by Kouno *et al.*[58] reported a T_c at 38 K in an $Fe(Se_{0.8}Te_{0.2})$ thin film on CaF_2 substrate. Similar to the top-down approach used by Shiogai[43], they were focusing on the interface between the $Fe(Se_{0.8}Te_{0.2})$ layer and the ionic liquid electrolyte. Inspired by that, we expected that the upper surface of the Fe-*Ch* thin film would be critical in overcoming the T_c suppression in ultrathin Fe-*Ch* films grown on non-STO substrates.

In this work, we achieved a superconducting transition in an ultrathin 7 nm FeSe film grown on CaF_2 substrate by simply coating an FeTe capping layer on top. In this bilayer heterostructure, the highest T_c reaches 17.6 K, although superconductivity is generally lacking in ultrathin Fe-*Ch* films grown on non-STO substrates by the PLD method. The enhanced superconductivity is considered to probably result from a several-unit-cell-thick Fe(Se,Te) diffusion layer formed near the FeTe/FeSe interface. Our bilayer films were found to be hole-dominated according to Hall measurements, which excludes them from the heavily electron-doping HTS scenario. Localized electron energy loss spectroscopy (EELS) results revealed the abnormal electronic orbital behaviour of the interfacial region and hinted at a possible relationship between the low Fe 3d electron occupancy and the enhanced superconductivity in Fe-*Ch* thin films. This work is valuable for improving our current understanding of the common suppression of superconductivity in ultra-thin Fe-*Ch* films grown on non-STO substrates.

5.2 Experimental Details

FeSe and FeTe thin films were grown on CaF_2 (100) single crystal substrates (lattice parameter a = 5.462 Å) via PLD (neodymium doped yttrium aluminium garnet (Nd:YAG) laser, λ = 355 nm, 10 Hz, 2 W output, ~ 1.7 nm/min) under a vacuum better than 4×10^{-6} Torr. Firstly, an FeSe film with a thickness of 7 nm (determined by cross-sectional micrographs) was deposited at a substrate temperature as 300 ℃. Afterwards, by directly switching to an FeTe target, the as-grown FeSe film was covered *in-situ* by an FeTe layer (same deposition time) with the temperature unchanged. Finally, the bi-layer FeTe/FeSe heterostructure (denoted as *#FT-300*) was naturally cooled down in the evacuated chamber. For comparison, a counterpart (denoted as *#FT-r.t.*) was separately prepared based on the same procedure for the FeSe layer. The only difference between *#FT-300* and *#FT-r.t.* was that the FeTe layer of the latter was deposited only after the substrate temperature was cooled down to room temperature. Hence, the chemical reaction between FeSe and FeTe composite was minimized in *#FT-r.t.* compared with *#FT-300*. To ensure the identical properties of the as-grown FeSe in two samples, the post-annealing effect on the as-grown FeSe in *#FT-300* during the FeTe-deposition at 300 ℃ was taken into consideration. A heating process at 300 ℃ for the same time period was added right after finishing the FeSe deposition in *#FT-r.t.*

The phase and structure were identified by X-ray diffraction (XRD, GBC MMA)

θ-2θ scans with Cu Kα radiation. For microstructure characterizations, an aberration-corrected high-angle annular dark field − scanning transmission electron microscope (HAADF-STEM, JEOL ARM-200F) equipped with a detector for energy dispersive X-ray spectroscopy (EDS, Centurio SDD) was employed for acquiring high-resolution micrographs as well as information about elemental distributions from a cross-sectional view. Further STEM-EELS measurements at a spectral resolution of 0.05 eV were performed at room temperature to acquire chemical and bonding information on the specimens. Lamellae for STEM were prepared through the *in-situ* lift-out technique in a focused ion beam (FIB, FEI Helios 600 NanoLab) system. The electrical transport measurements were carried out in a 9 T physical properties measurement system (PPMS, Quantum Design). Commercial gold wires (dia. 25 μm) and conductive silver paint were used in preparing the electrodes for transport resistance measurements.

5.3 Results and Discussion

Electrical Transport Results

Fig. 5-1 shows the transport superconducting performance obtained from the two samples in this work together with the results from Refs.[53-54] for comparison. The temperature dependence of the normalized resistance (R/R_{25K}) in the low temperature range (2 K - 25 K) is presented in Fig. 5-1(a). T_c^{onset} is defined as the crossing point at which the extrapolation from the normal state resistance intersects with the tangent line of the transition (shown by the dashed lines), while T_c^{zero} refers to the temperature at which the resistance drops to zero. We obtained a T_c^{onset}/T_c^{zero} = 17.6 K/14.4 K for *#FT-300* and 7.6 K/5.3 K for *#FT-r.t*. By applying magnetic fields up to 8 T perpendicular to the *ab* plane of the sample, the *ρ-T* curves of *#FT-300* under external field were plotted, as shown in Fig. 5-1(b) as an example, and the upper critical field (B_{c2}) was calculated (inset of Fig. 5-1(b)) depending on the linear extrapolation of the T_c^{mid}, which is defined as the temperature at which the resistivity has dropped to one-half of the value at 25 K. It should be noted that T_c and B_{c2} are both higher in the *#FT-300* sample than those from the optimized results obtained in a 127 nm FeSe film in our previous work[53]. Considering that the entire thickness of *#FT-300* is no more than 15 nm (including both FeSe and FeTe layers), normally, no superconducting transition would be expected in this sample, which is because traditional FeSe or FeSeTe films with ultra-thin thickness always show insulating behaviour[53, 59], just as in the case of 8 nm FeSe (black triangles) plotted in Fig. 5-1(a) (excluding the cases of HTS FeSe involving heavy electron-

doping[26-35, 43-44]), and superconductivity is also absent in pure FeTe thin films down to 2 K[60-61]. Thus the discovery of a superconducting transition in a surprisingly thin FeTe/FeSe bi-layer structure is unexpected and definitely worth further exploration to clarify the mechanism. Furthermore, the T_c^{onset} of *#FT-300* is 2.5 K higher than the T_c^{onset} = 15.1 K from a 127 nm FeSe film in our recent work[53] (shown by magenta diamonds in Fig. 5-1(a)) which is one of the highest T_cs that can be obtained in a pristine PLD-FeSe thin film grown on CaF_2 substrate. Similar T_c enhancement was also reported in FeSe/FeTe superlattices[50]. FeTe has been widely used as a protective layer on unit-cell FeSe films[26-28, 45, 62-63]. Although the possibility of Se/Te atom diffusion cannot be excluded, no enhancement in superconductivity was reported after introducing an FeTe layer onto an FeSe film (T_c ~ 53 K in Si/FeSe/STO from Ref. [26] while T_c ~ 54.5 K in Si/FeTe/FeSe/STO from Ref. [27]). It was further found by transport measurements that a 14-unit-cell (UC) (~ 8.7 nm) FeTe film was dominated by hole carriers throughout the temperature range from 5 K to 300 K[45], which may affect the overall carrier situation of the bi-layer structure. There is no distinct change in the Hall resistance results (R_{xy}), however, of 1-UC and 2-UC FeSe films after subtracting the influence of the FeTe layers[63]. Hence, the doping effect on FeSe from the FeTe should be negligible in our case, as the 7 nm FeSe is even thicker than the 2-UC FeSe. The enhanced superconductivity in *#FT-300* is probably related to an interface effect between the FeSe and FeTe layers.

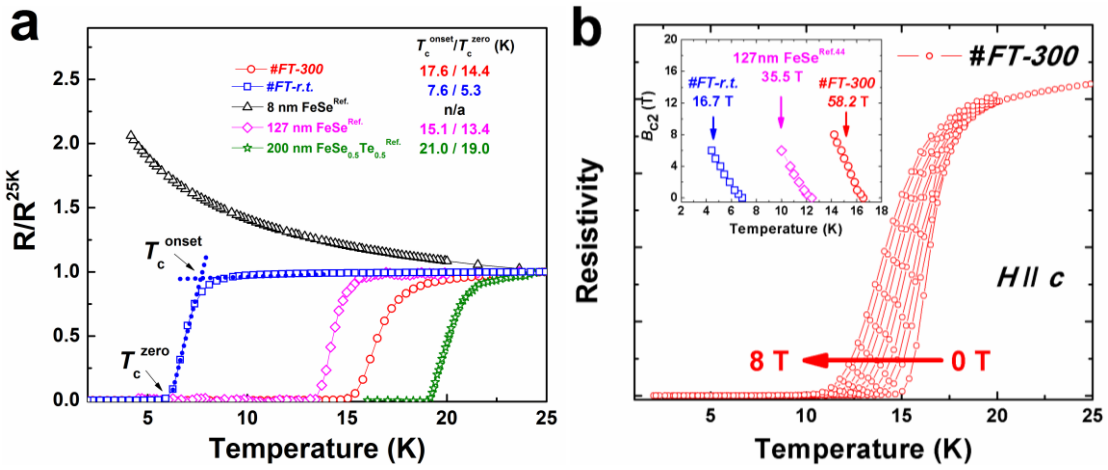

Figure 5-1. ρ-T curves for the FeTe/FeSe thin films in this work and the counterparts for reference. (a) Temperature dependence of the normalized resistance (R/R_{25K}) at self-field for *#FT-300* and *#FT-r.t.* in this work from 2 to 25 K. Additionally, the results from a 8 nm FeSe thin film[53] (black triangles), a 127 nm FeSe thin film[53] (magenta diamonds) and a 200 nm $FeSe_{0.5}Te_{0.5}$ thin film[54] (olive stars) are added on the same coordinates for comparison. The T_c^{onset}/T_c^{zero} values for each sample are also given. (b) ρ-T measurements of *#FT-300* under external fields up to 8 T along the *c*-axis. The inset shows the plots of *B*-

T_c. The upper critical field (B_{c2}) is estimated from the linear extrapolation of T_c^{mid}. The results from a 127 nm FeSe thin film[53] are also plotted for comparison.

Iron-based superconductors always show complex Hall behaviour[64-70] due to their multi-band nature. We performed Hall measurements for both samples to reach a greater understanding of their transport properties. In order to eliminate the longitudinal resistivity component resulting from the misalignment of electrode contacts, we acquired the transverse resistivity (ρ_{xy}) in both positive and negative fields and then calculated the difference, i.e., $\rho_{xy}(H) = [\rho_{xy}(+H) - \rho_{xy}(-H)]/2$. The final results for the Hall coefficient (R_H) are shown in Fig. 5-2(a) for *#FT-300* and 5-2(b) for *#FT-r.t.* The R_H is determined by the linear fitting of the ρ_{xy} curves between 1 to 4 Tesla so that the contribution from the anomalous Hall effect can be excluded. Herein, the noticeable temperature dependence of R_H provides solid evidence of the multiband nature of the band structure. On cooling down from room temperature, the nearly temperature-independent R_H with positive absolute values above the characteristic temperature T^* ~ 125 K is considered as proof of a hole-dominated two-band model. That is to say, the hole-pockets around the Γ point in the Fermi surface are governing the transport properties in the high temperature range. We found that the R_H behaviour differs between the two samples near T^*. In *#FT-300*, R_H changes to a negative small value near T^*, which indicates a predominance of electron-type charge carriers. Below T^*, R_H immediately switches back to positive and exhibits a clear upward deviation. The phenomenon that the sign of R_H changes twice is very similar to that in FeSe flakes without a gate voltage[23] and in an 8-UC FeSe film grown on STO substrate[45]. It can be interpreted as due to the coexistence of electron- and hole-type carriers with different contributions from various bands[28]. On the contrary, R_H is nearly constant (~ 5×10^{-9} m^3/C) above T^* in *#FT-r.t.*, indicating an unchanged domination by hole-type carriers. Below T^*, R_H in both samples exhibits a rapid increase on the positive side with decreasing temperature. It reflects the decrease in the electron contribution at low temperature. Similarly, the predominance of hole-type carriers in PLD-grown multilayer FeSe thin films grown on CaF_2 substrates was also verified by angle-resolved photoemission spectroscopy (ARPES) measurements by Shen *et al.*[71] In other words, the enhanced T_c in *#FT-300* could be excluded from the heavily electron-doping HTS scenarios[23, 28, 42, 45, 63-64].

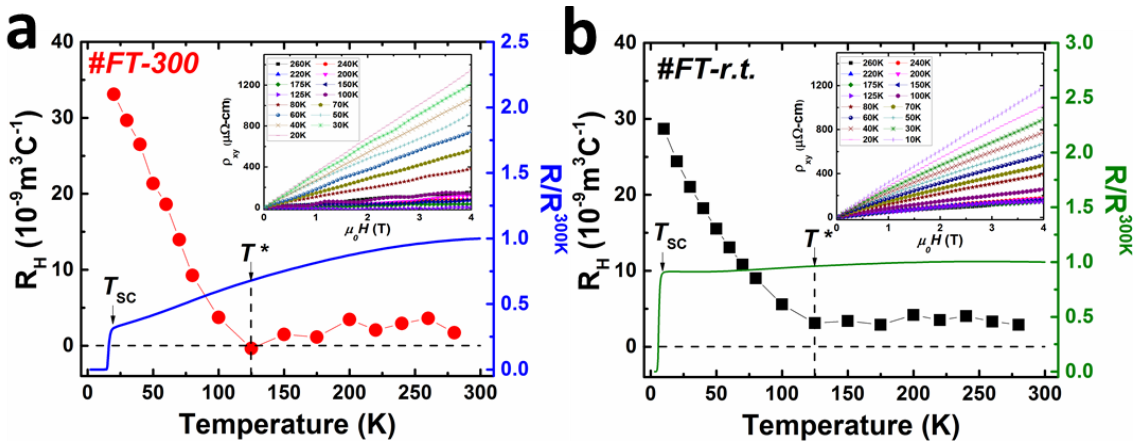

Figure 5-2 Temperature dependence of the Hall coefficient R_H (left *y*-axis) and zero-field normalized resistance (R/R^{300K}) (right *y*-axis) for (a) *#FT-300* and (b) *#FT-r.t.* Insets: Hall resistivity ρ_{xy} versus $\mu_0 H$ at different temperatures.

Phase Identifications

To determine the phase composition, XRD measurements were carried out, and the results are shown in Fig. 5-3(a) (detection angle, 2θ = 10 - 55 °) and (b) (2θ = 12 - 18 °). The spectra are normalized by to the CaF_2 (200) diffraction peak. Overall, both FeTe/FeSe bi-layer films in this work have a high-quality *c*-axis orientation. The Ag phase in *#FT-r.t.* has resulted from the residual silver paste on the sample surface after transport measurements. For *#FT-r.t.*, two sets of peaks indexed as FeTe (00l) and FeSe (00l) are shown in the spectrum. The FeTe (00l) peaks are located at lower 2θ angles compared with those of FeSe, which is consistent with the fact that the interplanar distance in the FeTe[72] lattice is larger than that of FeSe[10]. For *#FT-300*, a similar configuration is also observed, except for the absence of the FeTe (003) peak (due to low intensity). We noticed an additional diffraction peak allocated between FeSe (001) and FeTe (001), suggesting the presence of an isostructural phase with the lattice sitting between FeSe and FeTe. Here, the Fe(Se,Te) phase refers to a diffusion layer between the FeTe and the FeSe, which shows a continuum between the two phases rather than an $FeSe_xTe_{1-x}$ phase with a fixed chemical composition. We are unable to determine the specific composition due to the gradual transition near the FeTe/FeSe interface. The enlarged 2θ range near FeSe (001) is presented in Figure 3(b) on a logarithmic scale on the *y*-axis. From this viewpoint, an identical FeSe phase is confirmed in *#FT-300*, and the Fe(Se,Te) (001) peak is clearly distinguished. The FeTe (001) peak in *#FT-r.t.* is broader, perhaps due to the small amount of Fe(Se,Te) phase unavoidably formed at the FeTe/FeSe interface. Nevertheless, the thickness of the Fe(Se,Te) layer in *#FT-r.t.* is

much lower, so that only a broadened FeTe (001) peak is detected rather than a separate Fe(Se,Te) (001) diffraction peak, as appears in *#FT-300*. The presence of Fe(Se,Te) phase is thought to be the determinant that triggers the superconductivity in the sample combined from two non-superconducting layers, although why the T_c of *#FT-300* is unusually high requires further investigation and will be discussed later in this article.

After the identification of the crystal structure by XRD from a macroscopic perspective, we confirmed that an Fe(Se,Te) diffusion layer with a lattice parameter located between those of FeSe and FeTe exists in *#FT-300*, while a only tiny amount of similar phase is present in *#FT-r.t.* With the help of HAADF-STEM analysis, we can further reveal the local microstructure and determine the morphology of the interface. Fig. 5-3(c) and (d) presents STEM cross-sectional micrographs focusing on the FeTe/FeSe interface. Along the [010] zone axis, well-aligned tetragonal FeSe films with no more than 10 unit-cells are found stacked with a tetragonal FeTe layer. Due to the larger atomic number in Te than in Se, a distinct difference in contrast is observed in both HAADF-STEM images, leading to the brighter appearance of the upper FeTe layer. On the right side of the HAADF STEM images, EDS analysis generated in the same area illustrates the distribution of the major elements in the films, including Ca, Se, Te, Fe, and O. The EDS results help to demonstrate the configuration of the different layers and illustrate the elemental inter-diffusion. Much more Se diffuses into the upper FeTe film in *#FT-300* compared with the case of *#FT-r.t.*, due to higher evaporation rate at 300 ℃, as shown more evidently by the EDS line scans. The atomic percentage (at. %) ratio of Fe remains almost stable and starts to decrease in the middle of the FeTe layer due to oxidation, while in the case of Se, the two Se-rich regions refer to the CaSe[53] interlayer (lower) and the FeSe layer (upper), respectively. Clearly, the diffusion of Se in *#FT-300* even extended into the middle of the FeTe layer, leading to a much broader Fe(Se,Te) transition region compared with the much sharper FeTe/FeSe interface in *#FT-r.t.* In addition, O and Fe are detected in the top few nanometers of both samples without Se or Te elements, which hints at the probable existence of an Fe-oxide (FeO_x) layer above FeTe (not shown here). Similar oxidized Fe layers were also reported by Kouno *et al.*[58] in their $Fe(Se_{0.8}Te_{0.2})/CaF_2$ thin films.

In order to quantitatively investigate the layout of the Fe(Se,Te) diffusion layer at the FeSe/FeTe interface, the lattice parameters of each atomic layer were calculated from the HAADF-STEM images. To minimize error, the relative trend in the variation of the *c*-axis lattice parameter is defined as c/c^{FeSe}, where c and c^{FeSe} refer to the *c*-axis

lattice parameter of the particular atomic layer and the first FeSe atomic layer adjacent to the CaSe interlayer, respectively. The atomic-layer dependence of the relative *c*-axis lattice parameter is plotted in the insets of Fig. 5-3(c) and (d), ranging from the first FeSe atomic layer to the upper FeTe layers. Typical 2-stage heterostructures with the same *c*-axis lattice parameters for the FeSe and FeTe layers are clearly exhibited in both specimens. The only difference is in the transition span of the Fe(Se,Te) diffusion layer which could be simply estimated by counting the number of atomic layers. *#FT-300* has a diffusion layer about 3 unit cells in thickness, while in the case of *#FT-r.t.*, the transition is much sharper (~ 1 unit cell). This is in good agreement with the XRD results, where the diffraction peak indexed as Fe(Se,Te) is only visible in *#FT-300* but absent in *#FT-r.t.*

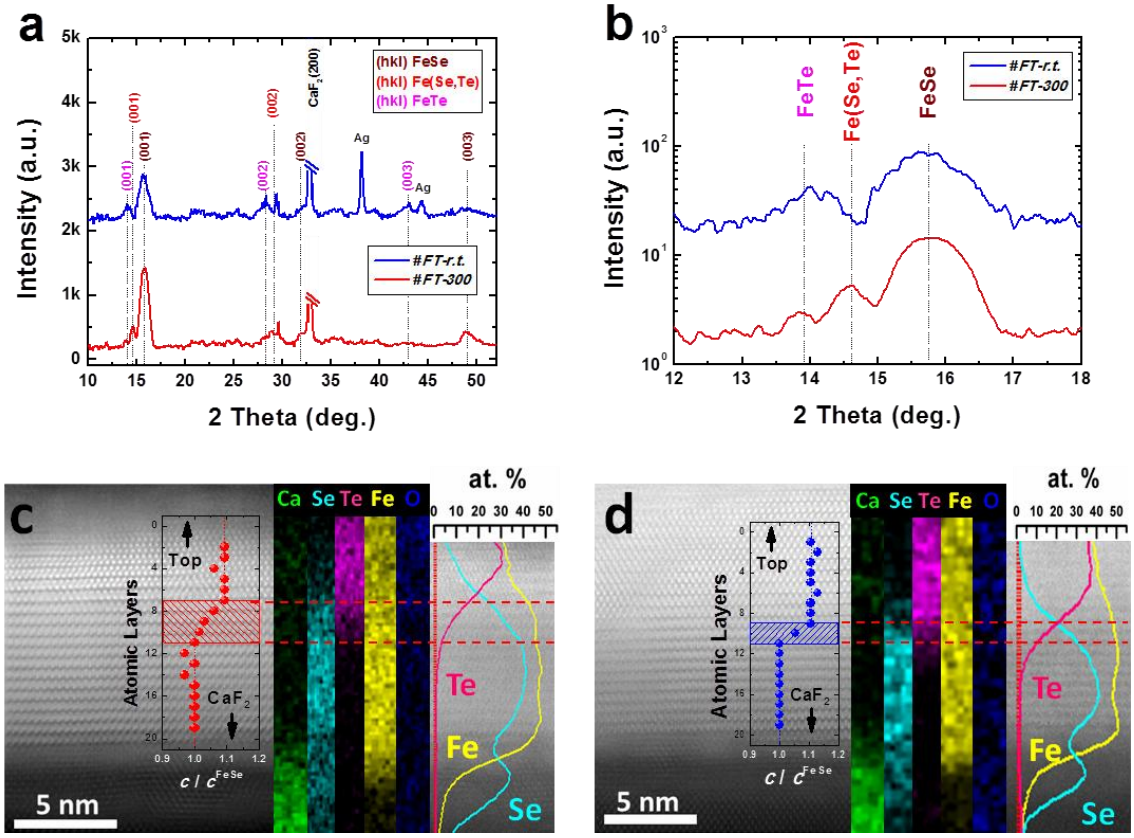

Figure 5-3. The experiments performed for phase identification, including XRD 2θ, TEM-EDS mapping/profile, and the *c*-axis lattice constants of each unit-layer measured in HRTEM images. (a) XRD patterns for *#FT-300* (red) and *#FT-r.t.* (blue) ranging from 2θ = 10-55 °. The indices (hkl) represent the reflections of FeSe (brown), Fe(Se,Te) (red) and FeTe (magenta) phases, respectively. The Ag phase in #FT-r.t. comes from the residual silver paste after transport measurements. Dashed lines are guides for the eyes to mark the locations of the Fe-Chalcogenide peaks. (b) Enlarged 2θ interval near the β-FeSe (001) peak. The *y*-axis is set to a logarithmic scale. The locations of peaks are marked by dashed lines. Fe(Se,Te) phase is found co-existing with FeSe and FeTe in *#FT-300*, while it is almost absent in *#FT-r.t.* (c) & (d)

Dark-field high-resolution STEM micrographs focusing on the FeTe/FeSe transition region from a cross-sectional viewpoint for *#FT-300* (c) and *#FT-r.t.* (d). The two micrographs are exactly identical in scale after normalization. The corresponding EDS-mapping results are shown on the right side of each STEM images, showing the distribution of Ca (green), Se (cyan), Te (magenta), Fe (yellow), and O (blue) elements. The EDS line scans of the same region show the relative variation of Fe, Se, and Te elements in the form of atomic ratio percentages. For reference only, the relative variation trend of the *c*-axis lattice parameter of each Fe-chalcogenide layers was measured and is plotted on the micrograph in the form of c/c^{FeSe} versus atomic layer (c^{FeSe} refers to the *c*-axis lattice parameter of the first FeSe layer adjacent to CaSe interlayer). A much broader Fe(Se,Te) diffusion layer is found in *#FT-300*. Red dashed lines are only guides for the eyes.

EELS Measurements

So far, we have proposed enhanced superconductivity in an FeTe/FeSe heterostructure with an Fe(Se,Te) diffusion layer forming near the FeTe/FeSe interface. Considering the original non-superconducting property of FeTe and ultra-thin FeSe grown on CaF_2, a unique property from the additional Fe(Se,Te) interlayer is expected, especially for the case of *#FT-300*. How does a 3 unit-cell Fe(Se,Te) diffusion layer generate a T_c comparable to those of regular Fe-Se-Te films[73] with a thickness of at least one order of magnitude higher? Here, atomic-resolution EELS analysis is utilized to clarify the local electronic orbital behaviour of Fe ions in FeSe, FeTe, Fe(Se,Te), etc. It is now clear that the electron filling of the Fe 3d orbital plays a critical role in determining the electronic environment on the Fermi level and the local magnetic moment in Fe-related materials[74] such as Fe metal[75-76], Fe oxides[77-78], and Fe-based superconductors[79-82]. The 3d-state occupancy can be quantitatively characterized[78] by analysing "white line" features in EELS spectra. In the case of Fe, the major core-loss "white lines" are the Fe-L_3 and Fe-L_2 edges generated due to the excitations from the Fe $2p_{3/2}$ and Fe $2p_{1/2}$ core level to unoccupied Fe 3d states (shown in Fig. 5-4(a)). One typical example of Fe-$L_{3,2}$ white lines from this work is illustrated in Fig. 5-4(b), showing two intense edges located at the onsets near 708 eV and 721 eV. The method of picking an integrated area of Fe-L_3 and Fe-L_2 is based on the model proposed by Graetz *et al*[78]. Both low-loss and core-loss spectra were collected to carry out Fourier ratio deconvolution[83] to remove the plural scattering effect. The reliability of the analysis was reflected by the value of t/λ (the quotient of the sample thickness *t* and the local inelastic mean free path λ) that can be calculated from the low-loss EELS spectra. The t/λ was found to range from 0.34 to 0.53 for *#FT-300* and from 0.46 to 0.71 for

#FT-r.t., respectively. The obtained t/λ values remained less than 1, indicating good reliability of the EELS analysis in this work.

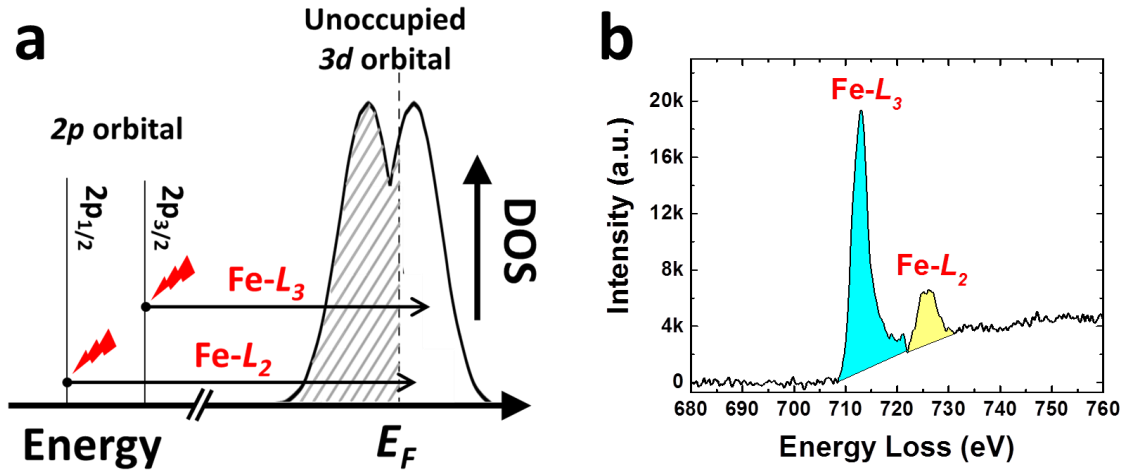

Figure 5-4. The schematic diagram and an example of Fe-$L_{3,2}$ edges in EELS results. (a) Schematic diagram of the electronic excitation process shows how the Fe-L_3 and Fe-L_2 edges appear in EELS. (b) An example of the Fe-L_3 (cyan) and Fe-L_2 (yellow) edges. The shaded areas are the integrals of L_3 and L_2 white-lines.

Fig. 5-5 shows the core-loss EELS analyses for the two samples in this work. The spectra were extracted from the dashed rectangular area shown in Fig. 5-5(a). Based on the data analysis method shown in Fig. 5-4(b), the "white line" ratio Fe-L_3/L_2 as a function of position in the sample is plotted in the inset of Fig. 5-5(a). Overall, the trend in the position-dependent Fe-L_3/L_2 in *#FT-300* and *#FT-r.t.* is mostly identical, with an L_3/L_2 value of ~ 3.5 in the first 6 nm close to the CaF_2 substrate, followed by a few nanometers with a low L_3/L_2 value of ~ 3.2, and finally boosted up to $L_3/L_2 \approx 4.9$ in the top region. The highest Fe-L_3/L_2 value of ~ 4.9 found in the top layer in this work is correlated with the fact that the Fe ions in Fe oxides are usually in a high spin state and have a quite large local magnetic moment[84]. This high L_3/L_2 ratio value corresponds well with a variety of EELS analyses on iron-oxygen systems done by Leapman *et al.*[85], Colliex *et al.*[86], and Chen *et al.*[77] It evidences the existence of an FeO_x layer which arises from the degradation of FeTe surface. As a result, the actual thickness of the FeTe layer must be lower than the nominal 7 nm, which is proved by a thin layer which spans ~ 3 nm with the lowest L_3/L_2 value of ~ 3.2 below the FeO_x layer. On the contrary, the FeSe layer with an L_3/L_2 value of ~ 3.5 is thicker (~ 7 nm) because of the effective protection provided by the upper FeTe layer. The phenomenon that the FeTe layer shows a lower L_3/L_2 value than FeSe layer resembles the results of EELS studies on inhomogeneous $Fe_{1+y}Te_xSe_{1-x}$ single crystals done by Hu *et al.*[80], where a higher/lower

L_3/L_2 intensity ratio reflects the Te-poor/Te-rich region, respectively. Intriguingly, a distinct difference in L_3/L_2 between the two samples is observed in a several-unit-cells-thick region lying between the FeTe and FeSe layers. A relatively high Fe-L_3/L_2 ratio of ~ 4.0 is found in *#FT-300*, while that of *#FT-r.t.* shows no big variation in the same region. In consideration of the principle of "white line" excitation, the abnormal L_3/L_2 behaviour in the FeTe/FeSe interfacial region of *#FT-300* might suggest particular properties related to the electronic orbital status and will be discussed soon. Fig. 5-5(b) presents the core-loss EELS mapping of *#FT-300*, with the *z*-axis and *y*-axis referring to the "white line" edge intensity and position, respectively. The horizontal lines indicate the typical positions of four different regions (FeO_x, FeTe, Fe(Se,Te), and FeSe). The Fe-L_3 edge in the FeO_x region is distinctly higher in energy than in the other regions. Taftø *et al.*[87] verified the determination of Fe^{2+} and Fe^{3+} ions in a mixed-valence spinel by the EELS technique and demonstrated that Fe^{3+} ions lead to higher Fe-L_3 energy than Fe^{2+} ions. van Aken and Liebscher[88] also reported that their Fe-L_3 edge of Fe^{3+} was 1.7 eV higher than that of Fe^{2+}. Hence, it is reasonable here for the FeO_x region to show higher energy loss in the Fe-L_3 edge, as it is the only place in our samples that could possibly possess Fe^{3+} ions.

The corresponding EELS spectra taken at four indicated positions are plotted in Fig. 5-5(c) with each pair of spectra (*#FT-300* in red circles and *#FT-r.t.* in black squares) compared in a separate image. Obviously, the FeO_x and FeSe regions in the two samples show exactly the same "white line" behaviour, with the two sets of spectra overlapping with each other. In the case of the FeTe region, the tail part with energy loss higher than the Fe-L_2 edge of *#FT-r.t.* is still somewhat lower than that of *#FT-300*, which is probably due to the different growth conditions of the FeTe layer. Nevertheless, the "white line" features (Fe-$L_{3,2}$ edges) still show identical shapes in two samples, indicating the negligible effect on the ultimate phase composition of the FeTe layer despite the different heat-treatment temperatures. Among all the four regions, the only difference is found in the region of the Fe(Se,Te) diffusion layer in *#FT-300*. In Fig. 5-5(d), an enlarged range of EELS spectra from 704 eV to 720 eV (Fe-L_3 edge) for the Fe(Se,Te) region in Fig. 5-5(c) is presented. It is clearly seen that the energy loss of Fe-L_3 is 0.61 eV lower in *#FT-300* compared with that in *#FT-r.t.* That is to say, a red shift in the Fe-L_3 edge occurs in this region if an Fe(Se,Te) diffusion layer is formed at the FeTe/FeSe interface. Several factors might result in a redshift in the Fe-L_3 edge. Hu *et al.*[80] reported a Fe-L_3 edge shifted by 0.13 eV to lower energy in their Te-rich

$FeTe_{0.7}Se_{0.3}$ specimen. In our work, it may imply slightly more Te content in the Fe(Se,Te) region in *#FT-300* than in *#FT-r.t.*, although the energy redshift in our work is much larger than in the case of Hu *et al.*[80], thus more factors are expected to be at work. Zhao *et al.*[45] conducted high-resolution EELS analyses on their MBE-FeSe/STO thin films and observed a blue shift of the Fe-L_3 edge near the FeSe/STO interface. The energy shift was then proved to be direct evidence of electron-doping in the first 1−2 UC FeSe layers from the STO substrate. Therefore, the electron-doping state of the Fe(Se,Te) diffusion layer can be excluded as a reason for the enhanced T_c in this work, as we observed a redshift instead. On the contrary, extra hole carriers are likely to be introduced by FeTe deposition[45]. Moreover, the simulation carried out in the same work indicated that 3 % tensile stress at FeSe/STO interface can also result in a slight redshift in Fe-$L_{3,2}$ edges. Considering that FeTe has a larger lattice parameter than the FeSe beneath, it should experience compressive stress. Owing to the high growth temperature of the FeTe layer in *#FT-300*, the stress was effectively relieved, so that a Fe-L_3 edge at lower energy should be expected in *#FT-300*, which coincides with the data on hand. To sum up, the phenomenon that the Fe-L_3 edge in *#FT-300* shows a 0.61 eV shift to lower energy in the Fe(Se,Te) diffusion layer than in *#FT-r.t.* results from a hybrid effect, including local fluctuation of Te content, additional hole carrier doping, and/or different stress conditions.

An empirical relationship has been established in 3d transition-metal oxides (TMO_x), that a maximum white line ratio Fe-L_3/L_2 is obtained when the filling of the 3d state is approximately half-full[78, 89], and deviation toward either side from half-full 3d occupancy will lead to lower Fe-L_3/L_2 ratio. The results are redrawn in Fig. 5-5(e) with dashed arrows showing the correlation between the "L_3/L_2 ratio" and "3d occupancy". The Fe-L_3/L_2 ratios for the four regions (FeO_x ≈ 4.9, FeTe ≈ 3.2, Fe(Se,Te) ≈ 4.0, and FeSe ≈ 3.5) in *#FT-300* are added into the results for comparison. We note that a direct L_3/L_2 ratio comparison of Fe-*Ch* with 3d TMO_x to obtain the information about 3d electron occupancy might not be quantitatively accurate due to their different electronic structures. Even so, the qualitative conclusion is still valuable for reflecting tiny fluctuations of Fe 3d electron occupancy in different regions, considering that O, Se, and Te all belong to the chalcogen family. According to the empirical conclusion[78] that the L_3/L_2 ratio decreases when 3d occupancy is between d^5 and d^{10}, the higher L_3/L_2 ratio in the Fe(Se,Te) region probably implies less electron occupancy in Fe 3d orbitals. A different point of view was proposed by Cantoni *et al.*[79] in regard to the effect of 3d

orbital occupancy on iron-based superconductors. They believed that the total amount of holes in Fe 3d orbitals is nearly constant (~ 4) in all types of iron-based compounds, with a small fluctuation in the ratio of holes in the j = 5/2 and j = 3/2 levels ($h_{5/2}/h_{3/2}$), depending on variations in the local magnetic moment. Therefore, the abnormal 3d electronic orbital behaviour found in the Fe(Se,Te) diffusion layer in *#FT-300* hints that the status of Fe 3d orbital occupancy is one of the key factors determining the enhanced superconductivity in the present work.

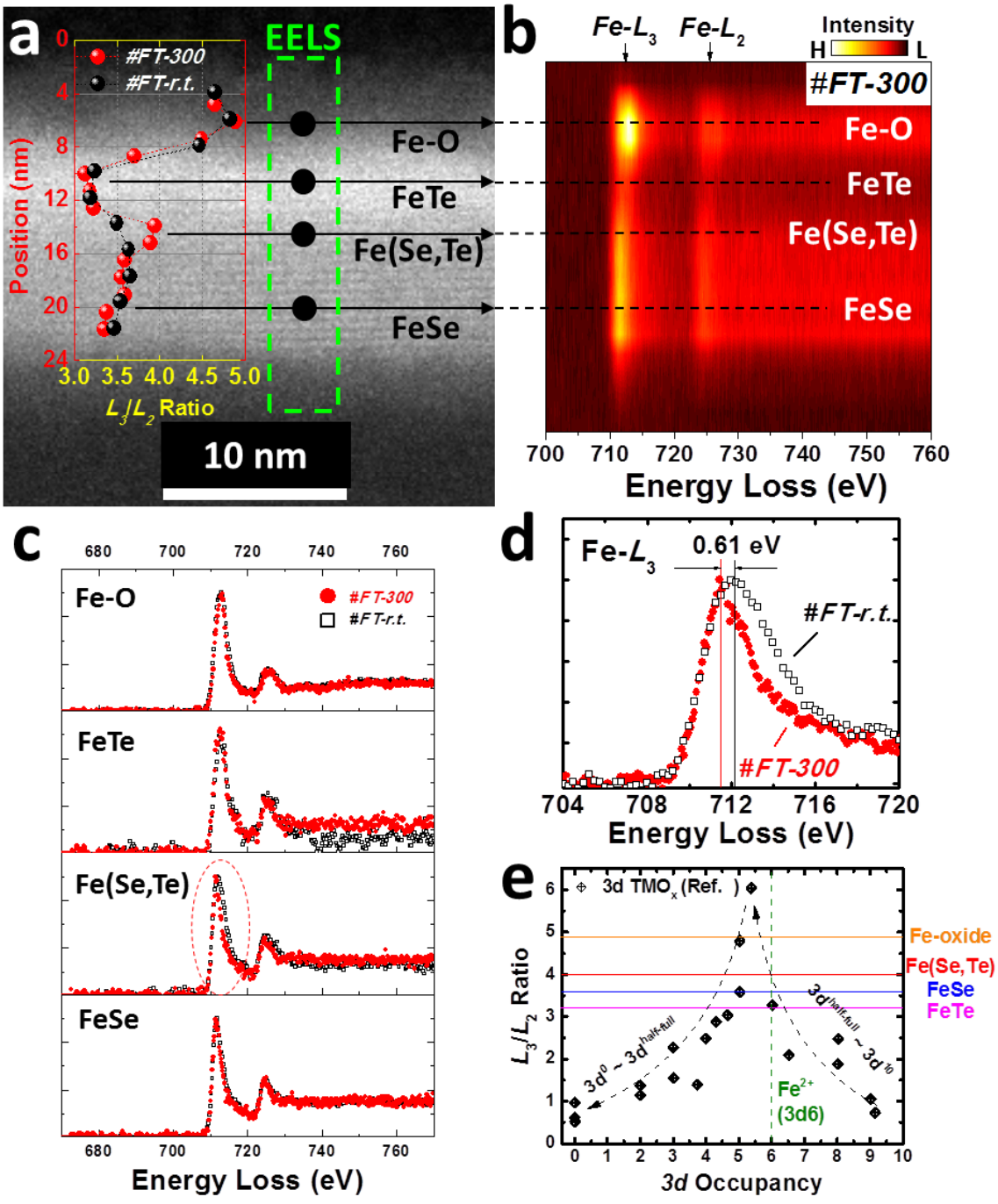

Figure 5-5. Core-loss EELS results acquired at room temperature for the two samples in this work. (a) A HAADF image of *#FT-300* with a dashed rectangle indicating the area where spectra were collected. The

HAADF image of #FT-r.t. was taken under the same conditions (not shown here). The inset shows the position-dependent Fe-L_3/L_2 ratio in *#FT-300* (red circles) and *#FT-r.t.* (black squares) along the EELS scan direction. A relatively high Fe-L_3/L_2 ratio in *#FT-300* in the Fe(Se,Te) region is the only difference. The regions denoted as Fe-O, FeTe, Fe(Se,Te), and FeSe layers, are defined based on the EDS results on *#FT-300*. The same definition is utilized in *#FT-r.t.* despite the much sharper transition. The typical areas of different regions are indicated by horizontal lines on the HAADF image as well as in the core-loss EELS mapping shown in (b). (c) Separate EELS spectra for the four regions in the two samples (red circles: *#FT-300*, black squares: *#FT-r.t.*). A dashed oval in the region of Fe(Se,Te) highlights the only difference in a "white line" feature. (d) A magnified range of the EELS spectra showing the energy shift of the Fe-L_3 edge in the Fe(Se,Te) region of *#FT-300* compared with that of *#FT-r.t.* from the same area. (e) White-line Fe-L_3/L_2 ratios for the four regions in *#FT-300* are presented in the form of horizontal lines. The "L_3/L_2 ratio-3d occupancy" results from Graetz *et al.*[78] and Sparrow *et al.*[89] are reproduced as solid diamonds for reference. The dashed arrows are guide for the eye to show the empirical correlation between the white-line ratio and the 3d occupancy of transition-metal oxides (TMO_x) that was summarized in Ref. [78].

5.4 Conclusions

To summarize, the common T_c suppression in ultrathin Fe-*Ch* thin films grown on a non-STO substrate is overcome in an FeTe/FeSe bilayer heterostructure by coating an FeTe capping layer on top of the FeSe layer. The enhanced T_c^{onset} in this work is 17.6 K, which is considered mostly related to a several-unit-cell-thick Fe(Se,Te) diffusion layer near the FeTe/FeSe interface observed by phase identification. The Hall coefficient results exclude the present work from the HTS Fe-*Ch* scenarios, which are usually dominated by electron-type carriers. According to EELS analyses near the interfacial region, variation in the electronic orbital structure of different regions is revealed by "white line" features. Compared with the reference sample, an energy shift of the Fe-L_3 edge is noticed in the additional Fe(Se,Te) diffusion layer, indicating a hybrid consequence of the Te-rich condition, extra hole doping, and/or less compressive strain in this region. Moreover, the Fe(Se,Te) diffusion layer exhibits a higher Fe-L_3/L_2 ratio than those of either the upper FeTe or the lower FeSe layer. Following the empirical correlation established in 3d transition-metal oxides, lower Fe 3d electron occupancy is expected in the Fe(Se,Te) region. Our nanoscale EELS analysis together with macroscopic transport and phase characterizations confirm the importance of the FeTe/FeSe interface in realizing enhanced superconductivity in regular Fe-*Ch* thin films. These results will provide constructive guidance for a unified understanding of unconventional iron-based superconductivity.

5.5 References

(1) Božović, I.; He, X.; Wu, J.; Bollinger, A. T. Dependence of the critical temperature in overdoped copper oxides on superfluid density. *Nature* **2016,** *536*, 309.
(2) Mann, A. High-temperature Superconductivity at 25: Still in Suspense. *Nature* **2011,** *475*, 280-282.
(3) Bednorz, J. G.; Müller, K. A. Possible high T_c superconductivity in the Ba−La−Cu−O system. *Zeitschrift für Physik B Condensed Matter* **1986,** *64*, 189-193.
(4) Kamihara, Y.; Watanabe, T.; Hirano, M.; Hosono, H. Iron-based Layered Superconductor La[$O_{1-x}F_x$]FeAs (x = 0.05-0.12) with T_c = 26 K. *J. Am. Chem. Soc.* **2008,** *130*, 3296-3297.
(5) Chen, X. H.; Wu, T.; Wu, G.; Liu, R. H.; Chen, H.; Fang, D. F. Superconductivity at 43 K in $SmFeAsO_{1-x}F_x$. *Nature* **2008,** *453*, 761-762.
(6) Rotter, M.; Tegel, M.; Johrendt, D. Superconductivity at 38 K in the Iron Arsenide ($Ba_{1-x}K_x$)Fe_2As_2. *Phys. Rev. Lett.* **2008,** *101*, 107006.
(7) Sefat, A. S.; Jin, R.; McGuire, M. A.; Sales, B. C.; Singh, D. J.; Mandrus, D. Superconductivity at 22 K in Co-doped $BaFe_2As_2$ crystals. *Phys. Rev. Lett.* **2008,** *101*, 117004.
(8) Wang, X. C.; Liu, Q. Q.; Lv, Y. X.; Gao, W. B.; Yang, L. X.; Yu, R. C.; Li, F. Y.; Jin, C. Q. The Superconductivity at 18 K in LiFeAs System. *Solid State Commun.* **2008,** *148*, 538-540.
(9) Pitcher, M. J.; Parker, D. R.; Adamson, P.; Herkelrath, S. J. C.; Boothroyd, A. T.; Ibberson, R. M.; Brunelli, M.; Clarke, S. J. Structure and superconductivity of LiFeAs. *Chem. Commun.* **2008,** *0*, 5918-5920.
(10) Hsu, F.-C.; Luo, J.-Y.; Yeh, K.-W.; Chen, T.-K.; Huang, T.-W.; Wu, P. M.; Lee, Y.-C.; Huang, Y.-L.; Chu, Y.-Y.; Yan, D.-C.; Wu, M.-K. Superconductivity in the PbO-type Structure Alpha-FeSe. *Proc. Natl. Acad. Sci. U.S.A.* **2008,** *105*, 14262-14264.
(11) McQueen, T. M.; Huang, Q.; Ksenofontov, V.; Felser, C.; Xu, Q.; Zandbergen, H.; Hor, Y. S.; Allred, J.; Williams, A. J.; Qu, D.; Checkelsky, J.; Ong, N. P.; Cava, R. J. Extreme Sensitivity of Superconductivity to Stoichiometry in $Fe_{1+\delta}Se$. *Phys. Rev. B* **2009,** *79*, 014522.
(12) Mizuguchi, Y.; Tomioka, F.; Tsuda, S.; Yamaguchi, T.; Takano, Y. Superconductivity at 27K in Tetragonal FeSe Under High Pressure. *Appl. Phys. Lett.* **2008,** *93*, 152505.
(13) Margadonna, S.; Takabayashi, Y.; Ohishi, Y.; Mizuguchi, Y.; Takano, Y.; Kagayama, T.; Nakagawa, T.; Takata, M.; Prassides, K. Pressure Evolution of the Low-temperature Crystal Structure and Bonding of the Superconductor FeSe (T_c = 37 K). *Phys. Rev. B* **2009,** *80*, 064506.
(14) Medvedev, S.; McQueen, T. M.; Troyan, I. A.; Palasyuk, T.; Eremets, M. I.; Cava, R. J.; Naghavi, S.; Casper, F.; Ksenofontov, V.; Wortmann, G.; Felser, C. Electronic and Magnetic Phase Diagram of beta-$Fe_{1.01}Se$ with Superconductivity at 36.7 K Under Pressure. *Nat. Mater.* **2009,** *8*, 630-633.
(15) Millican, J. N.; Phelan, D.; Thomas, E. L.; Leão, J. B.; Carpenter, E. Pressure-induced Effects on the Structure of the FeSe Superconductor. *Solid State Commun.* **2009,** *149*, 707-710.
(16) Bendele, M.; Ichsanow, A.; Pashkevich, Y.; Keller, L.; Strässle, T.; Gusev, A.; Pomjakushina, E.; Conder, K.; Khasanov, R.; Keller, H. Coexistence of Superconductivity and Magnetism in $FeSe_{1-x}$ Under Pressure. *Phys. Rev. B* **2012,** *85*, 064517.
(17) Yeh, K.-W.; Huang, T.-W.; Huang, Y.-l.; Chen, T.-K.; Hsu, F.-C.; Wu, P. M.; Lee, Y.-C.; Chu, Y.-Y.; Chen, C.-L.; Luo, J.-Y.; Yan, D.-C.; Wu, M.-K. Tellurium Substitution Effect on Superconductivity of the α-phase Iron Selenide. *EPL* **2008,** *84*, 37002.
(18) Liu, T. J.; Hu, J.; Qian, B.; Fobes, D.; Mao, Z. Q.; Bao, W.; Reehuis, M.; Kimber, S. A.; Prokes, K.; Matas, S.; Argyriou, D. N.; Hiess, A.; Rotaru, A.; Pham, H.; Spinu, L.; Qiu, Y.; Thampy, V.; Savici, A. T.; Rodriguez, J. A.; Broholm, C. From (pi,0) Magnetic Order to Superconductivity with (pi,pi) Magnetic Resonance in $Fe_{1.02}Te_{1-x}Se_x$. *Nat. Mater.* **2010,** *9*, 716-720.
(19) Moore, S. A.; Curtis, J. L.; Di Giorgio, C.; Lechner, E.; Abdel-Hafiez, M.; Volkova, O. S.; Vasiliev, A. N.; Chareev, D. A.; Karapetrov, G.; Iavarone, M. Evolution of the superconducting

properties in $FeSe_{1-x}S_x$. *Phys. Rev. B* **2015,** *92*, 235113.
(20) Guo, J.; Jin, S.; Wang, G.; Wang, S.; Zhu, K.; Zhou, T.; He, M.; Chen, X. Superconductivity in the iron selenide $K_xFe_2Se_2$ ($0 \leq x \leq 1.0$). *Phys. Rev. B* **2010,** *82*, 180520.
(21) Wang, A. F.; Ying, J. J.; Yan, Y. J.; Liu, R. H.; Luo, X. G.; Li, Z. Y.; Wang, X. F.; Zhang, M.; Ye, G. J.; Cheng, P.; Xiang, Z. J.; Chen, X. H. Superconductivity at 32 K in single-crystalline $Rb_xFe_{2-y}Se_2$. *Phys. Rev. B* **2011,** *83*, 060512.
(22) Telesca, D.; Nie, Y.; Budnick, J. I.; Wells, B. O.; Sinkovic, B. Impact of valence states on the superconductivity of iron telluride and iron selenide films with incorporated oxygen. *Phys. Rev. B* **2012,** *85*, 214517.
(23) Lei, B.; Cui, J. H.; Xiang, Z. J.; Shang, C.; Wang, N. Z.; Ye, G. J.; Luo, X. G.; Wu, T.; Sun, Z.; Chen, X. H. Evolution of High-Temperature Superconductivity from a Low-T_c Phase Tuned by Carrier Concentration in FeSe Thin Flakes. *Phys. Rev. Lett.* **2016,** *116*, 077002.
(24) Lu, N.; Zhang, P.; Zhang, Q.; Qiao, R.; He, Q.; Li, H.-B.; Wang, Y.; Guo, J.; Zhang, D.; Duan, Z.; Li, Z.; Wang, M.; Yang, S.; Yan, M.; Arenholz, E.; Zhou, S.; Yang, W.; Gu, L.; Nan, C.-W.; Wu, J.; Tokura, Y.; Yu, P. Electric-field control of tri-state phase transformation with a selective dual-ion switch. *Nature* **2017,** *546*, 124.
(25) Cui, Y.; Zhang, G.; Li, H.; Lin, H.; Zhu, X.; Wen, H.-H.; Wang, G.; Sun, J.; Ma, M.; Li, Y.; Gong, D.; Xie, T.; Gu, Y.; Li, S.; Luo, H.; Yu, P.; Yu, W. Protonation induced high-T_c phases in iron-based superconductors evidenced by NMR and magnetization measurements. *Sci. Bull.* **2017**.
(26) Wang, Q.; Li, Z.; Zhang, W.; Zhang, Z.; Zhang, J.; Li, W.; Ding, H.; Ou, Y.; Deng, P.; Chang, K.; Wen, J.; Song, C.; He, K.; Jia, J.; Ji, S.; Wang, Y.; Wang, L.; Chen, X.; Ma, X.; Xue, Q.-K. Interface-Induced High-Temperature Superconductivity in Single Unit-Cell FeSe Films on $SrTiO_3$. *Chin. Phys. Lett.* **2012,** *29*, 037402.
(27) Zhang, W.; Sun, Y.; Zhang, J.; Li, F.; Guo, M.; Zhao, Y.; Zhang, H.; Peng, J.; Xing, Y.; Wang, H.; Fujita, T.; Hirata, A.; Li, Z.; Ding, H.; Tang, C.; Wang, M.; Wang, Q.; He, K.; Ji, S.; Chen, X.; Wang, J.; Xia, Z.; Li, L.; Wang, Y.; Wang, J.; Wang, L.; Chen, M.; Xue, Q.-K.; Ma, X. Direct Observation of High-Temperature Superconductivity in One-Unit-Cell FeSe Films. *Chin. Phys. Lett.* **2014,** *31*, 017401.
(28) Zhang, W.; Li, Z.; Li, F.; Zhang, H.; Peng, J.; Tang, C.; Wang, Q.; He, K.; Chen, X.; Wang, L.; Ma, X.; Xue, Q.-K. Interface Charge Doping Effects on Superconductivity of Single-unit-cell FeSe Films on $SrTiO_3$ Substrates. *Phys. Rev. B* **2014,** *89*, 060506(R).
(29) Peng, R.; Shen, X. P.; Xie, X.; Xu, H. C.; Tan, S. Y.; Xia, M.; Zhang, T.; Cao, H. Y.; Gong, X. G.; Hu, J. P.; Xie, B. P.; Feng, D. L. Measurement of an Enhanced Superconducting Phase and a Pronounced Anisotropy of the Energy Gap of a Strained FeSe Single Layer in FeSe/Nb: $SrTiO_3$/$KTaO_3$ Heterostructures Using Photoemission Spectroscopy. *Phys. Rev. Lett.* **2014,** *112*, 107001.
(30) He, S.; He, J.; Zhang, W.; Zhao, L.; Liu, D.; Liu, X.; Mou, D.; Ou, Y.-B.; Wang, Q.-Y.; Li, Z.; Wang, L.; Peng, Y.; Liu, Y.; Chen, C.; Yu, L.; Liu, G.; Dong, X.; Zhang, J.; Chen, C.; Xu, Z.; Chen, X.; Ma, X.; Xue, Q.; Zhou, X. J. Phase diagram and electronic indication of high-temperature superconductivity at 65 K in single-layer FeSe films. *Nat. Mater.* **2013,** *12*, 605-610.
(31) Liu, D.; Zhang, W.; Mou, D.; He, J.; Ou, Y.-B.; Wang, Q.-Y.; Li, Z.; Wang, L.; Zhao, L.; He, S.; Peng, Y.; Liu, X.; Chen, C.; Yu, L.; Liu, G.; Dong, X.; Zhang, J.; Chen, C.; Xu, Z.; Hu, J.; Chen, X.; Ma, X.; Xue, Q.; Zhou, X. J. Electronic Origin of High-temperature Superconductivity in Single-layer FeSe Superconductor. *Nat. Commun.* **2012,** *3*, 931.
(32) Tan, S.; Zhang, Y.; Xia, M.; Ye, Z.; Chen, F.; Xie, X.; Peng, R.; Xu, D.; Fan, Q.; Xu, H.; Jiang, J.; Zhang, T.; Lai, X.; Xiang, T.; Hu, J.; Xie, B.; Feng, D. Interface-induced Superconductivity and Strain-dependent Spin Density Waves in FeSe/$SrTiO_3$ Thin Films. *Nat. Mater.* **2013,** *12*, 634-640.
(33) Cui, Y. T.; Moore, R. G.; Zhang, A. M.; Tian, Y.; Lee, J. J.; Schmitt, F. T.; Zhang, W. H.; Li, W.; Yi, M.; Liu, Z. K.; Hashimoto, M.; Zhang, Y.; Lu, D. H.; Devereaux, T. P.; Wang, L. L.; Ma, X. C.; Zhang, Q. M.; Xue, Q. K.; Lee, D. H.; Shen, Z. X. Interface Ferroelectric Transition near the Gap-Opening Temperature in a Single-Unit-Cell FeSe Film Grown on Nb-Doped $SrTiO_3$ Substrate. *Phys. Rev. Lett.* **2015,** *114*, 037002.
(34) Ge, J.; Liu, Z.; Liu, C.; Gao, C.; Qian, D.; Xue, Q.-K.; Liu, Y.; Jia, J. Superconductivity

Above 100 K in Single-layer FeSe Films on Doped $SrTiO_3$. *Nat. Mater.* **2015,** *14*, 285-289.
(35) Wang, Z. F.; Zhang, H.; Liu, D.; Liu, C.; Tang, C.; Song, C.; Zhong, Y.; Peng, J.; Li, F.; Nie, C.; Wang, L.; Zhou, X. J.; Ma, X.; Xue, Q. K.; Liu, F. Topological Edge States in a High-temperature Superconductor FeSe/$SrTiO_3$(001) Film. *Nat. Mater.* **2016,** *15*, 968-973.
(36) Phan, G. N.; Nakayama, K.; Kanayama, S.; Kuno, M.; Sugawara, K.; Sato, T.; Takahashi, T. High-Temperature Superconductivity and Lattice Relaxation in Lithium-Deposited FeSe on $SrTiO_3$. *J. Phys. Soc. Jpn.* **2017,** *86*, 033706.
(37) Tang, C.; Liu, C.; Zhou, G.; Li, F.; Ding, H.; Li, Z.; Zhang, D.; Li, Z.; Song, C.; Ji, S.; He, K.; Wang, L.; Ma, X.; Xue, Q.-K. Interface-enhanced Electron-phonon Coupling and High-temperature Superconductivity in Potassium-coated Ultrathin FeSe Films on $SrTiO_3$. *Phys. Rev. B* **2016,** *93*, 020507.
(38) Song, C.; Zhang, H.; Zhong, Y.; Hu, X.; Ji, S.; Wang, L.; He, K.; Ma, X.; Xue, Q.-K. Observation of Double-Dome Superconductivity in Potassium-Doped FeSe Thin Films. *Phys. Rev. Lett.* **2016,** *116*, 157001.
(39) Miyata, Y.; Nakayama, K.; Sugawara, K.; Sato, T.; Takahashi, T. High-temperature Superconductivity in Potassium-coated Multilayer FeSe Thin Films. *Nat. Mater.* **2015,** *14*, 775-779.
(40) Tang, C.; Zhang, D.; Zang, Y.; Liu, C.; Zhou, G.; Li, Z.; Zheng, C.; Hu, X.; Song, C.; Ji, S.; He, K.; Chen, X.; Wang, L.; Ma, X.; Xue, Q.-K. Superconductivity Dichotomy in K-coated Single and Double Unit Cell FeSe Films on $SrTiO_3$. *Phys. Rev. B* **2015,** *92*, 180507.
(41) Zhang, W. H.; Liu, X.; Wen, C. H. P.; Peng, R.; Tan, S. Y.; Xie, B. P.; Zhang, T.; Feng, D. L. Effects of Surface Electron Doping and Substrate on the Superconductivity of Epitaxial FeSe Films. *Nano Lett.* **2016,** *16*, 1969-1973.
(42) Wang, Q. Y.; Zhang, W. H.; Zhang, Z. C.; Sun, Y.; Xing, Y.; Wang, Y. Y.; Wang, L. L.; Ma, X. C.; Xue, Q. K.; Wang, J. Thickness dependence of superconductivity and superconductor–insulator transition in ultrathin FeSe films on $SrTiO_3$ (001) substrate. *2D Mater.* **2015,** *2*, 044012.
(43) Shiogai, J.; Ito, Y.; Mitsuhashi, T.; Nojima, T.; Tsukazaki, A. Electric-field-induced superconductivity in electrochemically etched ultrathin FeSe films on $SrTiO_3$ and MgO. *Nat. Phys.* **2016,** *12*, 42-46.
(44) Shiogai, J.; Miyakawa, T.; Ito, Y.; Nojima, T.; Tsukazaki, A. Unified trend of superconducting transition temperature versus Hall coefficient for ultrathin FeSe films prepared on different oxide substrates. *Phys. Rev. B* **2017,** *95*, 115101.
(45) Zhao, W.; Li, M.; Chang, C.-Z.; Jiang, J.; Wu, L.; Liu, C.; Moodera, J. S.; Zhu, Y.; Chan, M. H. W. Direct imaging of electron transfer and its influence on superconducting pairing at FeSe/$SrTiO_3$ interface. *Sci. Adv.* **2018,** *4*, eaao2682.
(46) Si, W.; Lin, Z.-W.; Jie, Q.; Yin, W.-G.; Zhou, J.; Gu, G.; Johnson, P. D.; Li, Q. Enhanced superconducting transition temperature in $FeSe_{0.5}Te_{0.5}$ thin films. *Appl. Phys. Lett.* **2009,** *95*, 052504.
(47) Yuan, P.; Xu, Z.; Ma, Y.; Sun, Y.; Tamegai, T. Optimization of Deposition Conditions to Grow High-Quality Fe-Se-Te Thin Films. *IEEE Trans. Appl. Supercond.* **2017,** *27*, 1-5.
(48) Imai, Y.; Akiike, T.; Hanawa, M.; Tsukada, I.; Ichinose, A.; Maeda, A.; Hikage, T.; Kawaguchi, T.; Ikuta, H. Systematic Comparison of Eight Substrates in the Growth of $FeSe_{0.5}Te_{0.5}$ Superconducting Thin Films. *Appl. Phys. Express* **2010,** *3*, 043102.
(49) Mele, P.; Matsumoto, K.; Fujita, K.; Yoshida, Y.; Kiss, T.; Ichinose, A.; Mukaida, M. Fe–Te–Se epitaxial thin films with enhanced superconducting properties. *Supercond. Sci. Technol.* **2012,** *25*, 084021.
(50) Nabeshima, F.; Imai, Y.; Ichinose, A.; Tsukada, I.; Maeda, A. Growth and transport properties of FeSe/FeTe superlattice thin films. *Jpn. J. Appl. Phys.* **2017,** *56*, 020308.
(51) Nabeshima, F.; Imai, Y.; Hanawa, M.; Tsukada, I.; Maeda, A. Enhancement of the Superconducting Transition Temperature in FeSe Epitaxial Thin Films by Anisotropic Compression. *Appl. Phys. Lett.* **2013,** *103*, 172602.
(52) Tsukada, I.; Ichinose, A.; Nabeshima, F.; Imai, Y.; Maeda, A. Origin of Lattice Compression of $FeSe_{1-x}Te_x$ Thin Films on CaF_2 Substrates. *AIP Adv.* **2016,** *6*, 095314.
(53) Qiu, W.; Ma, Z.; Patel, D.; Sang, L.; Cai, C.; Shahriar Al Hossain, M.; Cheng, Z.; Wang,

X.; Dou, S. X. The Interface Structure of FeSe Thin Film on CaF_2 Substrate and its Influence on the Superconducting Performance. *ACS Appl. Mater. Interfaces* **2017,** *9*, 37446-37453.
(54) Bellingeri, E.; Pallecchi, I.; Buzio, R.; Gerbi, A.; Marrè, D.; Cimberle, M. R.; Tropeano, M.; Putti, M.; Palenzona, A.; Ferdeghini, C. T_c=21K in epitaxial $FeSe_{0.5}Te_{0.5}$ thin films with biaxial compressive strain. *Appl. Phys. Lett.* **2010,** *96*, 102512.
(55) Wang, M. J.; Luo, J. Y.; Huang, T. W.; Chang, H. H.; Chen, T. K.; Hsu, F. C.; Wu, C. T.; Wu, P. M.; Chang, A. M.; Wu, M. K. Crystal Orientation and Thickness Dependence of the Superconducting Transition Temperature of Tetragonal $FeSe_{1-x}$ Thin Films. *Phys. Rev. Lett.* **2009,** *103*, 117002.
(56) Tsukada, A.; Luna, K. E.; Hammond, R. H.; Beasley, M. R.; Zhao, J. F.; Risbud, S. H. Pulsed laser deposition conditions and superconductivity of FeSe thin films. *Applied Physics A* **2011,** *104*, 311-318.
(57) Nie, Y. F.; Brahimi, E.; Budnick, J. I.; Hines, W. A.; Jain, M.; Wells, B. O. Suppression of superconductivity in FeSe films under tensile strain. *Appl. Phys. Lett.* **2009,** *94*, 242505.
(58) Kouno, S.; Sato, Y.; Katayama, Y.; Ichinose, A.; Asami, D.; Nabeshima, F.; Imai, Y.; Maeda, A.; Ueno, K. Superconductivity at 38 K in an electrochemical interface between ionic liquid and $Fe(Se_{0.8}Te_{0.2})$ on various substrates. *arXiv:1805.02380* **2018**.
(59) Schneider, R.; Zaitsev, A. G.; Fuchs, D.; H, V. L. Superconductor-insulator Quantum Phase Transition in Disordered FeSe Thin Films. *Phys. Rev. Lett.* **2012,** *108*, 257003.
(60) Si, W.; Jie, Q.; Wu, L.; Zhou, J.; Gu, G.; Johnson, P. D.; Li, Q. Superconductivity in epitaxial thin films of $Fe_{1.08}Te{:}O_x$. *Phys. Rev. B* **2010,** *81*, 092506.
(61) Nie, Y. F.; Telesca, D.; Budnick, J. I.; Sinkovic, B.; Wells, B. O. Superconductivity induced in iron telluride films by low-temperature oxygen incorporation. *Phys. Rev. B* **2010,** *82*, 020508.
(62) Zhou, G.; Zhang, D.; Liu, C.; Tang, C.; Wang, X.; Li, Z.; Song, C.; Ji, S.; He, K.; Wang, L.; Ma, X.; Xue, Q.-K. Interface Induced High Temperature Superconductivity in Single Unit-cell FeSe on $SrTiO_3$(110). *Appl. Phys. Lett.* **2016,** *108*, 202603.
(63) Sun, Y.; Zhang, W.; Xing, Y.; Li, F.; Zhao, Y.; Xia, Z.; Wang, L.; Ma, X.; Xue, Q. K.; Wang, J. High temperature superconducting FeSe films on SrTiO3 substrates. *Sci. Rep.* **2014,** *4*, 6040.
(64) Lei, B.; Xiang, Z. J.; Lu, X. F.; Wang, N. Z.; Chang, J. R.; Shang, C.; Zhang, A. M.; Zhang, Q. M.; Luo, X. G.; Wu, T.; Sun, Z.; Chen, X. H. Gate-tuned superconductor-insulator transition in (Li,Fe)OHFeSe. *Phys. Rev. B* **2016,** *93*, 060501.
(65) Maeda, A.; Nabeshima, F.; Takahashi, H.; Okada, T.; Imai, Y.; Tsukada, I.; Hanawa, M.; Komiya, S.; Ichinose, A. Synthesis, characterization, Hall effect and THz conductivity of epitaxial thin films of Fe chalcogenide superconductors. *Appl. Surf. Sci.* **2014,** *312*, 43-49.
(66) Rullier-Albenque, F.; Colson, D.; Forget, A.; Thuéry, P.; Poissonnet, S. Hole and electron contributions to the transport properties of $Ba(Fe_{1-x}Ru_x)_2As_2$ single crystals. *Phys. Rev. B* **2010,** *81*, 224503.
(67) Rullier-Albenque, F.; Colson, D.; Forget, A.; Alloul, H. Hall Effect and Resistivity Study of the Magnetic Transition, Carrier Content, and Fermi-Liquid Behavior in $Ba(Fe_{1-x}Co_x)_2As_2$. *Phys. Rev. Lett.* **2009,** *103*, 057001.
(68) Terashima, T.; Kikugawa, N.; Kasahara, S.; Watashige, T.; Matsuda, Y.; Shibauchi, T.; Uji, S. Magnetotransport study of the pressure-induced antiferromagnetic phase in FeSe. *Phys. Rev. B* **2016,** *93*, 180503.
(69) Huynh, K. K.; Tanabe, Y.; Urata, T.; Oguro, H.; Heguri, S.; Watanabe, K.; Tanigaki, K. Electric transport of a single-crystal iron chalcogenide FeSe superconductor: Evidence of symmetry-breakdown nematicity and additional ultrafast Dirac cone-like carriers. *Phys. Rev. B* **2014,** *90*, 144516.
(70) Sun, Y.; Pyon, S.; Tamegai, T. Electron carriers with possible Dirac-cone-like dispersion in $FeSe_{1-x}S_x$ (x = 0 and 0.14) single crystals triggered by structural transition. *Phys. Rev. B* **2016,** *93*, 104502.
(71) Shen, B.; Feng, Z.-P.; Huang, J.-W.; Hu, Y.; Gao, Q.; Li, C.; Yu, X.; Liu, G.-D.; Yu, L.; Zhao, L.; Jin, K.; Zhou, X. J. Electronic structure and nematic phase transition in superconducting multiple-layer FeSe films grown by pulsed laser deposition method. *Chin.*

Phys. B **2017,** *26*, 077402.
(72) Mizuguchi, Y.; Tomioka, F.; Tsuda, S.; Yamaguchi, T.; Takano, Y. FeTe as a candidate material for new iron-based superconductor. *Physica C* **2009,** *469*, 1027-1029.
(73) Zhuang, J. C.; Yeoh, W. K.; Cui, X. Y.; Kim, J. H.; Shi, D. Q.; Shi, Z. X.; Ringer, S. P.; Wang, X. L.; Dou, S. X. Enhancement of transition temperature in $Fe_xSe_{0.5}Te_{0.5}$ film via iron vacancies. *Appl. Phys. Lett.* **2014,** *104*, 262601.
(74) Miedema, P. S.; de Groot, F. M. F. The iron L edges: Fe 2p X-ray absorption and electron energy loss spectroscopy. *J. Electron. Spectrosc. Relat. Phenom.* **2013,** *187*, 32-48.
(75) Pearson, D. H.; Ahn, C. C.; Fultz, B. White lines and d-electron occupancies for the 3d and 4d transition metals. *Phys. Rev. B* **1993,** *47*, 8471-8478.
(76) Pearson, D. H.; Fultz, B.; Ahn, C. C. Measurements of *3d* state occupancy in transition metals using electron energy loss spectrometry. *Appl. Phys. Lett.* **1988,** *53*, 1405-1407.
(77) Chen, K.-F.; Lo, S.-C.; Chang, L.; Egerton, R.; Kai, J.-J.; Lin, J.-J.; Chen, F.-R. Valence state map of iron oxide thin film obtained from electron spectroscopy imaging series. *Micron* **2007,** *38*, 354-361.
(78) Graetz, J.; Ahn, C. C.; Ouyang, H.; Rez, P.; Fultz, B. White lines and *d*-band occupancy for the *3d* transition-metal oxides and lithium transition-metal oxides. *Phys. Rev. B* **2004,** *69*, 235103.
(79) Cantoni, C.; Mitchell, J. E.; May, A. F.; McGuire, M. A.; Idrobo, J. C.; Berlijn, T.; Dagotto, E.; Chisholm, M. F.; Zhou, W.; Pennycook, S. J.; Sefat, A. S.; Sales, B. C. Orbital occupancy and charge doping in iron-based superconductors. *Adv. Mater.* **2014,** *26*, 6193-6198.
(80) Hu, H.; Zuo, J.-M.; Wen, J.; Xu, Z.; Lin, Z.; Li, Q.; Gu, G.; Park, W. K.; Greene, L. H. Phase separation in the iron chalcogenide superconductor $Fe_{1+y}Te_xSe_{1-x}$. *New J. Phys.* **2011,** *13*, 053031.
(81) Singh, D. J. Electronic structure and doping in $BaFe_2As_2$ and LiFeAs: Density functional calculations. *Phys. Rev. B* **2008,** *78*, 094511.
(82) Subedi, A.; Zhang, L.; Singh, D. J.; Du, M. H. Density functional study of FeS, FeSe, and FeTe: Electronic structure, magnetism, phonons, and superconductivity. *Phys. Rev. B* **2008,** *78*, 134514.
(83) Egerton, R. F. *Electron Energy-Loss Spectroscopy in the Electron Microscope*, 3 ed.; Springer US: 2011; p XII, 491.
(84) de Groot, F. M. F. X-ray absorption and dichroism of transition metals and their compounds. *J. Electron Spectrosc. Relat. Phenom.* **1994,** *67*, 529-622.
(85) Leapman, R. D.; Grunes, L. A.; Fejes, P. L. Study of the L_{23} edges in the *3d* transition metals and their oxides by electron-energy-loss spectroscopy with comparisons to theory. *Phys. Rev. B* **1982,** *26*, 614-635.
(86) Colliex, C.; Manoubi, T.; Ortiz, C. Electron-energy-loss-spectroscopy near-edge fine structures in the iron-oxygen system. *Phys. Rev. B* **1991,** *44*, 11402-11411.
(87) Taftø, J.; Krivanek, O. L. Site-Specific Valence Determination by Electron Energy-Loss Spectroscopy. *Phys. Rev. Lett.* **1982,** *48*, 560-563.
(88) van Aken, P. A.; Liebscher, B. Quantification of ferrous/ferric ratios in minerals: new evaluation schemes of Fe L_{23} electron energy-loss near-edge spectra. *Phys. Chem. Minerals* **2002,** *29*, 188-200.
(89) Sparrow, T. G.; Williams, B. G.; Rao, C. N. R.; Thomas, J. M. L3/L2 white-line intensity ratios in the electron energy-loss spectra of 3d transition-metal oxides. *Chem. Phys. Lett.* **1984,** *108*, 547-550.

Chapter 6

6 Tuning Superconductivity in FeSe Thin Films by a Magnesium Coating Process

6.1 Introduction

The HTS achieved in FeSe superconductors reflects the exotic and unique properties in this type of unconventional superconductors. Although doping process has been confirmed to dramatically affect the iron-based superconductivity, a comprehensive understanding in regard to the doping dependence of FeSe superconductivity is still being expected. Various kinds of approached have been developed to investigate the doping effect onto FeSe superconductors and boosted T_c was realized in many ways. It is well accepted that the limited electron dopants transferred from STO substrate is not sufficient to drive the HTS in the second and upper unit-cells[1-4]. A challenging issue has been raised to call for new ideas to supply more charge carriers. Miyata *et al*.[5] firstly reported the revival of HTS (~ 48 K) in multi-layer FeSe thin films by an *in-situ* post-deposition of K element. Extra electrons were introduced to FeSe thin films and the highest level of electron-doping in FeSe thin films was achieved. Shiogai *et al*.[6] reported a novel method involving electrochemical etching and electric double-layer transistor to realize the accurate thickness controlling as well as the electron-doping into ultrathin FeSe thin films. Lei *et al*.[7] published the success of introducing massive electron carriers into FeSe thin flakes by a liquid-gating technique. A T_c^{onset} of 48 K was induced in bulk FeSe and a Lifshitz transition was observed, indicating the dramatic change happening in the Fermi energy as a result of the applied gate voltage. The deposition effect of Li element onto FeSe thin films was studied by Phan *et al*.[8] An enhanced T_c of 43 K was reported in a heavily-doped multilayer FeSe film. However, the lattice relaxation found in Li-doped FeSe films is in sharp contrast to the case of K-doping. Apart from the common scenarios of electron-doping, Sun *et al*.[9] transformed the superconducting phase of FeSe single-crystal from low-T_c to high-T_c by increasing pressure. They pointed out that the pressurization effect brings about inter-band spin fluctuation and reconstructs the Fermi surface of FeSe to a

hole-dominated condition which is similar to the high-T_c FeAs superconductors and opposite to the heavily electron-doped FeSe thin films. Inspired by the works of alkali metal (K, Li) deposition, a similar post-deposition process is performed onto the PLD-prepared FeSe thin films with a typical alkaline-earth metal, Mg, which is much stable than K or Li. External electron-doping from the simple Mg-coating process and the corresponding enhancement in the superconducting performance of FeSe thin films are expected. Two types of FeSe thin films with different thicknesses and resistivity behaviors are used in this work: (1) FeSe film with a practical thickness of ~ 60 nm and T_c^{onset} as 10.7 K; (2) ultrathin FeSe film (~ 7 nm) which exhibits semiconducting behavior in the ρ-T curve.

6.1.1 Enhanced Superconductivity in FeSe Films with a Practical Thickness by a Mg-Coating Processes

In this work, the superconducting performance of 60 nm FeSe films was found improved by an *in-situ* Mg-coating process. A distinct enhancement of T_c was obtained from 10.7 K in a pristine FeSe film to 13.4 K in the Mg-coated FeSe with optimized deposition time of Mg. The measurement of Hall coefficient confirmed the trace of electron-doping introduced by a mild Mg-coating process. However, the concentration of electron-type carriers was not high enough to overturn the hole-dominant condition in all the Mg-coated FeSe samples in this work. It is probably due to the fact that Mg only diffused into top few layers of FeSe thin films, which was revealed by Cross-sectional TEM images and EELS results. Hence, the Mg was coated on FeSe in the present work rather than the intercalated case of KFe_2Se_2 formed by K-intercalated FeSe[10-11]. With increasing the amount of Mg-coating, a dome-shaped Mg-content dependence of T_c is observed. That is to say T_c degrades under over-coated circumstance. Supported by XRD results, excessive content of Mg-coating would lead to the destruction in FeSe lattice and a consequent collapse of superconductivity of FeSe thin films. This work took examples from the realizations of enhanced T_c in K-coated[5, 12-16] multilayer FeSe thin films and firstly attempted to study how the superconducting performance of FeSe thick film (60 nm) is affected after being coated with the alkaline-earth-metal, Mg, onto the surface. Although the positive electron-doping effect on T_c (~ 25 % increment upon 10.7 K) by the Mg-coating process was proved by Hall measurements, the improvement was not comparable to the scenario of K-coated multilayer FeSe films. The possible reason could be the difficulty for Mg to diffuse into

thick film, and also the less electron-type carriers that can be provided by Mg than by K.

In order to investigate the influence of Mg content on the FeSe thin film, the thickness of FeSe layer was fixed at 60 nm which shows a reproducible T_c of 10.7 K. Right after the deposition of FeSe film, Mg-coating process was performed by directly switching a Mg-target to upfront. All the deposition conditions were kept same as those of the FeSe layer (300 ℃, 2.0 W output power, < 5 × 10^{-4} Pa). By controlling the deposition time of Mg as 1.5, 3, 10, and 20 minutes, a batch of Mg-coated FeSe thin films are obtained and denoted in the rest of the article as #FM0 (pristine FeSe), #FM1, #FM2, #FM3, and #FM4, respectively.

The superconducting performance of the samples was first characterized. Fig. 6-1 (a) shows the temperature dependence of electrical resistivity for all thin films (#FM0, #FM1, #FM2, #FM3, and #FM4) in the magnified temperature range (4 K - 20 K) while the full range up to 300 K is plotted in the inset. The ρ-T curves with positive slopes are exhibited in all of them, indicating a classical metallic behavior. At normal state, the resistivity of FeSe films keeps at low level owing to the good conductivity after introducing small amount of Mg. Nevertheless, it dramatically increases in #FM4 probably due to the severe scattering effect in the over-coated sample. In order to recognize the variation of T_c clearly, d(R/R_{300K})/dT curves are illustrated in Fig. 6-1 (b). In the pristine FeSe film (#FM0), the resistivity drops sharply at $T_c^{onset} \approx 10.7$ K and reaches zero at $T_c^{zero} \approx 9.8$ K. By coating Mg on FeSe surface, higher T_c^{onset} was obtained and in sample #FM2 with the optimized amount of Mg-coating, the highest $T_c^{onset} \approx 13.4$ K is approximately 1.5 times higher than that of FeSe single-crystal bulks. Further increasing the amount of Mg-coating, a slight degradation in T_c^{onset} was observed in #FM3 but T_c^{onset} still remains higher than that of the pristine #FM0. Interestingly, an incomplete transition down to 4.2 K is detected in sample #FM4 with the longest deposition time of Mg. The possible explanation will be given below combined with other characterizations including XRD and Hall measurement. The temperature dependence of the upper critical magnetic field H_{c2}(T) is plotted in Fig. 6-1 (c) and the linear extrapolations to T = 0 K are shown in the inset. The H_{c2} in this work was determined based on the 50 % point during the superconducting transition, T_c^{mid}. The H_{c2} result of #FM4 is not shown here because of the incompleteness of superconducting transition. The estimated H_{c2} in the other four samples are about 27.8 T, 31.2 T, 32.7 T and 29.1 T for #FM0, #FM1, #FM2, and #FM3, respectively. One can clearly notice that FeSe thin films with Mg-coating exhibit higher H_{c2} than the pristine

one. The highest H_{c2} of 32.7 T obtained in #FM2 shows good potential for the high-field applications based on the atmosphere-stable FeSe superconducting films. According to the ρ-T results above, the present work is the first one to achieve enhancement of superconducting transition temperature in atmosphere-stable FeSe thin films with a practical thickness (60 nm) via a simple Mg-coating process. Despite the current T_c is not comparable to the result of Te-substituted FeSe films[17], Li-doped[8] or K-doped[5, 12-16] multilayer FeSe films, the finding here is a new inspiring way to improve the superconducting performance of the regular FeSe thin films prepared by PLD method.

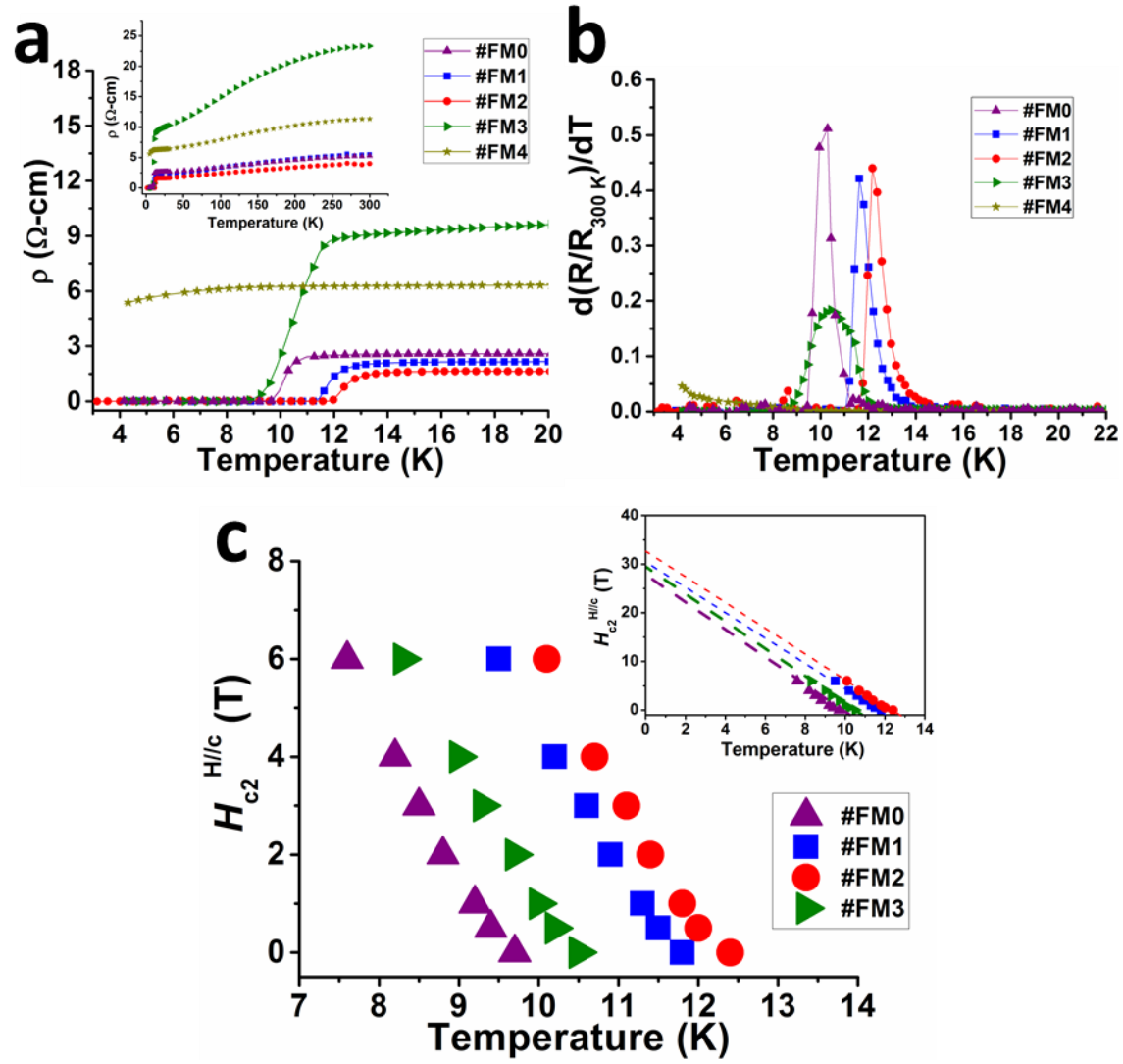

Figure 6-1. Temperature dependences of Resistivity and the derived plot of upper critical field H_{c2} results of all the thin film samples with different deposition time of Mg. (a) ρ-T curves with the temperature range near T_c. Inset: the ρ-T curves in a full temperature range from room temperature to 4.2 K. (b) $d(R/R_{300K})/dT$ curves with the temperature range near T_c. (c) Plot of H_{c2} as a function of T_c^{mid}. Inset: the linear extrapolations to T = 0 K.

Fig. 6-2 shows the cross-sectional STEM-EDS mappings and EELS spectra of #FM2 (highest T_c) to investigate the elemental distribution of Mg-coated FeSe thin

films. The lamella for STEM characterization was prepared by an *in-situ* lift-out technique performed in a FIB instrument and it is less than one hundred nanometers in thickness. The EDS-mappings of Mg-*K*, Fe-*K*, and Se-*K* are displayed in Fig. 6-2 (a). Obviously, a homogeneous FeSe film with the thickness of ~ 60 nm is observed with a Mg-rich region appearing at the top surface of FeSe layer. No Mg was found distributing into the body of FeSe film. Considering of the relative low-accuracy of EDS, high-resolution EELS analysis was also performed to clarify how far Mg diffuses into FeSe layer. As shown in the lower image in Fig. 6-2 (b), one hundred energy loss spectra across the entire cross-section from gold capping layer to CaF_2 substrate were collected and illustrated as a contour image. The scale of *y*-axis (position) is identical to the original ADF image on the left side. The level of darkness represents the intensity of the characteristic edges. EELS results are very sensitive in distinguishing different elements because that the mode of orbital excitation in every element is unique. As the Mg-*K* edge and Se-$L_{3,2}$ edges appears at the energy of ~ 1320 eV and ~ 1450 eV, respectively, the energy loss range was set from 1200 eV to 1700 eV to ensure both of the elements can be simultaneously analyzed. By comparing the contrast features, the detailed distribution of Mg and Se elements are clearly seen. In addition to the Mg coating on the top of FeSe layer which was verified by EDS-mappings, a region with the existences of both Mg-*K* and Se-$L_{3,2}$ edges is found at Mg/FeSe interface (the marked area within two horizontal dashed lines) according to the contrast information. Three spectra were separately picked (the middle of Mg coating layer, the Mg/FeSe interface, and the body of FeSe layer), and depicted in the upper image of Fig. 6-2 (b). Vertical offset was applied for the ease of comparison. It is unambiguous that the spectrum of Mg/FeSe interface exhibits both of the features of Mg-*K* and Se-$L_{3,2}$ edges, while only one of the edge features of Mg or Se element is found in the upper Mg-coating layer or nether FeSe body. Therefore, two conclusions can be made based on the STEM results: (1) Most of the Mg dwelled on the top of FeSe layer. That is to say, almost no Mg element distributes into the FeSe body. It ruled out the samples in this work from the possibility of Mg-intercalation. (2) EELS results revealed that Mg diffused into the top few layers of FeSe film, which might be responsible for the evolution of superconductivity in this work.

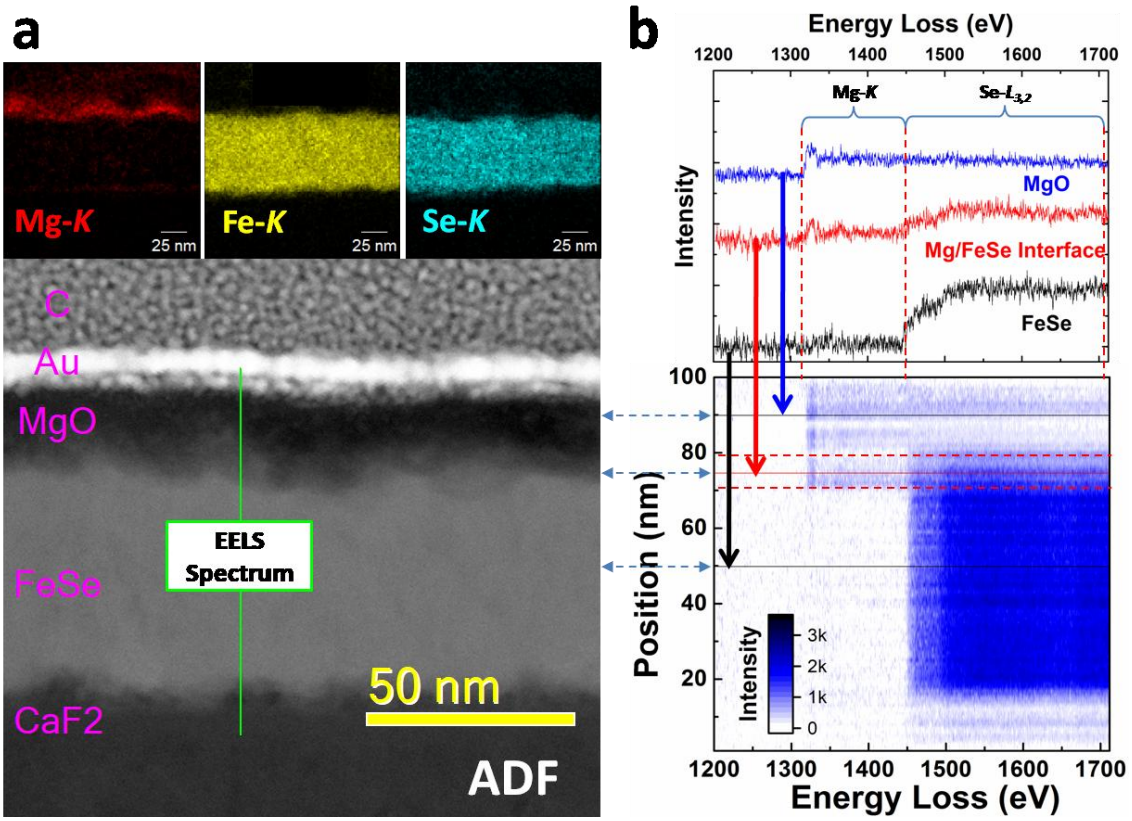

Figure 6-2. The STEM-EDS and EELS results of #FM2 from a cross-sectional view. (a) Lower: a STEM-ADF image showing a cross-section area of #FM2. Upper: EDS mappings for Mg, Fe, and Se elements. Mg-rich region is observed on the top surface of FeSe layer. (b) Lower: the EELS spectra scanning the green strip shown in the ADF image. The scale of *y*-axis is exactly identical to the ADF image. The step size of scanning was set as 0.88 nm. Upper: the separate EELS spectra of three particular positions (MgO, Mg/FeSe interface, and FeSe) indicated as solid lines in the lower image. The vertical dashed lines highlight the approximate energies of Mg-*K* edge (~ 1320 eV) and Se-$L_{3,2}$ edges (~ 1450 eV). The coexistence of Mg-*K* and Se-$L_{3,2}$ edges is detected at Mg/FeSe interface, indicating that Mg only diffused into the top few FeSe layers.

As shown in Fig. 6-1, improvement in superconductivity of FeSe thin films can be achieved by Mg-coating process. It is of great importance to understand its intrinsic enhancement mechanism. It is well known that charge carrier concentration is one of the most crucial factors that determine the superconductivity in FeSe superconductors[2, 5, 18-19]. Considering that Mg element belongs to the group of alkaline-earth-metal in the periodic table, abundant electron carriers are supposed to be provided via Mg doping. Here, Hall measurements were performed to reveal the condition of the charge carriers in all the samples. In Fig. 6-3 (a), the temperature dependences of Hall coefficient (R_{H}) are illustrated. R_{H} is defined as $R_H = \rho_{xy}/B$, where ρ_{xy} stands for the Hall transverse resistivity and B is designated field under fixed temperatures ranging from 20 K to 300 K. From room temperature to 150 K, the R_{H} of all samples is almost temperature

independent. Below 100 K, positive R_H values were obtained in all the samples, indicating a hole-dominated situation of charge carriers. The absolute value of R_H starts to increase from 150 K to lower temperatures, implying the multiband nature in typical FeSe system. Carrier concentration (n) indicates the amount of carriers in unit volume. The correlation between R_H and n is deduced by

$$R_H = \frac{E_y}{j_x B} = \frac{V_H t}{IB} = -\frac{1}{ne}$$

(R_H - Hall coefficient, E_y - induced electric field, j - the current density of the carrier electrons, B - magnetic field, V_H - Hall voltage, t - the thickness of the plate, I - the current across the plate length, e - elementary charge, n - carrier concentration). As n is inversely proportional to R_H, the increasing R_H in positive side at lower temperature region represents that n decreases with lowering temperature. Similar Temperature dependence of R_H is observed in pristine #FM0, lightly-coated #FM1, #FM2 and heavily-coated #FM3. However, large absolute value of R_H is obtained in over-coated #FM4, suggesting a severe reduction in carrier concentration. It could be the result of Mg oxide layer formed on the film surface due to the excessive Mg-coating. The transport property of #FM4 was somehow altered dramatically, which is consistent with the decaying behaviour in the temperature dependence of resistivity (shown in Fig. 6-1 (a)). Thus, Hall measurements offered a strong evidence for the degradation of the superconductivity in #FM4 by revealing the collapse in carrier concentration.

In order to distinguish the tendency of #FM0, #FM1, #FM2 and #FM3, magnified view of R_H in the low-temperature region is shown in the inset of Fig. 6-3 (a). Interestingly, an abnormal lower carrier concentration is found below 80 K in lightly-coated #FM1 which shows higher T_c than #FM0. It might result from a competitive mechanism between "self-doping" and "external electron-doping" in #FM1. Actually, in the pristine FeSe films, the "self-doping" induced by Fe-vacancy disorder exists. The discovery of disorder-induced "self-doping" is raised by Berlijn *et al.*[20] in the system of KFe_2Se_2. By using ARPES technique, they found that Fe-vacancy disorder can provide significant electron concentration (n_e) into the system. This might explain why the pristine FeSe film (#FM0) still shows relatively low R_H value (high carrier concentration). Once Mg is coated onto FeSe films, "external electron-doping" starts to affect the electronic state of FeSe system together with the original "self-doping" mechanism. It is speculated that a "mixed-doping state" exists once the two doping types are comparable to each other. In lightly-coated sample (#FM1), only very little

electron was implanted into FeSe layers. In this case, doping performance would be partly compensated, resulting in even lower n_e than the pristine one (#FM0). Nevertheless, the superconducting performance still improved because some Fe-vacancies were occupied by Mg, which will be discussed in detail later combined with the XRD results. Further increasing the amount of Mg-coating, the effect of "self-doping" was weakened whilst plenty of electron-carriers were introduced into FeSe films, reflecting by the decrease of $|R_H|$ from the positive side in #FM2 and #FM3. As a result, the "external-doping" finally became dominating rather than "self-doping". It is noteworthy that the superconducting performance in #FM3 is not as good as that in #FM2, even though they possess the similar carrier concentration. It is due to the decreased orientation quality of FeSe layer in #FM3, which will be discussed later based on the XRD results. In the case of over-doped #FM4, abrupt deterioration is found in both carrier concentration and superconducting performance. It is ascribed to the severe inter-grain scattering from Mg oxide layer as well as the destruction of superconducting structure resulting from excessive Mg-coating process.

The sign reversal of R_H generally suggests a dramatic change happen in charge-carrier conditions in the form of carrier domination or carrier concentration, or both. The temperature range from 100 K to 200 K of R_H-T results is magnified and shown in Fig. 6-3 (b). It is noted that the sign of R_H of #FM1 and #FM2 changed twice during cooling near 150 K, while the R_H of pristine and over-coated FeSe stayed on the positive side. Sun *et al.*[21] observed similar sign change of R_H in their FeSe and $FeSe_{0.86}S_{0.14}$ single crystals. Clearly, electron-type charge carriers provide more contribution to the transport properties of #FM1 and #FM2 near 150 K. It is the direct evidence that Mg-coating process provided effective electron-type carriers into the FeSe system. However, the external electron-doping was not high enough to completely overturn the hole-dominated condition in pristine FeSe thin film. This explains why the T_c of #FM1 and #FM2 is higher than that of #FM0, but not comparable to the case of K-coated multilayer FeSe[5, 14-15] or liquid-gating treated FeSe thin flakes[7] which showed an electron-dominated state in low-temperature region. Further increasing the deposition time of Mg-coating, no sign of more electron contribution was detected in #FM3 and #FM4. It suggested the limited amount of electron-doping that can be afforded by external Mg-coating. In addition, as the highest thickness of the superconducting FeSe films doped with K was 50-UC[13] with a superconducting gap opened at 46 K, the FeSe layer in this work might be too thick (over 100-UC FeSe) so that the average electron-

doping level was brought down. The result shown in Fig. 6-3 (b) suggests that the sign reversal of R_H acts as a signature of higher T_c value induced by electron-doping.

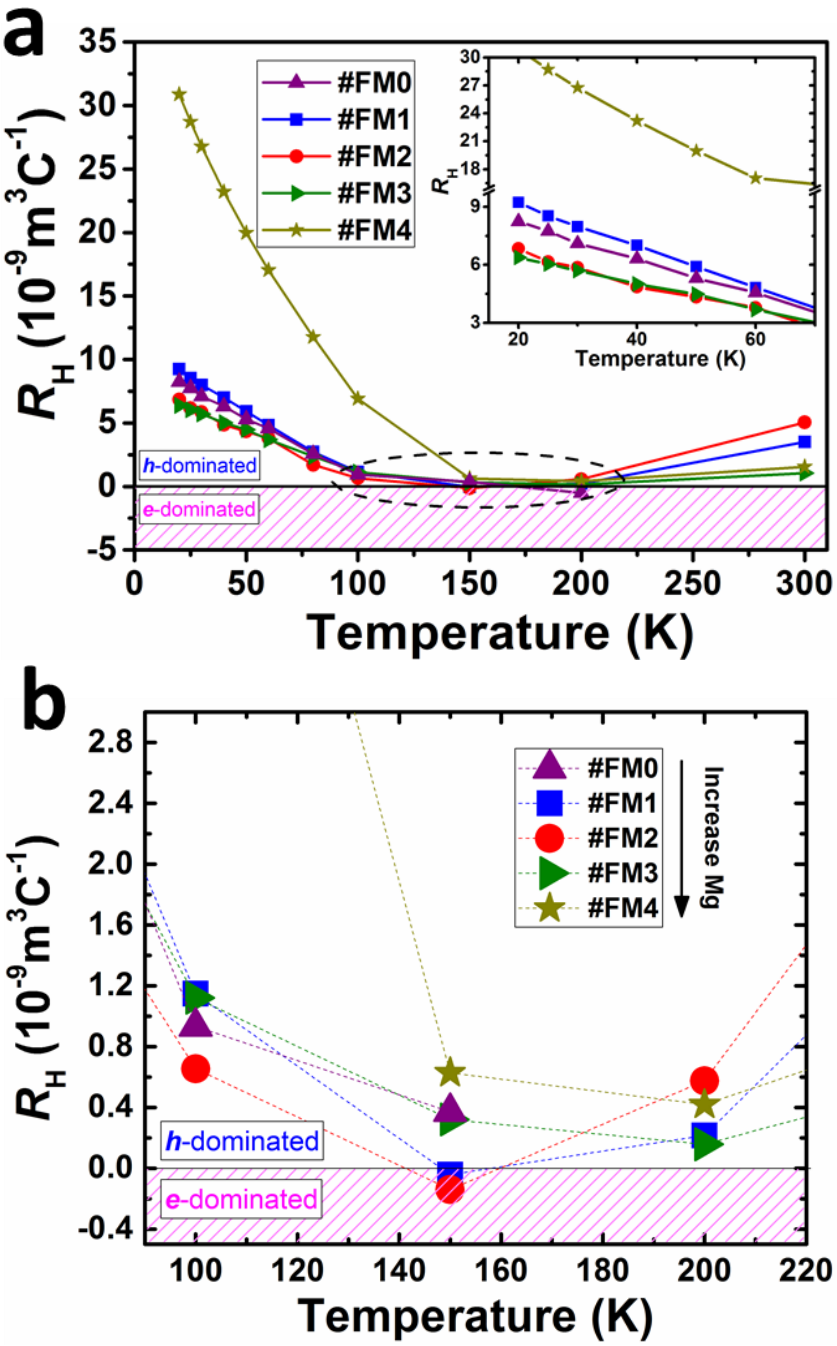

Figure 6-3. Hall coefficient R_H as a function of temperature for all five thin film samples. (a) R_H-T plots in the full temperature range from 20 K to 300 K. Inset: an enlarged area of 20 K - 100 K. (b) A magnified area from 100 K to 200 K (dashed area in (a)) is illustrated to show the twice-sign-reversal of R_H in #FM1 and #FM2 near 150 K.

Typical XRD *θ-2θ* results are illustrated in Fig. 6-4 (a), ranging from 10 °to 80 °. Highly (00l) oriented FeSe texture based on PbO structure exists in all 5 samples. No MgSe phase was formed in the samples, which is quite different from the Mg-doped

FeSe bulk samples[22] where lattice parameters of FeSe remain unchanged and the MgSe phase is formed with Mg addition. Hence, the mechanism in Mg-coated FeSe films is different from that of Mg-doped bulks. In Mg-doped FeSe bulks made by solidstate sintering, small and reactive Mg particles are prone to react with FeSe so that lots of secondary phases are formed at a relatively higher sintering temperature. Oppositely, in the present work, Mg-coating is performed at a relatively low temperature. It enables homogeneous distribution of Mg into Fe-vacancies without reacting with FeSe. Moreover, in Fig. 6-4 (a), it is also found that the β-FeSe (101) diffraction peak appears in the over-coated #FM3 and #FM4, which reflects the degraded texture degree and could bring about deterioration on superconductivity, as shown in Fig. 6-1. Fig. 6-4 (b) shows the enlarged interval near FeSe (001) diffraction peak. A shift of diffraction peaks is observed in all Mg-coated FeSe films compared with the pristine FeSe film. The 2θ values are extracted and plotted in the inset of Fig. 6-4 (b), where the dashed line represents the 2θ value of the pristine #FM0. It was recognized that the FeSe (001) peaks of #FM1, #FM2, and #FM3 locate at lower 2θ than that of #FM0, demonstrating the elongation of the *c*-axis parameter after Mg-coating process. On the contrary, the FeSe (001) peak of #FM4 with excessive amount of Mg-coating lies at higher 2θ angle; that is to say, the lattice along *c*-axis shrinks in this case. The phenomenon can be well-explained based on the interaction with Mg atoms and Fe-vacancies. It has been confirmed that plenty of Fe-vacancies exist in as-grown FeSe thin films[23]. During the Mg-coating process onto FeSe layer, Mg enters FeSe lattice and occupies Fe-vacancies, resulting in the elongation of lattice parameter. Simultaneously, extra electron-type charge carriers are introduced to improve the superconductivity in this sample. Further increasing the amount of Mg-coating could lead to the replacement of Fe-sites in FeSe lattice by excessive Mg. As the radius of Mg^{2+} cations is smaller than that of Fe^{2+}, shrinkage in the *c*-axis parameter is expected to occur. Because of the substitution of Mg for Fe, destruction of the superconducting structure brings about the strong suppression in superconductivity, which is corresponding to the results of superconducting performance in Fig. 6-1.

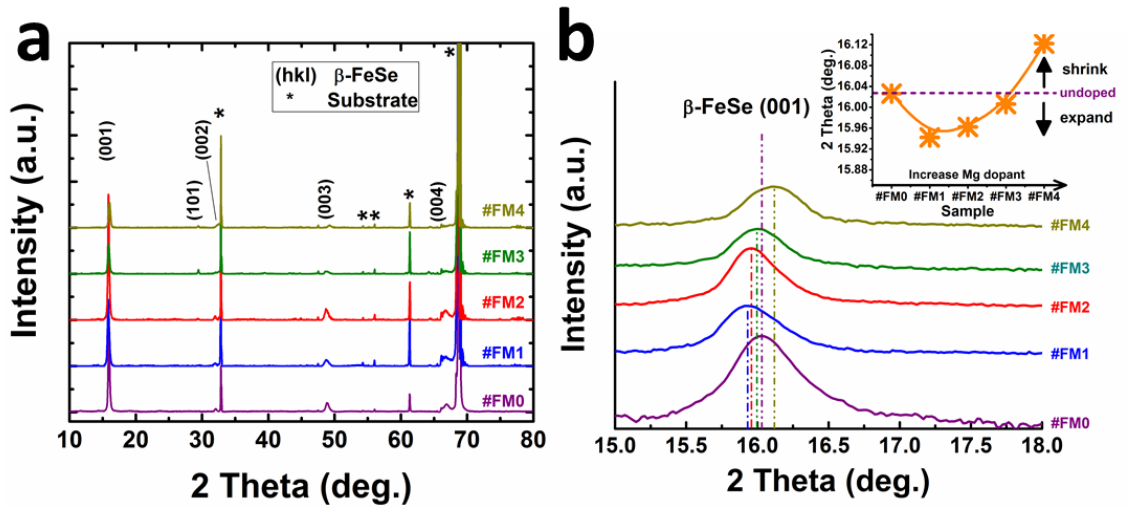

Figure 6-4. XRD θ-2θ results of five thin films samples. (a) 2θ ranges from 10 ° to 80 °. (hkl) represents the β-FeSe phases, and the asterisk signs indicate the diffraction peaks originating from the CaF_2 substrate. FeSe (101) orientation is detected in #FM3 and #FM4 with higher amount of Mg-deposition. (b) The magnified 2θ range near FeSe (001) diffraction peak. The intensity axis is set on a logarithmic scale, and the peak positions are marked by dashed lines. Inset: the variation in FeSe (001) peak as a function of the amount of Mg-coating process. The dashed line indicates the situation of the pristine FeSe sample. The judgement that the *c*-axis lattice constant is either shrink or expand is based on the 2θ variation of FeSe (001) peak.

Speculation can be easily made that the different amount of Mg-coating rendered the evolution of superconducting properties in all FeSe films. For the elucidation of how much Mg is introduced, surface EDS analysis is employed. It is a qualified characterizing technique owing to the high penetration depth (several μm) as well as the high accuracy for analyzing chemical composition. In this work, the elemental contents of Mg, Fe, and Se elements were acquired from a large scale and the atomic ratio of Mg/(Fe+Se) was calculated to represent the implantation content of Mg-coating. Detailed specifications including the atomic ratio of Mg/(Fe+Se), the carrier concentration at 30 K, and the superconducting performance of all five samples are listed in Table 6-1. These results will support and give reference to the following discussions on the mechanism of Mg-coating effect on the FeSe thin films.

Table 6-1. Specifications of all five samples in this work.

	Mg/(Fe+Se) (at. %)	***n* at 30 K (×10^{20} cm^{-3})**	***n*/$n_{\#FM3}$ at 30 K (%)**	**T_c^{onset} (K)**	**ΔT_c (K)**	**H_{c2} (T)**
#FM0	0	8.2	80.4	10.7	1.9	27.8
#FM1	6.4	7.8	71.6	12.7	1.2	31.2
#FM2	13.1	10.6	97.4	13.4	1.4	32.7
#FM3	26.2	10.9	100	11.4	1.8	29.1
#FM4	75.3	2.3	21.3	4.9	n/a	n/a

On the basis of Table 6-1, the relative carrier concentration $n/n_{\#FM3}$ at 30 K and T_c of all five samples are illustrated in Fig. 6-5 as a function of the Mg-content represented by the atomic ratio of Mg at.% and the combination of Fe-at.% and Se-at.%. As detected, the Mg content within #FM0, #FM1, #FM2, #FM3, and #FM4 is 0%, 6.4%, 13.1%, 26.2%, and 75.3%. It is in an approximate linear-dependence with the increment of Mg-deposition time, demonstrating the reliable technique in proportionally controlling the deposition-yield. However, T_c varies in a more complicated way. When a small amount of Mg is coated, an improvement in T_c by 2 K is obtained in #FM1 despite the carrier concentration is slightly reduced due to the presence of the "mixed-state" mentioned above in this sample. It is explained that Mg occupies Fe-vacancies on the surface of FeSe layer so that the defects introduced by Fe-vacancy disorders are eliminated and better superconducting structure would be achieved. Further increasing the amount of Mg-coating, "external electron-doping" becomes dominating rather than the "self-doping" induced by original Fe-vacancy disorders[20]. With the highest carrier concentration, T_c^{onset} up to 13.4 K is obtained in #FM2, which is an increment of more than 25% compared with the pristine #FM0. In the case of #FM3, a diffraction peak referring to β-FeSe (101) plane emerges in the XRD pattern (see Fig. 6-4 (a)). The deterioration in the texture degree of FeSe films led to degraded superconductivity in #FM3 regardless of the fact that this sample retains a high level of carrier concentration which is comparable to that of #FM2 with the highest T_c. In the case of over-coated

sample #FM4, an abrupt drop in T_c^{onset} was found and the superconducting transition was not complete. It is ascribed to the destruction of superconducting structure owing to the substitution effect. Ultimately, a dome-shaped tendency of T_c is observed based on the amount of Mg-coating. It is noticed that the highest T_c appears in the region with a relatively high charge concentration while the collapse of T_c occurs when the carrier concentration drops to a very low level. Therefore, the carrier concentration is verified to have significant impact on the superconductivity in FeSe films. In addition, the feasibility of tuning the superconductivity of FeSe thin films by an external Mg-coating technique was demonstrated and the alkaline-earth metal, Mg, was proved to be effective in offering electron dopants. However, the amount of electron-doping in this work is much less than the cases of alkalis-coating process such as K[5, 12-16] and Li[8]. Further investigations are necessary to figure out why Mg only provides limited electrons.

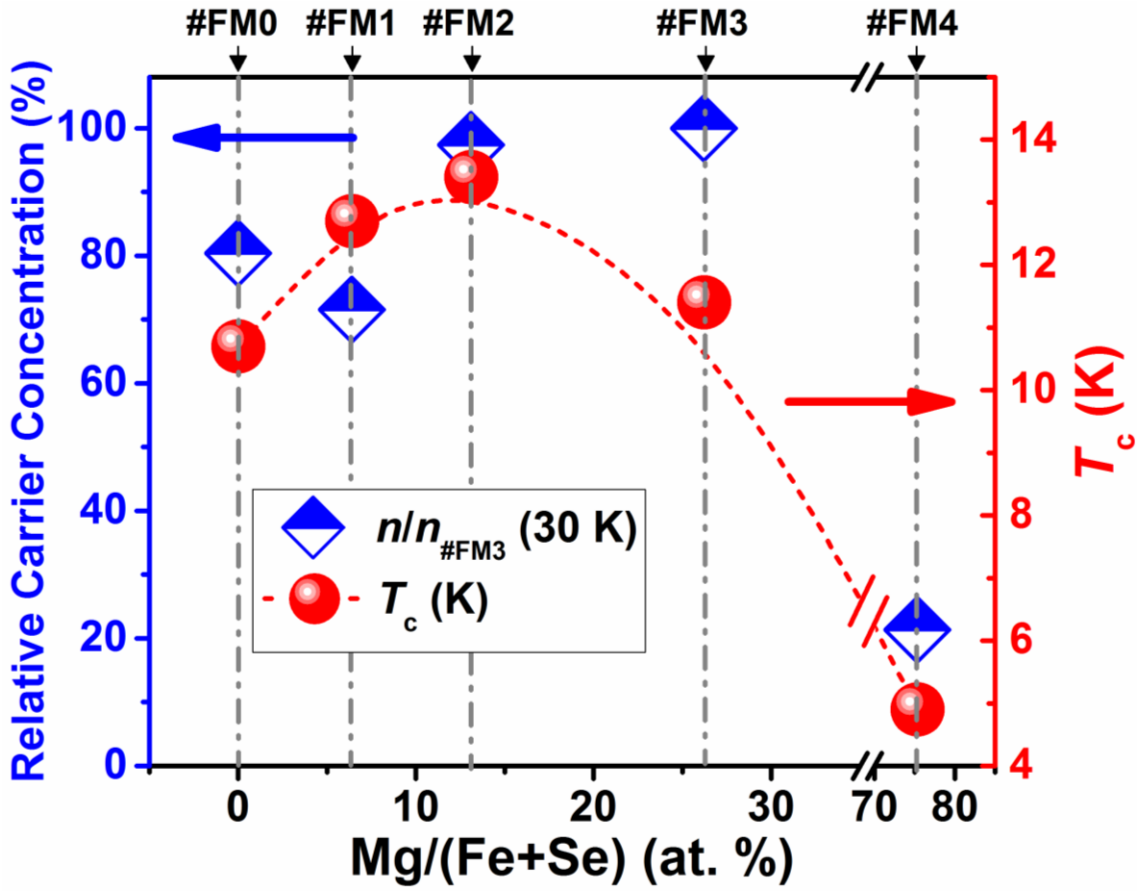

Figure 6-5. The Mg-content dependence of relative carrier density (left *y*-axis) and T_c (right *y*-axis) of all five samples. The *x*-axis represents the atomic ratio of Mg element and the combination of Fe and Se elements detected by EDS characterization. The carrier concentration n is calculated by $n = 1/(qR_H)$, and it is normalized by being divided by the $n_{\#FM3}$ at 30 K. A dome-shaped tendency is observed in the T_c as a function of Mg/(Fe+Se).

6.1.2 Induced Superconducting Transition in Ultra-Thin FeSe Films by a Mg-Coating Process

The lacking of electron-doping in non-superconducting multi-layer FeSe has been successfully overcome by an external K deposition process. Based on the discovery from the section of 5.1.2 that Mg deposition provides a few extra electron carriers into the PLD-prepared FeSe superconducting films with a relatively high thickness as 60 nm and improves T_c, it was decided to deposit Mg onto the PLD-prepared ultrathin FeSe films (~ 8 nm, non-superconducting) and investigate whether Mg-coating can also induce the superconductivity alike the case of K-deposition.

Most of the experimental details are identical to those in the section of 5.1.2, except for the as-grown ultrathin FeSe films and the amount of Mg-coating. The thickness of the PLD-prepared ultrathin FeSe films is fixed at ~ 8 nm. These pristine FeSe films are non-superconducting by showing a semiconducting behaviour in the image of temperature dependence of resistivity. Right after the deposition of FeSe layer, the *in-situ* Mg-coating was performed at the same substrate temperature and the amount of Mg-coating was organized by controlling the deposition time as 3, 6.5, 10, 15, and 20 minutes. All the samples are denoted in the order of Mg-amount as #UFM0 (pristine ultrathin FeSe), #UFM1 (3 min.-Mg), #UFM2 (6.5 min.-Mg), #UFM3 (10 min.-Mg), #UFM4 (15 min.-Mg), and #UFM5 (20 min.-Mg), respectively.

STEM characterizations from a cross-sectional view were carried out to investigate the properties of Mg-coating and its interaction with FeSe film. Fig. 6-6 shows the results of #UFM3, involving EDS, EELS and FFT analyses. The EDS linear-profiles for the elements of Mg, O, Fe, Se and Ca are illustrated in Fig. 6-6 (a). According to the diverse appearance of the net-count curves, the distribution of different elements can be estimated. Apparently, most of the Mg dwells above the FeSe layer together with a big amount of O. The inter-diffusion of Mg into FeSe layer degrades rapidly and almost no Mg element is detected deep inside the FeSe film. Fig. 6-6 (b) is an EELS contour containing the position-dependent energy loss spectra for Mg-*K* and Se-*K* edges. Darker contrast indicates higher intensity of the characteristic edges. A region with the presence of both Mg-*K* and Se-*K* edges is distinguished near the Mg/FeSe interface. This observation is in good consistency with the EELS results of Mg-coated 60-nm-FeSe films (section 5.1.2). Therefore, the external Mg-deposition has been reconfirmed to result in a Mg-coating on the top of FeSe layer, regardless of the

thickness of beneath FeSe films. A bright-field STEM image from the zone axis of [-1 0 1] is displayed in Fig. 6-6 (c). The FeSe layer with larger atomic mass appears as lattice with dark contrast in the middle. Above FeSe layer, the region of Mg-coating is mixed with polycrystalline lattices and little amorphous phases. The FFT result was extracted on a 10 nm × 10 nm area which is indicated by a red square. The FFT pattern is shown in Fig. 6-6 (d) and they are found to be well matched with the cubic MgO (a = 4.2170 Å, space group: Fm-3m). Thus, the excess Mg-coating on the surface of FeSe layer finally gets oxidized and transforms into polycrystalline MgO. The high stability of MgO is considered to offer protection to the beneath FeSe thin film.

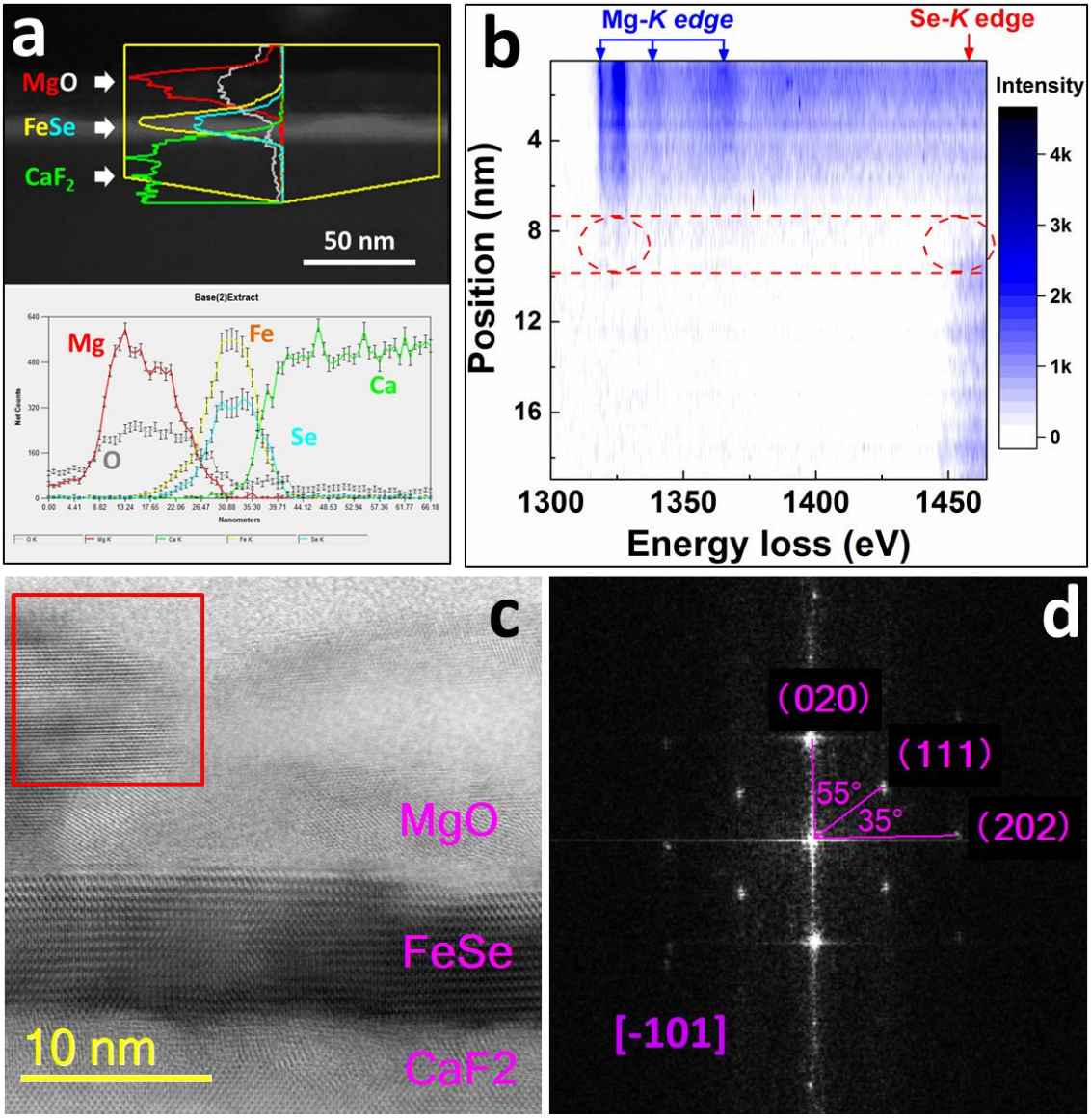

Figure 6-6. The STEM-related results of #UFM3 from a cross-sectional view. (a) EDS linear profile showing the distribution of major elements in the sample. The intensity refers to the net counts. (b) The EELS contour image exhibiting the evolution of the feature of Mg- and Se- edges along the cross-section. The energy loss of Mg-*K* and Se-*K* edges are indicated by the arrows. The region in which Mg and Se

coexist is marked by horizontal lines. Ovals highlight the Mg-*K* and Se-*K* edges in the same region. (c) A bright-field STEM image captured from the zone axis of [-1 0 1]. The FFT pattern of the lattice in the square area is displayed in (d). It is indexed as cubic MgO.

Fig. 6-7 illustrates the temperature dependence of electrical resistivity for all six thin film samples in the magnified temperature range up to 20 K. The full range (up to room temperature) curves are shown in the inset of Fig. 6-7 (a). As for the pristine #UFM0, a semiconducting behaviour without any signal of superconducting transition is observed, which is similar to the other ultrathin FeSe thin films prepared by regular methods such as PLD and sputtering, but in strong contrast to the metallic behaviour of normal FeSe bulks. Interestingly, metallic behaviour and superconducting transition are observed in all the samples after Mg-coating process, even in #UFM1 with a small amount of Mg-coating. The detailed specifications of the T_cs are summarized and plotted in Fig. 6-7 (b). With increasing the amount of Mg-coating, T_c^{onset} raises from 5.2 K for #UFM1 to 9.7 K for #UFM3. The sharpest transition width of #UFM3 (~ 1.9 K) suggests the good crystallinity of this sample, which can also be deduced based on the clear single-crystal lattice shown in Fig. 6-6 (c). The further increment of Mg-coating gives rise to the degradation in T_c^{onset}. As a result, a dome-shaped dependence of T_c^{onset} is obtained depending on the amount of Mg-coating. Considering MgO is non-metallic, the transformation of the resistivity behaviour of FeSe layer from semiconducting to metallic should be related to the doping effect of external Mg. The effect of extra electron-doping from Mg-coating is believed to be one of the key factors that induce the superconductivity in ultra-thin FeSe thin films, which was the case in the section of 5.1.2. Following investigation is necessary to clarify the mechanism in detail.

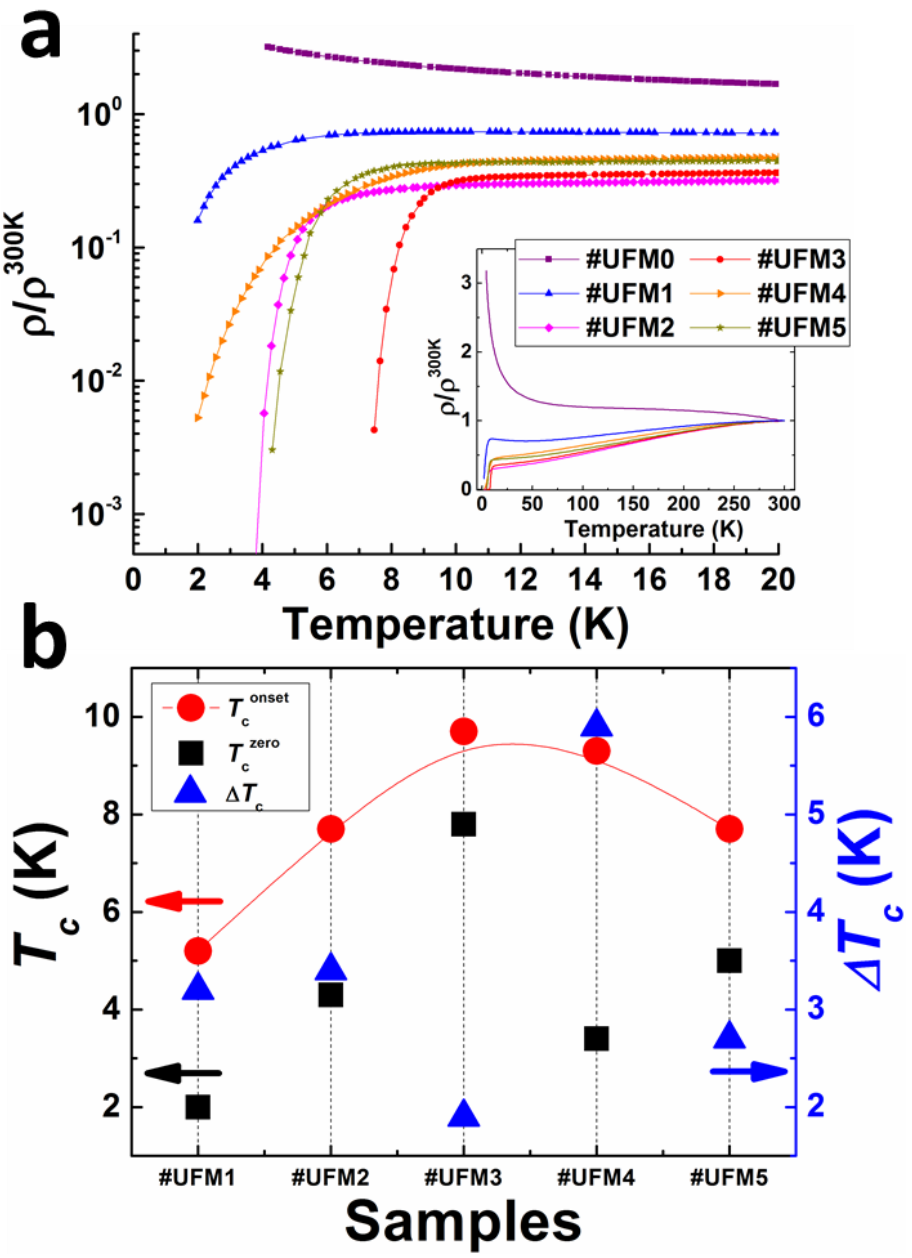

Figure 6-7. The results of resistivity behaviours of all the thin film samples in this work. (a) The temperature dependence of normalized resistivity ρ/ρ^{300K} with the temperature ranging up to 20 K. The *y*-axis is in logarithmic scale. Inset: the ρ-T curves with a full temperature range. The *y*-axis is in linear scale. (b) The evolution of T_c^{onset}, T_c^{zero}, and ΔT_c with different amount of Mg-coating. The left *y*-axis refers to the T_c^{onset} and T_c^{zero}, and the right *y*-axis stands for the ΔT_c.

6.2 Conclusions

The positive effect of a simple *in-situ* Mg-coating process to the superconducting performances of as-grown FeSe thin films was proposed. For a 60 nm PLD-prepared FeSe thin film, the T_c^{onset} was increased from 10.7 K to 13.4 K under the optimal Mg-coating process. Although extra electron-doping from external Mg-coating was confirmed by Hall measurement, the number of electron carriers was not sufficient

enough to overturn the hole-dominated situation in the Mg-coated FeSe samples. Nevertheless, a phenomenon that the sign of R_H reversed twice near 150 K was noticed in the samples with a mild amount of Mg-coating and better superconductivity. According to the STEM-EDS and EELS analyses, Mg was found only interacted with the top few layers of FeSe film rather than diffused deep into the FeSe body. Hence, the case of Mg-intercalation is excluded in this work. Severe degradation in superconducting performance and carrier concentration occurred once excess amount of Mg-coating was applied. Furthermore, the Mg-coating process was able to realize a superconducting transition in ultrathin FeSe thin films (~ 8 nm) which were originally non-superconducting. The result resembles the case of K-doped multilayer FeSe thin films and requires further investigation. Overall, this is the first attempt of studying the doping effect of Mg-coating process on the superconductivity of PLD-prepared FeSe thin films. The Mg-coating induced enhancement in T_c in this work suggests a unified understanding that the alkali (Li, K) or alkaline-earth metal (Mg) families of elements can always offer electron-doping into FeSe thin films by means of an external coating process, and the improved superconductivity is highly anticipated.

6.3 References

(1) Wang, Q.; Li, Z.; Zhang, W.; Zhang, Z.; Zhang, J.; Li, W.; Ding, H.; Ou, Y.; Deng, P.; Chang, K.; Wen, J.; Song, C.; He, K.; Jia, J.; Ji, S.; Wang, Y.; Wang, L.; Chen, X.; Ma, X.; Xue, Q.-K. Interface-Induced High-Temperature Superconductivity in Single Unit-Cell FeSe Films on $SrTiO_3$. *Chin. Phys. Lett.* **2012,** *29*, 037402.
(2) He, S.; He, J.; Zhang, W.; Zhao, L.; Liu, D.; Liu, X.; Mou, D.; Ou, Y.-B.; Wang, Q.-Y.; Li, Z.; Wang, L.; Peng, Y.; Liu, Y.; Chen, C.; Yu, L.; Liu, G.; Dong, X.; Zhang, J.; Chen, C.; Xu, Z.; Chen, X.; Ma, X.; Xue, Q.; Zhou, X. J. Phase diagram and electronic indication of high-temperature superconductivity at 65 K in single-layer FeSe films. *Nat. Mater.* **2013,** *12*, 605-610.
(3) Shen, B.; Feng, Z.-P.; Huang, J.-W.; Hu, Y.; Gao, Q.; Li, C.; Yu, X.; Liu, G.-D.; Yu, L.; Zhao, L.; Jin, K.; Zhou, X. J. Electronic structure and nematic phase transition in superconducting multiple-layer FeSe films grown by pulsed laser deposition method. *Chin. Phys. B* **2017,** *26*, 077402.
(4) Tan, S.; Zhang, Y.; Xia, M.; Ye, Z.; Chen, F.; Xie, X.; Peng, R.; Xu, D.; Fan, Q.; Xu, H.; Jiang, J.; Zhang, T.; Lai, X.; Xiang, T.; Hu, J.; Xie, B.; Feng, D. Interface-induced Superconductivity and Strain-dependent Spin Density Waves in FeSe/$SrTiO_3$ Thin Films. *Nat. Mater.* **2013,** *12*, 634-640.
(5) Miyata, Y.; Nakayama, K.; Sugawara, K.; Sato, T.; Takahashi, T. High-temperature Superconductivity in Potassium-coated Multilayer FeSe Thin Films. *Nat. Mater.* **2015,** *14*, 775-779.
(6) Shiogai, J.; Ito, Y.; Mitsuhashi, T.; Nojima, T.; Tsukazaki, A. Electric-field-induced superconductivity in electrochemically etched ultrathin FeSe films on $SrTiO_3$ and MgO. *Nat. Phys.* **2016,** *12*, 42-46.
(7) Lei, B.; Cui, J. H.; Xiang, Z. J.; Shang, C.; Wang, N. Z.; Ye, G. J.; Luo, X. G.; Wu, T.; Sun, Z.; Chen, X. H. Evolution of High-Temperature Superconductivity from a Low-T_c Phase Tuned by Carrier Concentration in FeSe Thin Flakes. *Phys. Rev. Lett.* **2016,** *116*, 077002.
(8) Phan, G. N.; Nakayama, K.; Kanayama, S.; Kuno, M.; Sugawara, K.; Sato, T.; Takahashi, T. High-Temperature Superconductivity and Lattice Relaxation in Lithium-Deposited FeSe on $SrTiO_3$. *J. Phys. Soc. Jpn.* **2017,** *86*, 033706.
(9) Sun, J. P.; Ye, G. Z.; Shahi, P.; Yan, J. Q.; Matsuura, K.; Kontani, H.; Zhang, G. M.; Zhou, Q.; Sales, B. C.; Shibauchi, T.; Uwatoko, Y.; Singh, D. J.; Cheng, J. G. High-T_c Superconductivity in FeSe at High Pressure: Dominant Hole Carriers and Enhanced Spin Fluctuations. *Phys. Rev. Lett.* **2017,** *118*, 147004.
(10) Guo, J.; Jin, S.; Wang, G.; Wang, S.; Zhu, K.; Zhou, T.; He, M.; Chen, X. Superconductivity in the iron selenide $K_xFe_2Se_2$ ($0 \le x \le 1.0$). *Phys. Rev. B* **2010,** *82*, 180520.
(11) Ivanovskii, A. L. New ternary $ThCr_2Si_2$-type iron–selenide superconducting materials: Synthesis, properties and simulations. *Physica C* **2011,** *471*, 409-427.
(12) Tang, C.; Zhang, D.; Zang, Y.; Liu, C.; Zhou, G.; Li, Z.; Zheng, C.; Hu, X.; Song, C.; Ji, S.; He, K.; Chen, X.; Wang, L.; Ma, X.; Xue, Q.-K. Superconductivity Dichotomy in K-coated Single and Double Unit Cell FeSe Films on $SrTiO_3$. *Phys. Rev. B* **2015,** *92*, 180507.
(13) Wen, C. H. P.; Xu, H. C.; Chen, C.; Huang, Z. C.; Lou, X.; Pu, Y. J.; Song, Q.; Xie, B. P.; Abdel-Hafiez, M.; Chareev, D. A.; Vasiliev, A. N.; Peng, R.; Feng, D. L. Anomalous Correlation Effects and Unique Phase Diagram of Electron-doped FeSe Revealed by Photoemission Spectroscopy. *Nat. Commun.* **2016,** *7*, 10840.
(14) Song, C.; Zhang, H.; Zhong, Y.; Hu, X.; Ji, S.; Wang, L.; He, K.; Ma, X.; Xue, Q.-K. Observation of Double-Dome Superconductivity in Potassium-Doped FeSe Thin Films. *Phys. Rev. Lett.* **2016,** *116*, 157001.
(15) Tang, C.; Liu, C.; Zhou, G.; Li, F.; Ding, H.; Li, Z.; Zhang, D.; Li, Z.; Song, C.; Ji, S.; He, K.; Wang, L.; Ma, X.; Xue, Q.-K. Interface-enhanced Electron-phonon Coupling and High-temperature Superconductivity in Potassium-coated Ultrathin FeSe Films on $SrTiO_3$. *Phys. Rev.*

B **2016,** *93*, 020507.
(16) Zhang, W. H.; Liu, X.; Wen, C. H. P.; Peng, R.; Tan, S. Y.; Xie, B. P.; Zhang, T.; Feng, D. L. Effects of Surface Electron Doping and Substrate on the Superconductivity of Epitaxial FeSe Films. *Nano Lett.* **2016,** *16*, 1969-1973.
(17) Bellingeri, E.; Buzio, R.; Gerbi, A.; Marrè, D.; Congiu, S.; Cimberle, M. R.; Tropeano, M.; Siri, A. S.; Palenzona, A.; Ferdeghini, C. High quality epitaxial $FeSe_{0.5}Te_{0.5}$ thin films grown on $SrTiO_3$ substrates by pulsed laser deposition. *Supercond. Sci. Technol.* **2009,** *22*, 105007.
(18) Wang, Q. Y.; Zhang, W. H.; Zhang, Z. C.; Sun, Y.; Xing, Y.; Wang, Y. Y.; Wang, L. L.; Ma, X. C.; Xue, Q. K.; Wang, J. Thickness dependence of superconductivity and superconductor–insulator transition in ultrathin FeSe films on $SrTiO_3$ (001) substrate. *2D Mater.* **2015,** *2*, 044012.
(19) Zhang, W.; Li, Z.; Li, F.; Zhang, H.; Peng, J.; Tang, C.; Wang, Q.; He, K.; Chen, X.; Wang, L.; Ma, X.; Xue, Q.-K. Interface Charge Doping Effects on Superconductivity of Single-unit-cell FeSe Films on $SrTiO_3$ Substrates. *Phys. Rev. B* **2014,** *89*, 060506(R).
(20) Berlijn, T.; Hirschfeld, P. J.; Ku, W. Effective doping and suppression of Fermi surface reconstruction via Fe vacancy disorder in $K_xFe_{2-y}Se_2$. *Phys. Rev. Lett.* **2012,** *109*, 147003.
(21) Sun, Y.; Pyon, S.; Tamegai, T. Electron carriers with possible Dirac-cone-like dispersion in $FeSe_{1-x}S_x$ (x = 0 and 0.14) single crystals triggered by structural transition. *Phys. Rev. B* **2016,** *93*, 104502.
(22) Lan, F.; Ma, Z.; Liu, Y.; Chen, N.; Cai, Q.; Li, H.; Barua, S.; Patel, D.; Hossain, M. S. A.; Kim, J. H.; Dou, S. X. The formation of nano-layered grains and their enhanced superconducting transition temperature in Mg-doped $FeSe_{0.9}$ bulks. *Sci. Rep.* **2014,** *4*.
(23) Chen, T. K.; Chang, C. C.; Chang, H. H.; Fang, A. H.; Wang, C. H.; Chao, W. H.; Tseng, C. M.; Lee, Y. C.; Wu, Y. R.; Wen, M. H.; Tang, H. Y.; Chen, F. R.; Wang, M. J.; Wu, M. K.; Van Dyck, D. Fe-vacancy order and superconductivity in tetragonal beta-$Fe_{1-x}Se$. *Proc. Natl. Acad. Sci. U.S.A.* **2014,** *111*, 63-68.

6.4 Note: Chapter Publication and Text Usage Detail

Part of this Chapter has been published in *ACS Applied Materials and Interfaces* as a paper (see below reference). Part of the written text in this chapter has been taken from my published paper, as shown below.

- **W. Qiu**, Z. Ma, Y. Liu, M. S. A. Hossain, X. Wang, C. Cai, & S. X. Dou, Tuning Superconductivity in FeSe Thin Films via Mg Doping. *ACS Appl. Mater. Interfaces* 2016, **8,** 7891-7896.

Chapter 7

7 Conclusions and Future Prospects

7.1 Conclusions

A T_c^{zero} of 13.4 K which is the highest reported to date in regular FeSe films, was obtained in a high-quality FeSe thin film grown on CaF_2 (100) substrate by the PLD method. Via controlling the film thickness, a dome-shaped evolution of superconductivity was observed, namely, T_c is degraded in an over-thick FeSe film. The interfacial interaction between the FeSe layer and the CaF_2 substrate was carefully investigated by the high-resolution STEM technique. Based on the structural and elemental evidence, a cubic CaSe interlayer was confirmed to universally exist in the interfacial region with a 3-nm-thickness, regardless of the thickness of the FeSe layer. The existence of the CaSe interlayer is thought to be responsible for the high excess-Fe of 38 at. % in the 8 nm FeSe film, which exhibits insulating resistivity-temperature behaviour. With increasing FeSe thickness, the negative effect of the CaSe interlayer on the stoichiometry of the FeSe composition becomes negligible. In this work, the highest T_c was obtained in the FeSe with a thickness of 127 nm. The emergence of massive Fe-rich precipitates (α-Fe) in the over-thick FeSe film suppressed the superconductivity and prevented it from further increasing. In this work, the interface between FeSe and CaF_2 was first studied, and the universal existence of a CaSe interlayer was clarified. The feasibility of exploring the microstructure of FeSe superconducting thin films by utilizing the HAADF-STEM technique was proved.

A FeTe capping layer was found to be able to overcome the common T_c suppression in PLD-prepared ultrathin FeSe thin films grown on CaF_2 substrate. The surprisingly high T_c^{onset} of 17.6 K was related to the Fe(Se,Te) diffusion layer at the FeTe/FeSe interface with a thickness of several unit-cells, rather than the HTS Fe-*Ch* scenarios with heavy electron-doping. Precise EELS analysis suggested some unique properties in the Fe(Se,Te) diffusion layer, including Te-rich conditions, extra hole-doping, and/or a compressive strain effect. The studies on “white line” features revealed a higher Fe-L_3/L_2 ratio in the Fe(Se,Te) diffusion layer than that of the adjacent layers, whether FeTe or FeSe. An electronic orbital structure with lower Fe 3d electron

occupancy was expected in this region according to an empirical correlation established in 3d transition-metal oxides. The EELS analysis together with electrical transport measurements and phase characterizations in this work indicated the importance of the FeTe/FeSe interface for the realization of the enhanced superconductivity in regular Fe-Se thin films fabricated by PLD. Constructive guidance is expected, paving the way to understanding the unconventional iron-based superconductivity.

A simple Mg-coating process on as-grown FeSe thin film was demonstrated to affect the electronic states and lattice structure of the original FeSe. Enhancements of T_c and H_{c2} were obtained up to 13.4 K and 32.7 T, respectively, under the optimized amount of Mg-coating. According to the Hall coefficient measurements, electron-carriers were introduced into FeSe thin film by the Mg-coating process, but the overall charge carrier condition was hole-dominated. This is probably because the Mg element only overlapped with the top few layers of the FeSe thin film rather than being diffused much into the FeSe layer, which was revealed by STEM-EDS and EELS results. It was also found that a small amount of Mg-coating can result in a double sign reversal of R_H near 150 K and bring about a better superconductivity. An abnormal reduction of the carrier concentration was found in the FeSe film with excess Mg-coating, however, leading to severe degradation in superconducting performance. Moreover, the semiconducting-superconducting transition was realized in ultrathin-FeSe thin films by a similar Mg-coating process. This work is the first attempt to study the effects of the external Mg-coating process on traditional FeSe thin films prepared via PLD technique. Considering the successful realization of T_c enhancement by K and L doping in other works, a unified understanding is deduced, that the elements from the family of alkali metals or alkaline-earth metals can always provide electron-doping of FeSe thin films by the external coating process.

7.2 Future Prospects

Iron-based superconductors show extremely good potential for high-field applications. Clarifying the physical mechanism of iron-based superconductivity is even more valuable to progressing scientific understanding of these materials. In particular, FeSe thin film has attracted huge attention in the field of condensed matter physics in recent years due to the exotic HTS found in several-unit-cell thick FeSe films. In considering the various proposals relating to this unusual phenomenon, the ultimate explanation for this special system still remains pending.

The recognition of a CaSe interlayer in the FeSe/CaF_2 structure has reemphasized the importance of interfacial effects in FeSe superconductors. As the formation of CaSe layer is inevitable during the deposition of FeSe on the CaF_2 surface, an additional process needs to be considered to minimize the negative effects of the CaSe interlayer on the stoichiometry and corresponding superconductivity of the FeSe layer, especially for the ultrathin FeSe films. Here, a pre-deposition process for the Se element prior to the regular deposition process of the FeSe layer was proposed. Based on speculation, carefully controlled Se pre-deposition might occupy the F-vacancies on the CaF_2 surface and form the CaSe layer in advance so that the Se-loss during the growth of the follow-up FeSe layer would no longer take place. As for the massive α-Fe precipitates appearing in the thick FeSe films, the volatilization of Se during the long-period heat-treatment process could be reduced by introducing a Se-vapor atmosphere during FeSe deposition or co-depositing FeSe and Se at the same time. Thus, the key to dealing with the suppression of superconductivity in FeSe thin films is believed to be avoiding any Se-loss, not only in the initial growth stage but also during the entire term of deposition.

Interfaces and heterostructures are prone to induce novel properties into the composite materials, which makes this research topic always appealing. The enhanced superconductivity found in the FeTe/FeSe heterostructures indicates that the upper interface of FeSe might be as important as the FeSe/substrate interface in determining the ultimate superconductivity. Different superconducting behavior were expected in: (1) similar FeTe/FeSe heterostructures with different thicknesses of FeTe or FeSe layers; (2) FeTe/FeSe heterostructures with more than one period of FeTe/FeSe bilayers; (3) a reversed heterostructure with FeSe on top; and (4) FeS/FeSe heterostructures with FeS as the capping layer. Furthermore, the clarification of the correlation between iron-based superconductors and the electronic state of the Fe 3d orbital is another promising research subject that might be useful to unveil the mystery of unconventional iron-based superconductivity.

In addition to Mg, Li, and K, the post-deposition of other alkali or alkaline-earth metals, such as Na or Ca, are also worth attempting on Fe-*Ch* thin films to study whether they are able to introduce extra electron carriers as well. In terms of the work of Mg-coated ultrathin FeSe thin films, there is still margin for improvement. It was noticed that the superconducting transition had already occurred with the lowest amount of Mg-coating. In order to find the critical transition point when Mg-coating induces

semiconducting-superconducting transition, it is essential to perform refined experiments on ultrathin FeSe films with a lesser amount of Mg-coating. Moreover, considering that the upper surfaces of the FeSe films are covered by rough MgO layers that are not suitable for STM or ARPES analyses, an alternative measurement technique should be developed to reflect the variation in charge-carrier conditions. For instance, a low-temperature EELS characterization from the cross-sectional view could be useful in monitoring the electron-transfer from the Mg-coating layer to the internal area of the FeSe film. Hall measurements might also be helpful, as long as the possible influence from excess Mg and other materials (e.g. MgO, protecting layers) could be quantified and eliminated.

Chapter 8

Appendix A: Additional Work - Improvement in the Transport Critical Current Density and Microstructure of Isotopic $Mg^{11}B_2$ Monofilament Wires by Optimizing the Sintering Temperature

Abstract

Superconducting wires are widely used in fabricating magnetic coils in fusion reactors. In consideration of the stability of ^{11}B against neutron irradiation and lower induced radio-activation properties, a MgB_2 superconductor with ^{11}B serving as boron source is an alternative candidate to be used in fusion reactor with severe irradiation environment. In present work, a batch of monofilament isotopic $Mg^{11}B_2$ wires with amorphous ^{11}B powder as precursor were fabricated using powder-in-tube (PIT) process at different sintering temperatures, and the evolution of their microstructure and corresponding superconducting properties was systemically investigated. Accordingly, the best transport critical current density (J_c) = 2 $\times 10^4$ A/cm^2 was obtained at 4.2 K and 5 T, which is even comparable to multi-filament $Mg^{11}B_2$ isotope wires reported in other work. Surprisingly, transport J_c vanished in the wire which was heat-treated at an excessively high temperature (800 ℃). Combined with microstructure observation, it was found that lots of big interconnected microcracks and voids that can isolate the MgB_2 grains formed in this whole sample, resulting in significant deterioration in inter-grain connectivity. The results can be a constructive guide in fabricating $Mg^{11}B_2$ wires to be used as magnet coils in fusion reactor systems such as ITER-type tokamak magnet.

Introduction

Fusion power is one of the most promising candidate energy sources that may

solve global energy problems, considering its safer and greener merits compared with the conventional mineral energy sources. In the world-class International Thermonuclear Experimental Reactor (ITER) fusion energy project, the superconducting magnet system serves as a key determinant. A high and steady magnetic field needs to be produced to confine the deuterium (D)–tritium (T) burning plasma inside the ITER tokamak nuclear fusion reactor. According to the previous ITER plan, hundreds of tons of superconducting magnets made from NbTi and Nb_3Sn will be fabricated to assemble 18 Nb_3Sn toroidal field (TF) coils, a 6-module Nb_3Sn central solenoid (CS) coil, 6 Nb-Ti poloidal field (PF) coils, and 9 pairs of Nb-Ti correction coils (CC)[1-2]. There is one major drawback, however, for the application of Nb-based superconductors in this project. After irradiation, ^{93}Nb will be transformed into the long-lived nuclide ^{94}Nb with a half-life of about 20,000 years[3-4]. Hence, before irradiated Nb-based alloys are safe to be recycled, tens of thousands of years are required for them to "cool down", and meanwhile, thicker shielding is necessary for long-term operation. For the convenience of radioactive waste treatment and environmental protection, the radioactivation properties of superconducting components within the fusion reactor should be taken into account. Compared with conventional Nb-based superconductors, MgB_2 features "low activation" and a much shorter decay time. Within 1 year, the dose rate of MgB_2 materials will be reduced to the hands-on maintenance level, which is considered as desirable for a fusion reactor magnet system[3]. Additionally, because of the reaction

$$^{10}B + n \rightarrow {}^{7}Li + He\ (gas)$$

under the heavy irradiation condition, ^{10}B can no longer guarantee the stability of the MgB_2 superconducting magnet. By replacing ^{10}B with the isotope ^{11}B, $Mg^{11}B_2$ superconducting wires will be much more stable in a neutron irradiation environment due to the smaller neutron capture cross-section of ^{11}B[5]. Considering the abundant reserves of ^{11}B on Earth (20 wt. % for ^{10}B, 80 wt. % for ^{11}B), the anticipated cost for extracting the isotope from natural boron is expected to be decreased during the chemical synthesis.

The superconductivity of MgB_2 was discovered in 2001[6]. It is well-known for its simple binary chemical composition and much higher critical transition temperature (T_c) of 39 K than that of NbTi at 9.3 K. In order to operate Nb-based low-temperature superconductors, the core of the magnet needs to be cooled down to 4 K. The only eligible cryogen is liquid helium, which is extremely expensive, not always available on

hand, and very difficult to handle. In the case of MgB_2, a working temperature as high as 20 K is low enough to achieve acceptable performance. Remarkably, the operating cost is expected to be cut by over 50 % by substituting cryocooler-cooled MgB_2 materials for LHe-cooled Nb-based superconductors. Furthermore, the fabrication cost of MgB_2 superconducting wire itself ($ 2.64/kA·m) is less than 1/3 of that of Nb_3Sn wire ($ 9/kA·m). Therefore, due to the advantages of cost-effectiveness, lower radioactivation, and the shorter decay time of isotopic $Mg^{11}B_2$, fundamental research on $Mg^{11}B_2$ superconducting wires will be valuable for improving the efficiency of practical application in high-irradiation environments such as fusion reactors.

$Mg^{11}B_2$ wires using isotopically pure ^{11}B powder always show lower J_c values, however, than the wires fabricated with natural boron powder. According to previous work[7-8], this lower J_c is a result of the increased amount of non-reactive precursor, which decreases the superconducting fraction. On the other hand, inter-grain connectivity is considered another crucial factor in the current-carrying capability of $Mg^{11}B_2$ superconducting wires[9-11]. In this work, with the aim of further improving J_c in $Mg^{11}B_2$ wires, the evolution of the microstructure and superconducting performance in $Mg^{11}B_2$ wires sintered at different temperatures was investigated in detail. The influence of both the superconducting fraction and the inter-grain connectivity on the J_c performance is discussed. The best transport performance can be obtained at the optimized temperature of the heat-treatment. Surprisingly, in the case of $Mg^{11}B_2$ wire sintered at high temperature, the transport J_c vanished, although magnetic J_c was still detected. According to detailed microstructure observations, this could be ascribed to the formation of a unique microstructure that was only obtained in the sample sintered at excessively high temperature. This kind of microstructure leads to significant deterioration in inter-grain connectivity and ultimately, poor transport current performance.

Experimental Details

The standard *in-situ* powder-in-tube (PIT) procedure was applied to all the samples. The starting materials for the $Mg^{11}B_2$ wire consisted of ^{11}B amorphous powder (from Pavezyum Kimya, Turkey, Moissan method[12], 95.5 %) and Mg powder (100–200 mesh, 99 %). The isotopic purity and particle size with respect to the ^{11}B enriched boron powder was > 99.5 % and 840 nm, respectively. After mixing the precursor powders, the mixture was tightly packed into Nb/Monel tubes with 10 mm outer diameter and 6 mm inner diameter. The composite wire was swaged and drawn to a final outer diameter

of 1.08 mm. Then, the fabricated $Mg^{11}B_2$ wires were sintered at different temperatures ranging from 700 ℃, 750 ℃, 770 ℃, and 800 ℃ for 60 min (ramp rate: 5 ℃/min) under high purity flowing argon gas. Finally, the samples were furnace-cooled to room temperature.

The transport critical current (I_c) measurements were carried out by using an American Magnetics superconducting magnet with DC current (with the upper limit of the current source 200 A) under possible magnetic field up to 15 T, with the standard four-probe method and the criterion of 1 μ V/cm. The critical current density J_c was calculated by dividing I_c by the cross-section of the $Mg^{11}B_2$ core, which was examined with an optical microscope (Leica M205A). Scanning electron microscopes (SEM, JEOL JSM-6490LV & JEOL JSM-7500) were employed to observe the microstructure under different magnifications. X-ray diffraction (XRD) θ - 2θ scans (GBC-MMA) were used to identify the phase composition. Measurements of electrical resistivity and magnetic moment were conducted in a 9 T Physical Properties Measurement System (PPMS, Quantum Design). In case of XRD, SEM, and PPMS measurements, the outer sheaths of the $Mg^{11}B_2$/Nb/Monel wires were removed for better data accuracy.

Results and Discussion

Typical transport J_c - B performances of all four wires sintered at different temperatures are shown in Fig. 8-1. For reference purposes, transport J_c data for the multi-filament $Mg^{11}B_2$/Ta/Cu wire reported by Hishinuma[7] is also plotted in the figure. It should be noted that the best monofilament $Mg^{11}B_2$ wire shows comparable transport J_c performance to the multifilament wire fabricated by the National Institute for Fusion Science (NIFS)[7]. This result is considered as a big breakthrough, and it strongly supports the feasibility of replacing commercial NbTi with high-performance $Mg^{11}B_2$ wires in highly radioactive fusion reactors. In the $Mg^{11}B_2$ wires, 750 ℃ is the optimized temperature for heat treatment. The corresponding wire possesses a J_c value near 2×10^4 A/cm^2 at 4.2 K and 5 T. Slight J_c degradation is observed in the wire treated at temperatures deviating from 750 ℃. Surprisingly, no transport current was detected in the wire treated at 800 ℃. For verification, five attempts at measurement were carried out on three batches of wires produced under the same sintering conditions. Ultimately, none of them gave detectable transport current data. It is speculated that some unexpected qualitative change inside the wire might occur once the heating temperature reaches a certain level. This should probably be attributed to a unique property of the ^{11}B starting powder. It is believed that investigations of the phase composition,

microstructure, and inter-grain connectivity will give an explanation for this abnormal phenomenon.

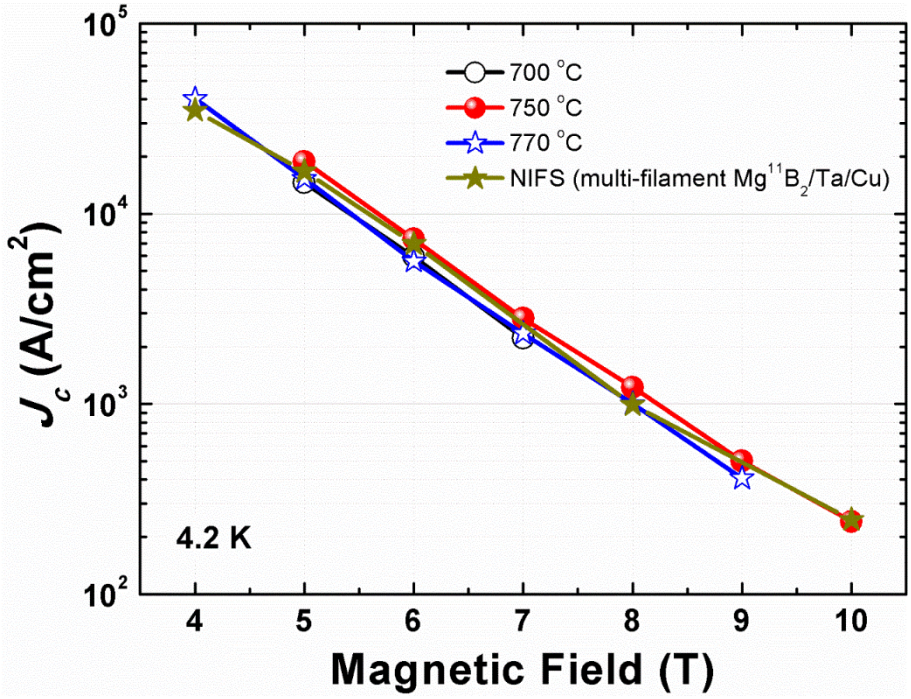

Figure 8-1. Transport J_c - B performance at 4.2 K of $Mg^{11}B_2$ wires using amorphous ^{11}B isotope as the boron source. Results from NIFS are also plotted for reference. No transport I_c was detected in the wire treated at 800 ℃.

To confirm the phase composition, $Mg^{11}B_2$ cores were removed from their outer sheaths and finely ground as XRD specimens. In Fig. 8-2 (a), the main peaks indexed as $Mg^{11}B_2$ can be observed in all spectra, indicating that the temperature is high enough to permit the formation of $Mg^{11}B_2$ phase. Very little oxidation was detected, according to the negligible MgO peak. Un-reacted Mg and ^{11}B-rich phase are found in the wire sintered at relatively low temperature. Apparently, it is very hard for Mg to completely diffuse into boron particles if the sintering temperature is not high enough. A diminishing gradient of Mg concentration exists along the radial direction of the boron particle. As a result, the $Mg^{11}B_2$ phase can only be formed on the outer layers of boron particles. The rest of the Mg will either stay in the elemental state (un-reacted Mg) or participate in other secondary reactions. Hence, the ^{11}B-rich phase is prone to form in this case, which can be deduced from the Mg-B phase diagram[13]. The presence of those impurities (un-reacted Mg and ^{11}B-rich phase) will reduce the fraction of superconducting phase, which is crucial for the final performance of superconductors. It has to be pointed out that the chemical activity of ^{11}B is lower in comparison with natural boron due to the isotope kinetic effect[14]. This might explain why 700 ℃ is not

high enough for the complete reaction in this work. Fig. 8-2 (b) shows the mass fractions of $Mg^{11}B_2$ phase in the wires as a function of sintering temperature. The mass fractions were calculated using Rietveld refinement. The smallest $Mg^{11}B_2$ fraction as low as 84.7 wt. % is found in the wire treated at 700 ℃. This is mainly due to the presence of impurities, as reflected by the XRD results. Furthermore, the degradation in transport J_c performance also confirms its relatively poor superconductivity (see Fig. 8-1). With increasing sintering temperature, un-reacted Mg peaks become smaller and almost disappear. Correspondingly, the mass fractions of $Mg^{11}B_2$ phase in the rest of the wires all remain at a high level (> 90 wt. %). Since the crystallization of $Mg^{11}B_2$ phase is confirmed to be good in the $Mg^{11}B_2$ wire sintered at 800 ℃, while its mass fraction of superconducting phase is also satisfactory, the observed abrupt disappearance of transport current in the wire sintered at 800 ℃ is related to neither the phase composition nor a low superconducting fraction.

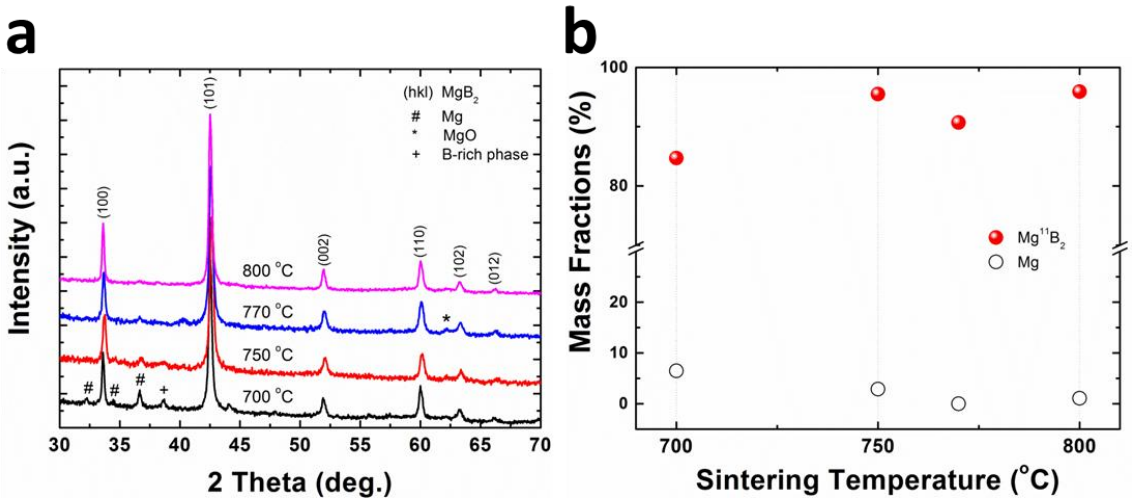

Figure 8-2. XRD results of the $Mg^{11}B_2$ wires in this work. (a) XRD θ - 2θ patterns of all $Mg^{11}B_2$ wires sintered at different temperatures. The numbered labels (hkl) represent $Mg^{11}B_2$ phases. The pound sign (hashtag) stands for unreacted Mg. A small amount of B-rich phase (with its peak marked by the plus sign) is detected only in samples sintered at 700 ℃. (b) Mass fractions, obtained from Rietveld refinement, of $Mg^{11}B_2$ and Mg as functions of the different sintering temperatures.

Fig. 8-3(a) shows the zero-field-cooled (ZFC) and field-cooled (FC) magnetization results as functions of the sintering temperature for all four samples. An excitation field H = 100 Oe was applied in this measurement. A clear normal-superconducting transition was observed in all samples, including the wire sintered at 800 ℃, which did not show any current value in the transport measurements. The magnetic J_c (H) of the samples was estimated at 5 K based on the magnetization hysteresis loops and the Bean critical state model. Generally, the formula for a

rectangularly shaped sample is

$$J_c = 20(\Delta M/V)/[a(1 - a/3b)]$$

where $\Delta M = [M(+) - M(-)]$ is the difference between the upper and lower branches of the M (H) loop, V refers to the volume, and a and b ($a < b$) stand for the length and width of the cross-section which is perpendicular to the direction of the applied magnetic field[15]. In this case, the $Mg^{11}B_2$ cores are in cylindrical shape. Hence, the formula can be simplified to

$$J_c = 30(\Delta M/V)/d$$

where d is the diameter of the circular cross-sectional area[16-17]. According to the calculations, the magnetic J_c (H) results at 5.0 K are shown in Fig. 8-3 (b). The wire sintered at 750 ℃ shows the best magnetic J_c (H) performance throughout the entire range of fields, which is consistent with the transport J_c results shown in Fig. 8-1. Some differences can be found between the values of magnetic J_c and transport J_c. Other than measurement deviation, the intrinsic distinction between the magnetic J_c signal and the transport J_c signal also needs to be taken into consideration. Generally, due to the existence of negative structures such as porosity and cracks, not all the MgB_2 in a sample is capable of passing transport current. Inter- or intra-grain connectivity should always be considered when dealing with transport performance. On the contrary, as long as they possess superconductivity, all the MgB_2 fragments will contribute to the magnetic J_c. It should be noted that the magnetic J_c was detected and showed good performance in the wire sintered at 800 ℃. This indicates that the $Mg^{11}B_2$ superconducting phase in the wire was not badly damaged by the high sintering temperature. Therefore, after ruling out the effects of inferior superconducting phase, it can be speculated that the transport current in the wire sintered at 800 ℃ disappeared as a result of a problem with inter-grain connectivity. A high sintering temperature might introduce some defects and significantly destroy the connection between $Mg^{11}B_2$ superconducting grains.

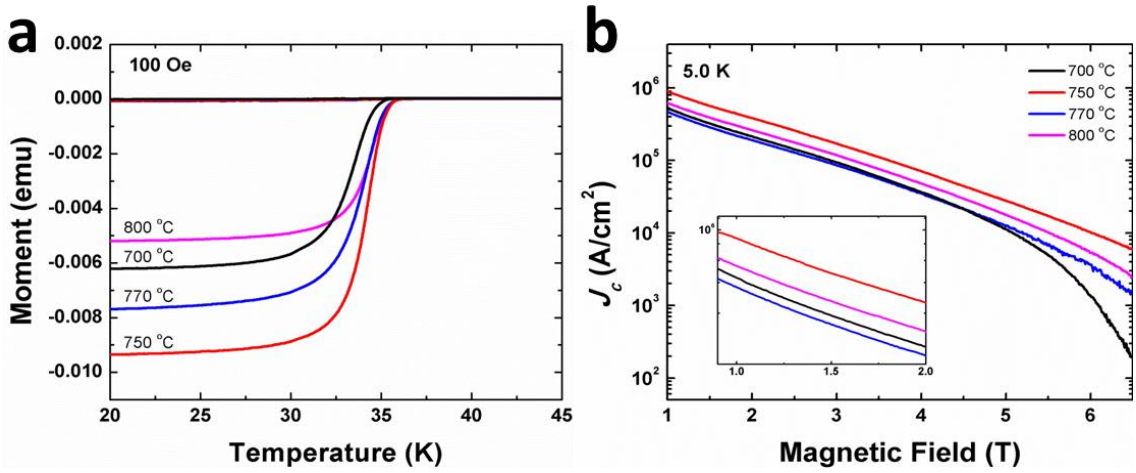

Figure 8-3. The T_c and J_c results obtained by magnetic measurements. (a) Temperature dependence of the ZFC and FC DC magnetization measured in a field of 100 Oe. (b) Field dependence of the magnetic J_c at 5.0 K on the logarithmic scale (with the inset showing an enlargement of the J_c (H) at low fields) for all samples.

It is estimated that the vanishing of transport current in the $Mg^{11}B_2$ wire is caused by the severe deterioration of inter-grain connectivity, which can be visually confirmed by SEM micrographs. The low-magnification SEM images of the cross-sections of $Mg^{11}B_2$ wires sintered at 700 ℃, 750 ℃ and 800 ℃ are presented in Fig. 8-4. Obvious evolution of the surface morphology is exhibited with increasing temperature. In the wire treated at 700 ℃, it was already proved by the XRD results that the Mg had partially reacted with the boron. As the particle size of the Mg powder is much bigger than for the boron powder, un-reacted Mg melted and smoothly covered the $Mg^{11}B_2$ grains. Therefore, the morphology of this sample was fairly plain and incompact. A dense surface is observed in Fig. 8-4 (b) on the optimal sample sintered at 750 ℃, indicating complete reaction and good inter-grain connectivity. This is consistent with the results of J_c - B and XRD discussed above. Once the sintering temperature reached 800 ℃, big cracks (marked by black arrows) were observed, as shown in Fig. 8-4 (c). They are much bigger than the normal microcracks in other samples. Note that most of the big cracks are connected with each other. This feature is considered to be highly detrimental to the inter-grain connectivity. The resultant superconducting fragments are isolated from each other, and eventually, very little current can pass through the entire wire, which will significantly reduce the transport performance. On further increasing the magnification, the porous structure is found in the same sample (marked by white arrows in Fig. 8-4 (d)). When the wire was heat-treated at 800 ℃, both the grain size and the mobility of the $Mg^{11}B_2$ grains were increased. The separate grains are prone to aggregate with each other, leaving plenty of

voids in the morphology. Consequently, the effective current capacity is sharply reduced with the emergence of the porous structure. This is considered to be another barrier to obtaining high transport current in $Mg^{11}B_2$ wires. In addition, this kind of microstructure with abundant voids can be more brittle and thus be more prone to fracture and form big microcracks (see Fig. 8-4 (c)) resulting from heat stress during the furnace-cooling process from high temperature to room temperature.

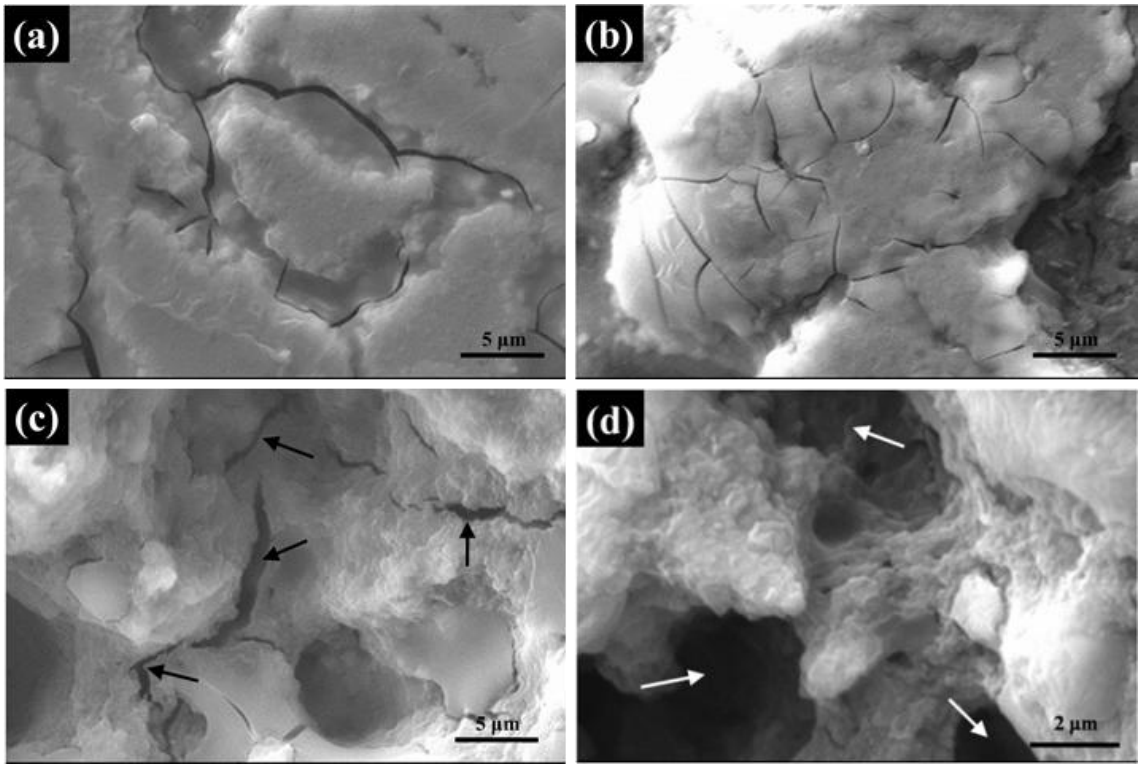

Figure 8-4. SEM micrographs of cross-sections of the $Mg^{11}B_2$ wires sintered at (a) 700 ℃, (b) 750 ℃, and (c & d) 800 ℃. Evolution of the surface morphology is clearly shown. Black arrows indicate big cracks. (d) SEM image of the wire sintered at 800 ℃ under higher magnification. White arrows indicate the porous structure in the sample.

Further SEM images were taken on the longitudinal cross-sections of the wires to characterize their macro-connectivity (as displayed in Fig. 8-5). The observed fibrous microstructure (elongated grains) is similar to the MgB_2 core images published by Shi *et al.*[18] It has to be pointed that plenty of abnormal voids with the size of 5 - 10 μm exist in the sintered at 800 ℃. It is corresponding to the porous microstructure observed in the cross-section of the same wire. Therefore, the interpretation is reinforced that the absence of the transport current in this wire is attributed to the porosity and cracks which are detrimental to the inter-grain connectivity in $Mg^{11}B_2$ wires.

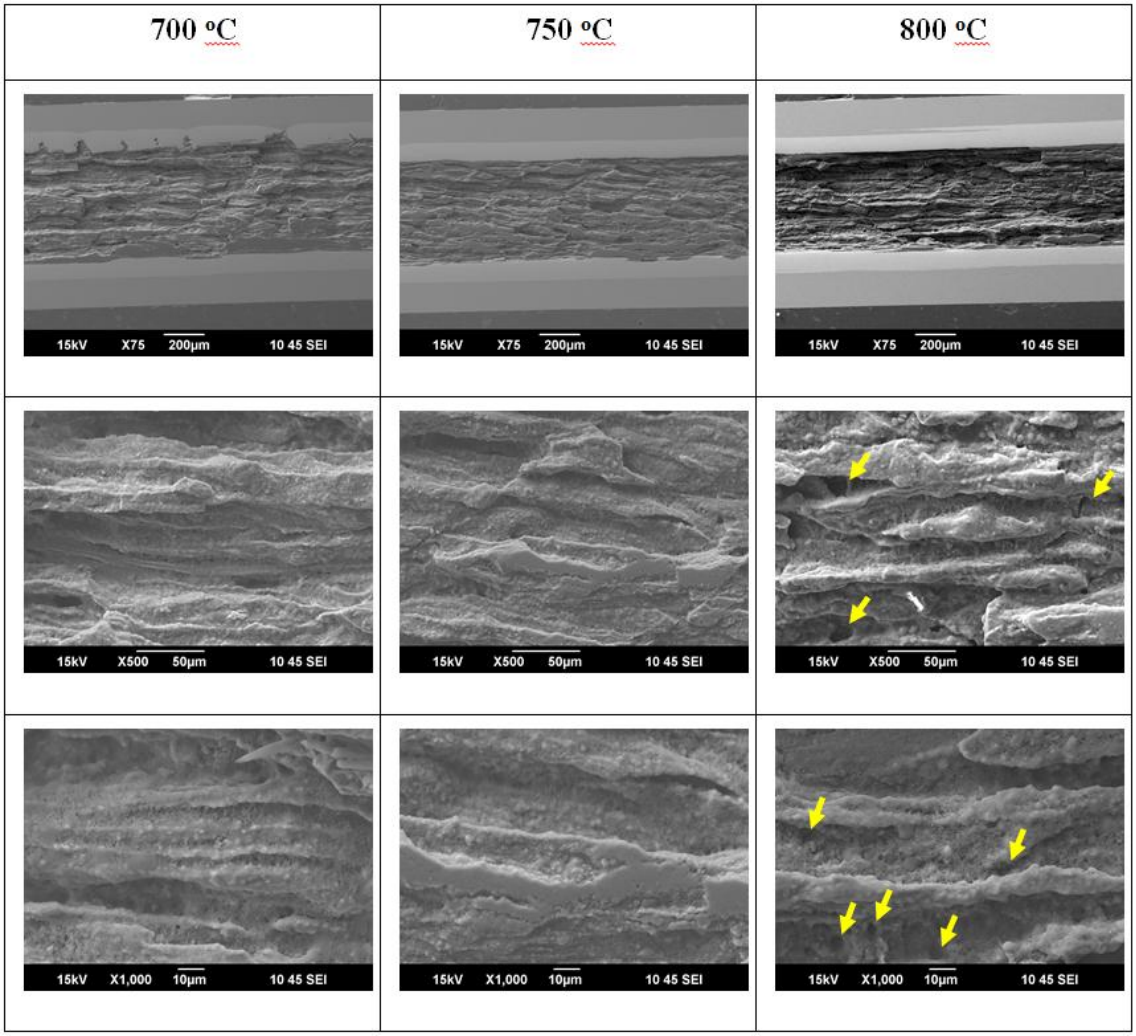

Figure 8-5. Low-magnification longitudinal cross-sections of the $Mg^{11}B_2$ wires sintered at 700 ℃, 750 ℃, and 800 ℃. The yellow arrows indicate the location of the voids.

High-resolution SEM was employed to investigate the details of the crystalline structure in the four $Mg^{11}B_2$, wires, and the results are presented in Fig. 8-6. In the sample with the lowest sintering temperature, the crystalline grains have a wide range of sizes, and all of them are dispersed in a melted matrix, as shown in Fig. 8-6 (a). Referring to the XRD results above, the melted matrix is un-reacted Mg, which cannot be fully reacted with boron at a relatively low temperature. This is strong evidence for the smaller mass fraction of $Mg^{11}B_2$ phase and lower transport performance in this sample. In the wires sintered at a higher temperature, the amount of un-reacted Mg is greatly reduced, and the $Mg^{11}B_2$ crystalline grains keep growing and form typical hexagonal shapes, which can be observed in Fig. 8-6 (b) & (c). Figure 8-6 (d) shows the morphology of the wire sintered at 800 ℃, in which some grains grow in an abnormal way with the result of the abundant amount of big clusters. These clusters are formed by the localized aggregation of $Mg^{11}B_2$ grains at the relatively high heat-treatment

temperature. This phenomenon further increases the porosity on the macroscale and significantly reduces the effective superconducting fraction for transporting current. As a result, the inter-grain connectivity is badly degraded. Combining these results with the low-magnification SEM images, it is thus concluded that the vanishing of transport current in the $Mg^{11}B_2$ sintered at high temperature should be attributed to the depression of inter-grain connectivity in the wire that is caused by the big microcracks and high porosity.

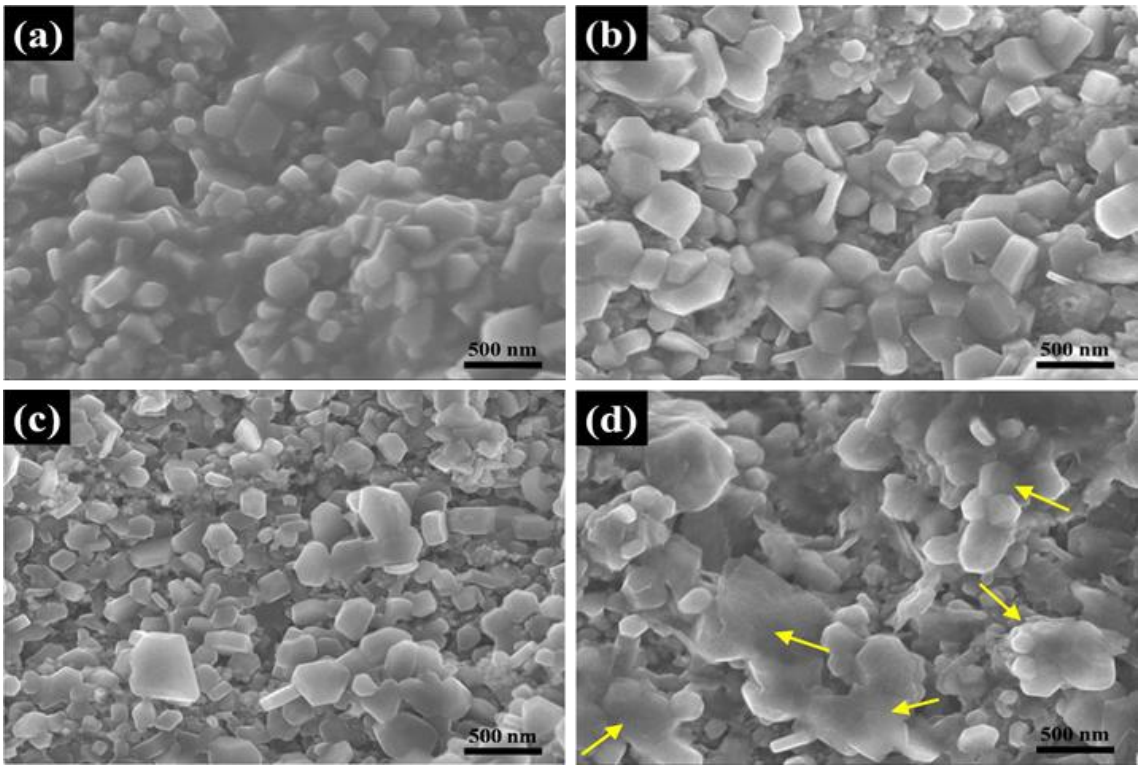

Figure 8-6. High-resolution SEM micrographs of longitudinal sections of $Mg^{11}B_2$ wires sintered at (a) 700 ℃, (b) 750 ℃, (c) 770 ℃, and (d) 800 ℃. The shapes of grains can be easily distinguished. The yellow arrows in (d) indicate clusters composed of multiple $Mg^{11}B_2$ grains.

Conclusions

The effects of sintering temperature on the superconducting performance and morphology of $Mg^{11}B_2$ monofilament wires made from isotopically pure boron powder were investigated in this work. It was found that increasing the sintering temperature led to the evolution of microstructure and characteristic changes in the transport current capacity. Un-reacted Mg and B-rich phase existed in the wire sintered at low temperature. The $Mg^{11}B_2$ fraction, as well as the transport performance, was reduced because of the un-reacted Mg and B-rich phase impurities. With increasing sintering temperature, better phase composition and crystallinity were obtained. The best transport $J_c = 2 \times 10^4$ A/cm^2 was reached at 4.2 K and 5 T in the $Mg^{11}B_2$ wire sintered

at 750 ℃. It should be noted that although high magnetic J_c was detected in the wire sintered at 800 ℃, the transport current was totally absent. The evolution of the morphology could be clearly seen in the wires corresponding to different sintering temperatures. Due to the abnormal growth and high mobility of $Mg^{11}B_2$ grains at relatively high ambient temperature, numerous big microcracks, voids, and $Mg^{11}B_2$ clusters formed in the wire sintered at 800 ℃. As a result, the inter-grain connectivity was significantly suppressed, resulting in the inferior transport performance. The results obtained in this work can be a constructive guide for fabricating $Mg^{11}B_2$ wires to be used as magnet coils in fusion reactor systems such as ITER-type tokamak magnets.

References

(1) Mitchell, N.; Bessette, D.; Gallix, R.; Jong, C.; Knaster, J.; Libeyre, P.; Sborchia, C.; Simon, F. The ITER Magnet System. *IEEE Trans. Appl. Supercond.* **2008,** *18*, 435-440.
(2) Devred, A.; Backbier, I.; Bessette, D.; Bevillard, G.; Gardner, M.; Jong, C.; Lillaz, F.; Mitchell, N.; Romano, G.; Vostner, A. Challenges and status of ITER conductor production. *Supercond. Sci. Technol.* **2014,** *27*, 044001.
(3) Noda, T.; Takeuchi, T.; Fujita, M. Induced activity of several candidate superconductor materials in a tokamak-type fusion reactor. *J. Nucl. Mater.* **2004,** *329-333*, 1590-1593.
(4) Noda, T.; Maki, K.; Takeuchi, T.; Suzuki, H.; Araki, H.; Yang, W. Induced activity and damage of superconducting materials for a fusion reactor. *Fusion Eng. Des.* **2006,** *81*, 1033-1037.
(5) Mooring, F. P.; Monahan, J. E.; Huddleston, C. M. Neutron cross sections of the boron isotopes for energies between 10 and 500 keV. *Nucl. Phys.* **1966,** *82*, 16-32.
(6) Nagamatsu, J.; Nakagawa, N.; Muranaka, T.; Zenitani, Y.; Akimitsu, J. Superconductivity at 39 K in Mg diboride. *Nature* **2001,** *410*, 63-64.
(7) Hishinuma, Y.; Kikuchi, A.; Shimada, Y.; Kashiwai, T.; Hata, S.; Yamada, S.; Muroga, T.; Sagara, A. Development of MgB_2 superconducting wire for the low activation superconducting magnet system operated around core D-T plasma. *Fusion Eng. Des.* **2015,** *98-99*, 1076-1080.
(8) Hishinuma, Y.; Kikuchi, A.; Shimada, Y.; Hata, S.; Takeuchi, T.; Yamada, S.; Sagara, A. Effect of boron particle size on microstructure and superconducting properties of in-situ Cu addition MgB_2 multifilamentary wire. *J. Phys. Conf. Ser.* **2014,** *507*, 022009.
(9) Glowacki, B. A.; Majoros, M.; Vickers, M.; Evetts, J. E.; Shi, Y.; McDougall, I. Superconductivity of powder-in-tube MgB_2 wires. *Supercond. Sci. Technol.* **2001,** *14*, 193.
(10) Matsumoto, A.; Kumakura, H.; Kitaguchi, H.; Fujii, H.; Togano, K. The annealing effects of MgB_2 superconducting tapes. *Physica C* **2002,** *382*, 207-212.
(11) Serquis, A.; Civale, L.; Hammon, D. L.; Coulter, J. Y.; Liao, X. Z.; Zhu, Y. T.; Peterson, D. E.; Mueller, F. M. Microstructure and high critical current of powder-in-tube MgB_2. *Appl. Phys. Lett.* **2003,** *82*, 1754.
(12) Markovskii L. Y. Chemistry of magnesiothermal preparation of boron. *Electron. Technol.* **1970,** *3*, 95-102.
(13) Massalski, T. B.; Okamoto, H.; R., S. P.; Kacprzak, L. *Binary Alloy Phase Diagrams*, ASM International: 1990.
(14) Chkhartishvili, L. Isotopic effects of boron. *Trends Inorg. Chem.* **2009,** *11*, 105-167.
(15) Bean, C. P. Magnetization of High-Field Superconductors. *Rev. Mod. Phys.* **1964,** *36*, 31-39.
(16) Fietz, W. A.; Webb, W. W. Hysteresis in Superconducting Alloys—Temperature and Field Dependence of Dislocation Pinning in Niobium Alloys. *Phys. Rev.* **1969,** *178*, 657-667.
(17) Takano, Y.; Oguro, N.; Kaieda, Y.; Togano, K. Superconducting properties of combustion synthesized MgB_2. *Physica C* **2004,** *412-414*, 125-129.
(18) Shi, Z. X.; Susner, M. A.; Majoros, M.; Sumption, M. D.; Peng, X.; Rindfleisch, M.; Tomsic, M. J.; Collings, E. W. Anisotropic connectivity and its influence on critical current densities, irreversibility fields, and flux creep in *in situ* processed MgB_2 strands. *Supercond. Sci. Technol.* **2010,** *23*, 045018.

Note: Chapter Publication and Text Usage Detail

Part of this Chapter has been published in *Scientific Reports* as a paper (see below reference). Part of the written text in this chapter has been taken from my published paper, as shown below.

- **W. Qiu**, H. Jie, D. Patel, Y. Lu, V. Luzin, A. Devred, M. Somer, M. Shahabuddin, J. H. Kim, Z. Ma, S. X. Dou & M. S. A. Hossain, Improvement in the transport critical current density and microstructure of isotopic $Mg^{11}B_2$ monofilament wires by optimizing the sintering temperature. *Sci. Rep.* 2016, **6,** 36660

Chapter 9

Appendix B: Publications, Presentations, Awards, and Scholarships

Publications during the Ph. D. period

1. **W. Qiu**, Z. Ma, D. Patel, L. Sang, C. Cai, M. S. A. Hossain, Z. Cheng, X. Wang, & S. X. Dou, The Interface Structure of FeSe Thin Film on CaF_2 Substrate and its Influence on the Superconducting Performance. *ACS Appl. Mater. Interfaces* 2017, **9,** 37446-37453.
2. **W. Qiu**, Z. Ma, Y. Liu, M.S.A. Hossain, X. Wang, C. Cai, & S. X. Dou, Tuning Superconductivity in FeSe Thin Films via Mg Doping. *ACS Appl. Mater. Interfaces* 2016, **8,** 7891-7896.
3. **W. Qiu**, H. Jie, D. Patel, Y. Lu, V. Luzin, A. Devred, M. Somer, M. Shahabuddin, J. H. Kim, Z. Ma, S. X. Dou, & M. S. A. Hossain, Improvement in the Transport Critical Current Density and Microstructure of Isotopic $Mg^{11}B_2$ Monofilament Wires by Optimizing the Sintering Temperature. *Sci. Rep.* 2016, **6,** 36660.
4. D. Patel, **W. Qiu**, M. Mustapic, J. Knott, Z. Ma, D. Gajda, M. Shahabuddin, J. Xu, S. Choi, M. Tomsic, S. Dou, Y. Yamauchi, J. H. Kim, & M. S. A. Hossain. Evaluation of a solid nitrogen impregnated MgB_2 racetrack coil. *Supercond. Sci. Technol.* 2018, Accepted.
5. H. Jie, **W. Qiu**, M. Billah, M. Mustapic, D. Patel, Z. Ma, D. Gajda, A. J. Morawski, T. Cetner, M. Shahabuddin, E. Yanmaz, M. Rindfleisch, J. H. Kim, & S. Hossain. Superior transport J_c obtained in in-situ MgB_2 wires by tailoring the starting materials and using a combined cold high pressure densification and hot isostatic pressure treatment. *Scripta Mater.* 2017, **129,** 79-83.
6. D. Patel, S. Hossain, **W. Qiu**, H. Jie, M. Maeda, M. Tomsic, S. Choi, & J. H. Kim. Solid cryogen: A cooling system for future MgB_2 MRI magnet. *Sci. Rep.* 2017, **7,** 43444.

7. Y. Liu, F. Cheng, **W. Qiu**, Z. Ma, S. Hossain, & S. X. Dou. High performance MgB_2 superconducting wires fabricated by improved internal Mg diffusion process at a low temperature. *J. Mater. Chem. C* 2016, **4,** 9469.
8. L. Sang, B. Shabbir, P. Maheshwari, **W. Qiu**, Z. Ma, S. Dou, C. Cai, V. Awana, & X. Wang, Hydrostatic pressure-induced huge enhancement of critical current density and flux pinning in $Fe_{1-x}Co_xSe_{0.5}Te_{0.5}$ single crystals. *Supercond. Sci. Technol.* 2018, **31,** 025009.
9. Y. Liu, F. Cheng, Q. Cai, **W. Qiu**, Y. Lu, & Z. Ma. The kinetics mechanism of MgB_2 layer formation within MgB_2 superconducting wire fabricated using improved internal Mg diffusion process. *J. Alloys Compd.* 2017, **697,** 37-42.
10. D. Patel, S. Hossain, K. W. See, **W. Qiu**, H. Kobayashi, Z. Ma, S. J. Kim, J. Hong, J. Y. Park, S. Choi, M. Maeda, M. Shahabuddin, M. Rindfleisch, M. Tomsic, S. X. Dou, & J. H. Kim. Evaluation of persistent-mode operation in a superconducting MgB_2 coil in solid nitrogen. *Supercond. Sci. Technol.* 2016, **29,** 04LT02.
11. D. Zhang, G. Zhao, P. Li, Y. Zhang, **W. Qiu**, J. Shu, Y. Jiang, S. X. Dou, & W. Sun. Readily Exfoliated $TiSe_2$ Nanosheets for High-Performance Sodium Storage. *Chem. Eur. J.* 2018, **24,** 1193-1197.
12. A. Kundu, D. Patel, N. Kumar, A. G. Panchal, **W. Qiu**, H. Jie, Z. Ma, E. Yanmaz, M. Shahabuddin, J. H. Kim, S. Pradhan, & S. Hossain. Fabrication, Transport Current Testing, and Finite Element Analysis of MgB_2 Racetrack Coils. *J. Supercond. Nov. Magn.* 2017, **30,** 2957-2962.
13. Q. Cai, Q. Guo, Y. Liu, Z. Ma, H. Li, **W. Qiu**, D. Patel, H. Jie, J. H. Kim, M. Somer, E. Yanmaz, A. Devred, V. Luzin, A. Fatehmulla, A. Farooq, D. Gajda, Y. Bando, Y. Yamauchi, S. Pradhan, & S. Hossain. Doping-Induced Isotopic $Mg^{11}B_2$ Bulk Superconductor for Fusion Application. *Energies* 2017, **10,** 409.

Presentations

1. "Tuning Superconductivity in FeSe Thin Films via Mg Doping or Fe-vacancy Disorders Controlling" (Poster), Applied Superconductivity Conference (ASC), 2016, Denver, USA.
2. "Tuning superconductivity in FeSe thin films on CaF_2 substrate via studying the interface structure, Fe-rich precipitates and metallic coating" (Poster), National Conference of Superconductivity (NCSC), 2017, Tianjin, China.

Awards

1. “2017 Postgraduate Student Excellence Award”, Institute for Superconducting and Electronic Materials (ISEM), University of Wollongong.
2. “Excellent Poster Award”, 2017 NCSC, Tianjin, China
3. “AIIM HDR Student Conference and International Travel Grants”, 2016

Scholarships

1. University Post Graduate Award (UPA), University of Wollongong
2. International Postgraduate Tuition Fee Award (IPTA), University of Wollongong